GEOSYNTHETICS FOR DEVELOPMENT OF TRANSPORTATION INFRASTRUCTURES

EDITED BY: Sujit Kumar Dash and Castorina Silva Vieira

PUBLISHED IN: Frontiers in Built Environment

frontiers Research Topics

frontiers

ISSN 1664-8714
ISBN 978-2-88966-741-3
DOI 10.3389/978-2-88966-741-3

About Frontiers

Frontiers is more than just an open-access publisher of scholarly articles: it is a pioneering approach to the world of academia, radically improving the way scholarly research is managed. The grand vision of Frontiers is a world where all people have an equal opportunity to seek, share and generate knowledge. Frontiers provides immediate and permanent online open access to all its publications, but this alone is not enough to realize our grand goals.

Frontiers Journal Series

The Frontiers Journal Series is a multi-tier and interdisciplinary set of open-access, online journals, promising a paradigm shift from the current review, selection and dissemination processes in academic publishing. All Frontiers journals are driven by researchers for researchers; therefore, they constitute a service to the scholarly community. At the same time, the Frontiers Journal Series operates on a revolutionary invention, the tiered publishing system, initially addressing specific communities of scholars, and gradually climbing up to broader public understanding, thus serving the interests of the lay society, too.

Dedication to Quality

Each Frontiers article is a landmark of the highest quality, thanks to genuinely collaborative interactions between authors and review editors, who include some of the world's best academicians. Research must be certified by peers before entering a stream of knowledge that may eventually reach the public - and shape society; therefore, Frontiers only applies the most rigorous and unbiased reviews.
Frontiers revolutionizes research publishing by freely delivering the most outstanding research, evaluated with no bias from both the academic and social point of view. By applying the most advanced information technologies, Frontiers is catapulting scholarly publishing into a new generation.

What are Frontiers Research Topics?

Frontiers Research Topics are very popular trademarks of the Frontiers Journals Series: they are collections of at least ten articles, all centered on a particular subject. With their unique mix of varied contributions from Original Research to Review Articles, Frontiers Research Topics unify the most influential researchers, the latest key findings and historical advances in a hot research area! Find out more on how to host your own Frontiers Research Topic or contribute to one as an author by contacting the Frontiers Editorial Office: frontiersin.org/about/contact

GEOSYNTHETICS FOR DEVELOPMENT OF TRANSPORTATION INFRASTRUCTURES

Topic Editors:
Sujit Kumar Dash, Indian Institute of Technology Kharagpur, India
Castorina Silva Vieira, University of Porto, Portugal

Citation: Dash, S. K., Vieira, C. S., eds. (2021). Geosynthetics for Development of Transportation Infrastructures. Lausanne: Frontiers Media SA.
doi: 10.3389/978-2-88966-741-3

Table of Contents

frontiers in Built Environment

EDITORIAL
published: 17 March 2021
doi: 10.3389/fbuil.2021.656498

Editorial: Geosynthetics for Development of Transportation Infrastructures

Sujit Kumar Dash[1]* *and Castorina Silva Vieira*[2]

[1]Department of Civil Engineering, Indian Institute of Technology Kharagpur, Kharagpur, India, [2]CONSTRUCT, Faculty of Engineering, University of Porto, Porto, Portugal

Keywords: geotechnical engineering, soil improvement, geosynthetics, transportation infrastructures, road, railway

Editorial on the Research Topic

Geosynthetics for Development of Transportation Infrastructures

BACKGROUND

Present days, several countries across the globe are making large investments in building transportation infrastructures such as highways, railways, airport runways etc. Due to scarcity of land, many times, these structures are being built over weak soils leading to design, construction and maintenance hazards. Geosynthetics in form of geogrids, geotextiles, and geocells, are being widely used to mitigate such problems. Owing to cost economy and ease of construction the reinforced soil technology finds favour with the practicing engineers. Contributions serving this special issue cover a range of topics, from evaluation of material properties, physical modelling, and numerical modelling, to reliability and sustainability analyses of reinforced soils relevant to transportation infrastructures.

OPEN ACCESS

Edited and reviewed by:
Sakdirat Kaewunruen, University of Birmingham, United Kingdom

***Correspondence:**
Sujit Kumar Dash
sujit@civil.iitkgp.ac.in

Specialty section:
This article was submitted to Transportation and Transit Systems, a section of the journal Frontiers in Built Environment

Received: *20 January 2021*
Accepted: *02 February 2021*
Published: *17 March 2021*

Citation:
Dash SK and Vieira CS (2021) Editorial: Geosynthetics for Development of Transportation Infrastructures. Front. Built Environ. 7:656498. doi: 10.3389/fbuil.2021.656498

HIGHLIGHTS OF CONTRIBUTIONS

Marques and Lins da Silva have evaluated the confined stiffness of a non-woven geotextile under different molding conditions in a lateritic soil mass, using monotonic pullout tests. It is observed that the geotextile stiffness is significantly influenced by the matrix suction and the grain size structure at its interface with the soil mass. Even under small vertical pressures, the apparent confined stiffness improves considerably compared to the unconfined stiffness which indicates that the use of the unconfined stiffness obtained by index tests may be a conservative measure in paving projects.

Through large-scale pullout tests, Ferreira et al. have observed that soil density is a key parameter for the pullout behaviour of geosynthetics reinforcements. Apart from ultimate pullout resistance it has great influence on the failure mode of the reinforcement, i.e., pullout or tensile rupture. The moisture condition too influences the pullout capacity of geosynthetics, particularly when the soil is in medium dense state. As reinforced soil embankments for railways and highways are compacted at different density and moisture conditions these observations are of significant importance.

Bhatra and Maheshwari have modelled the behaviour of rail tracks on stone column-geocell composite earth beds. To understand the influence of spacing, diameter and stiffness of stone columns on response of the system parametric studies and sensitivity analyses have been carried out. The impact of other relevant parameters such as the applied load and its velocity, the stiffness of top and bottom soil layers, the relative flexural rigidity and depth of placement of geocell has also been considered in this study. The sensitivity analyses of the rail deflection have shown that the maximum upward

deflection of top beam is not very sensitive toward variation of the relative compressibility of the soil and relative stiffness of the stone column, but exceptionally sensitive to all the other above mentioned parameters.

Hussaini and Sweta have studied the shear behaviour of geogrid-reinforced ballast-sub-ballast interface and the deformation and degradation behaviour of geogrid-reinforced ballast in railway tracks under the cyclic loading conditions. The direct shear tests results have shown that the inclusion of geogrids enhances the shear strength of ballast-sub-ballast interface and decreases the Marsal's breakage index (an index to quantify the breakage of ballast). The results of cubical triaxial tests have also revealed that the inclusion of geogrids reduces the extent of lateral displacement and vertical settlement of ballast.

Through model tests and numerical analyses Dash et al. have investigated the influence of geocell reinforcement on the performance of foundation beds. It is observed that with provision of geocell reinforcement the contact pressure on the subgrade soil reduces significantly, leading to increased bearing capacity of the foundation bed. The numerical analyses have shown that the geocells right under the footing directly sustain the surcharge loading through mobilization of their compressive stiffness and bending rigidity, whereas the end portions of the geocell mattress contribute to the performance improvement through mobilization of anchorage, derived from soil passive resistance and friction.

The experimental and numerical work reported by Hegde and Palsule has highlighted the efficacy of planar and three-dimensional geosynthetic reinforcements in improving the performance of subgrade under dynamic loads. The estimated parameters illustrated the three-fold reduction in settlement of the subgrade in the presence of reinforcement. The three-dimensional geocell reinforcement performed effectively as compared to planar geogrids under dynamic load.

Existing flexible pavement design procedures based on Layer Coefficient Ratio (LCR) and Traffic Benefit Ratio (TBR) values have been extended to the design of geogrid-reinforced flexible pavements by Goud et al. This study has shown that the geogrid reinforcement can reduce the thickness of granular base and subbase layers by at least 10–45% for subgrades with CBR <5%, and the thickness of the bituminous layer by at least 7%. A reduction of the embodied carbon generated by the construction in the range of 58–85 tCO_2 e/km has also been reported for geogrid-reinforced pavements in comparison with unreinforced pavements.

Reinforced soil structures are often affected by uncertainties related to material properties. Through reliability analysis, Belo and Lins da Silva have studied the influence of such uncertainties in the stability of reinforced soil embankments. The results obtained can be of use in the design and construction of railways and highways on embankments.

Choudhuri and Chakraborty have studied the influence of spatial variability of soil properties on the probabilistic bearing capacity of roadway pavement supported on fibre reinforced earth embankment. The importance of considering spatial variability of the soil shear strength and that of the out of plane length of the embankment are among the main conclusions of their study.

SUMMARY

The findings of the studies presented in this issue open up new horizons for application of reinforced geosynthetics in design and construction of transportation infrastructures, worldwide. We, editors, hope that the readers will find these contributions valuable.

AUTHOR CONTRIBUTIONS

All authors listed have made a substantial, direct, and intellectual contribution to the work and approved it for publication.

Conflict of Interest: The authors declare that the research was conducted in the absence of any commercial or financial relationships that could be construed as a potential conflict of interest.

frontiers in Built Environment

ORIGINAL RESEARCH
published: 16 October 2019
doi: 10.3389/fbuil.2019.00122

Modeling of Rail Tracks on Stone Column Reinforced Tensionless Foundations

*Shashank Bhatra and Priti Maheshwari**

Department of Civil Engineering, Indian Institute of Technology Roorkee, Roorkee, India

This research investigates the response of rails on geocell-stone column composite reinforced foundation beds under a moving load. Improved earth bed has been considered to respond only to compressive forces. The granular mat below the rail has been idealized as a Pasternak shear layer and geocell reinforcement as an infinite beam with finite bending stiffness. Soft soil and stone columns have been symbolized by Winkler springs of different stiffnesses. Analysis has been carried out with due consideration to viscous damping in the system. The governing differential equations have been established and simplified for general use with the help of dimensionless parameters. These equations have been solved in presence of appropriate boundary conditions by utilizing Finite difference method in combination with iterative Gauss-Seidel procedure. Inclusion of stone columns has been observed to significantly affect the onset of separation between rail and the soil layer underneath. Various parameters namely, applied load and its velocity, stiffnesses of top, bottom soil layers and stone columns, damping ratio, relative flexural rigidity, depth of placement of geocell, configuration of stone columns have been found to affect the response of soil-foundation system significantly. Improvement in the properties of soil by means of higher value of relative compressibility resulted in typical reduction of 50% in maximum deflection. It has been observed that the region of detachment reduces on increasing the depth of placement of the bottom beam. Sensitivity analysis highlighted the greater sensitivity of upward deflection as compared to the downward deflection of rail with respect to all the parameters except for relative compressibility of the soil and relative stiffness of the stone columns.

Keywords: rail tracks, tensionless foundation, moving load, geocell, stone columns

OPEN ACCESS

Edited by:
Castorina Silva Vieira, University of Porto, Portugal

Reviewed by:
Amarnath M. Hegde, Indian Institute of Technology Patna, India
Sireesh Saride, Indian Institute of Technology Hyderabad, India

****Correspondence:***
Priti Maheshwari
priti_mahesh2001@yahoo.com

Specialty section:
This article was submitted to Transportation and Transit Systems, a section of the journal Frontiers in Built Environment

Received: *25 July 2019*
Accepted: *02 October 2019*
Published: *16 October 2019*

Citation:
Bhatra S and Maheshwari P (2019) Modeling of Rail Tracks on Stone Column Reinforced Tensionless Foundations. Front. Built Environ. 5:122. doi: 10.3389/fbuil.2019.00122

INTRODUCTION

With the rapid infrastructural development worldwide, use of ground improvement techniques has increased drastically to enhance the suitability of construction activities over soft soils. Increased speed of trains in case of high-speed rail transportation systems may result in excessive settlement near poor soil strata. In this regard, various case studies have reported the utilization of appropriate ground improvement techniques like geosynthetic reinforcement layer, stone columns, prefabricated vertical drains (PVD) etc. (Arulrajah et al., 2009; Zhuang and Wang, 2017; Cui et al., 2018). Amongst the available techniques, stone columns and geosynthetic reinforcement have gained more popularity amongst geotechnical engineers due to their overall economy and ease in construction.

For unreinforced foundation beds, train-track-soil dynamic interaction have been studied by representing the system as an infinite beam resting on one or two parameter foundation system subjected to concentrated moving load (Kenney, 1954; Fryba, 1972; Kerr, 1974; Duffy, 1990; Jaiswal and Iyengar, 1997; Mallik et al., 2006; Basu and Rao, 2013). However, none of these studies considered ground improvement and therefore, may not be suitable in case of weak strata. In order to take care of this issue, Maheshwari and Khatri (2013) studied behavior of rails for improved ground i.e., geosynthetic membrane and stone column reinforced composite foundation.

Many researchers have carried out experimental and numerical studies to develop better understanding of these techniques. The experimental study conducted by Raymond (2002) and Indraratna et al. (2015) indicated the importance of bending stiffness of the reinforcement layer which can be incorporated in analytical models by idealizing it as a beam. This consideration results in a double beam model which were used to simulate pavement or foundation beam lying over geocell improved earth bed subjected to static load (Maheshwari and Viladkar, 2009; Zhao et al., 2016; Zhang et al., 2018). Other engineering systems were also studied by utilizing such models to understand the behavior of response under moving load considering perfect contact between the top beam and neighboring material (Hussein and Hunt, 2006; Yuan et al., 2009; Auersch, 2012; Mohammadzadeh et al., 2014; Deng et al., 2017).

Nevertheless, all above-mentioned studies considered the foundation bed to be in perfect contact with the infinite beam. As the soil essentially reacts only in compression, the above consideration contradicts the actual scenario where the rail is found to show a tendency to lift off the ground at rear as well as in front of applied load. Some of the works that considers this tensionless behavior for unreinforced earth beds include Rao (1974), Torby (1975), Lin and Adams (1987), Coşkun (2000), Chen and Chen (2011) and He et al. (2016) among others. For reinforced earth beds, Maheshwari et al. (2004, 2005) considered the tensionless foundations for geosynthetic membrane reinforced earth bed. Bhatra and Maheshwari (2019) considered finite bending stiffness of geosynthetics. Further, Maheshwari (2014) studied effect of inclusion of stone columns in such systems.

Review of literature shows that although analysis of infinite beams subjected to moving load for stone columns has already been carried out, the combined application of it with geocell is yet to be explored for such systems. In view of this, the authors proposed studying the behavior of rails under moving load on stone column-geocell composite earth beds which reacts to compressive forces only. Detailed parametric study and sensitivity analysis has been carried out to understand the influence of spacing, diameter and stiffness of stone columns on response of the system. The impact of other parameters like applied load and its velocity, stiffnesses of top and the bottom soil layers, damping, relative flexural rigidity, and depth of placement of geocell on the proposed system has also been presented in the study.

Few assumptions have been made in modeling and analysis of the system: (i) some components like cross-ties could not be modeled employing the present approach, (ii) degradation in the properties of geocell and granular material between rail and the geocell with time has not been considered, (iii) quasi-stationery state has been considered, (iv) smear effect due to installation of stone columns has been neglected. Although, the employed approach has few limitations, however, analysis being simple, it is easier to get an overall picture of the response of soil-foundation system under consideration. Detailed parametric study helps in getting the idea about effect of various parameters and accordingly track design can be carried out.

MODELING

Figure 1 represents the longitudinal section of a rail lying on granular mat and stone column-geocell composite improved soft soil bed. The rail as well as geocell composite with infill soil have been represented as infinite beams with flexural rigidity E_1I_1, E_2I_2 and mass per unit length ρ_1, ρ_2, respectively. The interface resistance for the beams with the soil has been assumed to be zero. The granular fill has been sandwiched between these two infinite beams having thickness h and shear modulus G. Stone columns with diameter, d and spacing, s have symmetrically been placed below the bottom beam. The applied load Q, has been considered to move with constant velocity v. Flexural responses of beams have to be determined and the effect of various parameters needed to be discussed.

ANALYSIS

The conceptual idealization of physical model (**Figure 2**) depicts the granular mat by a Pasternak shear layer (Selvadurai, 1979). The compressible nature of the fill/mat has been represented by stiffness k_1. The poor soil and stone columns have been represented as Winkler springs of stiffnesses $k_2 = k_s$ and $k_2 = k_c$, respectively. Viscous damping coefficients $c_1$and c_2 for upper and the lower soil layers, respectively, have also been considered in the analysis. An evenly distributed surcharge load $\gamma_1 h$ over the full length of bottom beam has been accounted for, where h denotes the location of reinforcing beam with respect to top beam and $\gamma_1$is the unit weight of the granular fill material. It is evident for track foundation system that when the load moves, rail tends to rise up at certain regions due to its inherent bending stiffness leading to its separation from the soil below. To include this effect appropriate contact conditions have been considered in the analysis.

The governing differential equation of motion based on the idealized model for top and the bottom beam can be expressed as: -

$$E_1I_1\frac{\partial^4 y_1}{\partial x^4} + \rho_1\frac{\partial^2 y_1}{\partial t^2} + j(x,t)\left[c_1\frac{\partial(y_g - y_2)}{\partial t} + k_1(y_g - y_2) - Gh\frac{\partial^2(y_g - y_2)}{\partial x^2}\right] = Q(x,t) + \rho_1 g \quad (1)$$

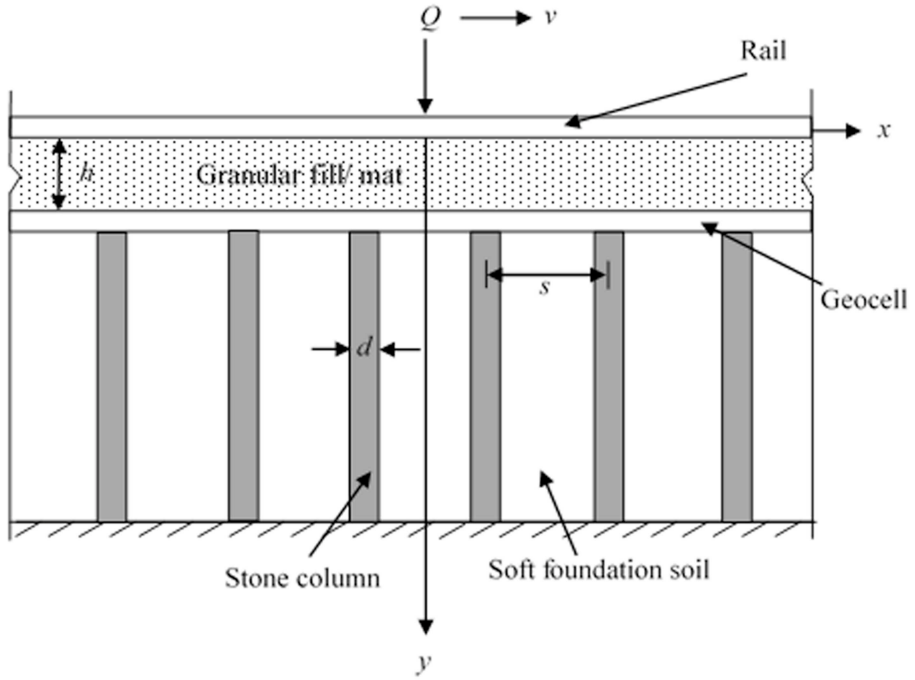

FIGURE 1 | Longitudinal section of rail resting on geocell-stone column composite reinforced earth bed.

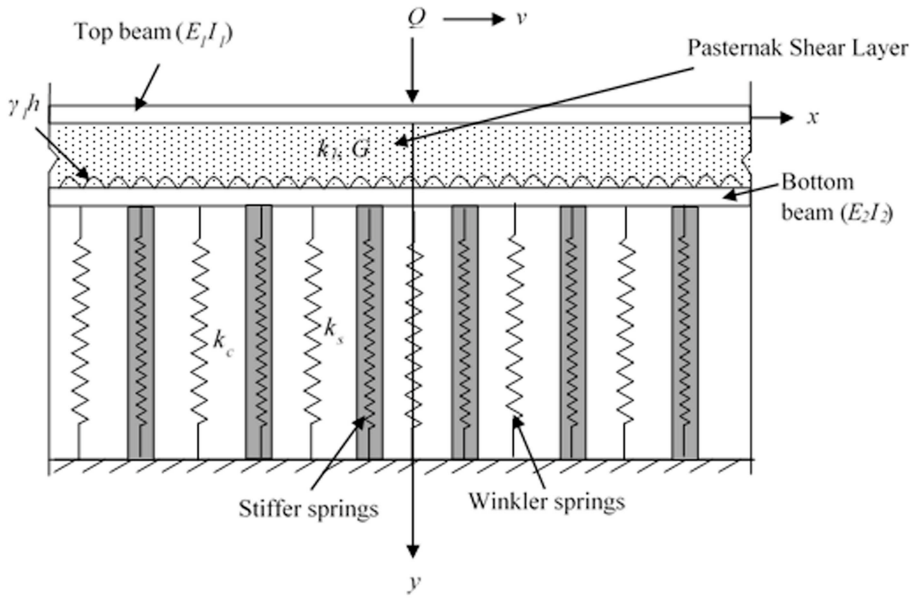

FIGURE 2 | Idealized representation of the problem.

$$E_2I_2\frac{\partial^4 y_2}{\partial x^4}+\rho_2\frac{\partial^2 y_2}{\partial t^2}+c_2\frac{\partial y_2}{\partial t}+k_2y_2-j(x,t)\left[c_1\frac{\partial(y_g-y_2)}{\partial t}+k_1(y_g-y_2)-Gh\frac{\partial^2(y_g-y_2)}{\partial x^2}\right]=\gamma_1 h+\rho_2 g \quad (2)$$

Where, the deflections of top and the bottom beam have been denoted by y_1 and y_2, respectively, and deflection of ground surface by y_g. g is the acceleration due to gravity and a contact function $j(x,t)$ has been included in the equations to represent the tensionless behavior of the soil. Also, it should be noted

that $k_2 = k_s$ in soft soil region and $k_2 = k_c$ within the stone column region.

The separation between top beam and the geocell-stone column composite foundation soil can be mathematically expressed as:

$$\left.\begin{array}{l}\text{When } y_1 \geq 0, j(x,t) = 1 \text{ and } y_g = y_1\\ \text{and when } y_1 < 0, j(x,t) = 0 \text{ and } y_g = y_2\end{array}\right\} \quad (3)$$

Solution of Developed Equations

In order to simplify the problem, a new variable ξ has been defined as $\xi = x–vt$, i.e., the distance from point of action of load in the quasi-stationary state. Equations (1) and (2) can now be modified as

$$E_1 I_1 \frac{d^4 y_1}{d\xi^4} + \rho_1 v^2 \frac{d^2 y_1}{d\xi^2} + j(\xi)\left[-c_1 v \frac{d(y_g - y_2)}{d\xi} + k_1(y_g - y_2) - Gh\frac{d^2(y_g - y_2)}{d\xi^2}\right] = Q(\xi) + \rho_1 g \quad (4)$$

and

$$E_2 I_2 \frac{d^4 y_2}{d\xi^4} + \rho_2 v^2 \frac{d^2 y_2}{d\xi^2} - c_2 v \frac{dy_2}{d\xi} + k_2 y_2 - j(\xi)\left[-c_1 v \frac{d(y_g - y_2)}{d\xi} + k_1(y_g - y_2) - Gh\frac{d^2(y_g - y_2)}{d\xi^2}\right] = \gamma_1 h + \rho_2 g \quad (5)$$

The above equations can be rephrased by utilizing the dimensionless parameters mentioned below:

$\xi^* = \frac{\xi}{L}$; $Y_1 = \frac{y_1}{L}$; $Y_2 = \frac{y_2}{L}$; $Y_g = \frac{y_g}{L}$; $\rho_1^* = \frac{\rho_1 v^2}{k_1 L^2}$; $\rho_2^* = \frac{\rho_2 v^2}{k_2 L^2}$; $I_1^* = \frac{E_1 I_1}{k_1 L^4}$; $I_2^* = \frac{E_2 I_2}{k_2 L^4}$; $c_1^* = \frac{c_1 v}{k_1 L}$; $c_2^* = \frac{c_2 v}{k_2 L}$; $Q^* = \frac{Q}{k_1 L^2}$; $G^* = \frac{Gh}{k_1 L^2}$; $w_1^* = \frac{\rho_1 g}{k_1 L}$; $w_2^* = \frac{\rho_2 g}{k_2 L}$; $\gamma_1^* = \frac{\gamma_1}{k_2}$; $H = \frac{h}{L}$; $r = \frac{k_1}{k_2}$; $R = \frac{E_1 I_1}{E_2 I_2}$ and $\alpha = \frac{k_c}{k_s}$, where L is half length of the beam. Thus, the generalized differential Equations (4) and (5) in non-dimensional form can be expressed as:

$$\frac{d^4 Y_1}{d\xi^{*4}} + \frac{\rho_1^*}{I_1^*}\frac{d^2 Y_1}{d\xi^{*2}} + \frac{j(\xi^*)}{I_1^*}\left[(Y_g - Y_2) - c_1^*\frac{d(Y_g - Y_2)}{d\xi^*} - G^*\frac{d^2(Y_g - Y_2)}{d\xi^{*2}}\right] = \frac{Q^*(\xi^*)}{I_1^* d\xi^*} + \frac{w_1^*}{I_1^*} \quad (6)$$

and

$$\frac{d^4 Y_2}{d\xi^{*4}} + \frac{\rho_2^*}{I_2^*}\frac{d^2 Y_2}{d\xi^{*2}} - \frac{c_2^*}{I_2^*}\frac{dY_2}{d\xi^*} + \frac{Y_2}{I_2^*} - \frac{j(\xi^*)r}{I_2^*}\left[(Y_g - Y_2) - c_1^*\frac{d(Y_g - Y_2)}{d\xi^*} - G^*\frac{d^2(Y_g - Y_2)}{d\xi^{*2}}\right] = \frac{w_2^*}{I_2^*} + \frac{\gamma_1^* H}{I_2^*} \quad (7)$$

Equations (6) and (7) are discretised for an internal node, i using finite difference method and can be written as:

$$Y_{1,i} = \frac{1}{A_2}\left[\frac{Q^*(\Delta\xi^*)^3}{I_1^*} + \frac{w_1^*(\Delta\xi^*)^4}{I_1^*} - (Y_{1,i+2} + A_1 Y_{1,i+1} + A_1 Y_{1,i-1} + Y_{1,i-2} + A_3 Y_{2,i+1} + A_4 Y_{2,i} + A_5 Y_{2,i-1} + A_6 Y_{g,i+1} + A_7 Y_{g,i} + A_8 Y_{g,i-1})\right] \quad (8)$$

and

$$Y_{2,i} = \frac{1}{B_2}\left[\frac{\gamma_1^* H(\Delta\xi^*)^4}{I_2^*} + \frac{w_2^*(\Delta\xi^*)^4}{I_2^*} - (Y_{2,i+2} + B_1 Y_{2,i+1} + B_3 Y_{2,i-1} + Y_{2,i-2} + B_4 Y_{g,i+1} + B_5 Y_{g,i} + B_6 Y_{g,i-1})\right] \quad (9)$$

Where,

$$A_1 = \frac{1}{I_1^*}\left[-4I_1^* + \rho_1^*(\Delta\xi^*)^2\right];$$

$$A_2 = \frac{1}{I_1^*}\left[6I_1^* - 2\rho_1^*(\Delta\xi^*)^2\right];$$

$$A_3 = \frac{j(\xi^*)}{I_1^*}\left[0.5c_1^*(\Delta\xi^*)^3 + G^*(\Delta\xi^*)^2\right];$$

$$A_4 = \frac{j(\xi^*)}{I_1^*}\left[-(\Delta\xi^*)^4 - 2G^*(\Delta\xi^*)^2\right];$$

$$A_5 = \frac{j(\xi^*)}{I_1^*}\left[-0.5c_1^*(\Delta\xi^*)^3 + G^*(\Delta\xi^*)^2\right];$$

$$A_6 = \frac{j(\xi^*)}{I_1^*}\left[-0.5c_1^*(\Delta\xi^*)^3 - G^*(\Delta\xi^*)^2\right];$$

$$A_7 = \frac{j(\xi^*)}{I_1^*}\left[(\Delta\xi^*)^4 + 2G^*(\Delta\xi^*)^2\right];$$

$$A_8 = \frac{j(\xi^*)}{I_1^*}\left[0.5c_1^*(\Delta\xi^*)^3 - G^*(\Delta\xi^*)^2\right];$$

$$B_1 = \frac{1}{I_2^*}\left[-4I_2^* + \rho_2^*(\Delta\xi^*)^2 - 0.5c_2^*(\Delta\xi^*)^3 - j(\xi^*)r\left\{0.5c_1^*(\Delta\xi^*)^3 + G^*(\Delta\xi^*)^2\right\}\right];$$

$$B_2 = \frac{1}{I_2^*}\left[6I_2^* - 2\rho_2^*(\Delta\xi^*)^2 + (\Delta\xi^*)^4 + j(\xi^*)r\left\{(\Delta\xi^*)^4 + 2G^*(\Delta\xi^*)^2\right\}\right];$$

$$B_3 = \frac{1}{I_2^*}\left[-4I_2^* + \rho_2^*(\Delta\xi^*)^2 + 0.5c_2^*(\Delta\xi^*)^3 + j(\xi^*)r\left\{0.5c_1^*(\Delta\xi^*)^3 - G^*(\Delta\xi^*)^2\right\}\right];$$

$$B_4 = \frac{j(\xi^*)r}{I_2^*}\left[0.5c_1^*(\Delta\xi^*)^3 + G^*(\Delta\xi^*)^2\right];$$

$$B_5 = \frac{j(\xi^*)r}{I_2^*}\left[-(\Delta\xi^*)^4 - 2G^*(\Delta\xi^*)^2\right];$$

$$B_6 = \frac{j(\xi^*)r}{I_2^*}\left[-0.5c_1^*(\Delta\xi^*)^3 + G^*(\Delta\xi^*)^2\right]$$

Mathematical expressions in Equation (3) can be modified as:

$$\left.\begin{array}{l}\text{For } Y_{1,i} \geq 0, j(\xi^*) = 1 \text{ and } Y_{g,i} = Y_{1,i}\\ \text{and when } Y_{1,i} < 0, j(\xi^*) = 0 \text{ and } Y_{g,i} = Y_{2,i}\end{array}\right\} \quad (10)$$

Boundary Conditions

Extent of the beams has been considered such that it behaves as an infinite beam (Selvadurai, 1979). Boundary conditions has been assumed according to Vlasov and Leontiev (1966) so as to obtain the solution of developed equation systems. The boundary conditions in non-dimensional form have been represented as:

For the top beam

$$\left.\begin{array}{l} \frac{d^3Y_1}{d\xi^{*3}} - \frac{G^*}{I_1^*}\frac{d(Y_g - Y_2)}{d\xi^*} = 0 \\ \frac{d^2Y_1}{d\xi^{*2}} = 0 \end{array}\right\} \quad (11)$$

For the bottom beam

$$\left.\begin{array}{l} \frac{d^3Y_2}{d\xi^{*3}} + \frac{rG^*}{I_2^*}\frac{d(Y_g - Y_2)}{d\xi^*} = 0 \\ \frac{d^2Y_2}{d\xi^{*2}} = 0 \end{array}\right\} \quad (12)$$

Convergence Study and Input Parameter Details

Based on the mathematical model established above, a computer code has been developed. The entire extent of track-foundation system ($-L \leq x \leq L$) has been discretised by utilizing finite difference method. It has been found that there is negligible change (<1–2%) in the deflection profile when the number of nodes is increased from 5,001 to 8,001 nodes. Hence, the mesh with 5,001 nodes has been considered for the analysis. The tolerance factor has been specified to be 10^{-6} for the analysis based on convergence study.

The range of parameters have been assumed as per the Indian railway track conditions and the values considered have been given in **Table 1**. The magnitude of viscous damping (c_1 and c_2) has been calculated with the help of the following expressions:

$$c_1 = 2\zeta_1\sqrt{k_1\rho_1} \; and \; c_2 = 2\zeta_2\sqrt{k_2\rho_2} \quad (13)$$

RESULTS AND DISCUSSION

Validation

In the absence of experimental data in existing literature for validation purpose, the same has been done by comparing the results with those given by Hussein and Hunt (2006). The latter discussed and analyzed floating slab track model to determine the behavior of response and critical velocity of the system by utilizing Fourier transformation method. In the study, a plot of displacement of the rails vs. velocity of applied load was obtained for the following set of parameters: $E_1I_1 = 10 \times 10^6$ N-m^2, $E_2I_2 = 1{,}430 \times 10^6$ N-m^2, $\rho_1 = 100$ kg/m, $\rho_2 = 3{,}500$ kg/m, $k_1 = 40 \times 10^6$ N/m^2, $k_2 = 50 \times 10^6$ N/m^2, $\zeta_1 = \zeta_2 = 5\%$, as considered by Hussein and Hunt (2006), to estimate critical velocity of the system. In order to verify proposed formulation, response obtained by current study for the similar conditions has been plotted and good agreement has been observed between the results as shown in **Figure 3**. Thus, verifying the adopted solution technique and methodology.

TABLE 1 | Input parameters.

Parameters	Notation	Value	Unit
Applied load	Q	100–250 (Bhatra and Maheshwari, 2019)	kN
Mass per unit length of the top beam	ρ_1	60 (Bhatra and Maheshwari, 2019)	kg/m
Mass per unit length of the bottom beam	ρ_2	43 (Indraratna et al., 2015)	kg/m
Relative compressibility of soil	$r = k_1/k_2$	5–20 (Das, 1999)	–
Relative stiffness of stone column with respect to surrounding soil	$\alpha = k_c/k_s$	10–100 (Das, 1999)	–
Diameter of the stone column	d	0.12–1.2 (IS 15284 (Part 1), 2003)	m
Spacing to diameter ratio of the stone columns	s/d	2–4 (IS 15284 (Part 1), 2003)	–
Relative flexural rigidity of the beams	$R = E_1I_1/E_2I_2$	2,400–5,400 (Shahu et al., 2000; Bhatra and Maheshwari, 2019)	–
Damping ratio	ζ	0–25 (Vucetic and Dobry, 1991)	%

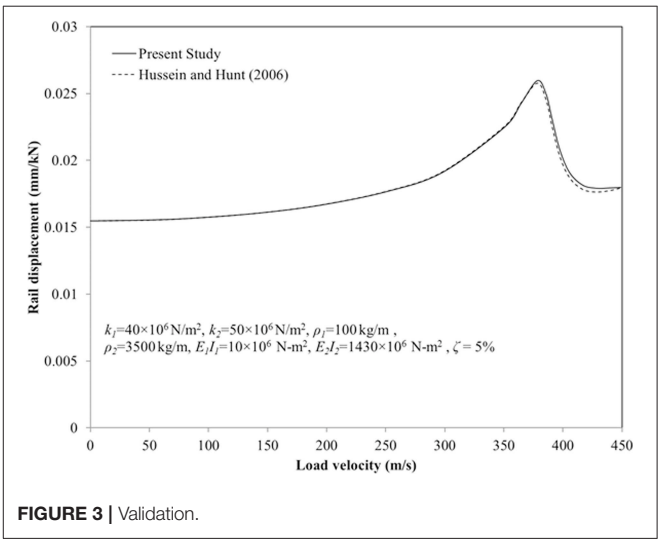

FIGURE 3 | Validation.

When top beam is getting lifted from the ground surface due to tensionless nature of the foundation, the deflection in upward direction has been taken as negative deflection for presenting all the results.

Ground Improvement

The effect of inclusion of stone column on deflection profile of top beam for the parameters: $Q = 175$ kN, $v = 36$ m/s, $k_1 = 150$ MN/m^3, $r = 10$, $E_1I_1 = 4{,}470$ kN-m^2, $R = 3{,}000$, $G = 650$ kN/m^2, $\gamma = 18$ kN/m^3, $\rho_1 = 60$ kg/m, $\rho_2 = 43$ kg/m, $\zeta = 10\%$, $h = 0.15$ m, $\alpha = 25$, $s/d = 2.5$, and $d/L = 0.004$ has been shown in **Figure 4**. It has been observed that maximum non-dimensional deflection of top beam reduces by 58% indicating substantial

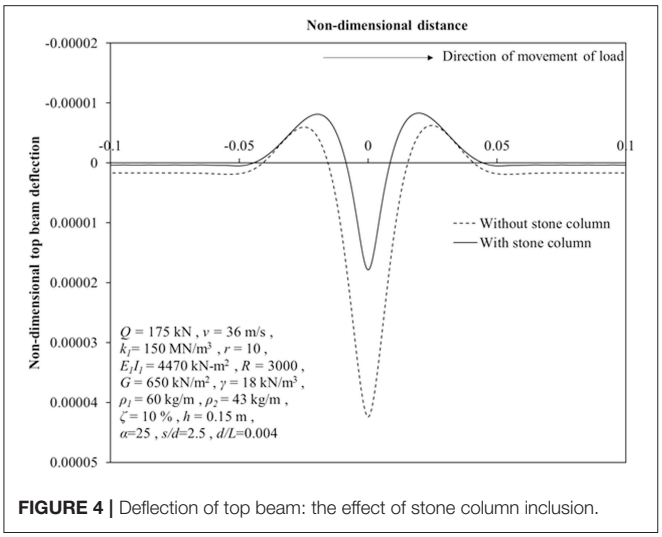

FIGURE 4 | Deflection of top beam: the effect of stone column inclusion.

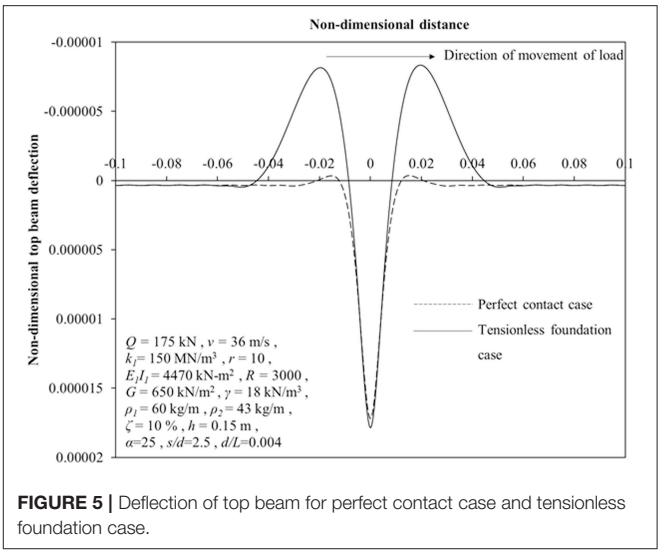

FIGURE 5 | Deflection of top beam for perfect contact case and tensionless foundation case.

improvement of the earth bed upon inclusion of stone columns. Furthermore, uplift of top beam has been observed to increase by 33% due to inclusion of stone columns.

Influence of Tensionless Nature of Foundation

Figure 5 presents the comparison between normalized deflection profiles of top beam for tensionless foundation case with that for the perfect contact case (i.e., foundation reacts both in compression and tension). The value of parameters considered have been stated in the figure. It has been found that the maximum downward normalized deflection is mildly affected showing an increase from 1.72×10^{-5} to 1.79×10^{-5} i.e., only 4%, when the earth bed is considered to react only in compression. However, the maximum normalized upward deflection has been significantly affected due to tensionless behavior of foundation showing an increase from 3.6×10^{-7} to 8.3×10^{-6}. It is evident that on considering tensionless behavior of the foundation bed, the maximum normalized upward deflection is immensely affected compared to the maximum normalized downward deflection. In view of this, tensionless behavior of soil should be considered while analyzing such systems.

Parametric Study

Magnitude of Moving Load (*Q*)

Figures 6, **7** present the effect of magnitude of moving load on deflection and the bending moment profiles of top beam, respectively, for input parameters mentioned in the figures. It has been found that maximum downward as well as upward deflection reduces by 60 and 83%, respectively, when the magnitude of moving load is varied from 250 to 100 kN. Also, for the same variation, a reduction of 61 and 51% has been observed for maximum positive and negative bending moment in top beam.

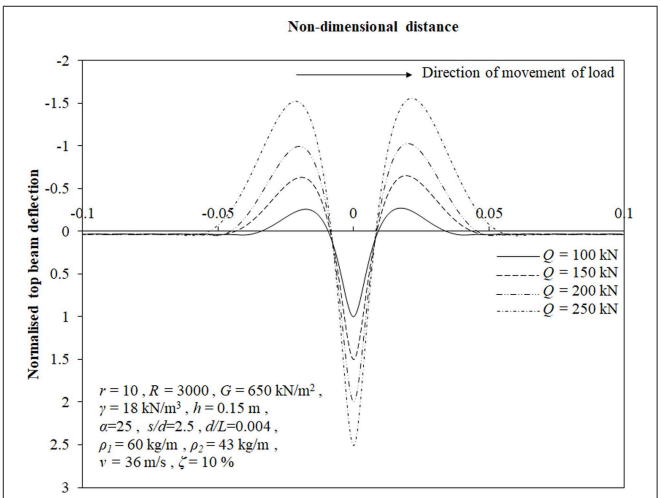

FIGURE 6 | Deflection of top beam for various magnitudes of applied load.

On further investigation with the same set of input values, it has been found that top beam begins to lift off the ground at a lower value of $Q = 68$ kN with the inclusion of stone columns. Without stone column, the onset of detachment has been observed at a higher value, $Q = 124$ kN which may be due to the reduced stiffness of the system which allowed more downward deflection of the top beam.

Relative Compressibility of Soil (*r*)

Figure 8 shows the result of variation in relative compressibility of soil on the deflection profile of the top beam. An increase of 48 and 12% in maximum downward and upward deflection of the top beam, respectively, has been found corresponding to an increase in ratio, *r* from 5 to 20. It can be concluded from these results that the downward deflection of top beam is more affected by the above variation compared to upward deflection which has further been discussed during the sensitivity analysis.

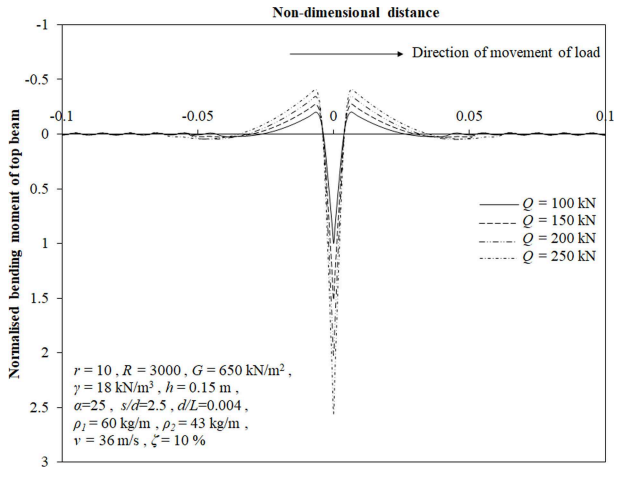

FIGURE 7 | Bending moment profile of top beam for various magnitudes of applied load.

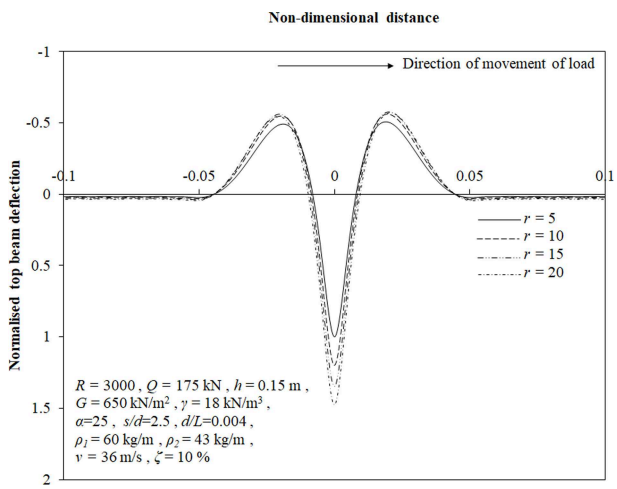

FIGURE 8 | Deflection profile of top beam at different values of *r*.

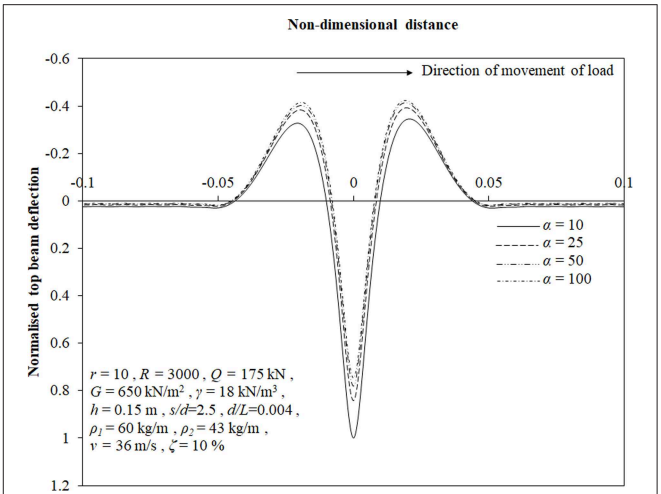

FIGURE 9 | Deflection profile of top beam for various values of α.

Relative Stiffness of Stone Columns (α)

Deflection profile of the top beam for different values of α has been presented in **Figure 9**. On increasing α from 10 to 100, maximum downward deflection has been found to decrease by 25% whereas maximum upward deflection has been observed to increase by 22%. It has been observed that for higher increment of α i.e., from 50 to 100, the decrease in maximum downward deflection in only 4% as compared to 16% reduction when α is increased from 10 to 25. For the similar variation, increment of 2 and 14%, respectively, has been observed for maximum upward deflection. From these observations, it can be concluded that at a higher value of α, effect of its increment diminishes on the deflection.

Configuration of Stone Columns

The influence of variation in spacing at a specific diameter on deflection profile of the top beam has been presented in **Figure 10A**. On varying *s/d* ratio from 3.5 to 2, maximum downward and upward deflection has been found to decrease by 50 and 75%, respectively. This decrement in deflection for both the directions is justified as the number of stone columns increases on reducing *s/d* ratio.

Figure 10B describes the effect of variation in diameter of stone columns on deflection profile of top beam for the set of input values stated in the figure. It has been found that maximum downward and upward deflection nominally decreases by 1.5 and 7%, respectively, when *d/L* ratio is increased from 0.0008 to 0.0016. However, on further increase in *d/L* ratio to 0.0048 and 0.008, the maximum deflection values increase by 58 and 80%, respectively. This may be due to the fact that now sufficient amount of soft soil material has been replaced by stiffer stone columns and in spite of reduction in number of stone columns, the deflections reduce upon increasing the diameter of stone columns.

Relative Flexural Rigidity of Beams (*R*)

Figure 11 shows the influence of relative flexural rigidity of beams on the deflection profile of top beam for considered set of input parameters. It has been found that maximum downward and upward deflection reduce by 28% and 66% on increasing ratio, *R* from 2,400 to 5,400. This reduction may be because higher values of *R* denotes lower flexibility of the top beam and consequently, the lower deflections.

Depth of Placement of Lower Beam (*h*)

Figure 12 presents the effect of location of bottom beam on the deflection profile of top beam. It has been observed that the variation in depth of bottom beam have substantial effect on upward deflection compared to the downward deflection which is negligibly affected. As the location of bottom beam has been varied from 0.05 to 0.45 m, maximum upward deflection of top beam has been found to reduce by 29%. It has also been observed that region of separation between top beam and the ground reduces on lowering the bottom beam till $h = 0.57$ m beyond which perfect contact is developed between them.

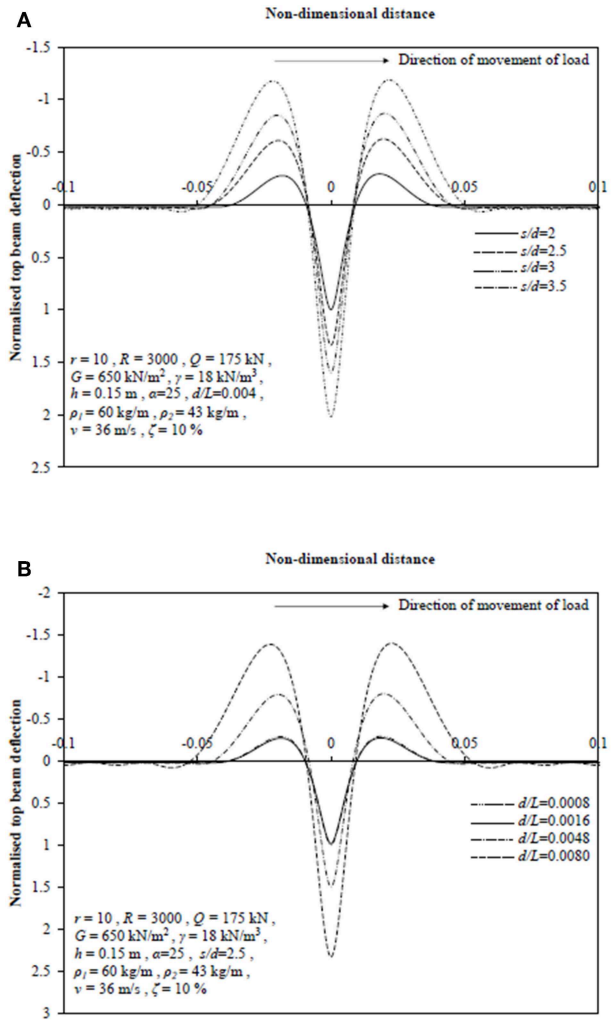

FIGURE 10 | (A) Deflection of top beam at different *s/d* values. **(B)** Deflection of top beam for various *d/L* values.

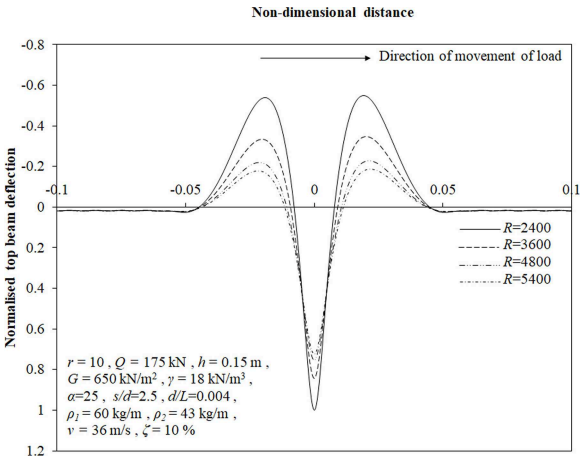

FIGURE 11 | Deflection of top beam at different values of *R*.

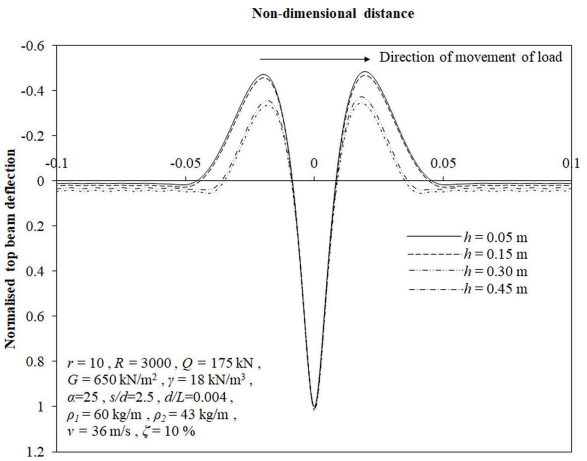

FIGURE 12 | Deflection of top beam for different depths of placement of the bottom beam.

Velocity of Applied Load (*v*)

Figure 13 shows the influence of velocity of moving load on deflection profile of the top beam. The maximum downward deflection of the top beam has been observed to increase by only 3% due to variation in load velocity from 0 to 80 m/s. However, the maximum upward deflection increases by 7% when *v* is increased from 0 to 40 m/s and shoots up to 22% increment on increasing the load velocity to 80 m/s.

Damping Ratio (ζ)

At lower velocity, it has been observed that bending of beams remain unaffected by variation in damping coefficients. At higher values of velocity ($v = 85$ km/h), on varying damping ratio from 0 to 25%, the maximum upward deflection has been found to increase by 8%. However, the maximum downward deflection of the top beam has still been observed to be unaffected by the variation. In view of nominal influence, this has not been depicted here.

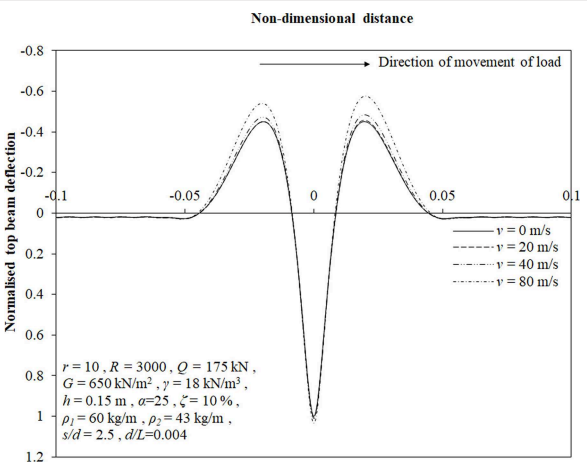

FIGURE 13 | Deflection of top beam at different velocities of applied load.

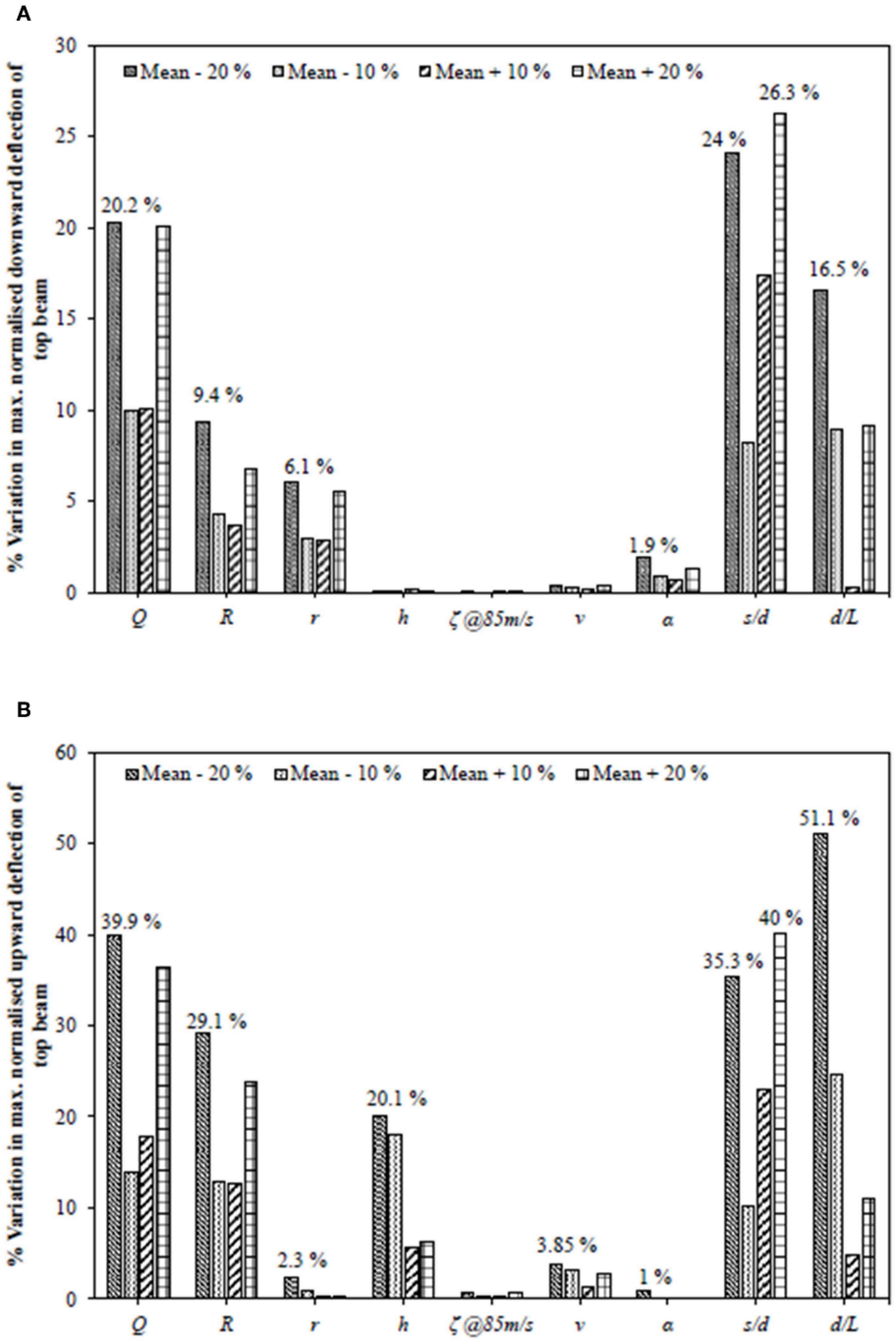

FIGURE 14 | Sensitivity analysis: **(A)** downward deflection, **(B)** upward deflection of top beam.

Sensitivity Study

Figures 14A,B show the typical plot of sensitivity analysis for maximum downward and upward deflection of top beam, respectively, for the following input values: $Q = 175$ kN, $v = 36$ m/s, $k_1 = 150$ MN/m^3, $r = 10$, $E_1I_1 = 4{,}470$ kN-m^2, $R = 3{,}000$, $G = 650$ kN/m^2, $\gamma = 18$ kN/m^3, $\rho_1 = 60$ kg/m, $\rho_2 = 43$ kg/m, $\zeta = 10\%$, $h = 0.15$ m, $\alpha = 25$, $s/d = 2.5$ and $d/L = 0.004$. For the study, the maximum values of top beam deflection in both the directions for each ± 20 and $\pm 10\%$ variations from the mean values have been obtained. These responses have been weighted with respect to maximum deflection in either direction for the mean value of respective parameters. It has been observed that the maximum upward deflection of top beam is substantially sensitive toward a greater number of parameters compared to

its maximum downward deflection. However, the sensitivity of maximum downward deflection has been found to be more toward relative compressibility of the soil and relative stiffness of the stone column compared to its counterpart. Configuration of stone columns has been found to be one of the most influential parameter affecting the response of soil-foundation system.

Practical Relevance

A practitioner can consider the input values conforming to conditions on site and determine the deflection and bending moment values of the rails. Under the circumstances, where this deformation works out to be more than the allowable values as per required track performance (Beranek, 2000), the non-dimensional charts based on the parametric study can be used to consider befitting improvement characteristics like appropriate configurations of stone columns, depth of placement and rigidity of geocell layer, thickness of granular layer etc. so that the resulting response of rails are within the permissible limit.

In addition to this, the sensitiveness of the rail deflection toward variation in different parameters has been highlighted during the sensitivity analysis giving the idea of the impact of that particular parametric variation on the response of rail.

CONCLUSIONS

A study has been proposed in order to analyze the combined effect of stone column and geocell improved beds for rails lying over it exposed to moving point load. Tensionless behavior of earth beds has been modeled and included in the analysis. Based on results, the following conclusions can be deduced:

(i) Inclusion of stone columns resulted in 58% reduction in maximum downward deflection of top beam indicating significant improvement from settlement point of view.
(ii) Beginning of parting between top beam and the ground surface has been observed at a lower value of $Q = 68$ kN due to increased stiffness of the foundation on inclusion of stone columns.
(iii) A prominent increase of 48% in maximum downward deflection of top beam has been observed when relative compressibility of soil layers is increased from $r = 5$ to 20. The corresponding increment in maximum upward deflection has been found to be only 12%.
(iv) Significant reduction in maximum upward and downward deflection has been observed when s/d is varied from 3.5 to 2. For the case of variation in diameter of stone columns, these deflections are observed to initially reduce only to increase later when d/L is varied from 0.0008 to 0.008 based upon whether the phenomenon of replacement of soil by coarser material is dominant or reduction in number of stone columns.
(v) Maximum upward deflection of top beam has been observed to reduce by 66% on increasing relative flexural rigidity, R from 2,400 to 5,400.
(vi) For the top beam, the variation in location of the bottom beam from $h = 0.05$ to 0.45 m results in 29% reduction in the maximum upward deflection. Furthermore, the region of detachment between top beam and the ground has been found to reduce on increasing the depth of placement of the bottom beam till it develops perfect contact.
(vii) Maximum upward deflection of top beam has been found to rise up by 22% compared to 7% initial increment when the velocity is increased up to 80 m/s.
(viii) Sensitivity analysis conducted suggested that maximum upward deflection of top beam is exceptionally sensitive toward variation in most of the parameters compared to maximum downward deflection except for the case of relative compressibility of the soil and relative stiffness of the stone columns.

DATA AVAILABILITY STATEMENT

All datasets generated for this study are included in the manuscript/supplementary files.

AUTHOR CONTRIBUTIONS

PM formed the idea and algorithm of the work. SB developed computer program and implemented the algorithm and conducted detailed parametric study. All authors reviewed and accepted the final version.

REFERENCES

Arulrajah, A., Abdullah, A., Bo, M. W., and Bouazza, A. (2009). Ground improvement techniques for railway embankments. *Proc. Inst. Civil Eng. Ground Improv.* 162, 3–14. doi: 10.1680/grim.2009.162.1.3

Auersch, L. (2012). Dynamic behavior of slab tracks on homogeneous and layered soils and the reduction of ground vibration by floating slab tracks. *J. Eng. Mech.* 138, 923–933. doi: 10.1061/(ASCE)EM.1943-7889.0000407

Basu, D., and Rao, N. S. V. K. (2013). Analytical solutions for Euler – Bernoulli beam on visco-elastic foundation subjected to moving load. *Int. J. Numerical Anal. Methods Geomech.* 37, 945–960. doi: 10.1002/nag.1135

Beranek, D. A. (2000). *Technical Instructions: Railroad Design and Rehabilitation. TI 850-02, AIR FORCE AFMAN 32-1125(I)*. Washington DC: Engineering and Construction Division, U.S. Army Corps of Engineers.

Bhatra, S., and Maheshwari, P. (2019). Double beam model for reinforced tensionless foundations under moving loads. *KSCE J. Civil Eng.* 23, 1600–1609. doi: 10.1007/s12205-019-1609-6

Chen, J. S., and Chen, Y. K. (2011). Steady state and stability of a beam on a damped tensionless foundation under a moving load. *Int. J. Non Linear Mech.* 46, 180–185. doi: 10.1016/j.ijnonlinmec.2010.08.007

Coşkun, I. (2000). Non-linear vibrations of a beam resting on a tensionless Winkler foundation. *J. Sound Vib.* 236, 401–411. doi: 10.1006/jsvi.2000.2982

Cui, X., Zhuang, Y., Hu, C., Liu, H., and Chiu, C. F. (2018). Improvement of soft foundations under a rapid transit tram rail system. *Soil Mech. Found. Eng.* 55, 181–189. doi: 10.1007/s11204-018-9523-3

Das, B. M. (1999). *Principles of Foundation Engineering, 4th Edn*. Boston, MA: PWS Publishing.

Deng, H., Chen, K., Cheng, W., and Zhao, S. (2017). Vibration and buckling analysis of double-functionally graded Timoshenko beam system

on Winkler-Pasternak elastic foundation. *Composite Struct*. 160, 152–168. doi: 10.1016/j.compstruct.2016.10.027

Duffy, D. G. (1990). The response of an infinite railroad track to a moving, vibrating mass. *J. Appl. Mech. Div. ASME* 57, 66–73. doi: 10.1115/1.2888325

Fryba, L. (1972). *Vibration of Solids and Structures Under Moving Loads*. London: Thomas Telford Ltd.

He, G., Li, X., and Lou, R. (2016). Nonlinear FEA of higer oder beam resting on tensionless foundation with friction. *Geomechan. Eng.* 11, 95–116. doi: 10.12989/gae.2016.11.1.095

Hussein, M. F. M., and Hunt, H. E. M. (2006). Modelling of floating-slab tracks with continuous slabs under oscillating moving loads. *J. Sound Vibration* 297, 37–54. doi: 10.1016/j.jsv.2006.03.026

Indraratna, B., Biabani, M. M., and Nimbalkar, S. (2015). Behavior of geocell-reinforced subballast subjected to cyclic loading in plane-strain condition. *J. Geotech. Geoenv. Eng.* 141, 04014081-1–16. doi: 10.1061/(ASCE)GT.1943-5606.0001199

IS 15284 (Part 1) (2003). *Design and Construction for Ground Improvement – Guidelines. Part 1 Stone Columns*. New Delhi: Bureau of Indian Standard.

Jaiswal, O. R., and Iyengar, R. N. (1997). Dynamic response of railway tracks to oscillatory moving masses. *J. Eng. Mech. Div. ASCE* 123, 753–757. doi: 10.1061/(ASCE)0733-9399(1997)123:7(753)

Kenney, J. T. Jr. (1954). Steady-state vibrations of beam on elastic foundation for moving load. *J. Appl. Mech. Div. ASME* 21, 359–364.

Kerr, A. D. (1974). The stress and stability analyses of railroad tracks. *J. Appl. Mech. Div. ASME* 41, 841–848. doi: 10.1115/1.3423470

Lin, L., and Adams, G. G. (1987). Beam on tensionless elastic foundation. *J. Eng. Mech. ASCE* 113, 542–553. doi: 10.1061/(ASCE)0733-9399(1987)113:4(542)

Maheshwari, P. (2014). Infinite beams on stone column reinforced tensionless earth beds under moving loads. *Int. J. Geotech. Eng.* 8, 21–25. doi: 10.1179/1938636213Z.00000000058

Maheshwari, P., Chandra, S., and Basudhar, P. K. (2004). Response of beams on a tensionless extensible geosynthetic-reinforced earth bed subjected to moving loads. *Comput. Geotech.* 31, 537–548. doi: 10.1016/j.compgeo.2004.07.005

Maheshwari, P., Chandra, S., and Basudhar, P. K. (2005). Steady state response of beams on a tensionless geosynthetic-reinforced granular fill-soft soil system subjected to moving loads. *Soils Found*. 45, 11–18. doi: 10.3208/sandf.45.5_11

Maheshwari, P., and Khatri, S. (2013). Response of infinite beams on geosynthetic-reinforced granular bed over soft soil with stone columns under moving loads. *Int. J. Geomech. ASCE* 13, 713–728. doi: 10.1061/(ASCE)GM.1943-5622.0000269

Maheshwari, P., and Viladkar, M. N. (2009). A mathematical model for beams on geosynthetic reinforced earth beds under strip loading. *Appl. Math. Model.* 33, 1803–1814. doi: 10.1016/j.apm.2008.03.009

Mallik, A. K., Chandra, S., and Singh, A. B. (2006). Steady-state response of an elastically supported infinite beam to a moving load. *J. Sound Vib.* 291, 1148–1169. doi: 10.1016/j.jsv.2005.07.031

Mohammadzadeh, S., Esmaeili, M., and Mehrali, M. (2014). Dynamic response of double beam rested on stochastic foundation under harmonic moving load. *Int. J. Numerical Anal. Methods Geomech*. 38, 572–592. doi: 10.1002/nag.2227

Rao, N. S. V. K. (1974). Onset of separation between a beam and tensionless foundation due to moving loads. *J. Appl. Mech. Div. ASME* 41, 303–305. doi: 10.1115/1.3423257

Raymond, G. P. (2002). Reinforced ballast behaviour subjected to repeated load. *Geotextiles Geomembr*. 20, 39–61. doi: 10.1016/S0266-1144(01)00024-3

Selvadurai, A. P. S. (1979). *Elastic Analysis of Soil-Foundation Interaction*. Amsterdam, Netherlands: Elsevier Scientific Publishing Company.

Shahu, J. T., Yudhbir, Kameswara Rao, N. S. V. (2000). A rational method for design of railroad track foundation. *Soils Found*. 40. 1–10. doi: 10.3208/sandf.40.6_1

Torby, B. J. (1975). Deflection results from moving loads on a beam that rests upon an elastic foundation reacting in compression only. *J. Appl. Mechanics. Div. ASME* 42, 738–739. doi: 10.1115/1.3423677

Vlasov, V. Z., and Leontiev, U. N. (1966). *Beams, Plates and Shells on Elastic Foundations, Israel Program for Scientific Translations.* Jerusalem: Israel Program for Scientific Translations.

Vucetic, M., and Dobry, R. (1991). Effect of soil plasticity on cyclic response. *J. Geotech. Eng. ASCE* 117, 89–107. doi: 10.1061/(ASCE)0733-9410(1991)117:1(89)

Yuan, J., Zhu, Y., and Wu, M. (2009). Vibration characteristics and effectiveness of floating slab track system. *J. Comput*. 4, 1249–1254. doi: 10.4304/jcp.4.12.1249-1254

Zhang, L., Ou, Q., and Zhao, M. (2018). Double-beam model to analyze the performance of a pavement structure on geocell-reinforced embankment. *J. Eng. Mech*. 144, 06018002-1–7. doi: 10.1061/(ASCE)EM.1943-7889.0001453

Zhao, L. S., Zhou, W. H., Fatahi, B., Li, X., Bin and Yuen, K. V. (2016). A dual beam model for geosynthetic-reinforced granular fill on an elastic foundation. *Appl. Math. Model.* 40, 9254–9268. doi: 10.1016/j.apm.2016.06.003

Zhuang, Y., and Wang, K. (2017). Numerical simulation of high-speed railway foundation improved by PVD-DCM method and compared with field measurements. *Eur. J. Env. Civil Eng.* 21, 1363–1383. doi: 10.1080/19648189.2016.1170728

Conflict of Interest: The authors declare that the research was conducted in the absence of any commercial or financial relationships that could be construed as a potential conflict of interest.

LIST OF NOTATIONS

A_1 to A_8	Coefficients of nodal deflection in the Finite Difference form equation for the top beam.
B_1 to B_6	Coefficients of nodal deflection in the Finite Difference form equation for the bottom beam
c_1	Viscous damping coefficient of the granular layer
c_1^*	Non-dimensional viscous damping co-efficient of the granular layer
c_2	Viscous damping coefficient of the foundation soil
c_2^*	Non-dimensional viscous damping co-efficient of the foundation soil
d	Diameter of stone columns
E_1	Young's modulus of top beam material
E_2	Young's modulus of bottom beam material
G	Shear modulus of granular layer
G^*	Non-dimensional shear parameter of granular layer
g	Acceleration due to gravity
H	Non-dimensional thickness of the granular layer
h	Thickness of the granular layer
I_1	Second moment of area of the top beam cross section
I_1^*	Non-dimensional modulus of flexural rigidity of the top beam
I_2	Second moment of area of the bottom beam cross section
I_2^*	Non-dimensional modulus of flexural rigidity of the bottom beam
i	Subscript referring to nodal points
$j(x,t)$	Contact function representing tensionless behavior
k_1	Compressibility of the granular layer
k_2	Compressibility of the foundation soil
k_c	Compressibility of foundation soil in stone column region
k_s	Compressibility of foundation soil in soft soil region
L	Half-length of beams
$Q(x,t)$	Applied moving load
Q^*	Non-dimensional applied moving load
R	Relative flexural rigidity of the beams
r	Relative compressibility of granular layer with respect to soft soil, k_1/k_s
r^*	Relative compressibility of granular layer with respect to foundation soil, k_1/k_2
s	Spacing between the stone columns
t	Time
v	Velocity of moving load
w_1^*	Non-dimensional self-weight of the top beam
w_2^*	Non-dimensional self-weight of the bottom beam
x	Horizontal space co-ordinate
Y_1	Non-dimensional top beam deflection
Y_2	Non-dimensional bottom beam deflection
Y_g	Non-dimensional deflection of the ground surface
y_1	Deflection of the top beam
y_2	Deflection of the bottom beam
y_g	Deflection of the ground surface
α	Relative stiffness of stone column with respect to the surrounding soft soil, k_c/k_s
γ_1	unit weight of granular mat

(Continued)

Continued

γ_1^*	Non-dimensional unit weight of granular mat
$\Delta\xi^*$	Non-dimensional distance between Finite Difference nodes
ζ	Damping ratio
ξ	Distance from point of action of load at time t
ξ^*	Non-dimensional distance from point of action of load at time t
ρ_1	Mass per unit length of the top beam
ρ_1^*	Non-dimensional mass per unit length of the top beam
ρ_2	Mass per unit length of the bottom beam
ρ_2^*	Non-dimensional mass per unit length of the bottom beam

frontiers in Built Environment

ORIGINAL RESEARCH
published: 19 November 2019
doi: 10.3389/fbuil.2019.00137

Contact Pressure Distribution on Subgrade Soil Underlying Geocell Reinforced Foundation Beds

Sujit Kumar Dash[1]*, *Rupam Saikia*[1] and *Sanjay Nimbalkar*[2]

[1] Department of Civil Engineering, Indian Institute of Technology Kharagpur, Kharagpur, India, [2] School of Civil and Environmental Engineering, University of Technology Sydney, Ultimo, NSW, Australia

OPEN ACCESS

Edited by:
Eduardo Cabrita Fortunato, National Laboratory for Civil Engineering, Portugal

Reviewed by:
Chayut Ngamkhanong, University of Birmingham, United Kingdom
Ping Liu, Jiangsu University of Science and Technology, China
Amarnath M. Hegde, Indian Institute of Technology Patna, India

***Correspondence:**
Sujit Kumar Dash
sujit@civil.iitkgp.ac.in

Specialty section:
This article was submitted to Transportation and Transit Systems, a section of the journal Frontiers in Built Environment

Received: 28 August 2019
Accepted: 04 November 2019
Published: 19 November 2019

Citation:
Dash SK, Saikia R and Nimbalkar S (2019) Contact Pressure Distribution on Subgrade Soil Underlying Geocell Reinforced Foundation Beds. Front. Built Environ. 5:137. doi: 10.3389/fbuil.2019.00137

High contact stresses generated in the foundation soil, owing to increased load, causes distress, instability, and large settlements. Present days, geocell reinforcement is being widely used for the performance improvement of foundation beds. Pressure distribution on subgrade soil in geocell reinforced foundation beds is studied through model tests and numerical analysis. The test data indicates that with provision of geocell reinforcement the contact pressure on the subgrade soil reduces significantly. Consequently, the subgrade soil tends to remain intact until large loadings on the foundation leading to significant performance improvement. Through numerical analysis it is observed that the geocells in the region under the footing were subjected to compression and beyond were in tension. This indicates that the geocell reinforcement right under the footing directly sustains the footing loading through mobilization of its compressive stiffness and bending rigidity. Whereas, the end portions of the geocell reinforcement, contribute to the performance improvement in a secondary manner through mobilization of anchorage derived from soil passive resistance and friction.

Keywords: soil, geocell reinforcement, strip loading, contact pressure, finite elements

INTRODUCTION

With increase in loading due to high-rise structures, contact pressures on foundation soils have increased by manifold leading to distress, instability and large settlements. Hence, the requirement for improvement of soil has increased markedly. Introduction of geosynthetic reinforcements in the foundation soil is a potential solution. In this avenue, *geocell* reinforcement is a recently developed technique which offers overall confinement to the soil within its three dimensional pockets, thereby increases the overall rigidity of the soil bed, leading to improved performance. Commercially available geocells manufactured from high-density polyethylene sheets, ultrasonically welded in a honeycomb pattern, are called geowebs. They are typical of 100–300 mm in height. The geocells with larger height are fabricated directly on-site using geogrids (Bush et al., 1990).

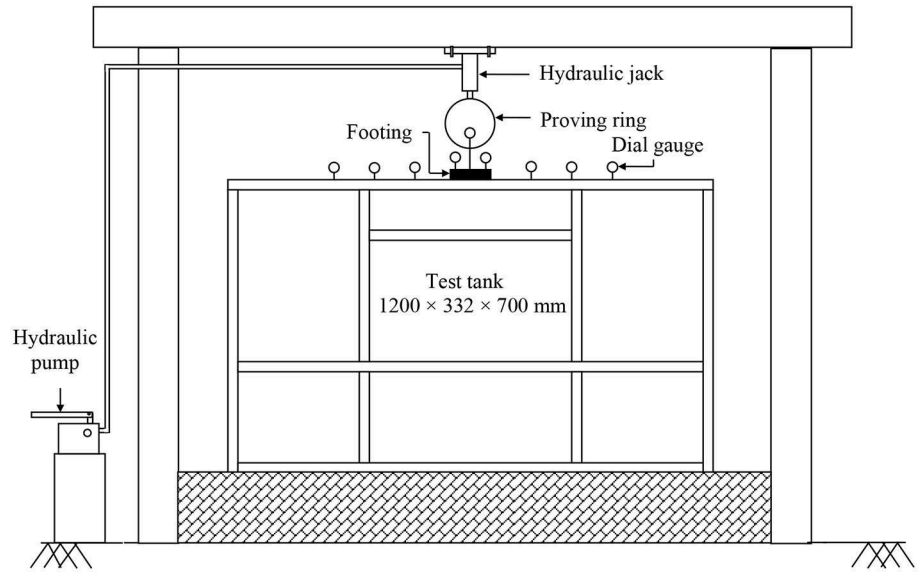

FIGURE 1 | Test setup.

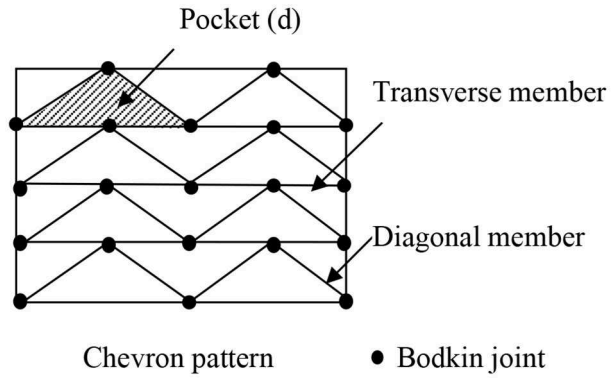

FIGURE 2 | Pattern of formation of geocell mattress.

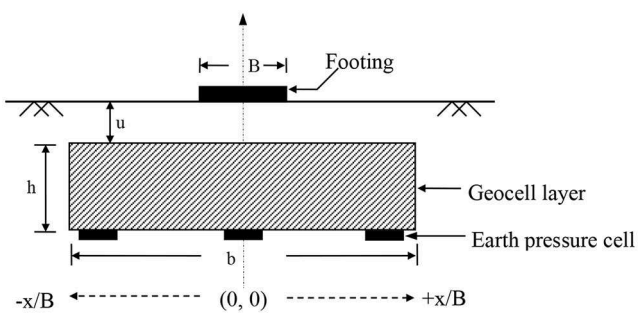

FIGURE 3 | Test geometry.

Several authors have reported the beneficial use of geocells. Rea and Mitchell (1978) and Mitchell et al. (1979) were the pioneers. Through model scale load tests on sand-filled paper made geocells they observed visible performance improvement. The test results were used to identify modes of failure and optimum dimensions of the geocells giving maximum performance. Bathurst and Jarrett (1989) have studied the application of geocells improving the performance of pavements over peat subgrades. Dash et al. (2001, 2008) through load tests have observed that geocells can increase the bearing capacity and subgrade modulus of sand beds significantly. This is primarily because of the bending and shear rigidity of the geocell mattress (Dash et al., 2007). Hegde and Sitharam (2015) through finite element modeling have analyzed the performance behavior of geocell reinforced foundation beds.

Contact pressure magnitude and its pattern of distribution on foundation soil is an important parameter that significantly influences the bearing capacity and settlement. Emersleben and Meyer (2008) through limited full scale tests have observed that with geocell reinforcement vertical stress on foundation soil tends to reduce by 50% as compared to that in unreinforced case. Finite difference analysis by Hegde and Sitharam (2015) indicates that with geocell reinforcement the depth of pressure bulb tends to reduce. However, mechanism of geocell reinforcement in altering the contact pressure especially with respect to the geometry of the geocell reinforcement and surcharge loading has not been studied in detail. This paper focuses on this critical issue through model tests and finite element analysis.

EXPERIMENTAL PROGRAM

The foundation beds were formed in a steel tank measuring 1,200 mm in length, 332 mm in width, and 700 mm in height. It was housed in a loading frame as shown in **Figure 1**. In order to reduce friction, the longitudinal side walls of the tests tank were made of thick Perspex sheets braced with steel angles. A steel plate having length 330 mm, width 100 mm, and thickness 25 mm was

used as the footing for loading the foundation beds. Its bottom surface was roughened through a thin layer of sand fixed with epoxy glue. The footing was placed at the center of the tank with its length along the width of the tank. As the footing length was kept almost equal to the width of the test tank (with 1 mm gap on both sides) a plane strain condition was generally maintained.

A dry river sand with effective grain size (D_{10}) of 0.22 mm, average grain size (D_{50}) of 0.46 mm, coefficient of uniformity (C_u) of 2.318 and coefficient of curvature (C_c) of 1.03; was used for making the foundation beds. As per the Indian standard specifications (IS: 1498, 1970) the soil was classified as poorly graded sand with letter symbol *SP*. Its maximum and minimum densities were found to be 17.4 and 14.3 kN/m^3, respectively. The soil was placed at a relative density of 70% which was achieved through pluviation technique. Geocells were formed using a biaxial geogrid made of oriented polymer. Aperture size of the geogrid was 35 × 35 mm. Its tensile strength and 5% strain secant modulus as per ASTM StandardD6637 (2009) were 20 and 160 kN/m, respectively. The geocells were formed using geogrid strips interconnected through bodkin joints (Bush et al., 1990), in chevron pattern as shown in **Figure 2**. The bodkin joints were made of thin plastic strips. The tensile strength of the joint was found to be 3.4 kN/m. **Figure 3**, shows the geometry of the problem investigated.

Through a hydraulic jack, fixed onto the reaction frame, loading was applied in increments. The load installments were maintained on the footing until the settlement stabilized. The settlement magnitudes were recorded through two dial gauges

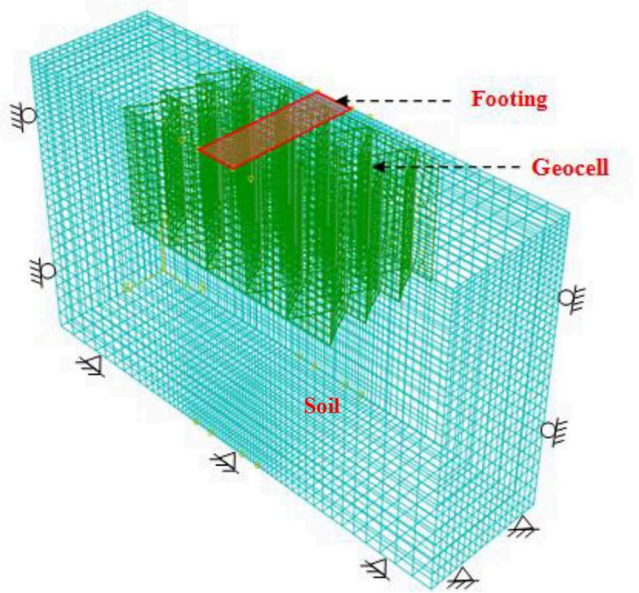

FIGURE 4 | ABAQUS model for geocell reinforced foundation bed.

TABLE 1 | Input parameters used in the finite element model.

Parameter	Sand	Geocell
Density, ρ (kg/m^3)	1,678	950
Modulus of elasticity, E (MPa)	10	75
Poison's ratio, ν	0.26	0.3
Friction angle, ϕ (°)	39	–
Dilation angle, δ (°)	7	–
Cohesion, c (kPa)	0	–

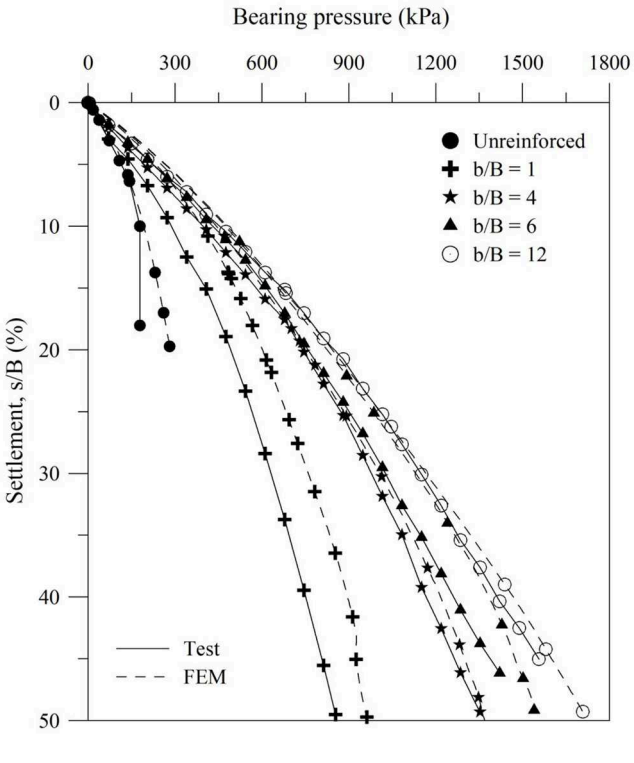

FIGURE 5 | Variation of bearing pressure with footing settlement for different widths of geocell mattress (d/b = 1.2, h/b = 2.75, u/b = 0.1, ID = 70%).

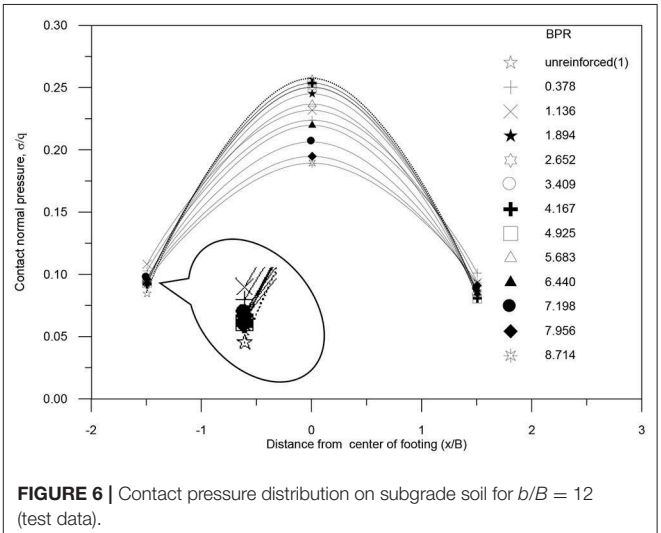

FIGURE 6 | Contact pressure distribution on subgrade soil for b/B = 12 (test data).

placed on diagonally opposite ends of the footing. Heave and settlement on the soil surface too were measured by dial gauges. The footing was loaded until settlement reached to about 50 mm or bearing failure took place, whichever was earlier.

The vertical contact pressure (σ) on the subgrade soil was measured through strain gauge type earth pressure cells. They were kept under geocell mattress, one below the footing center line and two others at a distance of 1.5B on either side as shown in **Figure 3**. The pressure cell diaphragms had a radius (R) of 20 mm and thickness (t) of 1.5 mm. They were made of steel having a modulus of elasticity (E_{cell}) of 2.1 $\times$ 10^5 N/mm^2. Modulus of elasticity of the soil (E_{soil}) was taken as 35 N/mm^2. Relative stiffness of the soil-diaphragm wall ($E_{soil} \times R^3/E_{cell} \times t^3$) was found to be 0.39. This is a reasonable value for the accuracy of measurement by the pressure cells (Clayton and Bica, 1993). The earth pressure cells were calibrated, by embedding them in sand bed inside a calibration chamber (Dunnicliff, 1988). Relative density of sand in the calibration chamber was same as that in the model tests (i.e., 70%). In unreinforced case, earth pressures were placed at the same depth as in the unreinforced case (i.e., base level of geocell mattress). As suggested by Hadala (1967), the pressure cells were set on the sand bed followed by raining until the test bed was formed. The measured pressures were normalized with respect to the applied footing pressure (q). The normalized pressures (σ/q) depicting the percentage of the footing pressures transmitted to the geocell mattress base are plotted at different footing loads in terms of bearing pressure ratio (BPR), defined as the ratio footing pressure with geocell reinforcement (q) to ultimate bearing pressure (q_{ult}) in the unreinforced case.

The model tests were conducted for the geocell mattress width ratios (b/B) of 1, 2, 4, 6, 8, 10, and 12. The pocket size of geocells (d/B), height of geocell mattress (h/B), and depth to the top of the geocell layer below footing (u/B) were kept constant as 1.2, 2.75, and 0.1, respectively. d is the diameter of an equivalent circular area of the geocell pocket opening (**Figure 2**).

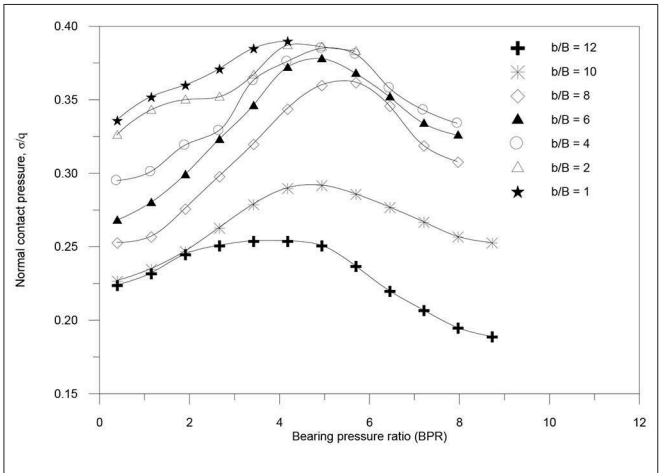

FIGURE 7 | Variation of Contact pressure with bearing pressure at center of footing (0, 0) for different widths of geocell mattress (test data).

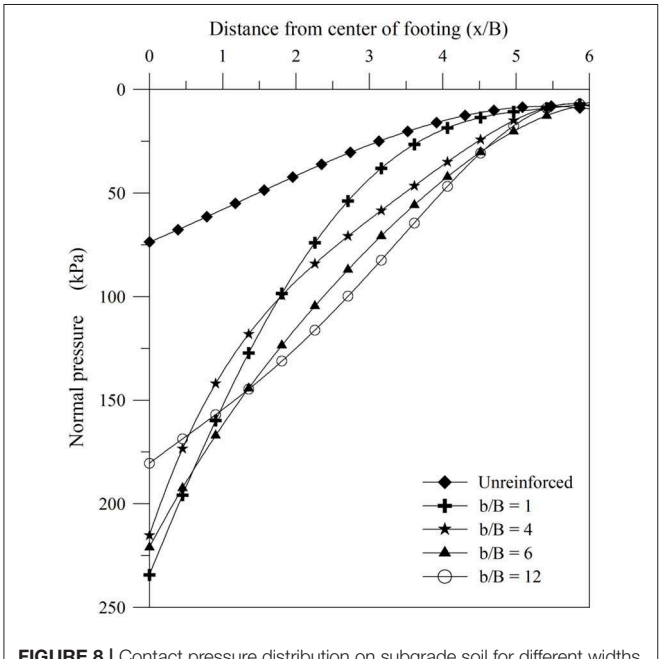

FIGURE 8 | Contact pressure distribution on subgrade soil for different widths of geocell mattress (FEM data, s/B = 20%).

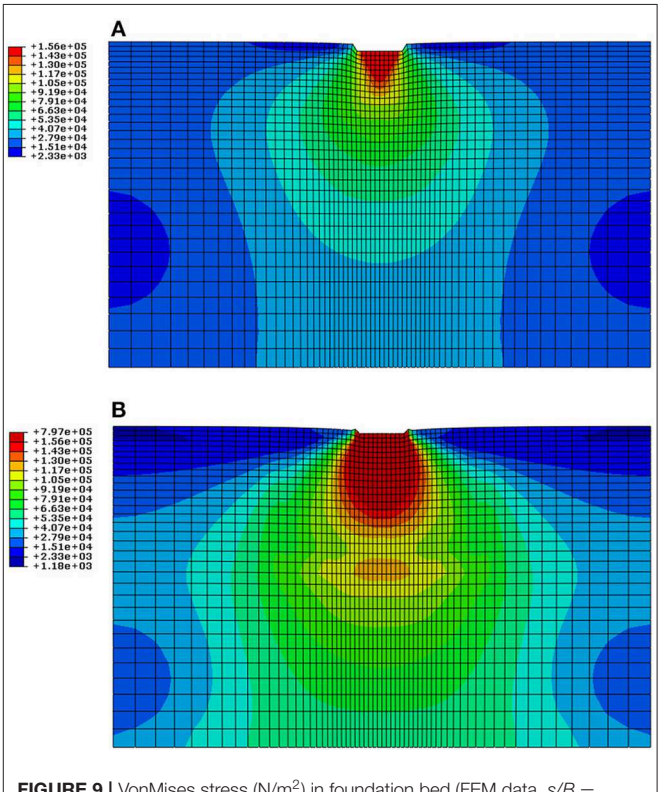

FIGURE 9 | VonMises stress (N/m^2) in foundation bed (FEM data, s/B = 20%). **(A)** Unreinforced. **(B)** Geocell reinforced.

NUMERICAL MODELING

To generate additional data, numerical analysis was carried out using the finite element code, ABAQUS 6.14. A typical model used in the analysis is shown in **Figure 4**. Using hexahedral eight noded elements (C3D8R) the foundation bed was discretized into 32,640 elements which were found to be adequate for both unreinforced and geocell reinforced models. The geocells were modeled as a continuous sheet, meshed with four noded membrane elements (M3D4R). The minimum number of membrane elements were 866 for geocell mattress of width $b/B = 1$ and maximum 9,652 for $b/B = 12$. Vertical

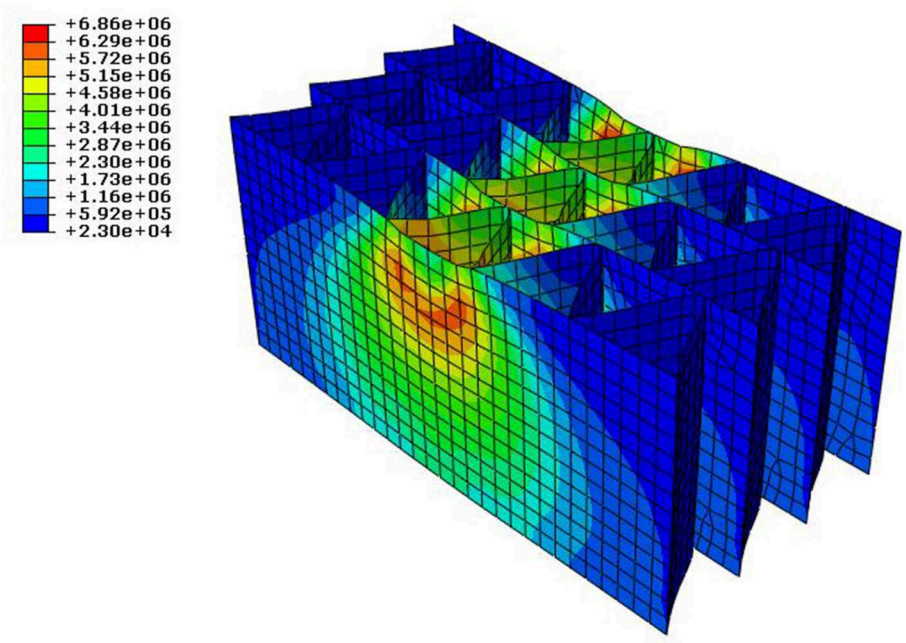

FIGURE 10 | VonMises stress (N/m^2) in geocell reinforcement (FEM data, $s/B = 20\%$).

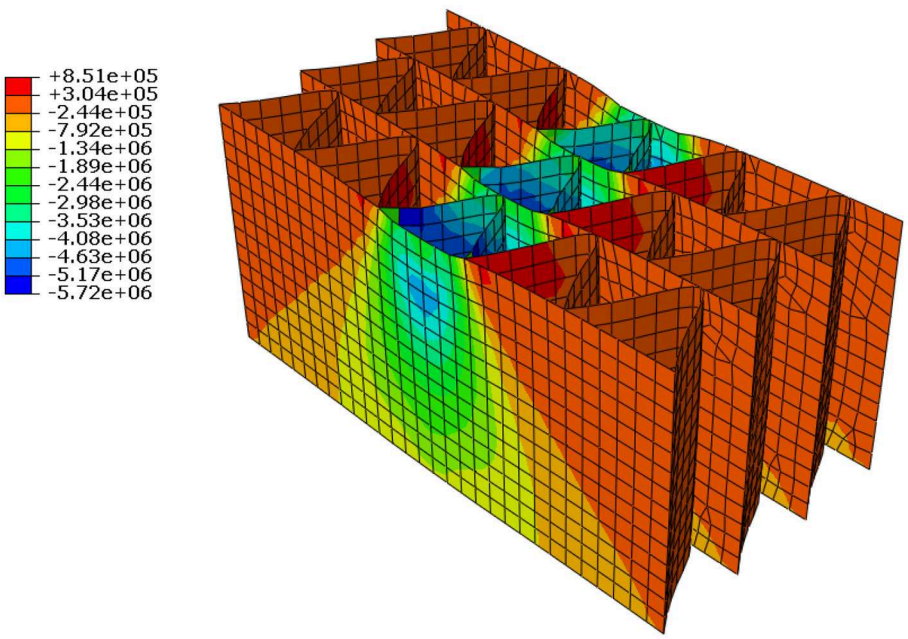

FIGURE 11 | Vertical stress (N/m^2) in geocell reinforcement (FEM data, $s/B = 20\%$).

boundaries of the foundation bed were constrained in horizontal directions, while its base was constrained both in vertical and horizontal directions.

The soil was modeled as an elastoplastic material obeying Mohr-Coulomb yield criterion with non-associated flow rule. The various material parameters were obtained from the interpretation of the triaxial test data. The geocell was modeled as an elastic material as it was observed that the strains in the geocell generally remained within the elastic range (Leshchinsky and Ling, 2013). As the geocell strength was scaled down during experiments using bodkin joints, the modulus of elasticity was obtained from the strain-strain response of the geocell joint. The geocell was embedded in the foundation bed that the interface friction angle was equivalent to the friction angle of the soil (Satyal et al., 2018). Properties of the foundation soil and geocells used in the analysis are summarized in **Table 1**.

After applying geostatic state from the outset, the vertical loading on the footing was simulated imposing equal vertical displacement over the entire width of the footing, in increments of 0.025 mm per load step. The results obtained are presented and discussed in the following section.

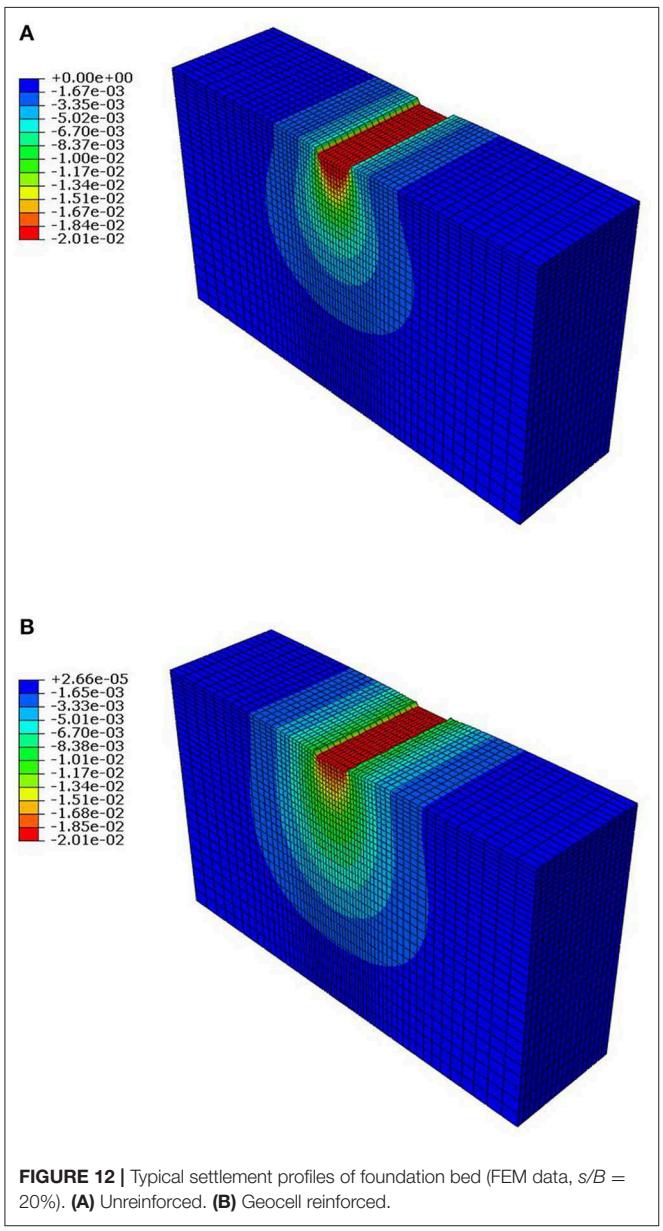

FIGURE 12 | Typical settlement profiles of foundation bed (FEM data, s/B = 20%). **(A)** Unreinforced. **(B)** Geocell reinforced.

RESULTS AND DISCUSSIONS

Typical bearing pressure-settlement responses of the foundation bed, with and without geocell reinforcement, are shown in **Figure 5**. It is evident that the numerical results are in reasonable agreement with the experimental data. At footing settlement of about 10% of its width, the unreinforced sand has undergone failure. Near vertical slope of the pressure-settlement response and heaving on the soil surface indicates that the failure was largely by shear. In case of geocell reinforcement, no such pronounced failure was noticed. Moreover, the bearing capacity tends to increase significantly.

Experimentally obtained typical contact pressure (σ/q) distribution on the subgrade soil underlying geocell mattress is shown in **Figure 6**. The dotted line depicts the unreinforced case and solid lines depict the reinforced case. In both the cases, the contact pressure is maximum at the center of the footing and appreciably low in the region beyond the loaded region. As the foundation load tends to get dispersed the induced pressure on the soil bed gets reduced toward both the sides of the footing. With geocell reinforcement, the percentage of contact pressure on the subgrade soil tends to reduce significantly. This is because the geocell reinforcement through three-dimensional confinements inhibits shear failure in the soil mass. Indeed, with geocell reinforcement heaving on the soil surface was found to have reduced significantly. The coherent geocell mattress effectively transmits the footing loading to deeper depth leading to reduced pressure on the subgrade soil. At $x = 1.5B$, the contact pressure responses have almost superposed over each other which indicates that pressure transmitted onto the subgrade soil is proportional to the surcharge pressure on the footing, depicting an elastic behavior. This is because owing to relatively low magnitude of pressure at $x = 1.5B$, the geocell-soil structure has remained intact and coherent leading to the elastic response.

Variation of contact pressure with applied footing pressure (BPR) at mid-section of the foundation bed (i.e., along center line of the footing, $x/B = 0$), for different widths of geocell mattress (b/B), are presented in **Figure 7**. It can be seen that the percentage of contact pressure transmitted to the subgrade soil initially tends to increase with the increase in footing pressure to reach a peak value. Beyond that, it continues to decrease with increase in footing pressure. Initially the coherent geocell mattress in the foundation bed behaves as a secondary footing that tends to transmit an increased percentage of footing pressure to the subgrade soil, with increase in surcharge loading. At later stage of loading, as the geocell reinforcement tends to get pulled away, significant anchorage resistance is mobilized at both the ends primarily through soil passive resistance over its transverse walls

and frictional resistance over the longitudinal walls. As a result of which the geocell reinforcement effectively supports the footing loading leading to reduced pressure on the subgrade soil. Further, it is seen that the contact pressure on the subgrade soil tends to increase with decrease in the geocell width. This is because, with the decrease in the geocell area, the end anchorage reduces. As this anchorage was holding the mattress against bending under footing pressure, with its reduction it deflects more and thereby bringing forth an increase in pressure at the base of the mattress. Moreover, with reduced extent of the geocell mattress, the surcharge load instead of getting redistributed over a wider area tends to get concentrated in the region under the footing leading to an increase in pressure on the underlying soil layer.

Contact normal pressure profile on subgrade soil over the middle half of the foundation bed, obtained from numerical analysis, at 20% footing settlement (s/B) for reinforced and unreinforced cases are depicted in **Figure 8**. It could be seen that over a distance of about thrice the footing width ($x/B = 3$) pressure on subgrade soil in the geocell reinforced case is significantly higher than that in the unreinforced case. It indicates that the geocell mattress has effectively transmitted the footing pressure to deeper depths leading to large performance improvement. In contrast, the unreinforced soil has failed in shear and hence could not disperse the footing load over a larger area. It can be seen that beyond a distance (x) of $3B$, the difference of contact pressure between unreinforced and geocell reinforced case tends to reduce and beyond $x = 5.5B$, the difference is significantly less. This is because at a large distance, owing to load dispersion, the footing influence on subgrade soil tends to reduce significantly. Another important point to note is that with increase in the geocell mattress width, contact pressure in the region under the footing tends to reduce. This once again establishes that geocell mattress of larger width mobilizes end anchorage and thereby effectively sustains the footing loading leading to reduced pressure on the subgrade soil.

Von Mises stress contours in foundation bed for unreinforced and reinforced cases, at 20% footing settlement, are depicted in **Figures 9A,B**, respectively. It is shown that with geocell mattress the Von Mises stress in the foundation bed has spread over larger area which indicates that the geocell mattress has transmitted the footing pressure to greater depth in the foundation bed. Correspondingly, the geocell reinforcement is found to have been stressed significantly (**Figure 10**) which testifies that the geocell reinforcement has actively participated in sharing the footing load leading to increased performance improvement. Vertical stress contours depicted in **Figure 11** shows that the geocells in the region under the footing are subjected to compression and beyond are in tension. This indicates that the geocell reinforcement right under the footing directly sustains the footing loading through mobilization of its compressive stiffness and bending rigidity. Whereas, its end portions contribute to performance improvement through mobilization of anchorage which is derived from soil passive resistance and friction.

Typical vertical settlement profiles of unreinforced and geocell reinforced foundation beds are shown in **Figures 12A,B**, respectively. Both are plotted at a constant footing penetration level (s/B) of 20%. It could be seen that with geocell reinforcement the settlement in the foundation bed has distributed over larger area. This is because the geocell reinforcement has effectively confined the soil mass within its pockets forming a semi rigid coherent body that stands against the footing loading and effectively redistributes it leading to settlement over larger area.

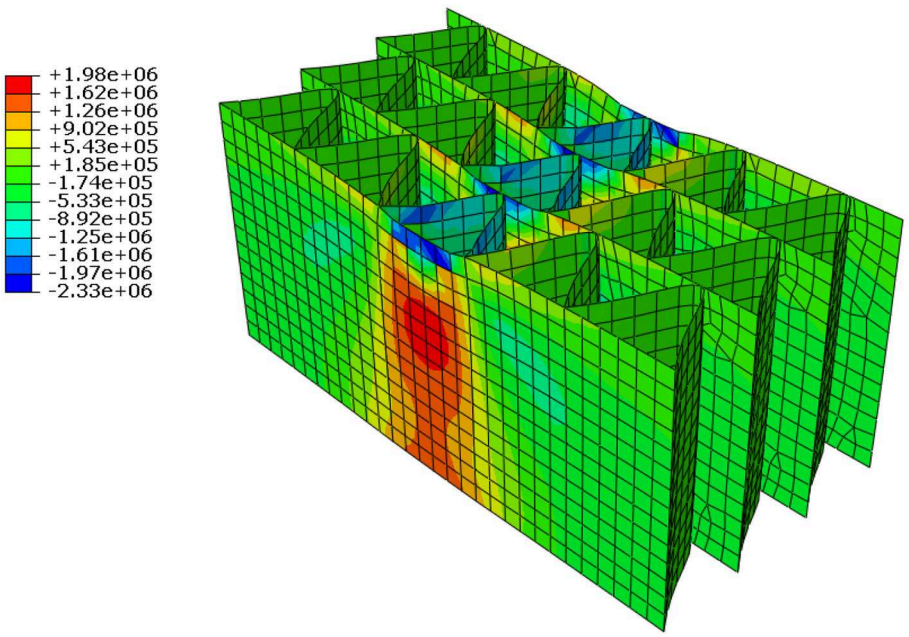

FIGURE 13 | Lateral stress (N/m^2) in geocell reinforcement (FEM data, $s/B = 20\%$).

Indeed, large lateral stress mobilized in the geocell pockets as shown in **Figure 13** testifies that geocells have effectively confined the soil mass against shearing under footing loading.

CONCLUSION

This paper through laboratory model tests and numerical analysis has investigated the influence of geocell reinforcement on the performance of foundation beds. With geocell reinforcement, the contact pressure on subgrade soil reduces significantly. Consequently, the subgrade soil remains undistorted until large loadings. Hence, the bearing capacity of the foundation bed increases significantly. With increase in width of the geocell mattress, the anchorage at both the ends of the geocell reinforcement tends to increase significantly. As a result, it sustains the footing load effectively leading to reduced contact pressure on the subgrade soil giving rise to a significant increase in performance improvement. Von Mises stress contours in the foundation bed indicate that the geocells right under the footing directly sustains the footing loading through mobilization of its compressive stiffness and bending rigidity. Whereas, end portions of the geocell mattress contribute to performance improvement through anchorage derived from soil passive resistance and friction.

DATA AVAILABILITY STATEMENT

The datasets generated for this study are available on request to the corresponding author.

AUTHOR CONTRIBUTIONS

All authors listed have made a substantial, direct and intellectual contribution to the work, and approved it for publication.

ACKNOWLEDGMENTS

The authors are thankful to Prof. Ben Leshchinsky, Oregon State University, USA; for kindly sharing the ABAQUS code for the current analysis.

REFERENCES

ASTM StandardD6637 (2009). *Standard Test Method for Determining Tensile Properties of Geogrids by the Single or Multi-Rib Tensile Test Method*. West Conshohocken, PA: ASTM International.

Bathurst, R. J., and Jarrett, P. M. (1989). Large scale model tests of geocomposite mattresses over peat subgrades. *Transport. Res. Rec.* 1188, 28–36.

Bush, D. I., Jenner, C. G., and Bassett, R. H. (1990). The design and construction of geocell foundation mattress supporting embankments over soft ground. *Geotext. Geomembranes* 9, 83–98. doi: 10.1016/0266-1144(90)90006-X

Clayton, C. R. I., and Bica, A. V. D. (1993). The design of diaphragm-type boundary total cells. *Geotechnique* 43, 523–535. doi: 10.1680/geot.1993.43.4.523

Dash, S. K., Krishnaswamy, N. R., and Rajagopal, K. (2001). Bearing capacity of strip footings supported on geocell-reinforced sand. *Geotext. Geomembranes* 19, 235–256. doi: 10.1016/S0266-1144(01)00006-1

Dash, S. K., Rajagopal, K., and Krishnaswamy, N. R. (2007). Behaviour of geocell-reinforcement sand beds under strip loading. *Can. Geotech. J.* 44, 905–916. doi: 10.1139/t07-035

Dash, S. K., Reddy, P. D., and Raghukanth, S. T. G. (2008). Subgrade modulus of geocell-reinforced sand foundation. *Ground Improv. Inst. Civil Eng. London* 161, 79–87. doi: 10.1680/grim.2008.161.2.79

Dunnicliff, J. C. (1988). *Geotechnical Instrumentation for Monitoring Field Performance*. New York, NY: John Wiley.

Emersleben, A., and Meyer, N. (2008). "Bearing capacity improvement of gravel base layers in road constructions using geocells," in *Proceedings of 12th International conference of International Association for Computer Methods and Advances in Geomechanics* (Goa: IACMG), 3538–3545.

Hadala, P. F. (1967). "The effect of placement method on the response of soil stress gauges," in *Proceedings of the International Symposium on Wave Propagation and Dynamic Properties of Earth Materials* (Albuquerque, NM: The University of New Mexico Press), 255–263.

Hegde, A., and Sitharam, T. G. (2015). 3-Dimensional numerical modelling of geocell reinforced sand beds. *Geotext. Geomembranes* 43, 171–181. doi: 10.1016/j.geotexmem.2014.11.009

IS: 1498 (1970). *Classification and Identification of Soils for General Engineering Purposes*. Bureau of Indian Standards.

Leshchinsky, B., and Ling, H. I. (2013). Numerical modeling of behavior of railway ballasted structure with geocell confinement. *Geotext. Geomembranes* 36, 33–43. doi: 10.1016/j.geotexmem.2012.10.006

Mitchell, J. K., Kao, T. C., and Kavazanjiam, E. Jr. (1979). *Analysis of Grid Cell Reinforced Pavement Bases*. Technical Report No. GL-79-8, U.S. Army Waterways Experiment Station.

Rea, C., and Mitchell, J. K. (1978). "Sand reinforcement using paper grid cells," in *ASCE Spring Convention and Exhibit, Preprint 3130* (Pittsburgh, PA).

Satyal, S. R., Leshchinsky, B., Han, J., and Neupane, M. (2018). Use of cellular confinement for improved railway performance on soft subgrades. *Geotext. Geomembranes* 46, 190–205. doi: 10.1016/j.geotexmem.2017.11.006

Conflict of Interest: The authors declare that the research was conducted in the absence of any commercial or financial relationships that could be construed as a potential conflict of interest.

frontiers in Built Environment

ORIGINAL RESEARCH
published: 15 January 2020
doi: 10.3389/fbuil.2019.00150

Reliability Analysis of a Controlled Stage-Constructed and Reinforced Embankment on Soft Ground Using 2D and 3D Models

Jean Lucas dos Passos Belo[1]* *and Jefferson Lins da Silva*[2]

[1] Department of Civil Engineering, Aeronautical Infrastructure Engineering, Technological Institute of Aeronautics, São José dos Campos, Brazil, [2] Laboratory of Geosynthetics, Department of Geotechnical Engineering, São Carlos School of Engineering, University of São Paulo, São Carlos, Brazil

Geosynthetic reinforcement has become a very practical technique to improve geotechnical structure safety. In spite of improved soil behavior, structures are affected by uncertainties related to soil and reinforcement material properties. This paper aims to present a reliability analysis in order to take statistical information (uncertainties) into account in a safety analysis of reinforced embankments. The analysis was used in a case study on a controlled stage-constructed embankment on soft ground in order to investigate its probabilistic stability. Modeling was performed by commercial geotechnical software usage (GeoStudio and RocScience packs, SIGMA/W + SLOPE/W, and SLIDE^3, respectively) and the reliability structural analysis was acquired by coupling this software with a reliability program. Then, two numerical models were simulated: a 2D and a 3D one. For this application, the First Order Reliability Method (FORM) was assumed for the reliability analyses. The statistical information, as well as the correlation between variable pairs, was based on a literature review. In total, 29 parameters were assumed as random variables (splitting parameters from different zones and layers). At the same time, the influence of the uncertainty level on reliability analysis and the sensitivity of parameters (assumed as random variables) were investigated. As a result, the reliability indexes obtained showed that the structure analyzed should not be considered with a satisfactory safety level. Meanwhile, the uncertainty level assumed for random variables can lead the probabilistic analysis to very different conclusions about the structural safety, and the most sensitivity parameters observed were the bulk unit weight (clay—soft soil—and fill material) and the undrained shear strength, followed by a slight importance of the initial void ratio.

Keywords: reliability, geosynthetics, embankment, soft ground, sensitivity

OPEN ACCESS

Edited by:
Sujit Kumar Dash,
Indian Institute of Technology Kharagpur, India

Reviewed by:
Anna Granà,
University of Palermo, Italy
Mohammed Y. Fattah,
University of Technology, Iraq

***Correspondence:**
Jean Lucas dos Passos Belo
belo.jeanlucas@gmail.com

Specialty section:
This article was submitted to Transportation and Transit Systems, a section of the journal Frontiers in Built Environment

Received: *17 August 2019*
Accepted: *20 December 2019*
Published: *15 January 2020*

Citation:
Belo JLP and Lins da Silva J (2020) Reliability Analysis of a Controlled Stage-Constructed and Reinforced Embankment on Soft Ground Using 2D and 3D Models. Front. Built Environ. 5:150. doi: 10.3389/fbuil.2019.00150

INTRODUCTION

Soil retaining structures are, sometimes, essential for several engineering constructions and designs. Generally, these structures are conceived and constructed by using cyclopean or reinforced concrete, anchored or not. However, with increasing soil heights to contain and eventual poor foundation soils, the cost of these structures has increased considerably. Therefore, an alternative

system has arisen to deal with these conditions. For example, according to Elias et al. (2001), the advantages provided by using geosynthetic materials to reinforce soil structures are noted under these conditions. Besides, the polymeric material can be employed with other solutions to improve lateral support, such as exposed by Fattah et al. (2015, 2016a,b).

Many deterministic methods have been proposed aiming to determine the key design features of geosynthetic-reinforced soil structures (Koerner, 2012; Ariyarathne and Liyanapathirana, 2015; Fonseca and Palmeira, 2018). Nevertheless, nowadays, probabilistic analysis, or reliability analysis, has gained attention, and is widely used in diverse areas. In the geotechnical area or, more specifically, in slope stability problems, this growing attention is easily noted. The main factor that improves this importance for geotechnical problems is the uncertainty associated with the material, i.e., soil. In particular, natural soil presents a great spatial variability, varying in all directions of space, but may also vary over time as a result of other factors, such as the environmental condition changes (precipitation, temperature, vegetation, water table, etc.) and anthropogenic conditions (superficial surcharge, profile modifications, materials insertion, etc.).

Since its first steps, reliability analysis used in slope stability has shown significant advantages (Cornell, 1971; Tang et al., 1976; McGuffey et al., 1982). Thus, this analysis has been more and more studied and performed, presenting many improvements over time. For example, in the beginning, only one pre-specified slip surface was investigated. After that, studies started to determine the deterministic critical slip surface and assumed it as a slip surface for probabilistic analysis. However, some authors affirmed that the deterministic and probabilistic slip surfaces were not coincident (Chowdhury and Tang, 1987; Li and Lumb, 1987). Therefore, probabilistic analysis used in the Limit Equilibrium Method (LEM) emerged, which was later adopted in the Finite Element Method (FEM).

Generally, the Monte Carlo simulation (MCS) is the most assumed method in order to perform probabilistic analyses of slopes stability (Genevois and Romeo, 2003; Chalermyanont and Benson, 2005; Salgado and Kim, 2014; Ferreira et al., 2016; Xia et al., 2017). This method is already available in most commercial geotechnical programs, making it even more common and easy to use. However, there are limitations to this usage, such as limited random variables, distribution types, statistical input information, analysis monitoring, and high computational costs. The high computational costs are the main limitation faced by the method because they require a significant number of samples in order to achieve an effective approximation of the failure probability, reducing this usability in design practice.

Nevertheless, there are alternative methods that aim to reduce this computational cost, such as transformation methods (analytical methods). Some examples are First-Order Second-Moment (FOSM), First-Order Reliability Method (FORM), and Second-Order Reliability Method (SORM). These methods usually speed-up the analyses and achieve good estimation for P_f and β values, when compared to MCS. Therefore, some authors have studied and adopted these methods in probabilistic analyses of slope stability (Xu and Low, 2006; Low, 2014; Wang et al., 2017; Xia et al., 2017).

In spite of the fact that recent studies have used alternative methods to carry out these probabilistic analyses, few studies have been carried out to evaluate geosynthetic-reinforced structures (Low and Tang, 1997; Ferreira et al., 2016; Luo and Bathurst, 2017). Studies that address these analyses and the alternative methods with well-known commercial geotechnical programs are even rarer, which does not encourage, or facilitate, the probabilistic analyses in practice, mainly via alternative methods that could significantly reduce the involved computational costs and achieve accurate results.

Therefore, this paper aims to present a reliability analysis in order to take statistical information (uncertainties) into account in a safety analysis of geosynthetic-reinforced embankments. To that end, an alternative reliability evaluation method was used, the FORM, and two well-known commercial geotechnical programs were adopted (GeoStudio and RocScience). The analysis was carried out using a reported case study of a controlled stage-constructed embankment on soft ground (Chai and Bergado, 1993) to investigate its probabilistic stability for each stage.

METHODS

Monte Carlo Simulation

The Monte Carlo simulation technique is the most common and used in practice and in the literature. This technique allows users to solve complex systems without limitations of complexity and number of variables, solving all of them just as easily and providing unbiased estimations. Conceptually, the method is simple, easy to implement, accurate and robust. The only limitation is associated with the computational capacity.

In structural analysis terms, simulation can be understood as a numerical way to simulate impractical experiments. The experiment consists of "testing" the structure for "all" possible combinations of resistances and solicitations. The probability of failure is estimated by calculating the relationship between the failure samples and the total of simulated samples.

Note that the variance in results is inversely proportional to the number of simulated samples. According to Melchers and Beck (2017), the MCS requires around $10^{(p+2)}$ samples in order to achieve a good estimative of P_f, where p assumes the order expected for the P_f of the analyzed structure ($P_f = x{\cdot}10^{-p}$). Therefore, a very high number of simulation samples can be required to evaluate a structure when expecting a significant low P_f, turning it into an impractical analysis due to its high computational costs.

Analytical Reliability Methods

In the literature, the main three analytical methods in use are FOSM, FORM, and SORM, all based on the transformation method proposed by Hasofer and Lind (1974). The transformation consists of mapping the random variables from the design space ($\mathbb{X}$, dimensional space) to the standard normal space ($\mathbb{Y}$, dimensionless space, where random variables

assume that means equal zero and standard deviations equal the unit).

Melchers and Beck (2017) address these three methods. In the FOSM solution, the limit state function [g(x)] is approximated by a linear function. The statistical information is limited up to the second-order moments (μ e σ). The method is simple to implement, and random variable distributions do not need to be reported but note that due to the limitation of statistical moments, it is equivalent to assuming the random variables with normal distributions. This hypothesis limits the solution of practical problems, mainly in significant non-linearity conditions of the performing function.

Nevertheless, the FORM, which is based on FOSM, allows the solution to take into account all statistical information about the random variables assumed for the problem. The statistical information includes the non-normal marginal distributions, as well as the correlation coefficients between variable pairs. In the FORM, the correlations are processed by the model proposed by Nataf (1962) and by the orthogonal decomposition or the Cholesky factorization (presented by Benoît, 1924) of the correlation matrix.

Limit State Function

Studies usually assume the limit state function as $g(\boldsymbol{X}) = FS(\boldsymbol{X})-1$. FS is the ratio between the sum of resisting (R) to activating (A) forces and/or moments along the slip surface, and $\boldsymbol{X}$ is the vector of random variables. However, note that this function introduces non-linearity to the evaluation, and as great as the non-linearity is, the advantages of using analytical methods are lost, increasing the computational costs. In some cases, non-linearity can lead the analysis to a non-convergence condition or equivocated results. Therefore, authors assumed another function for the performing function in order to avoid or reduce this possibility, $g(\boldsymbol{X}) = R(\boldsymbol{X}) - A(\boldsymbol{X})$.

CASE STUDY

The reliability analysis was used in a reported case, a controlled stage-constructed and reinforced embankment on soft ground, presented by Chai and Bergado (1993). The reinforcement was achieved by introducing a geogrid into the structure, i.e., the geosynthetic element. In addition to the reinforcement, vertical drains were installed into the soft clay layer in order to accelerate the settlement process and, consequently, the gain of resistance and stability of the structure.

Figure 1 shows the soil profile and the embankment geometry. On the one hand, according to Chai and Bergado (1993), the soil profile is comprised of a weathered crust at the top 2 meters which is underlain by about 5 meters of very soft silty clay. Adjacent to this layer is a 10 meters thick layer of soft clay which in turn is underlain by about 0.6 meters of peat. Finally, a thick deposit of medium dense to dense clayey silty sand is found below the peat layer.

On the other hand, the embankment has a base width of 44 meters, it is 50 meters long and has a crest width of 11.46 meters (final configuration), and 6.07 and 5.27 meters high for conditions with and without the surcharge layer, respectively. In total, five stages were assumed for the analyses: three constructive stages (two fill stages and one surcharge removal stage); and two non-constructive stages associated with the settlement process. The material parameters were based on the reference study. In short, **Tables 1**, **2** present the stages and parameters assumed for modeling, respectively.

Well-known commercial geotechnical software, such as GeoStudio (SIGMA/W and SLOPE/W) and RocScience (SLIDE^3), were used in order to perform the modeling. On the one hand, for the GeoStudio analyses, the stability verification was performed by stress-strain analyses. The SIGMA/W obtained the stress-strain state and then passed it on to SLOPE/W in order to carry out the stability analysis. On the other hand, RocScience performed the stability verification by using the limit

TABLE 1 | Stages assumed for analysis.

Stages	Description
1st stage	First fill stage, 3.90 m thickness
1st dissip.	First dissipation of the excess pore water pressure, 100 days
2nd stage	Second fill stage, 2.17 m thickness
2nd dissip.	Second dissipation of the excess pore water pressure, 60 days
Surcharge removal	Surcharge layer removal. 0.80 m thickness

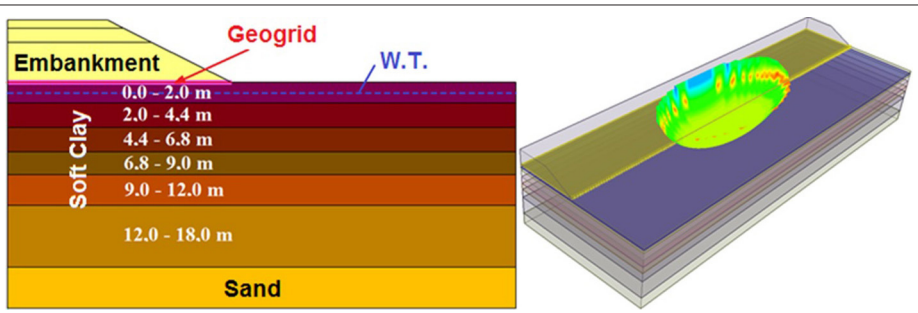

FIGURE 1 | Embank geometry (model via GeoStudio and RocScience).

TABLE 2 | Input parameters of the models.

Parameters	Fill	Sand	Inter-face	Soft clay (for each zone and constructive stage)																Reinf.
				0–2 m			2–4.4 m			4.4–6.8 m			6.8–9 m			9–12 m			12–18 m		
				1st	2nd	3rd	1st	2nd	3rd	1st	2nd	3rd	1st	2nd	3rd	1st	2nd	3rd	1st	2nd	3rd	
γ (kN/m^3)	20.5	17.0	20.5									15										–
ϕ (°)	26	38	13									30										–
c (kPa)	19.0	0.0	9.5									–										–
S_u (kPa)		–		25.6	30.4	33.1	11.5	17.4	20.7	15.1	18.7	20.7	18.9	22.7	24.8	22.8	24.9	26.1	22.8	24.9	26.1	–
e_0		–			1.2			2.5			2.5			1.5			1.5			1.7		–
λ		–			0.35			0.61			0.61			0.28			0.28			0.22		–
κ		–			0.06			0.1			0.1			0.06			0.06			0.04		–
E (MPa)	20	40	20									–										–
ν	0.30	0.20	0.30		0.35			0.25			0.25			0.25			0.25			0.25		–
R_f	0.85	–								–									–			
OCR		–										1.4										–
K_x (m/dia)		–			0.0024			0.0012			0.0012			0.0009			0.0009			0.0006		–
K_y/K_x		–										0.5										–
J (Mpa)		–										–										0.45
T (kN/m)		–										–										80

TABLE 3 | Materials and constitutive models assumed for each.

Materials	Constitutive model assumed	
	Sigma/W	**Slope/W and Slide[3]**
Fill, sand, and interface	Elastic-plastic drained	Mohr-Coulomb
Soft clay	Soft clay (modified cam-clay model with pore water pressure change)	Undrained model ($\phi = 0°$)
Geogrid	Structural beam with no inertial moments (0 m^4), allowing tension only	Reinforcement loads (particular model developed for geosynthetics)

equilibrium method (LEM), Morgenstern-Price precisely, but only to the final stage configuration. At this moment, only one configuration is assumed to enable the probabilistic analysis because this evaluation process, of the three-dimensional model, increases the data amount involved in the modeling, then high computational processing is required.

Table 3 presents the constitutive models assumed for each material. Circular and elliptical slip surfaces were assumed for models performed in GeoStudio and RocScience, respectively.

The soft clay layer was divided into horizontal parts. This division allowed the model to take into account the gain of resistance of foundation material due to the increasing vertical effective stress ($\Delta\sigma_v'$). $\Delta\sigma_v'$ results from the embankment filling and the dissipation of excess pore water pressure over time. Besides, the layer division was also applied to the vertical direction that allows the model to consider the increase in resistance with depth. **Table 2** shows the calculated and assumed values for each zone (split parts) of the foundation.

Among the parameters, specific weight (γ), cohesion (c), undrained shear strength (S_u), friction angle (ϕ), Young modulus (E), overconsolidation ratio (OCR), initial void ratio (e_0), *lambda* and *kappa* (λ and κ, parameters related to the soil compression, inputs of Cam-Clay constitutive model), hydraulic conductivity (K), and stiffness modulus (J), and tensile strength (T) of the reinforcing material were assumed as random variables. The number of random variables for each analysis was limited by the analysis complexity.

Based on the literature, **Table 4** presents statistical information about some geotechnical parameters. The distribution types and statistical moments related to these distributions are the main pieces of information collected.

The correlation between variable pairs is another piece of relevant statistical information that has to be taken into account when performing probabilistic analyses. **Table 5** shows the assumed correlation matrix for the problem. The matrix is based on applications and studies performed by Azzouz et al. (1976) and Low and Tang (1997). Since the LEM analysis needs a lower number of parameters when compared to stress-strain analysis, the correlation matrix may be reduced to the combination of highlighted terms of the basis matrix (**Table 5**).

The spatial correlation assumed for random variables, in the horizontal and vertical directions, was calculated by performing

TABLE 4 | Distribution and *CoV* of parameters assumed as random variables.

Parameter	Distribution	CoV (%)			References
		Min	Med	Max	
Bulk unit weight (γ)	Normal	2.5	7.5	12.5	Sherwood, 1970; Singh, 1971; Lumb, 1974; Ingles and Noble, 1975; Stamatopoulos and Kotzias, 1975
Cohesion (c)	Normal	10.0	40.0	70.0	Tan et al., 1993; Phoon and Kulhawy, 1999; Baker and Calle, 2006
Friction angle (ϕ)	Log-normal	5.0	10.0	15.0	Singh, 1971; Hoeg and Murarka, 1974; Lumb, 1974; Schultze, 1975
E-modulus (E)	Normal	2.0	22.0	42.0	Kennedy, 1978; Otte, 1978
Overconsolidation ratio (OCR)	Normal	10.0	22.5	35.0	Lumb, 1974; Lacasse and Nadim, 1996
Parameter λ of the MCC model	Normal	25.0	27.5	30.0	Lumb, 1974; Corotis et al., 1975; Schultze, 1975; Stamatopoulos and Kotzias, 1975
Parameter κ of the MCC model	Normal	25.0	27.5	30.0	Lumb, 1974; Corotis et al., 1975; Schultze, 1975; Stamatopoulos and Kotzias, 1975
Initial void ratio (e_0)	Normal	13.0	27.5	42.0	Kuhn, 1971; Lumb, 1974; Corotis et al., 1975; Schultze, 1975
Hydraulic conductivity (K)	Log-normal	200.0	250.0	300.0	Lumb, 1974
Undrained shear strength (S_u)	Log-normal	20.0	35.0	50.0	Sherwood, 1970; Lumb, 1974; Lacasse and Nadim, 1996
Reinforcement stiffness (J_{geo})	Normal	5.0	10.0	15.0	Assumed (Geosynthetics Lab.—EESC)
Reinforcement tensile strength (T_{geo})	Normal	5.0	10.0	15.0	Low and Tang, 1997; Assumed (Geosynthetics Lab.—EESC)

the exponential model, Equation 1, as applied by Low and Tang (1997).

$$\rho_{ij} = e^{\frac{|Position(i) - Position(j)|}{d}} \quad (1)$$

RESULTS AND DISCUSSIONS

Model Validation

Initially, deterministic analyses were performed in order to validate the model. The calculated excess pore water pressures and factors of safety were compared with Chai and Bergado (1993) published values. These comparisons are presented as follows.

Excess Pore Water Pressure

Figure 2 presents a comparison between excess pore water pressures. It is worth mentioning that, according to Chai and Bergado (1993), the reference values are associated with another similar embankment that has the same foundation profile, and therefore, obtained very similar responses. Therefore, the variations in results are most significant in the analysis of the intermediate stage, which may be explained by associating these variations to the difference in the embankments' height at this moment (5.70 < 6.07 meters). Yet, the results were satisfactory, validating the model, and thus enabling us to proceed with the analyses.

Deterministic Results

Figure 3 shows the factors of safety obtained by deterministic stability analyses. In the reference study, the authors affirm that the reinforcement insertion was implemented in order to achieve factors of safety around 1.3 for constructive stages. By considering the obtained results, note that the acquired factors were <1.3 and the target was beaten only once when analyzing the final period of the first consolidation stage. In the final configuration, the acquired factor was very close to that reported by Chai and Bergado (1993), both around 1.22.

Reliability Indexes

In the literature, Low and Tang (1997) also carried out a probabilistic analysis of this same case study (Chai and Bergado, 1993). However, the values of the coefficients of variation assumed for the problem were lower than the minimum values applied here, based on a literature review. Hence, in addition to the performed analyses, analyses assuming the *CoV* values adopted by Low and Tang (1997) were also carried out in order to compare these results. **Table 6** presents these *CoV* values.

Thus, **Figure 4** allows the comparison between both assumed configurations. First, the model considers the medium *CoV* values and all random values assumed (complete correlation matrix). Second, the model considers the *CoV* values adopted by Low and Tang (1997) and a reduced number of random variables, in order to comply with the authors' assumption (gray values of the basis correlation matrix). Note that the β behavior with stages was very similar for both configurations. For the Low and Tang (1997) configuration, the achieved indexes were significantly higher than others, which was coherent with the assumption of low *CoV*. Low and Tang (1997) analyzed only the final stage configuration, assuming a β value of 1.84, which was similar to that acquired in this study, around 1.77. This small difference may be associated with the assumed calculation methods or models, even with some geometry simplifications assumed by both the authors and Low and Tang (1997).

Note that either assuming medium values or Low and Tang (1997) values for *CoV*, unsatisfactory safety conditions were reached ($\beta < 2.5$ during construction, and $\beta < 3$ at final stage), except for the first dissipation stage.

TABLE 5 | Basis correlation matrix for reliability analyses of the models.

	Matriz de correlação base																												
Parameter	γ_{at}	c_{at}	ϕ_{at}	E_{at}	γ_{arg}	***OCR***	λ_{0-2}	$\lambda_{2-6.8}$	$\lambda_{6.8-12}$	λ_{12-18}	κ_{0-2}	$\kappa_{2-6.8}$	$\kappa_{6.8-12}$	κ_{12-18}	$e_{0.0-2}$	$e_{0.2-6.8}$	$e_{0.6.8-12}$	$e_{0.12-18}$	$K_{x.0-2}$	$K_{x.2-6.8}$	$K_{x.6.8-12}$	$K_{x.12-18}$	$S_{u.0-2}$	$S_{u.2-4.4}$	$S_{u.4.4-6.8}$	$S_{u.6.8-9}$	$S_{u.9-18}$	J	T
γ_{at}	1	0.5	0.5	0.5	0	0	0	0	0	0	0	0	0	0	0	0	0	0	0	0	0	0	0	0	0	0	0	0	0
c_{at}	0.5	1	−0.3	0	0	0	0	0	0	0	0	0	0	0	0	0	0	0	0	0	0	0	0	0	0	0	0	0	0
ϕ_{at}	0.5	−0.3	1	0	0	0	0	0	0	0	0	0	0	0	0	0	0	0	0	0	0	0	0	0	0	0	0	0	0
E_{at}	0.5	0	0	1	0	0	0	0	0	0	0	0	0	0	0	0	0	0	0	0	0	0	0	0	0	0	0	0	0
γ_{arg}	0	0	0	0	1	0	0	0	0	0	0	0	0	0	−0.5	−0.5	−0.5	−0.5	0	0	0	0	0.5	0.5	0.5	0.5	0.5	0	0
OCR	0	0	0	0	0	1	0	0	0	0	0	0	0	0	0	0	0	0	0	0	0	0	0	0	0	0	0	0	0
λ_{0-2}	0	0	0	0	0	0	1	0.558	0.243	0.097	0.68	0	0	0	0	0	0	0	0	0	0	0	0	0	0	0	0	0	0
$\lambda_{2-6.8}$	0	0	0	0	0	0	0.558	1	0.435	0.174	0	0	0	0	0	0	0	0	0	0	0	0	0	0	0	0	0	0	0
$\lambda_{6.8-12}$	0	0	0	0	0	0	0.243	0.435	1	0.4	0	0	0	0	0	0	0	0	0	0	0	0	0	0	0	0	0	0	0
λ_{12-18}	0	0	0	0	0	0	0.097	0.174	0.4	1	0	0	0	0	0	0	0	0	0	0	0	0	0	0	0	0	0	0	0
κ_{0-2}	0	0	0	0	0	0	0.68	0	0	0	1	0.558	0.243	0.097	0	0	0	0	0	0	0	0	0	0	0	0	0	0	0
$\kappa_{2-6.8}$	0	0	0	0	0	0	0	0	0	0	0.558	1	0.435	0.174	0	0	0	0	0	0	0	0	0	0	0	0	0	0	0
$\kappa_{6.8-12}$	0	0	0	0	0	0	0	0	0	0	0.243	0.435	1	0.4	0	0	0	0	0	0	0	0	0	0	0	0	0	0	0
κ_{12-18}	0	0	0	0	0	0	0	0	0	0	0.097	0.174	0.4	1	0	0	0	0	0	0	0	0	0	0	0	0	0	0	0
$e_{0.0-2}$	0	0	0	0	−0.5	0	0	0	0	0	0	0	0	0	1	0.558	0.243	0.097	0.68	0	0	0	0	0	0	0	0	0	0
$e_{0.2-6.8}$	0	0	0	0	−0.5	0	0	0	0	0	0	0	0	0	0.558	1	0.435	0.174	0	0	0	0	0	0	0	0	0	0	0
$e_{0.6.8-12}$	0	0	0	0	−0.5	0	0	0	0	0	0	0	0	0	0.243	0.435	1	0.4	0	0	0	0	0	0	0	0	0	0	0
$e_{0.12-18}$	0	0	0	0	−0.5	0	0	0	0	0	0	0	0	0	0.097	0.174	0.4	1	0	0	0	0	0	0	0	0	0	0	0
$K_{x.0-2}$	0	0	0	0	0	0	0	0	0	0	0	0	0	0	0.68	0	0	0	1	0.558	0.243	0.097	0	0	0	0	0	0	0
$K_{x.2-6.8}$	0	0	0	0	0	0	0	0	0	0	0	0	0	0	0	0	0	0	0.558	1	0.435	0.174	0	0	0	0	0	0	0
$K_{x.6.8-12}$	0	0	0	0	0	0	0	0	0	0	0	0	0	0	0	0	0	0	0.243	0.435	1	0.4	0	0	0	0	0	0	0
$K_{x.12-18}$	0	0	0	0	0	0	0	0	0	0	0	0	0	0	0	0	0	0	0.097	0.174	0.4	1	0	0	0	0	0	0	0
$S_{u.0-2}$	0	0	0	0	0.5	0	0	0	0	0	0	0	0	0	0	0	0	0	0	0	0	0	1	0.693	0.465	0.317	0.125	0	0
$S_{u.2-4.4}$	0	0	0	0	0.5	0	0	0	0	0	0	0	0	0	0	0	0	0	0	0	0	0	0.693	1	0.67	0.457	0.18	0	0
$S_{u.4.4-6.8}$	0	0	0	0	0.5	0	0	0	0	0	0	0	0	0	0	0	0	0	0	0	0	0	0.465	0.67	1	0.682	0.268	0	0
$S_{u.6.8-9}$	0	0	0	0	0.5	0	0	0	0	0	0	0	0	0	0	0	0	0	0	0	0	0	0.317	0.457	0.682	1	0.393	0	0
$S_{u.9-18}$	0	0	0	0	0.5	0	0	0	0	0	0	0	0	0	0	0	0	0	0	0	0	0	0.125	0.18	0.268	0.393	1	0	0
J	0	0	0	0	0	0	0	0	0	0	0	0	0	0	0	0	0	0	0	0	0	0	0	0	0	0	0	1	0
T	0	0	0	0	0	0	0	0	0	0	0	0	0	0	0	0	0	0	0	0	0	0	0	0	0	0	0	0	1

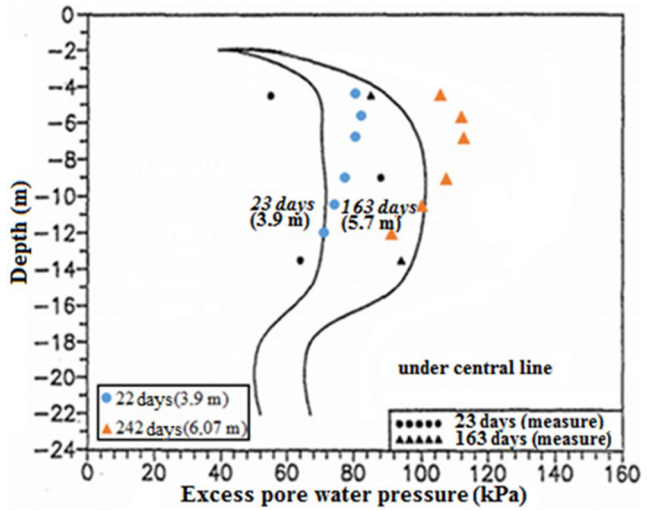

FIGURE 2 | Comparison between results of excess pore water pressure (adapted from Chai and Bergado, 1993, with permission from Bergado).

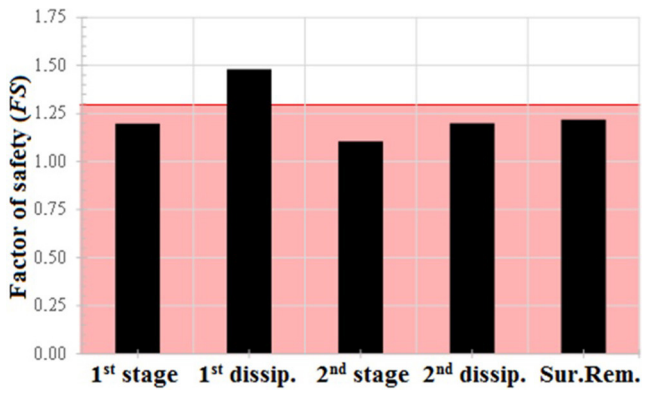

FIGURE 3 | The factor of safety (*FS*) vs. stages (SIGMA/W + SLOPE/W).

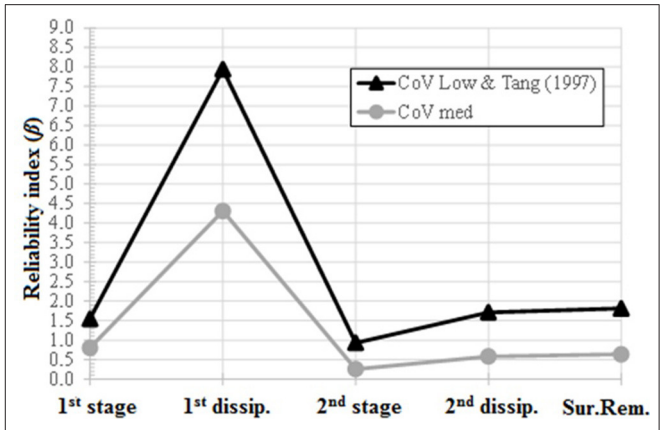

FIGURE 4 | Reliability indexes vs. stages, considering both medium and Low and Tang (1997) *CoV* levels (SIGMA/W + SLOPE/W).

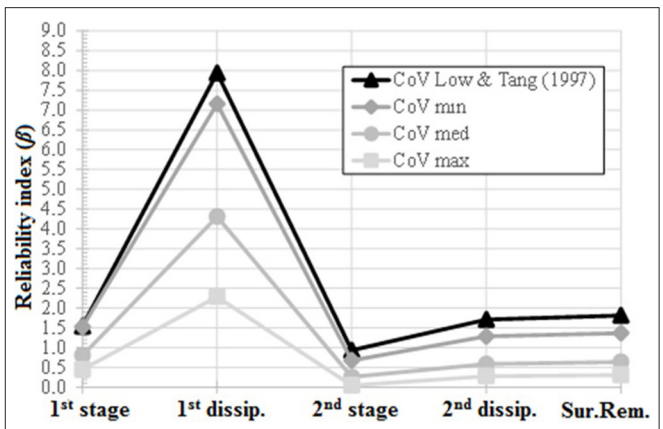

FIGURE 5 | Reliability indexes vs. stages, evaluation of uncertainty level influence (SIGMA/W + SLOPE/W).

TABLE 6 | Parameters and *CoV* assumed by Chowdhury and Tang (1987).

Parameters	*CoV* (%)
Bulk unit weight (γ)	5.0
Cohesion (c)	15.0
Friction angle (ϕ)	10.0
Undrained shear strength (S_u)	15.0
Reinforcement stiffness (J)	10.0

Influence of Uncertainty Level

Analyses considering four levels of *CoV* values (Low and Tang, 1997; minimum; medium; and maximum) were performed in order to evaluate their influence (uncertainty level) into probabilistic analyses. **Figure 5** shows the results.

In spite of the fact that different levels result in discrepant values of β, the overall behavior of this index was very similar in stages for each assumed uncertainty level. In addition, as expected, low uncertainty levels drove to high β, or safety levels. Note that the highest variation of the index was associated with the first dissipation stage, which varied from $\beta = 2.29$ (*CoV* maximum), considered with a safety level below average (USACE, 1997), to $\beta = 8.01$ (*CoV* assumed by Low and Tang, 1997), considered above the high safety level specified by USACE (1997).

Sensitivity Analysis

The sensitivity analysis is important to identify which random variables, or parameters, are more influencers to the structural safety in a probabilistic analysis condition. Therefore, the sensitivity analysis was performed by considering two conditions. First, a probabilistic analysis assuming all the random variables (contained in the basis correlation matrix) with medium *CoV* level. Second, a probabilistic analysis assuming only the random variables adopted by Low and Tang (1997), as well as the adopted *CoV*. **Figure 6** shows the results.

On the one hand, note that most of the assumed random variables are not influencers, which may be treated as deterministic variables. On the other hand, random variables

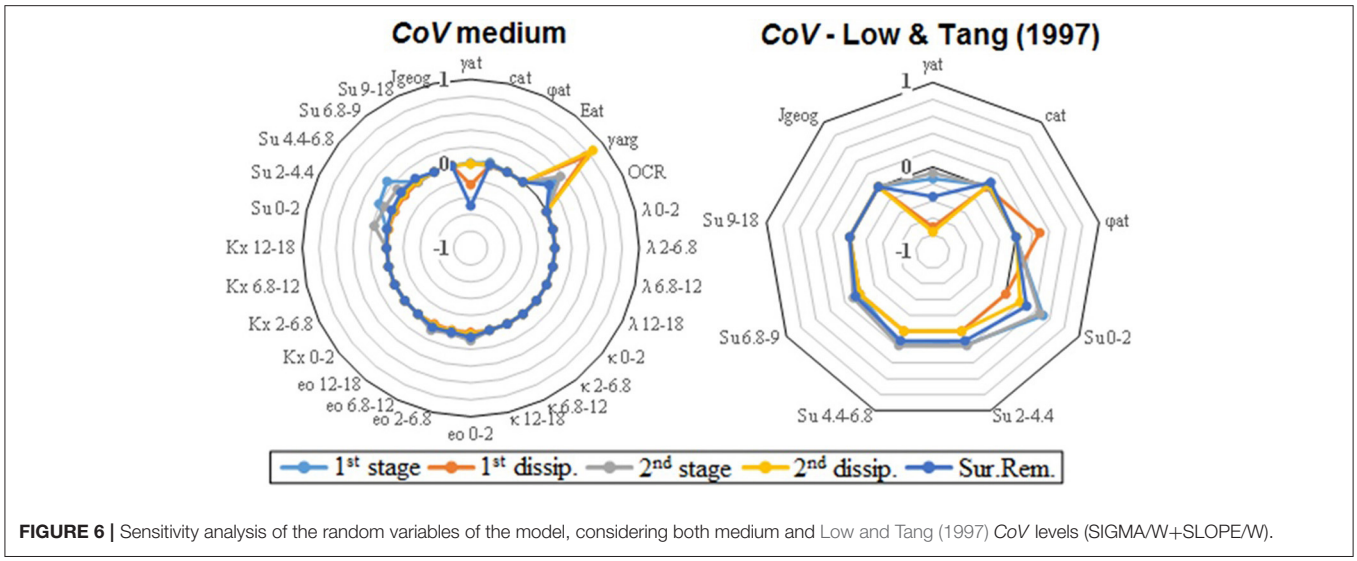

FIGURE 6 | Sensitivity analysis of the random variables of the model, considering both medium and Low and Tang (1997) *CoV* levels (SIGMA/W+SLOPE/W).

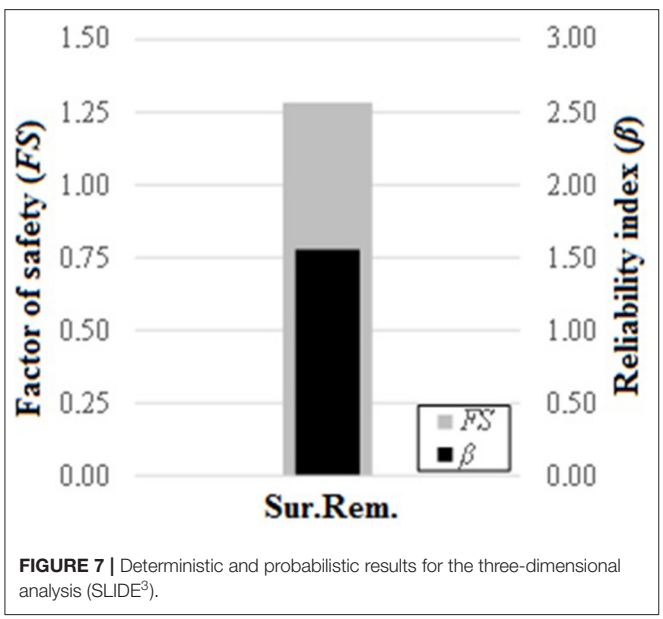

FIGURE 7 | Deterministic and probabilistic results for the three-dimensional analysis (SLIDE^3).

that are significantly more sensitive were similar for both configurations (γ_{fill} and S_u, for different layer zones). Besides, there is a significant sensitivity associated with γ_{clay} for the analysis that assumed more random variables, which was a parameter not considered by Low and Tang (1997).

Finally, note also that the parameters associated with the initial void ratios (e_0) of each layer exhibited a slight sensitivity, which also may be assumed as deterministic. However, it should be interesting to assume these parameters as random variables, even not showing high sensitivities, in order to approximate the real probability of the failure condition.

Three-Dimensional Analysis—Final Configuration

As mentioned, a three-dimensional analysis was carried out using the SLIDE^3, belonging to the RocScience pack. **Table 3** presents the constitutive models assumed for each material. The stability analysis was carried out by assuming elliptical slip surfaces for this three-dimensional model. Besides, for the probabilistic performance, the medium *CoV* level was assumed.

Figure 7 presents the acquired results for both deterministic and probabilistic analyses. Note that both *FS* and β values were coherent and close to the previous results, evaluated via two-dimensional analysis ($FS = 1.28$, and $\beta = 1.55$). Therefore, a two-dimensional analysis may be sufficient for the proposal of this analysis. This condition would change just in case of considerate the spatial variability over the three coordinate axes into the analysis.

CONCLUSIONS

This paper aimed to present a reliability analysis to consider statistical information in a safety analysis of reinforced embankments. The analysis was used in a case study of a controlled stage-constructed embankment on soft ground, reported by Chai and Bergado (1993). The conclusions about this analysis are as follows:

- Deterministically, the embankment was satisfactorily modeled, reaching the same *FS* published by Chai and Bergado (1993), for the final configuration (around 1.22). Besides, the excess pore water pressures acquired by the model agrees with the field-measured values. However, the reached *FS* values for all stages were below the predefined acceptance level.
- Probabilistically, the structure also assumed low safety levels, which were more a matter of concern than deterministic results ($\beta < 1$, or $P_f > 16\%$, for 4 out of all five stages, assuming medium *CoV*).
- The β obtained by this paper for the final structure configuration (around 1.77) was compared with the index

presented by Low and Tang (1997) (1.84), which was very similar. This slight difference was associated with some alterations and simplifications made to the model geometry, when compared with those presented by Chai and Bergado.
- The uncertainty level assumed for random variables in the analysis proved to be quite significant for the evaluations, greatly influencing the β values.
- The sensitivity analysis showed that the main sensitivity variables for the problem evaluation were S_u, γ_{clay}, and γ_{fill}. This result was acquired for both medium CoV and CoV, adopted by Low and Tang (1997) analysis.
- A three-dimensional analysis was carried out for the final configuration of the structure. The FS and β values were very coherent with results obtained via a two-dimensional analysis. This result demonstrates that a two-dimensional analysis may be sufficient for this proposal, requiring lower computational costs than three-dimensional evaluations.

DATA AVAILABILITY STATEMENT

All datasets generated for this study are included in the article/supplementary material.

AUTHOR CONTRIBUTIONS

All authors listed have made a substantial, direct and intellectual contribution to the work, and approved it for publication.

ACKNOWLEDGMENTS

The authors would like to thank the financial support from CAPES and the Laboratory of Geosynthetics at the Department of Geotechnical Engineering and the Department of Structural Engineering at the University of São Paulo (USP) that provided the GeoStudio, RocScience, and StRAnD software for this study.

REFERENCES

Ariyarathne, P., and Liyanapathirana, D. S. (2015). Review of existing design methods for geosynthetic-reinforced pile-supported embankments. *Soils Found.* 55, 17–34. doi: 10.1016/j.sandf.2014.12.002

Azzouz, A. S., Krizek, R. J., and Corotis, R. B. (1976). Regression analysis of soil compressibility. *Soils Found.* 16, 19–29. doi: 10.3208/sandf1972.16.2_19

Baker, J., and Calle, E. (2006). *Joint Committee on Structural Safety Probabilistic Model Code, Section 3.7: Soil Properties, Updated Version*. Technical Report, Joint Committee on Structural Safety (JCSS).

Benoît, C. (1924). Note sur une méthode de résolution des équations normales provenant de l'application de la méthode des moindres carrés à un système d'équations linéaires en nombre inférieur à celui des inconnues (Procédé de Commandant Cholesky). *Bull. Géodetic Sci.* 2, 67–77. doi: 10.1007/BF03031308

Chai, J., and Bergado, D. T. (1993). Performance of reinforced embankment on Muar Clay deposit. *Soils Found.* 33, 1–17. doi: 10.3208/sandf1972.33.4_1

Chalermyanont, T., and Benson, C. H. (2005). Reliability-based design for external stability of mechanically stabilized earth walls. *Int. J. Geomech.* 5, 196–205. doi: 10.1061/(ASCE)1532-3641(2005)5:3(196)

Chowdhury, R. N., and Tang, W. H. (1987). "Comparison of risk models for slopes," in *Proceedings of the 5th International Conference on Application of Statistics and Probability in Soil and Structural Engineering* (Vancouver, BC), 863–869.

Cornell, C. A. (1971). "First order uncertainty analysis of soils deformations and stability," in *Proceedings of the 1st International Conference on Application of Statistics and Probability in Soil and Structural Engineering* (Hong Kong: Hong Kong University Press), 129–144.

Corotis, R. B., Azzouz, A. S., and Krizek, R. (1975). "Statistical evaluation of soil index properties and constrained modulus," in *Proceedings of the 2nd International Conference on Application of Statistics and Probability in Soil and Structural Engineering* (Aachen), 273–294.

Elias, V., Christopher, B. R., and Berg, R. R. (2001). *Mechanically Stabilized Earth Walls and Reinforced Soil Slopes – Design and Construction Guidelines, Federal Hwy*. Administration Rep. No. FHWA-NH1–00-43. U.S. Department of Transportation, Federal Highway Administration, National Highway Institute, Washington, DC.

Fattah, M. Y., Mohammed, H. A., and Hassan, H. A. (2016a). Load transfer and arching analysis in reinforced embankment. *Proc. Inst. Civil Eng. Struct. Build.* 169, 797–808. doi: 10.1680/jstbu.15.00046

Fattah, M. Y., Zabar, B. S., and Hassan, H. A. (2015). Soil arching analysis in embankments on soft clays reinforced by stone columns. *Struct. Eng. Mech.* 56, 507–534. doi: 10.12989/sem.2015.56.4.507

Fattah, M. Y., Zabar, B. S., and Hassan, H. A. (2016b). Experimental analysis of embankment on ordinary and encased stone columns. *Int. J. Geomech.* 16:04015102. doi: 10.1061/(ASCE)GM.1943-5622.0000579

Ferreira, F. B., Topa Gomes, A., Vieira, C. S., and Lopes, L. M. (2016). Reliability analysis of geosynthetic-reinforced steep slopes. *Geosynth. Int.* 23, 301–315. doi: 10.1680/jgein.15.00057

Fonseca, E., and Palmeira, E. M. (2018). An evaluation of the accuracy of design methods for geosynthetic reinforced piled embankments. *Can. Geotech. J.* 56, 761–773. doi: 10.1139/cgj-2018-0071

Genevois, R., and Romeo, R. W. (2003). Probability of failure occurrence and recurrence in rock slopes stability analysis. *Int. J. Geomech.* 3, 34–42. doi: 10.1061/(ASCE)1532-3641(2003)3:1(34)

Hasofer, A. M., and Lind, N. C. (1974). Exact and invariant second-moment code format. *J. Eng. Mech.* 100, 111–121.

Hoeg, K., and Murarka, R. P. (1974). Probabilistic analysis of a retaining wall. *J. Geotech. Eng.* 100, 349–370.

Ingles, O. G., and Noble, C. S. (1975). "The evaluation of base course materials," in *Proceedings of the Soil Mechanics-Recent Developments*, eds S. Valliappan, S. J. Hain, and I. K. Lee (Sydney, NSW: Unisearch Ltd.), 399–410.

Kennedy, T. W. (1978). "Practical use of the indirect tensile test for the characterization of pavement materials," *Proceedings of the 9th Australian Road Research Board Conference* (Brisbane, QLD), 36–45.

Koerner, R. M. (2012). *Designing With Geosynthetics, 6th Edn*. New York, NY: Xlibris Publishing Co.

Kuhn, S. H. (1971). "Quality control in highway construction," in *Proceedings of the 1st International Conference on Applications of Statistics and Probability in Soil and Structural Engineering* (Hong Kong: Hong Kong University Press), 287–312.

Lacasse, S., and Nadim, F. (1996). "Uncertainties in characterizing soil properties," *Proceedings of the Uncertainty 96', Uncertainty in the Geologic Environment: From Theory to Practice*, eds C. D. Shackelford, P. P. Nelson, and M. J. S. Roth (Madison, WI: ASCE), 49–75.

Li, K. S., and Lumb, P. (1987). Probabilistic design slopes. *Can. Geotech. J.* 24, 520–535. doi: 10.1139/t87-068

Low, B. K. (2014). FORM, SORM, and spatial modeling in geotechnical engineering. *Struct. Saf.* 46, 56–64. doi: 10.1016/j.strusafe.2013.08.008

Low, B. K., and Tang, W. H. (1997). Reliability analysis of reinforced embankments on soft ground. *Can. Geotech. J.* 34, 672–685. doi: 10.1139/t97-032

Lumb, P. (1974). "Application of statistics in soil mechanics," in *Proceedings of the Soil Mechanics: New Horizons*, ed I. K. Lee (Newnes-Butterworth: ASCE), 44–112, 221–239.

Luo, N., and Bathurst, R. J. (2017). Probabilistic analysis of reinforced slopes using RFEM and considering spatial variability of frictional soil properties due to compaction. *Georisk Assess. Manag. Risk Eng. Syst. Geohazards* 12, 87–108. doi: 10.1080/17499518.2017.1362443

McGuffey, V., Grivas, D., Iori, J., and Kyfor, Z. (1982). Conventional and probabilistic embankment design. *J. Geotech. Eng.* 108, 1246–1254.

Melchers, R. E., and Beck, A. T. (2017). *Structural Reliability Analysis and Prediction, 3rd Edn*. New York, NY: Wiley.

Nataf, A. (1962). Détermination des distribution dont les marges sont données. *C. R. Acad. Sci.* 225, 42–43.

Otte, E. (1978). *A structural design procedure for cement-treated layers in pavements* (doctoral thesis). Faculty of Engineering, University of Pretoria, Pretoria, South Africa.

Phoon, K. K., and Kulhawy, F. H. (1999). Characterization of geotechnical variability. *Can. Geotech. J.* 36, 612–624. doi: 10.1139/t99-038

Salgado, R., and Kim, D. (2014). Reliability analysis of load and resistance factor design of slopes. *J. Geotech. Geoenviron. Eng.* 140, 57–73. doi: 10.1061/(ASCE)GT.1943-5606.0000978

Schultze, E. (1975). "Some aspects concerning the application of statistics and probability to foundation structures," in *Proceedings of the 2nd International Conference on Application of Statistics and Probability in Soil and Structural Engineering* (Aachen), 457–494.

Sherwood, P. T. (1970). *Reproducibility of Results of Soil Classification and Compaction Tests*. Report LR 339, Road Research Laboratory, Crowthorne.

Singh, A. (1971). "How reliable is the factor of safety in foundation engineering?" in *Proceedings of the 1st International Conference on Applications of Statistics and Probability in Soil and Structural Engineering* (Hong Kong: Hong Kong University Press), 389–424.

Stamatopoulos, A. C., and Kotzias, P. C. (1975). "The relative value of increasing number of observations," in *Proceedings of the 2nd International Conference on Application of Statistics and Probability in Soil and Structural Engineering* (Aachen), 495–510.

Tan, C. P., Donald, I. B., and Melchers, R. E. (1993). "Probabilistic slip circle analysis of earth and rockfill dams," in *Proceedings Probabilistic Methods in Geotechnical Engineering* (Canberra), 281–288.

Tang, W., Yucemen, M., and Ang, A. (1976). Probability-based short-term design of soil slopes. *Can. Geotech. J.* 13, 210–215. doi: 10.1139/t76-024

USACE (1997). *Engineering and Design Introduction to Probability and Reliability Methods for Use in Geotechnical Engineering*. CECW-EG – ETL 1110–2-547. Washington, DC.

Wang, F., Li, H., and Zhang, Q.-L. (2017). Response-surface-based embankment reliability under incomplete probability information. *Int. J. Geomech.* 17:06017021. doi: 10.1061/(ASCE)GM.1943-5622.0001017

Xia, Y., Mahmoodian, M., Li, C.-Q., and Zhou, A. (2017). Stochastic method for predicting risk of slope failure subjected to unsaturated infiltration flow. *Int. J. Geomech.* 17:04017037. doi: 10.1061/(ASCE)GM.1943-5622.0000908

Xu, B., and Low, B. K. (2006). Probabilistic analysis of structured rock/soil slopes-several methods compared. *J. Geotech. Geoenviron. Eng.* 132, 1444–1145. doi: 10.1061/(ASCE)1090-0241(2006)132:11(1444)

Conflict of Interest: The authors declare that the research was conducted in the absence of any commercial or financial relationships that could be construed as a potential conflict of interest.

frontiers in Built Environment

ORIGINAL RESEARCH
published: 18 February 2020
doi: 10.3389/fbuil.2020.00012

Pullout Behavior of Different Geosynthetics—Influence of Soil Density and Moisture Content

Fernanda Bessa Ferreira, Castorina Silva Vieira and Maria de Lurdes Lopes*

Construct-GEO, Faculty of Engineering, University of Porto, Porto, Portugal

Geosynthetics have increasingly been used as reinforcement in permanent earth structures, such as road and railway embankments, steep slopes, retaining walls, and bridge abutments. The understanding of soil-geosynthetic interaction is of primary importance for the safe design of geosynthetic-reinforced soil structures, such as those included in transportation infrastructure projects. In this study, the pullout behavior of three different geosynthetics (geogrid, geocomposite reinforcement, and geotextile) embedded in a locally available granite residual soil is assessed through a series of large-scale pullout tests involving different soil moisture and density conditions. Test results show that soil density is a key factor affecting the reinforcement pullout resistance and the failure mode at the interface, regardless of geosynthetic type or soil moisture content. The soil moisture condition may considerably influence the pullout response of the geosynthetics, particularly when the soil is in medium dense state. The geogrid exhibited higher peak pullout resistance than the remaining geosynthetics, which is associated with the significant contribution of the passive resistance mobilized against the geogrid transverse members to the overall pullout capacity of the reinforcement.

Keywords: geosynthetics, geosynthetic-reinforced soil structures, pullout behavior, soil moisture content, soil density

OPEN ACCESS

Edited by:
Sanjay Shrawan Nimbalkar, University of Technology Sydney, Australia

Reviewed by:
Amarnath M. Hegde, Indian Institute of Technology Patna, India
Ting Li, Southwest Jiaotong University, China

****Correspondence:***
Castorina Silva Vieira
cvieira@fe.up.pt

Specialty section:
This article was submitted to Transportation and Transit Systems, a section of the journal Frontiers in Built Environment

Received: *06 December 2019*
Accepted: *30 January 2020*
Published: *18 February 2020*

Citation:
Ferreira FB, Vieira CS and Lopes ML (2020) Pullout Behavior of Different Geosynthetics—Influence of Soil Density and Moisture Content. Front. Built Environ. 6:12. doi: 10.3389/fbuil.2020.00012

INTRODUCTION

Geosynthetics have been widely used as a reinforcement material in several geotechnical engineering applications, such as roadway and railway layers and embankments (Wu et al., 1992; Ashmawy and Bourdeau, 1995; Lee and Wu, 2004; Ravi et al., 2014; Ferreira et al., 2016a; Nimbalkar and Indraratna, 2016; Indraratna et al., 2018, 2019; Ngo et al., 2018; Byun and Tutumluer, 2019; Tatsuoka, 2019). In such applications, the interaction mechanism between the geosynthetic and the surrounding material is of primary importance. Recognizing the proper interaction mechanism (shear or pullout) and the selection of the most appropriate test for its characterization are key factors in the design of the above-mentioned structures. When the geosynthetic tends to be pulled out from the reinforced mass (e.g., in the upper zone of a reinforced soil slope or in geosynthetic basal reinforcement), the interaction mechanism shall be characterized through laboratory or field pullout tests.

By definition, the pullout resistance of a geosynthetic is the tensile load required to cause outward sliding of the geosynthetic through the reinforced soil mass. The pullout mechanism of a geogrid differs from that of a geotextile (with continuous surface). In the case of the geogrid,

the pullout resistance is composed of skin friction on the surface of the geogrid ribs (frictional resistance) and bearing resistance mobilized against the transverse members (passive resistance). For geotextiles (with continuous surface), only the frictional resistance contributes to the overall pullout capacity.

The great relevance of the interaction mechanism between the geosynthetic and the surrounding soil is patent in the high number of studies that have been published in the last decades. Several experimental studies related to the fundamentals of soil–geosynthetic interaction under pullout loading conditions have been reported (Raju, 1995; Lopes and Ladeira, 1996a; Palmeira, 2004; Moraci and Recalcati, 2006; Subaida et al., 2008; Tang et al., 2008; Hatami and Esmaili, 2015; Ferreira et al., 2016b, 2020; Mirzaalimohammadi et al., 2019; Morsy et al., 2019; Isik and Gurbuz, 2020). However, despite the wide range of studies available in the literature, most of them have been carried out using freely draining granular soils. The pullout behavior of geosynthetics when inserted in cohesive or residual soils has not been widely explored (Bakeer et al., 1998; Abu-Farsakh et al., 2006; Esmaili et al., 2014; Ferreira et al., 2016b) and more insights are needed.

This paper extends previous work on the pullout response of geosynthetics embedded in granite residual soil presented in Ferreira et al. (2016b). While the earlier study was carried out using dry soil, this current study involves soil compacted at the optimum moisture content, which more closely represents typical field conditions. Special emphasis is placed on the effects of soil dry density, moisture content and geosynthetic type on the pullout resistance and deformation behavior of the reinforcement when subjected to pullout loading. The obtained results will be useful to establish appropriate design parameters for geosynthetic-reinforced soil structures, such as those included in transportation infrastructure projects.

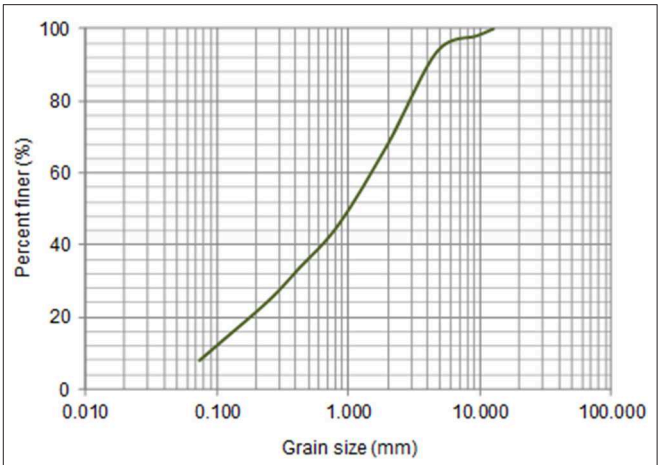

FIGURE 1 | Particle size distribution curve of the granite residual soil.

TABLE 1 | Physical properties of the granite residual soil.

Property	Unit	Value
D_{10}	mm	0.09
D_{30}	mm	0.35
D_{50}	mm	1.00
C_U	–	16.90
C_C	–	1.00
G	–	2.73
e_{max}[a]	–	0.998
e_{min}[a]	–	0.476
γ_{dmax}[b]	kN/m^3	18.93
w_{opt}[b]	%	11.45

[a] *Evaluated using the ASTM D 4253-93 (1993) and ASTM D 4254-93 (1993) standards.*
[b] *Evaluated using the Modified Proctor test [BS 1377-4:1990 (BSI, 1990)].*

MATERIALS AND METHODS

Materials

Soil

Granite residual soils are widely available in the northern region of Portugal and often used as backfill material for reinforced soil construction and sub-base layers of transportation infrastructures. In this regard, a locally available granite residual soil was procured from a local supplier and used throughout the current study. This soil can be classified as SW-SM (well-graded sand with silt and gravel) as per the Unified Soil Classification System (ASTM D 2487-11, 2011). The particle size distribution of this particular soil is presented in **Figure 1** and the main physical properties are summarized in **Table 1**.

Geosynthetics

Three different geosynthetics were analyzed in the present study (**Figure 2**): a biaxial woven geogrid (GGR), a uniaxial high-strength geotextile, commonly referred to as geocomposite reinforcement (GCR) and a non-woven geotextile (GTX). The GGR (**Figure 2A**) is manufactured from high-tenacity polyester yarns, which are covered with a protective polymeric coating. The GCR (**Figure 2B**) is composed of high-tenacity polyester yarns attached to a continuous filament non-woven polypropylene geotextile. The GTX (**Figure 2C**) consists of mechanically bonded (needle punched) continuous filaments of polypropylene.

Several laboratory and field studies have shown the beneficial effect of using non-woven geotextiles as reinforcement elements of fine-grained soils (poorly draining soils) due to their internal drainage capacity (Tan et al., 2001; Portelinha et al., 2013). Indeed, the hydraulic properties of non-woven geotextile reinforcements can assist in the pore-water pressure dissipation, hence improving the internal stability of the reinforced structure. Therefore, a non-woven geotextile and a geocomposite reinforcement (consisting of a non-woven geotextile reinforced with polyester yarns) were selected for the current study.

The in-isolation tensile strength of the geosynthetics was assessed through wide-width tensile tests, following the EN ISO 10319:2008 (CEN, 2008). The mean load-strain curves from five tensile tests carried out under repeatability conditions for each geosynthetic are shown in **Figure 3**. A summary of the relevant physical and mechanical properties of the reinforcements is given in **Table 2**.

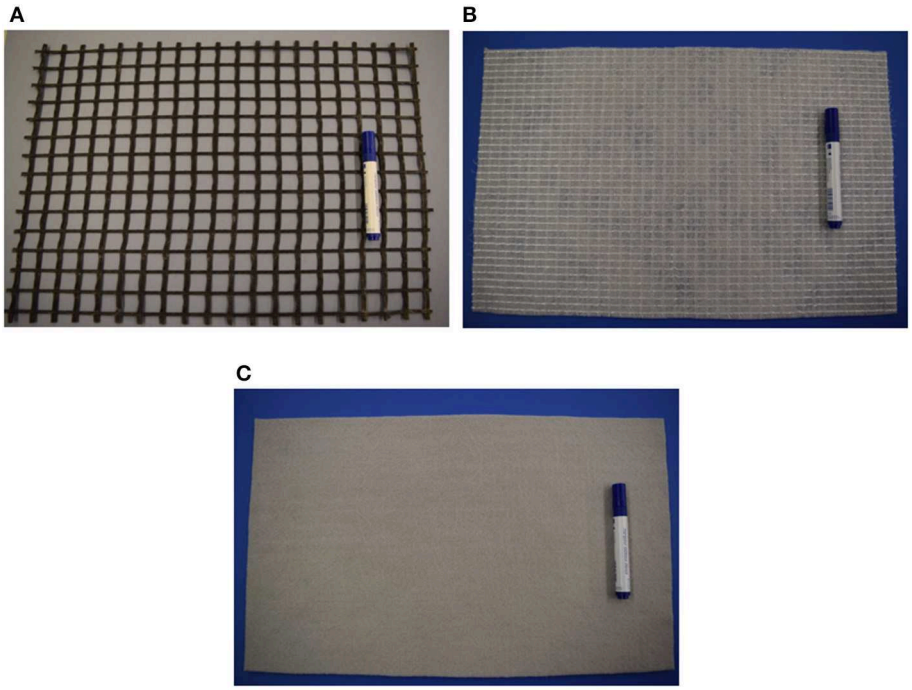

FIGURE 2 | Geosynthetics used: **(A)** GGR; **(B)** GCR; **(C)** GTX.

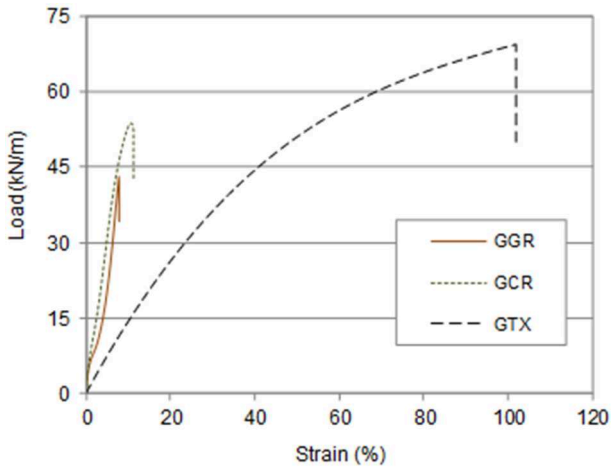

FIGURE 3 | Mean load-strain curves of the geosynthetics from in-isolation tensile tests performed according to EN ISO 10319:2008 (CEN, 2008).

TABLE 2 | Physical and mechanical properties of the geosynthetics.

Property	Unit	Geosynthetics		
		GGR	GCR	GTX
Raw material	–	PET	PET/PP	PP
Mass per unit area	g/m^2	380	310	1,000
Thickness-2 kPa	mm	–	2.3	7.2
Thickness of longitudinal ribs	mm	1.6	–	–
Thickness of transverse ribs	mm	1.6	–	–
Mean grid size	mm	25 × 25	–	–
Percent open area	%	68	–	–
Short term tensile strength[a]	kN/m	58	58	55
Elongation at maximum load[a]	%	10.5	11.5	105.0
Short term tensile strength[b]	kN/m	43.9	54.6	69.5
Elongation at maximum load[b]	%	7.9	10.6	100.9
Secant stiffness at 5% strain[b]	kN/m	401.6	600.9	156.3

[a] *As per the manufacturer specifications (machine direction).*
[b] *Obtained from tensile tests performed in accordance with EN ISO 10319:2008 (CEN, 2008).*

Pullout Test Device and Experimental Procedures

The large-scale pullout test apparatus used in the present study is illustrated in **Figure 4A**. The equipment consists of a large pullout box (internal dimensions of 1.53 m long × 1.00 m wide × 0.80 m high) fitted with a 0.20 m long (steel) sleeve, a clamping system (**Figure 4B**), a servo-hydraulic control system and a set of external transducers, such as load cells and potentiometers. A detailed description of the test facility can be found elsewhere (Lopes and Ladeira, 1996b; Ferreira et al., 2016b).

The pullout tests herein reported were performed in accordance with the European Standard EN 13738:2004 (CEN, 2004). For tests involving moist soil, the soil was thoroughly mixed with water to achieve the target moisture content and ensure the homogeneity of the sample. The soil was then compacted inside the pullout box to the required density in

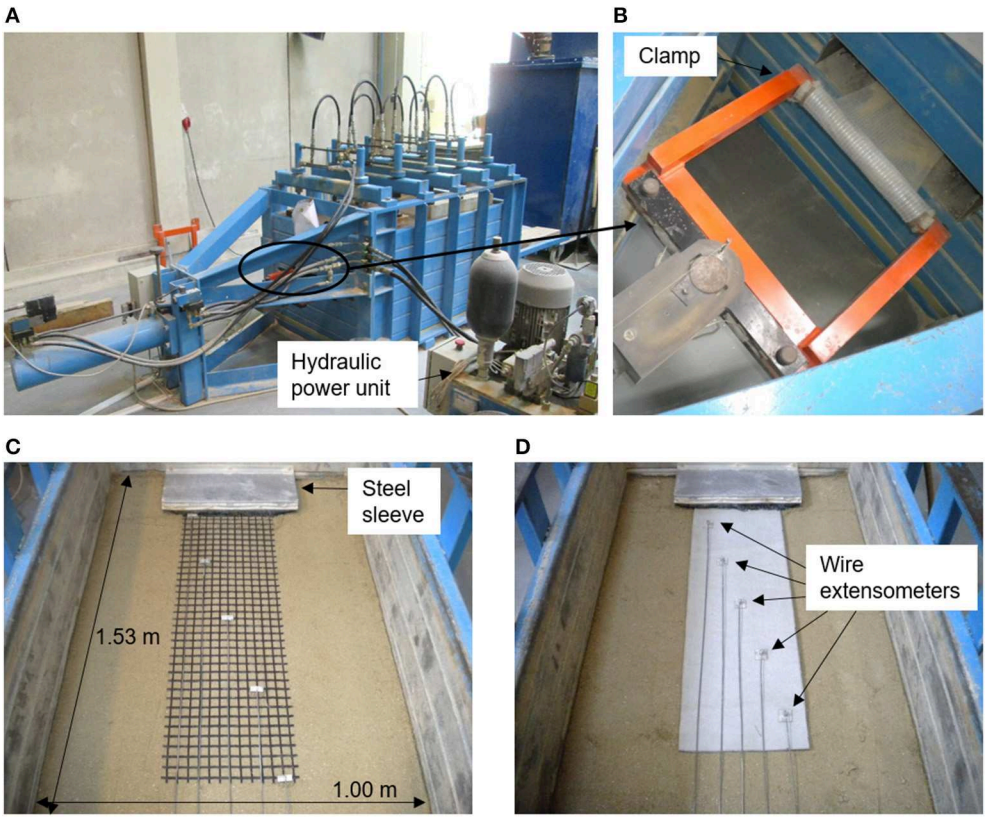

FIGURE 4 | Large-scale pullout test apparatus and instrumentation: **(A)** overall view; **(B)** clamping system; **(C)** inextensible wires fixed along a GGR specimen; **(D)** inextensible wires fixed along a GTX specimen.

0.15 m thick layers using an electric vibratory hammer. Once the first two layers were compacted, the geosynthetic specimen (with initial dimensions of 0.33 m wide and 1.0 m long) was clamped and laid over the compacted soil. To monitor the horizontal displacements along the length of the reinforcement during the test, a set of wire extensometers were fixed to the geosynthetic at selected measurement points (**Figures 4C,D**), with the opposite ends connected to linear potentiometers located at the back of the pullout box. Two additional soil layers were then placed and compacted, which resulted in a total height of soil of 0.60 m. A neoprene sheet was installed between the soil and the loading plate to reduce the influence of the top boundary and obtain more uniform distribution of the vertical stresses. The vertical load was applied to the upper layer of soil by a wooden plate loaded by 10 hydraulic jacks and its magnitude was controlled by a load cell. The pullout force was then applied to the geosynthetic specimen so as to achieve a constant rate of displacement of 2 mm/min, as recommended by the EN 13738:2004 (CEN, 2004). It should be noted that the recommended displacement rate for geosynthetic pullout testing varies according to different standards. For instance, the American Standard ASTM D6706-01 (2013) suggests the use of a displacement rate of 1 mm/min. Even though the rate of displacement under which the pullout tests are carried out may influence the results, the evaluation of this effect was beyond the scope of this study. The geosynthetic frontal displacement (i.e., clamp displacement) and the associated pullout force were measured by a linear potentiometer and a load cell, respectively. An automatic data acquisition system enabled the relevant parameters (i.e., the pullout force, frontal displacement, displacements throughout the length of the geosynthetic specimen, and the applied vertical stress) to be continuously monitored during the tests. To ensure accuracy of results, all the measurement devices have undergone calibration prior to testing.

Test Programme

Table 3 summarizes the test conditions investigated in this study. As previously mentioned, the pullout response of three distinct geosynthetics (geogrid, geocomposite reinforcement, and geotextile) when embedded in a locally available granite residual soil was assessed using a large pullout box. To analyse the influence of soil moisture content on the pullout resistance and deformation behavior of the reinforcements, the soil was tested in its air-dried moisture condition and at the optimum moisture content ($w_{opt} = 11.45\%$). In addition, two different dry densities were investigated: $\gamma_d = 15.3$ kN/m^3 (medium dense soil) and $\gamma_d = 17.3$ kN/m^3 (dense soil). To simulate low depths, where the pullout failure mechanism is most likely to occur in reinforced soil walls and slopes, all the tests were performed under a relatively low vertical stress at the reinforcement level

TABLE 3 | Test programme.

Test	Geosynthetic	Soil moisture content	Soil dry unit weight (kN/m^3)	Vertical stress (kPa)	Number of specimens
T1	GGR	Dry	15.3	25	3
T2	GGR	Dry	17.3	25	3
T3	GGR	w_{opt}	15.3	25	3
T4	GGR	w_{opt}	17.3	25	3
T5	GCR	Dry	15.3	25	3
T6	GCR	Dry	17.3	25	3
T7	GCR	w_{opt}	15.3	25	3
T8	GCR	w_{opt}	17.3	25	3
T9	GTX	Dry	15.3	25	3
T10	GTX	Dry	17.3	25	3
T11	GTX	w_{opt}	15.3	25	3
T12	GTX	w_{opt}	17.3	25	3

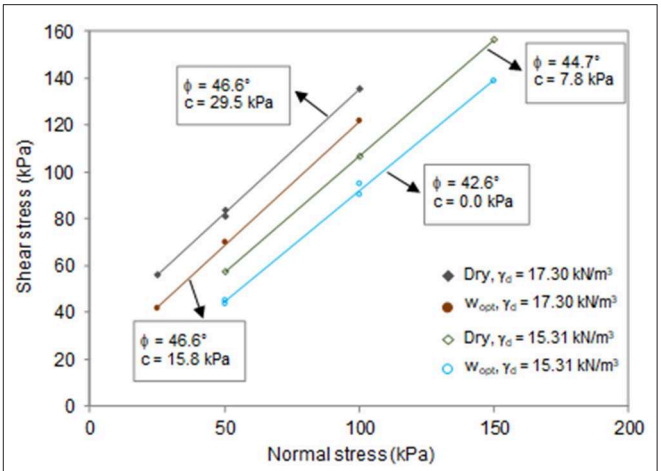

FIGURE 5 | Peak strength envelopes of the granite residual soil [modified from Ferreira et al. (2015)].

($\sigma_v = 25$ kPa). As recommended by the EN 13738:2004 (CEN, 2004), each test was carried out three times under identical physical conditions, to ensure repeatability of results. Therefore, 36 geosynthetic specimens were tested.

Additionally, large-scale direct shear tests were carried out to evaluate the internal shear strength of the soil. The direct shear tests were also performed for different conditions of moisture content (air-dried and optimum moisture content) and dry density ($\gamma_d = 15.3$ kN/m^3 and $\gamma_d = 17.3$ kN/m^3) and under normal stresses ranging from 25 to 150 kPa. The direct shear test apparatus used in this study enables the analysis of the direct shear behavior of soils, as well as soil-geosynthetic and geosynthetic-geosynthetic interfaces. The direct shear box comprises a lower box with dimensions of 800 × 340 mm in plan and 100 mm in height, and an upper box with plan dimensions of 600 × 300 mm and 150 mm in height. Details on this large-scale direct shear prototype can be found elsewhere (Vieira et al., 2013; Ferreira et al., 2015).

RESULTS AND DISCUSSION

Soil Internal Shear Strength

Figure 5 plots the maximum shear stresses mobilized in the direct shear tests as function of the normal stress, along with the corresponding linear best-fit lines, for different conditions of soil moisture content and dry density. Due to limitations of the fluid power unit, the direct shear tests for dense soil ($\gamma_d = 17.3$ kN/m^3) were carried out for the range 25−100 kPa.

Following the Mohr-Coulomb failure criterion, the peak shear strength parameters of the soil (i.e., internal friction angle, ϕ and cohesion, c) were obtained. As expected, the soil shear strength increased significantly with the placement density, with more emphasis on the cohesive component of the shear strength. On the other hand, the increase in soil moisture content adversely affected the soil internal strength. In fact, although the soil friction angle was not significantly affected by the moisture condition, the cohesion decreased considerably when the soil was tested at its optimum moisture content. According to Mitchell (1976) and Samtani and Nowatzki (2006), apparent cohesion in soils may derive from two main factors: (1) capillary stresses between particles in an unsaturated soil due to surface tension in the water (matric suction) and (2) apparent mechanical forces resulting from interlocking of angular soil particles, which is often the cause of cohesion measured in compacted soils (i.e., particle geometry and packing may induce an apparent cohesion with no physical or chemical attraction between soil particles). Therefore, the increment of cohesion observed in this study when the dry density of the soil changed from 15.3 to 17.3 kN/m^3 may be associated with an increase of the apparent mechanical forces due to enhanced interlocking of soil particles. On the other hand, the decrease of cohesion associated with an increase in soil moisture content is possibly related to the loss of soil matric suction.

Pullout Test Results

Influence of Soil Moisture Content

Figure 6 illustrates the effect of soil moisture content on the pullout resistance of the geosynthetics for different soil dry unit weights ($\gamma_d = 15.3$ kN/m^3 and $\gamma_d = 17.3$ kN/m^3). **Figures 6A,B** show the pullout force-displacement curves obtained when the geogrid reinforcement was tested in looser and denser soil specimens, respectively. Similarly, **Figures 6C,D** present the results obtained for the geocomposite reinforcement and **Figures 6E,F** plot the data concerning the geotextile.

Figures 6A,B indicate that the pullout resistance of the geogrid embedded in dry soil exceeded that for soil compacted at the optimum moisture content (at the same dry density). It can also be observed that the influence of soil moisture content on the geogrid pullout response was more pronounced when the soil was in medium dense conditions (**Figure 6A**). In fact, for $\gamma_d = 15.3$ kN/m^3 (**Figure 6A**), the peak pullout resistance (P_R) of the reinforcement decreased about 19% (on average) with the moisture content increase. However, for dense soil

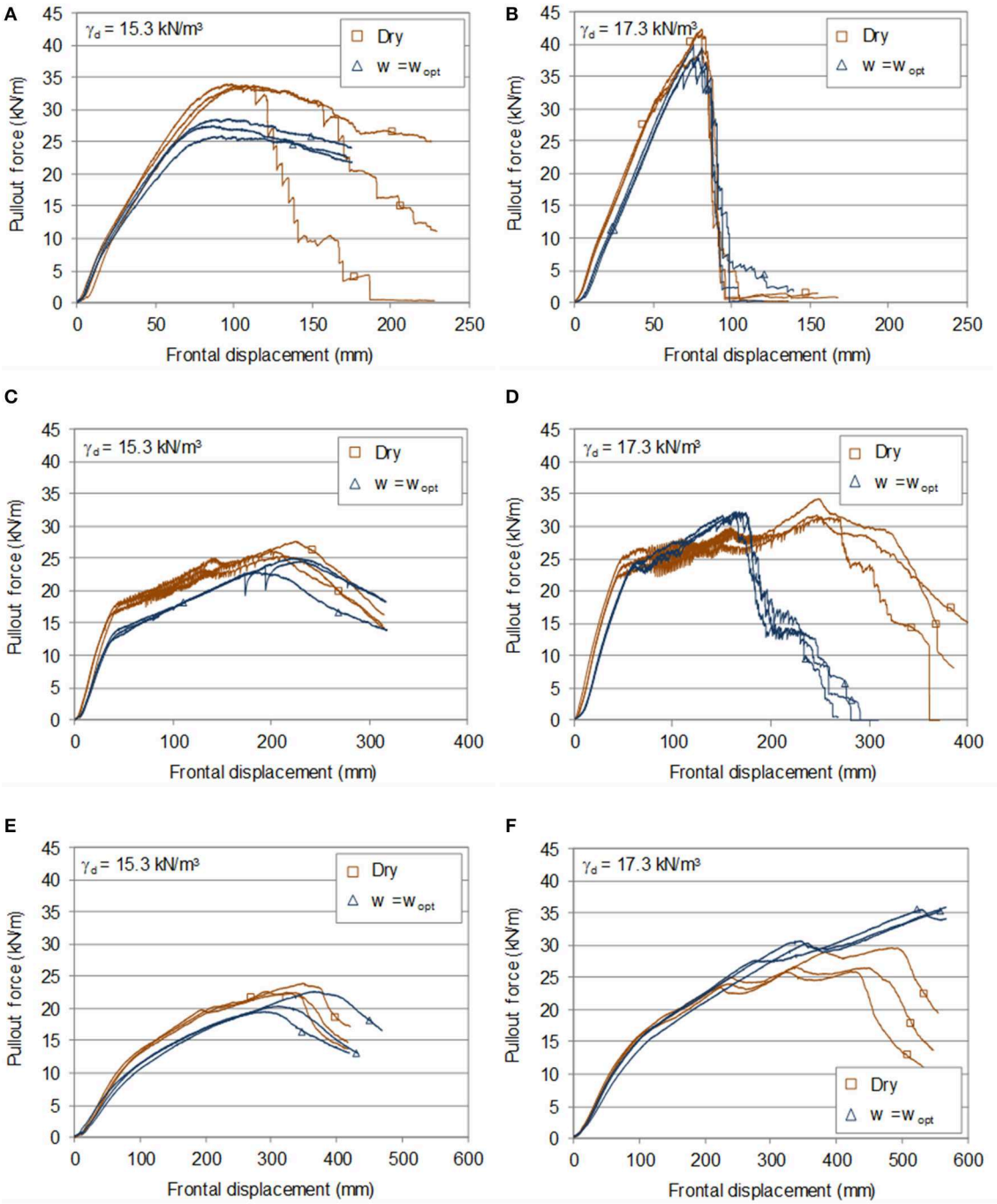

FIGURE 6 | Influence of soil moisture content on the pullout resistance of the geosynthetics: **(A,B)**: GGR; **(C,D)**: GCR; **(E,F)**: GTX.

(γ_d = 17.3 kN/m^3), the reduction of P_R due to the moisture content increase was only 7% (**Figure 6B**). This finding may be attributed to the different failure modes observed in these tests. In the tests involving medium dense soil, the failure occurred due to sliding of the reinforcement along the interface (pullout failure). In contrast, for dense soil, the specimens failed in tension (tensile failure).

Figure 6C shows that the increase in soil moisture content led to the reduction (8.5%) of the pullout resistance of the geocomposite reinforcement when embedded in medium dense soil. This reduction was considerably lower than that observed for the geogrid under identical conditions, which may be related to the favorable hydraulic properties of non-woven geotextiles (Ling et al., 1992; Tan et al., 2001; Portelinha et al., 2013). However, for

dense soil (**Figure 6D**) the moisture content did not significantly affect the peak pullout capacity of the geosynthetic (over the investigated range), but the frontal displacement at which the peak pullout resistance was mobilized decreased substantially when the optimum moisture content was tested.

The influence of soil moisture condition on the pullout response of the geotextile in medium dense soil was similar to that observed for the geocomposite. When the soil was compacted at the optimum moisture content, the peak pullout resistance decreased 9.4% (on average) in comparison with that obtained in the presence of dry soil (**Figure 6E**). As shown in **Figure 6F**, for dense soil it was not possible to evaluate the peak pullout resistance of the geotextile for $w = w_{opt}$, since a higher frontal displacement would be required to reach the ultimate capacity. Nevertheless, it can be concluded that the pullout resistance of this geotextile under these particular test conditions increased with moisture content (from air-dried to optimum moisture content), which contrasts with the behavior observed for the remaining geosynthetics. This is possibly associated with the high thickness of the geotextile (thickness = 7.2 mm) and the significant intrusion of soil particles into the geotextile pores during compaction at $w = w_{opt}$, thus leading to its higher tensile stiffness under moist conditions.

Influence of Soil Density

The effect of soil placement density on the pullout resistance of the different geosynthetics and on the average displacements recorded along the specimens at maximum pullout force is shown in **Figure 7**. **Figures 7A,B** present the results attained for the geogrid, while **Figures 7C,D** correspond to the geocomposite reinforcement. The results for the geotextile are shown in **Figures 7E,F**. Although the data in **Figure 7** were obtained for $w = w_{opt}$, similar conclusions were also drawn regarding the influence of soil density on the pullout load-displacement behavior of the geosynthetics when the soil was tested in its air-dried moisture condition.

Figures 7A,B clearly show that soil density is a key factor affecting the pullout behavior of the geogrid. The increase in soil density resulted in an increment of the pullout resistance of the geogrid of about 40% (**Figure 7A**). The secant stiffness at a pullout force corresponding to 50% of the maximum pullout resistance increased 14% with soil density. In turn, the frontal displacement at which the ultimate pullout load was achieved decreased about 16%. Soil density also affected the failure mode observed in the tests. For specimens tested in medium dense soil, the failure resulted from sliding of the reinforcement along the interface (i.e., pullout failure, see **Figure 8A**). In contrast, the specimens embedded in dense soil experienced tensile failure (i.e., breakage of the material in tension, see **Figure 8B**).

The profiles of the displacements measured throughout the length of the geogrid at maximum pullout force (plotted in **Figure 7B**) indicate that, for medium dense soil the reinforcement experienced pullout movement during the test (reflected by the displacement measured at the rear end of the specimens). However, for dense soil the displacements recorded over the geogrid length were mainly caused by the reinforcement deformation at the front half of its length (i.e., close to the point of application of the pullout load). In fact, neither sliding nor appreciable deformation at the back half of the geogrid length were observed in the tests involving dense soil. It can therefore be concluded that soil density restrained the transfer of stresses throughout the length of the geogrid specimens and high stresses/strains were mobilized close to the loaded end, thus leading to tensile failure of the specimens at the front part.

The influence of soil placement density on the pullout resistance of the geocomposite reinforcement (**Figure 7C**) was comparable to that for the geogrid. The maximum pullout force increased ∼33% with soil density, whereas the frontal displacement at peak decreased 22%. The secant stiffness for 50% of the maximum pullout force increased about 26% with soil density. The displacement distributions along the length of the specimens at maximum load (**Figure 7D**) indicate that, regardless of density, the deformations tended to decrease with increasing distance to the point of application of the pullout load. At the back of the geocomposite specimens, higher deformations were obtained for specimens tested in looser soil. This is associated with the effect of soil density, which restrains the transfer of stresses over the length of the specimens. Similar to the trend observed for the geogrid, soil density also affected the failure mode observed in these tests. The geocomposite specimens experienced pullout failure when embedded in medium dense soil, whereas for dense soil the specimens underwent internal rupture in tension.

It can be noted from **Figure 7E** that the pullout capacity of the geotextile embedded in dense soil could not be determined, since the maximum admissible frontal displacement was not enough to reach the peak load. Considering the maximum pullout force measured at the end of the test as the lower limit of the pullout resistance of this geotextile, it becomes apparent that the pullout resistance increased at least 70% with soil density. The deformations along the first three sections of the geotextile embedded in dense soil exceeded those for the specimens tested in looser soil. However, identical deformations were measured along the two sections closer to the back end of the specimens, regardless of soil density (**Figure 7F**).

Influence of Geosynthetic Type

Figures 9, **10** compare the pullout behavior of the three geosynthetics in looser and denser soil specimens. **Figure 9** presents the results for dry soil and **Figure 10** is related to soil optimum moisture content. The graphs on the left side show the pullout force-displacement curves and the graphs on the right side illustrate the displacements over the length of the geosynthetics at maximum pullout load.

Regardless of the conditions of soil moisture content and density, the geogrid exhibited significantly higher performance than the other geosynthetics in terms of peak pullout resistance and stiffness. This is associated with the relevant contribution of the passive resistance mechanism mobilized against the geogrid transverse members to the overall pullout capacity of the reinforcement. However, for small displacements, the geogrid stiffness was rather similar to that of the geocomposite reinforcement, suggesting that the latter geosynthetic may be as effective as the geogrid in applications where high deformation

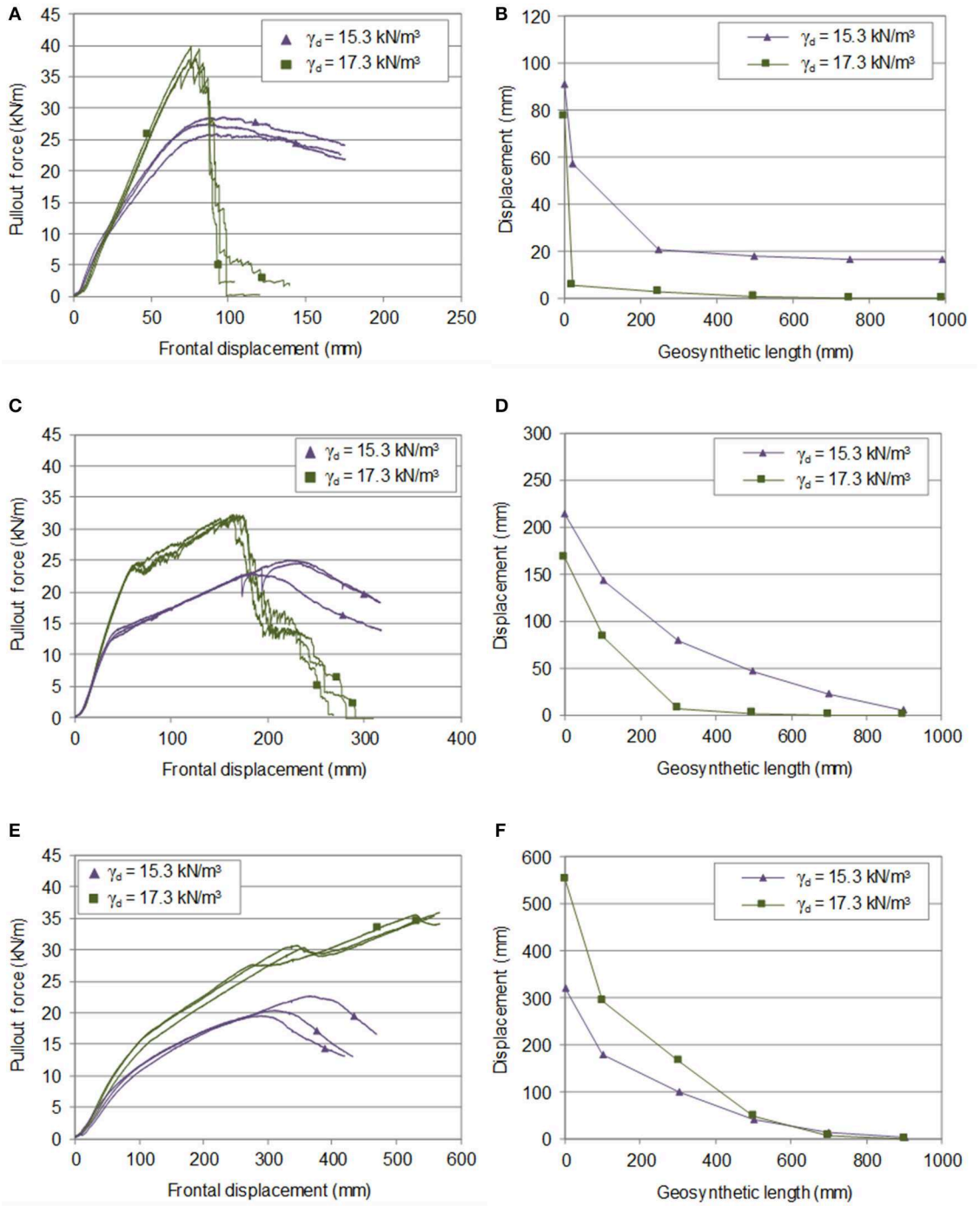

FIGURE 7 | Influence of soil density on the pullout resistance and displacement behavior of the geosynthetics for $w = w_{opt}$: **(A,B)**: GGR; **(C,D)**: GCR; **(E,F)**: GTX.

levels are not anticipated. On the other hand, the stiffness of the geotextile was clearly lower than that of the geogrid and the geocomposite, and hence the frontal displacement at which the maximum pullout force was achieved was substantially larger when the geotextile was used. This is associated with the higher extensibility of this geosynthetic, as previously observed from the in-isolation tensile tests (significantly lower tensile stiffness—**Table 2**).

Comparing the displacements measured throughout the length of the reinforcements at maximum load, it can be concluded that the deformations along the geotextile and the geocomposite reinforcement were significantly larger than those along the geogrid, regardless of the test conditions. This occurrence can be attributed to the higher extensibility of the geotextiles and the fact that the ultimate pullout load is reached at significantly larger frontal displacements.

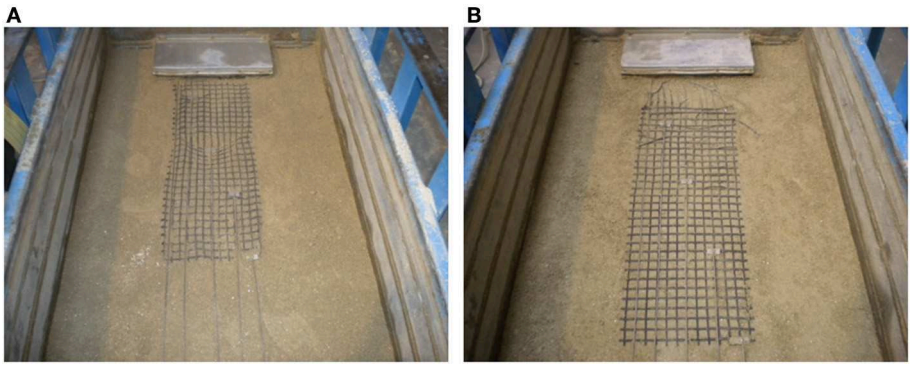

FIGURE 8 | Photographic views of two representative geogrid specimens: **(A)** after pullout failure; **(B)** after tensile failure.

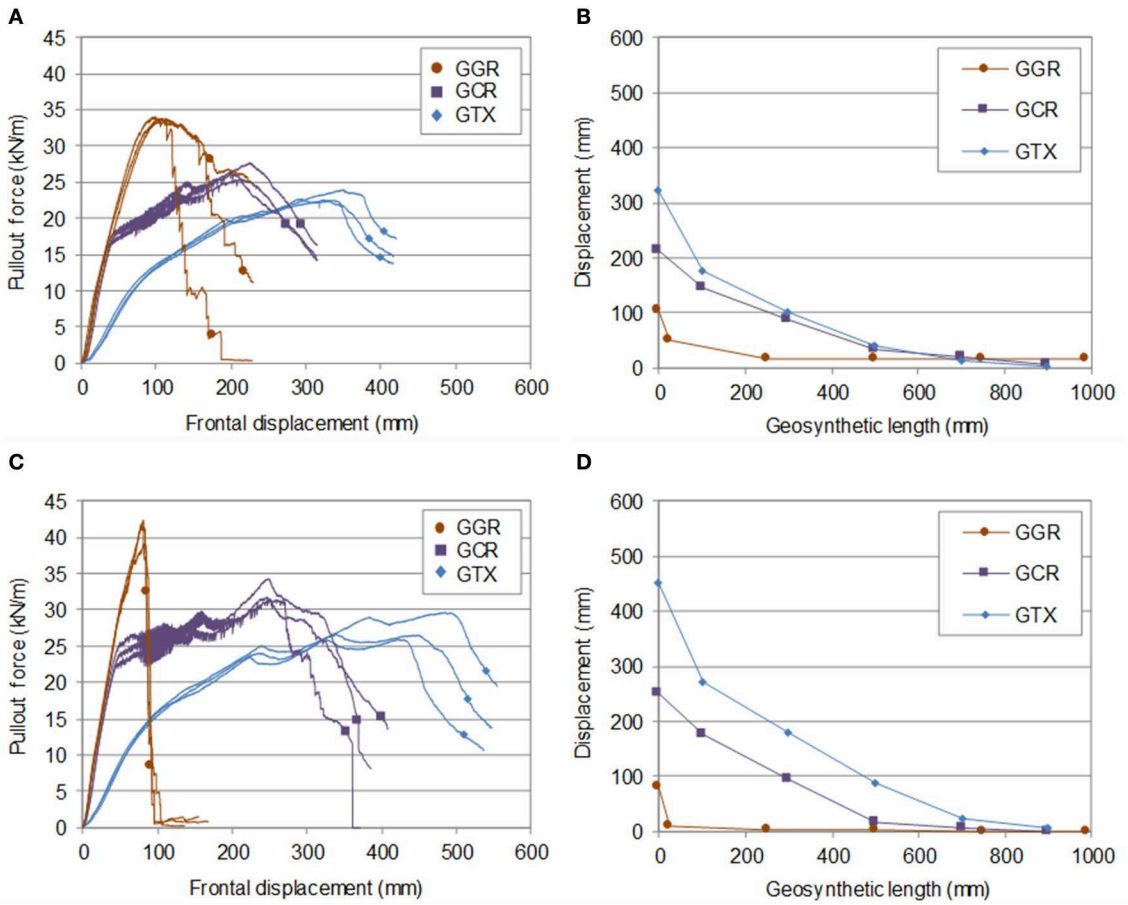

FIGURE 9 | Influence of geosynthetic type on the pullout resistance and displacement behavior of the specimens for dry soil: **(A,B)**: γ_d = 15.3 kN/m^3; **(C,D)**: γ_d = 17.3 kN/m^3.

DISCUSSION

Table 4 summarizes the results of the pullout test programme. The mean values of the pullout resistance (P_R), the frontal displacement for P_R (u_{PR}), and the in-soil secant stiffness for 50% of P_R (J_{50}) are reported in this table, along with the corresponding coefficients of variation (COV), which were computed as the ratio of the standard deviation to the mean value of the parameter, based on three repeatability tests. The conditions of each test can be found in **Table 3**.

Regardless of the geosynthetic or soil moisture content, the increase in soil density led to an increase in the pullout

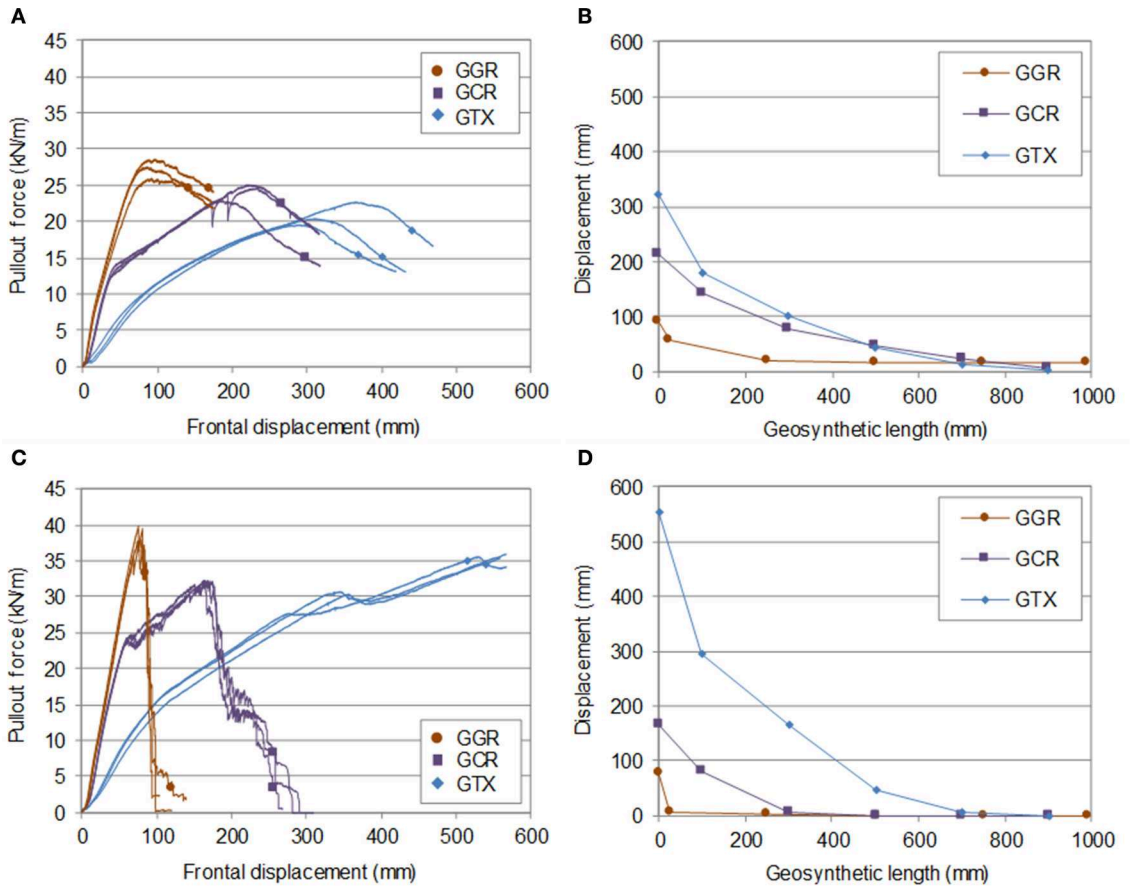

FIGURE 10 | Influence of geosynthetic type on the pullout resistance and displacement behavior of the specimens for $w = w_{opt}$: **(A,B)**: $\gamma_d = 15.3$ kN/m^3; **(C,D)**: $\gamma_d = 17.3$ kN/m^3.

TABLE 4 | Summary of pullout test results.

Test	Pullout resistance (P_R)		Frontal displacement (u_{PR})		Secant stiffness (J_{50})	
	Mean value (kN/m)	COV (%)	Mean value (mm)	COV (%)	Mean value (kN/m)	COV (%)
T1	33.78	0.95	104.55	7.02	461.95	6.50
T2	41.09	4.23	80.47	2.17	613.27	2.51
T3	27.40	4.82	91.47	5.86	444.35	5.38
T4	38.37	3.53	77.20	2.18	506.13	3.92
T5	26.44	4.30	212.04	6.08	458.60	7.08
T6	32.51	4.82	251.37	2.78	562.50	5.61
T7	24.20	4.85	213.82	11.23	336.24	4.30
T8	32.15	0.67	166.58	2.18	424.54	2.03
T9	23.08	3.32	321.80	8.56	143.88	5.22
T10	27.39	7.22	449.86	7.17	168.67	1.96
T11	20.91	7.77	322.53	11.94	116.06	9.36
T12	>35.65	0.76	>551.83	3.48	131.54	8.01

resistance, P_R and secant stiffness, J_{50}. The geogrid (GGR) and the geocomposite (GCR) failed in tension (tensile failure) in denser soil at $w = w_{opt}$ (see **Figure 7** and **Table 5**), which justifies the lower frontal displacements for P_R. In general, the soil moisture content increase (from dry to optimum) induced a decrease in the pullout resistance, P_R and secant stiffness, J_{50}.

When the soil is reinforced with geosynthetics, the interface strength is typically characterized through coefficients of

interaction. The pullout interaction coefficient (f_b) can be defined as:

$$f_b = \frac{\tau^{max}_{pullout}(\sigma)}{\tau^{max}_{direct\ shear}(\sigma)} \quad (1)$$

where $\tau^{max}_{pullout}(\sigma)$ is the maximum shear stress mobilized at the soil-geosynthetic interface during a pullout test under the confining pressure σ, and $\tau^{max}_{direct\ shear}(\sigma)$ is the soil direct shear strength under the same confining pressure.

The mean values of $\tau^{max}_{pullout}(\sigma)$, $\tau^{max}_{direct\ shear}(\sigma)$ and f_b obtained for each test condition are listed in **Table 5**. Also included in this table is the failure mode for each specimen (values in brackets represent the number of specimens). As shown in **Table 5**, the soil-geosynthetic pullout interaction coefficients ranged from 0.25 to 0.61. Under similar conditions, the geogrid exhibited higher pullout interaction coefficients, followed by the geocomposite reinforcement (test T1–T4 and T5–T8, respectively). It is noteworthy that for dense soil (tests T2, T4, and T8), the failure of the geogrid and the geocomposite occurred due to their internal breakage, and thus the coefficients of interaction provided in **Table 5** represent a lower bound for f_b.

A wide range of pullout interaction coefficients can be found in the literature. However, it is important to bear in mind that the pullout interaction coefficient depends on the shear strength of the surrounding soil, the friction between the soil and the geosynthetic, the percent open area, the ratio between the soil grain size and the geogrid aperture, the strength of the junctions, among other factors. For instance, Hsieh et al. (2011) reported values of the pullout interaction coefficient ranging from 0.18 to 1.25 from pullout tests of geosynthetics inserted in different granular soils. Pullout interaction coefficients varying from 0.44 to 1.04 were reported by Mohiuddin (2003) for different geosynthetics embedded in a cohesive soil. Vieira et al. (2016) presented values ranging from 0.58 to 0.63 for geogrids embedded in a recycled construction and demolition material.

Comparing the values of the pullout interaction coefficient achieved in the present study with those reported in the literature, it is possible to conclude that the upper bound of the range is generally lower. This may be due to the occurrence of geosynthetic tensile failure (breakage of the material in tension) when the specimens were embedded in dense soil.

Tables 4, **5** indicate that when the geosynthetics underwent tensile failure under pullout loading conditions, the measured peak pullout force was lower than the corresponding tensile strength obtained through in-isolation tensile tests (**Table 2**). This finding is in agreement with some previous related studies (Lopes and Ladeira, 1996a; Ferreira et al., 2016b; Vieira et al., 2016). It should be noted that in the pullout test the geosynthetic specimen is in contact with compacted soil and under a prescribed normal stress. In contrast, in the tensile test the specimen is tested under unconfined conditions. Furthermore, in the current study, the tensile and pullout tests were performed under different displacement rates. The displacement rates imposed in the tensile (20%/min) and pullout tests (2 mm/min) followed the recommendations of the European Standards EN ISO 10319:2008 (CEN, 2008) and EN 13738:2004 (CEN, 2004), respectively. Therefore, the comparatively lower forces reached in the pullout tests where reinforcement tensile failure occurred may be associated with the different test conditions, as well as some damage induced by the soil on the geosynthetic specimens.

TABLE 5 | Determination of the pullout interaction coefficient (f_b) and failure mode for each specimen.

Test	$\tau^{max}_{pullout}(\sigma)$ (kPa)	$\tau^{max}_{direct\ shear}(\sigma)$ (kPa)	f_b	Failure mode
T1	17.15	32.82	0.52	Pullout (2) + Tensile (1)
T2	20.55	55.89	0.37	Tensile (3)
T3	13.93	23.01	0.61	Pullout (3)
T4	19.18	41.68	0.46	Tensile (3)
T5	13.29	32.82	0.41	Pullout (3)
T6	16.26	55.89	0.29	Pullout (2) + Tensile (1)
T7	12.16	23.01	0.53	Pullout (3)
T8	16.08	41.68	0.39	Tensile (3)
T9	11.58	32.82	0.35	Pullout (3)
T10	13.77	55.89	0.25	Pullout (3)
T11	10.50	23.01	0.46	Pullout (3)
T12	>17.83	41.68	>0.43	–

It is interesting to point out that the highest pullout resistance was attained for the GGR interface, followed by the GCR and then the GTX (**Table 4**), whereas the corresponding tensile strength values (**Table 2**) followed the reverse trend. This is partly attributed to the interaction mechanisms developed under pullout loading conditions. As stated earlier, in the case of the geogrid, the pullout resistance is composed of frictional resistance (skin friction on the surface of the geogrid longitudinal and transverse ribs) and bearing resistance mobilized against the transverse members. For geotextiles, only the frictional resistance contributes to the overall pullout capacity. Hence, due to the relevance of the passive resistance mobilized under pullout conditions, the geogrid (GGR) presented higher pullout resistance than the remaining geosynthetics (GCR and GTX), despite the comparatively lower tensile strength. Regarding the comparison of results for the GCR and the GTX, this occurrence may be related to the higher extensibility of the geotextile (GTX). Although the ultimate tensile strength of the GTX exceeded that of the GCR, it was achieved at a substantially higher elongation. In fact, the GCR exhibited higher stiffness than the GTX both in the tensile and pullout tests carried out in this study.

From the above observations, it becomes apparent that a geosynthetic with higher tensile strength under unconfined conditions is not necessarily a geosynthetic with better performance when embedded in soil. This highlights the importance of conducting pullout tests with the specific materials to be used in the project if accurate predictions of the geosynthetic pullout capacity are required.

CONCLUSIONS

The pullout behavior of three different geosynthetics (geogrid, geocomposite reinforcement and geotextile) embedded in a locally-available granite residual soil was assessed through a series of large-scale pullout tests involving different soil moisture and density conditions. Based on the analysis of the results, the following conclusions can be drawn.

Soil density is a key factor for the reinforcement pullout resistance, with great influence on the failure mode (pullout or geosynthetic tensile rupture), regardless of geosynthetic type, or soil moisture content.

The soil moisture condition may considerably affect the pullout capacity of geosynthetics, particularly when the soil is in medium dense state. The maximum pullout resistance of the geosynthetics used in this study decreased by up to 19% when the soil was tested at the optimum moisture content, in comparison with the values obtained with dry soil.

The geogrid exhibited higher peak pullout resistance than the remaining geosynthetics, which is associated with the significant contribution of the passive resistance mobilized against the geogrid transverse members to the overall pullout capacity of the reinforcement.

The soil-geosynthetic pullout interaction coefficients ranged from 0.25 to 0.61, with the highest values obtained for the geogrid interface. The occurrence of geosynthetic tensile failure when the specimens were embedded in dense soil is the reason for lower pullout interaction coefficients, comparatively with those generally reported by other researchers.

DATA AVAILABILITY STATEMENT

The raw data supporting the conclusions of this article will be made available by the authors, without undue reservation, to any qualified researcher.

AUTHOR CONTRIBUTIONS

FF performed the pullout tests, analyzed the results and partially prepared the manuscript based on inputs and guidance of CV and ML. CV supervised all the works carried out and modified the initial draft of the manuscript. FF revised the manuscript after peer-review and prepared the final version for publication.

FUNDING

This work was financially supported by the Research Project CDW_LongTerm, POCI-01-0145-FEDER-030452, funded by FEDER funds through COMPETE2020—Programa Operacional Competitividade e Internacionalização (POCI) and by national funds (PIDDAC) through FCT/MCTES.

ACKNOWLEDGMENTS

The authors wish to thank TenCate for providing the geosynthetic samples used in this study. The authors declare that TenCate was not involved in the study design, collection, analysis, interpretation of data, the writing of this article or the decision to submit it for publication.

REFERENCES

Abu-Farsakh, M. Y., Almohd, I., and Farrag, K. (2006). Comparison of field and laboratory pullout tests on geosynthetics in marginal soils. *Transp. Res. Rec.* 1975, 124–136. doi: 10.1177/0361198106197500114

Ashmawy, A. K., and Bourdeau, P. L. (1995). Geosynthetic-reinforced soils under repeated loading: a review and comparative design study. *Geosynth. Int.* 2, 643–678. doi: 10.1680/gein.2.0029

ASTM D 2487-11. (2011). *Standard Practice for Classification of Soils for Engineering Purposes (Unified Soil Classification System)*. West Conshohocken, PA: ASTM International.

ASTM D 4253-93. (1993). *Standard Test Methods for Maximum Index Density and Unit Weight of Soils Using a Vibratory Table*. West Conshohocken, PA: ASTM International.

ASTM D 4254-93. (1993). *Standard Test Methods for Minimum Index Density and Unit Weight of Soils and Calculation of Relative Density*. West Conshohocken, PA: ASTM International.

ASTM D6706-01. (2013). *Standard Test Method for Measuring Geosynthetic Pullout Resistance in Soil*. West Conshohocken, PA: ASTM International.

Bakeer, R. M., Abdel-Rahman, A. H., and Napolitano, P. J. (1998). Geotextile friction mobilization during field pullout test. *Geotext. Geomembranes* 16, 73–85. doi: 10.1016/S0266-1144(97)10024-3

BSI. (1990). *BS 1377-4:1990. Methods of Test for Soils for Civil Engineering Purposes. Compaction-Related Tests*. London: British Standards Institution.

Byun, Y. H., and Tutumluer, E. (2019). Local stiffness characteristic of geogrid-stabilized aggregate in relation to accumulated permanent deformation behavior. *Geotext. Geomembranes* 47, 402–407. doi: 10.1016/j.geotexmem.2019.01.005

CEN. (2004). *EN 13738:2004. Geotextiles and Geotextile-Related Products—Determination of Pullout Resistance in Soil*. Brussels: European Committee for Standardization.

CEN. (2008). *EN ISO 10319:2008. Wide-Width Tensile Tests*. Brussels: European Committee for Standardization.

Esmaili, D., Hatami, K., and Miller, G. A. (2014). Influence of matric suction on geotextile reinforcement-marginal soil interface strength. *Geotext. Geomembranes* 42, 139–153. doi: 10.1016/j.geotexmem.2014.01.005

Ferreira, F. B., Vieira, C. S., and Lopes, M. L. (2015). Direct shear behaviour of residual soil–geosynthetic interfaces—influence of soil moisture content, soil density and geosynthetic type. *Geosynth. Int.* 22, 257–272. doi: 10.1680/gein.15.00011

Ferreira, F. B., Vieira, C. S., and Lopes, M. L. (2016a). "Cyclic and post-cyclic shear behaviour of a granite residual soil-geogrid interface," in *Procedia Engineering, Vol. 143, Advances in Transportation Geotechnics III*, ed A. G. Correia (Amsterdam: Elsevier Ltd), 379–386. doi: 10.1016/j.proeng.2016.06.048

Ferreira, F. B., Vieira, C. S., Lopes, M. L., and Carlos, D. M. (2016b). Experimental investigation on the pullout behaviour of geosynthetics embedded in a granite residual soil. *Eur. J. Environ. Civ. Eng.* 20, 1147–1180. doi: 10.1080/19648189.2015.1090927

Ferreira, F. B., Vieira, C. S., Lopes, M. L., and Ferreira, P. G. (2020). HDPE geogrid-residual soil interaction under monotonic and cyclic pullout loading. *Geosynth. Int.* doi: 10.1680/jgein.19.00057. [Epub ahead of print].

Hatami, K., and Esmaili, D. (2015). Unsaturated soil-woven geotextile interface strength properties from small-scale pullout and interface tests. *Geosynth. Int.* 22, 161–172. doi: 10.1680/gein.15.00002

Hsieh, C., Chen, G. H., and Wu, J.-H. (2011). The shear behavior obtained from the direct shear and pullout tests for different poor grades soil-geosynthetic systems Journal of *GeoEngineering* 6, 15–26.

Indraratna, B., Ferreira, F. B., Qi, Y., and Ngo, T. N. (2018). Application of geoinclusions for sustainable rail infrastructure under increased axle loads and higher speeds. *Innov. Infrastruct. Solut.* 3:69. doi: 10.1007/s41062-018-0174-z

Indraratna, B., Qi, Y., Ngo, T. N., Rujikiatkamjorn, C., Neville, T., Ferreira, F. B., et al. (2019). Use of geogrids and recycled rubber in railroad infrastructure for enhanced performance. *Geosciences*. 9:30. doi: 10.3390/geosciences9010030

Isik, A., and Gurbuz, A. (2020). Pullout behavior of geocell reinforcement in cohesionless soils. *Geotext. Geomembranes* 48, 71–81. doi: 10.1016/j.geotexmem.2019.103506

Lee, K. Z. Z., and Wu, J. T. H. (2004). A synthesis of case histories on GRS bridge-supporting structures with flexible facing. *Geotext. Geomembranes* 22, 181–204. doi: 10.1016/j.geotexmem.2004.03.002

Ling, H. I., Wu, J. T. H., and Tatsuoka, F. (1992). Short-term strength and deformation characteristics of geotextiles under typical operational conditions. *Geotext. Geomembranes* 11, 185–219. doi: 10.1016/0266-1144(92)90043-A

Lopes, M. L., and Ladeira, M. (1996a). Influence of the confinement, soil density, and displacement rate on soil-geogrid interaction. *Geotext. Geomembranes* 14, 543–554. doi: 10.1016/S0266-1144(97)83184-6

Lopes, M. L., and Ladeira, M. (1996b). Role of specimen geometry, soil height and sleeve length on the pull-out behaviour of geogrids. *Geosynth. Int.* 3, 701–719. doi: 10.1680/gein.3.0081

Mirzaalimohammadi, A., Ghazavi, M., Roustaei, M., and Lajevardi, S. H. (2019). Pullout response of strengthened geosynthetic interacting with fine sand. *Geotext. Geomembranes* 47, 530–541. doi: 10.1016/j.geotexmem.2019.02.006

Mitchell, J. K. (1976). *Fundamentals of Soil Behavior*. New York, NY: John Wiley & Sons.

Mohiuddin, A. (2003). *Analysis of Laboratory and Field Pull-Out Tests of Geosynthetics in Clayey Soils* (master's thesis). Faculty of the Louisiana State University and Agricultural and Mechanical College, United States.

Moraci, N., and Recalcati, P. (2006). Factors affecting the pullout behaviour of extruded geogrids embedded in a compacted granular soil. *Geotext. Geomembranes* 24, 220–242. doi: 10.1016/j.geotexmem.2006.03.001

Morsy, A. M., Zornberg, J. G., Han, J., and Leshchinsky, D. (2019). A new generation of soil-geosynthetic interaction experimentation. *Geotext. Geomembranes* 47, 459–476. doi: 10.1016/j.geotexmem.2019.04.001

Ngo, N. T., Indraratna, B., Ferreira, F. B., and Rujikiatkamjorn, C. (2018). Improved performance of geosynthetics enhanced ballast: laboratory and numerical studies. *Proc. Inst. Civ. Eng.* 171, 202–222. doi: 10.1680/jgrim.17.00051

Nimbalkar, S., and Indraratna, B. (2016). Improved performance of ballasted rail track using geosynthetics and rubber shockmat. *J. Geotech. Geoenviron. Eng.* 142:04016031. doi: 10.1061/(ASCE)GT.1943-5606.0001491

Palmeira, E. M. (2004). Bearing force mobilisation in pull-out tests on geogrids. *Geotext. Geomembranes* 22, 481–509. doi: 10.1016/j.geotexmem.2004.03.007

Portelinha, F. H. M., Bueno, B. S., and Zornberg, J. G. (2013). Performance of non-woven geotextile-reinforced walls under wetting conditions: laboratory and field investigations. *Geosynth. Int.* 20, 90–104. doi: 10.1680/gein.13.00004

Raju, M. (1995). *Monotonic and cyclic pullout resistance of geosynthetics* (PhD thesis), University of British Columbia, Vancouver, Canada.

Ravi, K., Dash, S. K., Vogt, S., and Braeu, G. (2014). Behaviour of geosynthetic reinforced unpaved roads under cyclic loading. *Indian Geotech. J.* 44, 77–85. doi: 10.1007/s40098-013-0051-9

Samtani, N. C., and Nowatzki, E. A. (2006). *Soils and Foundations Reference Manual: Volume I. Report No. FHWA-NHI-06-088*. Washington, DC: Federal Highway Administration.

Subaida, E. A., Chandrakaran, S., and Sankar, N. (2008). Experimental investigations on tensile and pullout behaviour of woven coir geotextiles. *Geotext. Geomembranes* 26, 384–392. doi: 10.1016/j.geotexmem.2008.02.005

Tan, S. A., Chew, S. H., Ng, C. C., Loh, S. L., Karunaratne, G. P., Delmas, P., et al. (2001). Large-scale drainage behaviour of composite geotextile and geogrid in residual soil. *Geotext. Geomembranes* 19, 163–176. doi: 10.1016/S0266-1144(01)00005-X

Tang, X., Chehab, G. R., and Palomino, A. (2008). Evaluation of geogrids for stabilising weak pavement subgrade. *Int. J. Pavement Eng.* 9, 413–429. doi: 10.1080/10298430802279827

Tatsuoka, F. (2019). Geosynthetic-reinforced soil structures for railways and roads: development from walls to bridges. *Innov. Infrastruct. Solut.* 4:49. doi: 10.1007/s41062-019-0236-x

Vieira, C. S., Lopes, M. L., and Caldeira, L. M. (2013). Sand–geotextile interface characterisation through monotonic and cyclic direct shear tests. *Geosynth. Int.* 20, 26–38. doi: 10.1680/gein.12.00037

Vieira, C. S., Pereira, P. M., and Lopes, M. L. (2016). Recycled construction and demolition wastes as filling material for geosynthetic reinforced structures. Interface properties. *J. Clean. Prod.* 124, 299–311. doi: 10.1016/j.jclepro.2016.02.115

Wu, J. T. H., Siel, B. D., Chou, N. N. S., and Helwany, H. B. (1992). The effectiveness of geosynthetic reinforced embankments constructed over weak foundations. *Geotext. Geomembranes* 11, 133–150. doi: 10.1016/0266-1144(92)90041-8

Conflict of Interest: The authors declare that the research was conducted in the absence of any commercial or financial relationships that could be construed as a potential conflict of interest.

frontiers in Built Environment

ORIGINAL RESEARCH
published: 21 February 2020
doi: 10.3389/fbuil.2020.00015

Performance of Geosynthetics Reinforced Subgrade Subjected to Repeated Vehicle Loads: Experimental and Numerical Studies

Amarnath M. Hegde[1] and Prasad S. Palsule[2]*

[1] Department of Civil and Environmental Engineering, Indian Institute of Technology Patna, Patna, India, [2] Research Scholar, Department of Civil and Environmental Engineering, Indian Institute of Technology Patna, Patna, India

Use of the geosynthetics to strengthen the soil is one of the highly desirable techniques under static and dynamic loads. The present study describes the experimental and numerical studies performed on the geosynthetic reinforced subgrade subjected to repeated vehicle loads. The cyclic plate load tests were conducted on the sand subgrade reinforced with planar and 3D geosynthetic reinforcements. The vehicle load was simulated by applying a repeated load of magnitude 275 kPa with 1 Hz frequency on the reinforced subgrade. Results of the experimental investigations revealed that the performance of the subgrade soil improved significantly in the presence of reinforcements. The estimated parameters illustrated the three-fold reduction in settlement of the subgrade in the presence of reinforcement. Further, the heaving of the subgrade soil was found completely arrested with the use of geosynthetic reinforcement. The three-dimensional geocell reinforcement performed effectively as compared to planar geogrids under dynamic load. The measured pressure values at different depth demonstrated a significant reduction in the pressure in the presence of reinforcements. Besides, numerical simulations were performed using PLAXIS^{2D} to understand pressure and settlement distribution patterns in the reinforced subgrade. In overall, a good agreement was observed between numerical and experimental results.

Keywords: geosynthetics, bearing pressure, settlement, PLAXIS, vehicle, repeated loads

OPEN ACCESS

Edited by:
Sujit Kumar Dash,
Indian Institute of Technology Kharagpur, India

Reviewed by:
Dinesh S. V.,
Siddaganga Institute of Technology, Tumakuru, India
Arghadeep Biswas,
Jalpaiguri Government Engineering College, India

****Correspondence:***
Amarnath M. Hegde
ahegde@iitp.ac.in

Specialty section:
This article was submitted to Transportation and Transit Systems, a section of the journal Frontiers in Built Environment

Received: *19 October 2019*
Accepted: *05 February 2020*
Published: *21 February 2020*

Citation:
Hegde AM and Palsule PS (2020) Performance of Geosynthetics Reinforced Subgrade Subjected to Repeated Vehicle Loads: Experimental and Numerical Studies. Front. Built Environ. 6:15. doi: 10.3389/fbuil.2020.00015

Abbreviations: B, width of geocell mattress (mm); C, cohesion of unreinforced sand (kPa); C_c, coefficient of curvature (dimensionless); C_r, increased apparent cohesion (kPa); C_u, uniformity coefficient (dimensionless); C', total apparent cohesion (kPa); d_0, equivalent geocell pocket diameter (mm); D, width of loading plate (mm); D_{10}, effective particle size (mm); δ, soil surface settlement (mm); e_{min}, minimum void ratio (dimensionless); e_{max}, maximum void ratio (dimensionless); E, young's modulus of elasticity (kPa); ε_a, axial strain (dimensionless); G, shear modulus (kPa); G_s, specific gravity of sand (dimensionless); γ_d, dry unit weight (kN/m^3); h, height of geocell (mm); H, height of sand bed (mm); k_p, coefficient of passive earth pressure (dimensionless); M, secant modulus of geocell material (kPa); N_r, number of loading cycles for reinforced case (dimensionless); N_u, number of loading cycles for unreinforced case (dimensionless); r, radial distance from the center of loading plate (mm); S_0, settlement of unreinforced subgrade (mm); S_r, settlement of reinforced subgrade (mm); σ_n, horizontal stress increment (kPa); σ'_{yy}, vertical effective stress (kPa); w, specific weight (kN/m/m); W, width of the sand bed (mm); μ, poisson's ratio (dimensionless); z, depth of geocell (mm); α/β, rayleigh damping parameters (dimensionless); ϕ, angle of internal friction (degrees); ψ, dilatancy angle (degrees).

INTRODUCTION

The modern geotechnical design practices ensure that the structures should be founded on soils which can perform satisfactorily under different kind of loads. These loads are of static as well as dynamic in nature in case of highways, railways, runways, machine foundations, and live loads for storage tanks, etc. The dynamic effects are generally considered as a fraction of static loads but act repetitively. Repetitive load application causes large settlements in substructure, which ultimately causes failure in the structure. Reinforcing weak soils with geosynthetics and metallic strips are very much acceptable in current construction practices (Gabr and Han, 2005; El Sawwaf and Nazir, 2010; Chen and Abu-Farsakh, 2015; Abu-Farsakh et al., 2016; Sahu et al., 2018). Planar geotextiles (woven and non-woven), geogrids, and three-dimensional geocell reinforcements are used to strengthen the weak subgrades. These are extensible inclusions and impart strength with increased interface friction and confinement of soil. It also helps in distributing stresses uniformly over a broader area. The geosynthetic reinforcements reduce the settlements and increase the load-carrying capacity of the subgrade soils.

The depression of the roadway surface is commonly known as the rut. The rut formation is observed in flexible pavements due to deformation of the subgrade layer. This deformation of subgrade layer generally caused due to the wheel load. Many researchers have highlighted the beneficial effects of geosynthetic reinforcements in foundation applications under static and dynamic loadings (Tafreshi and Dawson, 2010; Asakereh et al., 2013; Hegde and Sitharam, 2013; Abu-Farsakh et al., 2013; Elsaied et al., 2015; Chen and Abu-Farsakh, 2015; Saride et al., 2015; Abu-Farsakh et al., 2016; Hegde and Sitharam, 2016; Suku et al., 2016; Elleboudy et al., 2017; Sahu et al., 2018). However, the behavior of reinforced pavement sections under repeated wheel loads was studied by very few researchers. The dynamic loadings with varying amplitudes and frequency cause permanent deformations in subgrades (Leng and Gabr, 2002; Saride et al., 2015; Abu-Farsakh et al., 2016; Suku et al., 2016; Elleboudy et al., 2017). Thus, the subgrade soils should be tested under cyclic loads before construction of pavement. Tafreshi and Dawson (2010) compared the improvement in the performance of the pavement reinforced with different types of geosynthetics under repeated loading. Geocell reinforced subgrade showed better performance as compared to geogrid reinforced subgrade. Asakereh et al. (2013) analyzed strip footing placed over a void in sand bed under static and cyclic loadings. The study was performed by varying void depth, number of reinforcement layers and loading magnitude. It was observed that the maximum footing settlement was increased by three times for cyclic loading in comparison to static load. It was concluded that both depth of the void and number of geogrid layers have significant influence on footing behavior. Tafreshi et al. (2015) performed cyclic plate load tests on the pavement section reinforced with two layers of geocell. It was concluded that the optimum depth of top layer and intra-layer spacing of geocell layers should be 0.2 times width of the loading plate. The use of geocell mattress as a reinforcement decreased the accumulation of plastic strain in subgrade. Abu-Farsakh et al. (2016) conducted model tests on reinforced pavement sections using triaxial geogrid and woven geotextile under repeated loading. The study showed that the use of geosynthetic at base-subgrade interface increased the traffic benefit ratio (TBR) beyond 1.5. The accumulated permanent deformation was found reduced due to wider and uniform stress distribution in reinforced sections.

Elleboudy et al. (2017) assessed the effectiveness of geogrid layer at the interface of weak subgrade and gravel sub-base. The vertical deformation was reduced by 18–54% in the presence of geogrid reinforcement. The most effective location for geogrid reinforcement was found to be at the top quarter of the base layer. Suku et al. (2016) studied the geocell reinforced granular base under repeated loading for unpaved roads. The study showed that the resilient modulus increases due to the provision of reinforcement. Thakur et al. (2017) studied the influence of factors such as geocell reinforcement, subgrade strength on the deformations of the recycled asphalt pavement bases. The study highlighted a significant reduction of the permanent deformations of the subgrade in the presence of reinforcement. Mamatha and Dinesh (2019) evaluated the rutting behavior of geocell reinforced model pavement sections under repeated loading. The introduction of geocell reinforcement at the interface of subgrade and base reduced the rutting by 13–71%.

Sahu et al. (2018) conducted model footing tests on reinforced foundations incorporating human hair fibers and PET/HDPE geogrid. The free vibration tests showed that the natural frequency and damping properties were improved for reinforced sand. Pokharel et al. (2018) conducted repeated loading tests on reinforced bases with "Novel Polymeric Alloy" geocell filled using poorly graded river sand and quarry waste. The improvement in the working life of pavement was quantified with the help of the traffic benefit ratio. The TBR was observed in the range of 8–12 in the presence of geocell reinforcement. Saride et al. (2015) conducted a series of tests on sand subgrade sections under repeated application of equivalent single axle wheel load. The optimum geocell mattress size was determined for the reduced rut depth of the pavement section. The geocell mattress of height equal to the diameter of the loading plate and width equal to 4.33 times the loading plate diameter was determined as the optimum geometry of reinforcement.

In overall, a very limited literature is available related to comparison of the performance of planar and geocell reinforced subgrade under dynamic loads in pavement applications. In the present study, cyclic plate load tests have been carried out to compare the performance of sand subgrades reinforced with a single geogrid layer, geocell mattress, and geocell with a basal geogrid layer. In addition, numerical simulations have been performed using PLAXIS^{2D} to complement the experimental findings.

MATERIALS AND METHODS

Natural sand with specific gravity (G_s) of 2.59 and effective grain size (D_{10}) of 0.2 mm was used in the present study. It was characterized as poorly graded sand (SP) as per the Unified Soil Classification System. The coefficient of uniformity

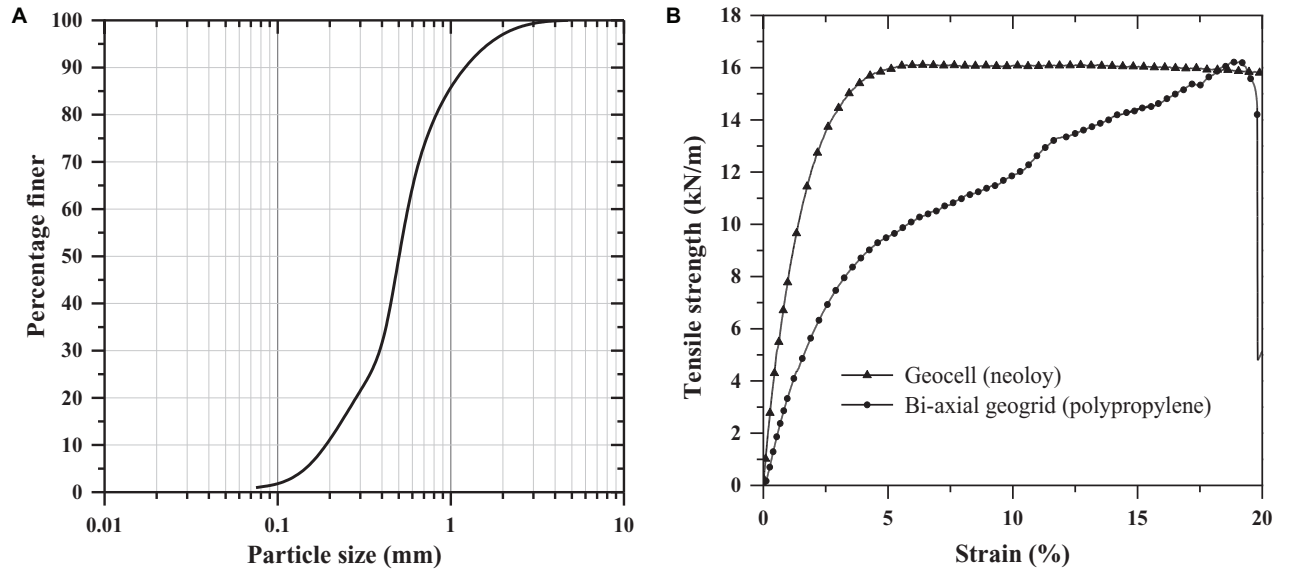

FIGURE 1 | Material properties: **(A)** grain size distribution of sand; **(B)** tensile strength of geocell and geogrid.

(C_u) and coefficient of curvature (C_c) values were obtained as 2.65 and 1.74, respectively. The grain size distribution of soil is shown in **Figure 1A**. The shear strength parameters were determined by the direct shear test as per IS 2720-13 (1986) part . The angle of internal friction of sand was determined as 34°. The relative density test was carried out as per IS 2720-14 (1983) part. The sand has a minimum void ratio (e_{min}) of 0.405 and a maximum void ratio (e_{max}) of 0.66. The two types of geosynthetics, namely geocell and geogrid were used. The biaxial geogrid with a square aperture opening of 35 mm was used. The tensile strength test was carried out on geogrid and geocell material as per ASTM D6637 (2011) and ASTM D6693 (2015), respectively. The results obtained are shown in **Figure 1B**. The properties of reinforcement materials are summarized in **Table 1**.

TABLE 1 | Mechanical and physical properties of geosynthetics.

Material property	Value
Geogrid	
Polymer	Polypropylene
Tensile Strength (kN/m)	16
Aperture Opening (mm)	35 × 35
Geocell	
Polymer	Neoloy
Tensile Strength (kN/m)	16
Cell Height (mm)	120
Number of cells/m^2	39
Strip thickness (mm)	1.53
Cell Pocket dimensions (mm)	210 × 245
Cell length (mm)	330
Cell wall surface	Perforated

Test Setup

The equipment used in the study was designed to test the soil subgrade under static and dynamic loading. The schematic view of the testing apparatus is shown in **Figure 2**. The whole system consists of three components, namely a test tank, loading assembly, and data acquisition system. The test tank with the dimensions of 1000 × 1000 × 1000 mm was used. The three sides of the tank were made up of rigid steel walls. Plexiglas was used on one side for visual observations. The internal faces of tank walls were smoothened to reduce friction between backfill material and wall surface. The loading assembly mainly consisted of reaction frame, hydraulic system with an actuator, and control module. The actuator can produce monotonic as well

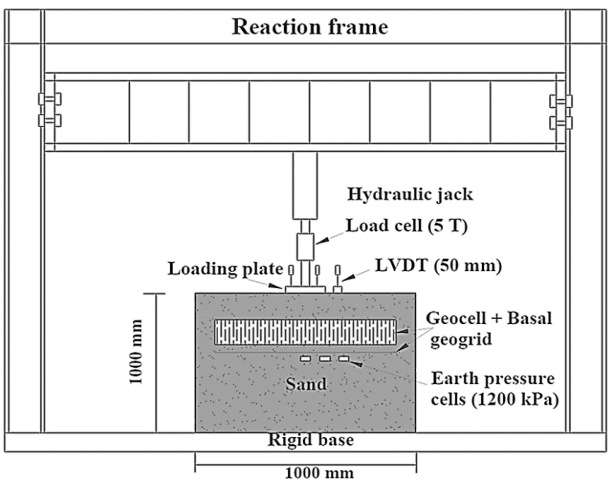

FIGURE 2 | Schematic view of test setup.

as harmonic loading with a frequency of 1 Hz. The load cell of 50 kN capacity along with LVDT having a measuring range of 0–150 mm was attached to the actuator. The rigid steel plate of diameter 150 mm and thickness of 25 mm was used to apply load on the subgrade. The loading plate dimensions are in accordance of the guidelines of ASTM D1195/1195M (2015). A plunger was connected between an actuator and the loading plate to apply the load vertically. The control module can be operated either manually or through software.

The data acquisition box was connected to a control module to collect data transmitted from instrumentation. The data was transferred to a computer for further processing and visual output. In total, five numbers of LVDTs were connected to measure the settlement of the loading plate and soil surface. Two LVDTs having a measuring range of 0–50 mm were placed vertically on either side of the loading plate. While two more LVDTs were placed perpendicular to each other at a radial distance of 120 mm from the center of bed. The plastic base plates were used to rest the LVDT tip. The LVDT with measuring range of 0–100 mm was placed on the loading plate to define failure criteria. The loading plate settlement of 50 mm was considered as a failure of subgrade system in the present study. Once the failure settlement value was reached, the mechanism was designed to stop the cyclic loading automatically. Three earth pressure cells with capacity ranges between 0 and 1000 kPa and having least count of 1 kPa were placed at a depth of 150 mm from the surface of the sand bed. The earth pressure cells were placed at a distance of r/D equal to 0, 0.5, and 1 (where r is the radial distance of pressure cell location from the center of the loading plate). The pressure cells were used to measure the transferred pressures to subgrade at different dynamic time intervals.

Preparation of Test Bed and Procedure

The sand bed with 630 mm thickness and a relative density of 72% was prepared using the pluviation technique. To formulate the height of fall required for each layer, a number of trial tests were performed. The depth of the reinforcement was decided based on recommendations given by previous researchers (Tafreshi and Dawson, 2010; Hegde and Sitharam, 2013; Tafreshi et al., 2015). The four test series, namely C0, C1, C2, and C3, were conducted, and corresponding details are presented in **Table 2**. For test series C1 and C2, the geogrid and geocell layer were placed at the depth equal to $0.3D$ and $0.1D$, respectively, where D was the diameter of the loading plate. In the test series "C3," the geogrid layer was placed just below the geocell reinforcement. The b/D ratio for geogrid layer and geocell reinforcement was 5.8 and 3.7, respectively. The loading plate was placed at the center of sand bed. The LVDTs were arranged to measure average settlement of loading plate and soil surface settlement as discussed in the previous section. **Figure 3** shows the geometry details of test arrangement. Each measurement was represented in terms of diameter of the loading plate, D. These dimensionless parameters are helpful in correlating the test results with large scale experiments.

The prepared sand bed was leveled without disturbing its density to prevent eccentric load application. In the present study, the dynamic loads originating from traffic movement are mainly considered as a driving force to cause failures. A load amplitude of 400 kPa was considered as an equivalent truck load at the surface (Brito et al., 2009). A thin asphalt layer was assumed at the top of the pavement. Considering the load dispersion effect, reduced single wheel load on the subgrade was calculated as 275 kPa using KENPAVE analysis. A similar load amplitude was also reported by Huang (1993). The harmonic loading of amplitude 275 kPa was applied with a frequency of 1 Hz. The load amplitude value was supported by previous studies. Most of the researchers used single wheel load between 108 kPa to 800 kPa with frequency ranging from 0.33 Hz to 2 Hz to simulate traffic loading (Faragher et al., 2000; Tafreshi and Khalaj, 2008; Tafreshi and Dawson, 2010; Cao et al., 2016; Abu-Farsakh et al., 2016; Khalaj et al., 2017; Wang et al., 2018). To apply the load uniformly, the ball-socket arrangement was used. The load was continued until the failure criteria achieved. For every test series, multiple tests were performed for the repeatability check.

RESULTS AND DISCUSSION

The settlement ratio (s/D) is calculated as the ratio of settlement to the diameter of the loading plate. **Figure 4** shows the typical variation of settlement ratio with applied pressure for the geocell with a basal geogrid. The settlement ratio was increased sharply for the first few cycles. The rate of increment in the settlement ratio decreased with increasing loading cycles. This decreased incremental rate attributed to the densification of soil below the loading plate.

The effectiveness of reinforcement in reducing the settlement was calculated using the percentage reduction in settlement (PRS). Mathematically, it is defined as,

$$PRS\ (\%) = \frac{(S_0 - S_r)}{S_0} \times 100 \tag{1}$$

where S_0 is the settlement of unreinforced case; S_r is the settlement of reinforced pavement section of equal thickness for an equal number of loading cycles. The percentage reduction in settlement (PRS) was determined for all the reinforced cases. **Figure 5** shows the reduction in settlement for reinforced test series. The $PRS$for each case was compared at the end of 75 numbers of loading cycles. The maximum PRS value of 57% was observed for the case of geocell with basal geogrid.

Figure 6A shows the variation of settlement ratio with the number of cycles for unreinforced and reinforced sand subgrades. The failure criterion was set equal to 50 mm for loading plate settlement. The maximum number of loading cycles counted for reinforced subgrade section until failure. As compared to the unreinforced pavement section, significant improvement was observed in reinforced pavements to undergo equal deformation with prolonged loading cycles. The number of loading cycles was increased by 11, 17, and 30 times, respectively, due to the provision of geogrid, geocell, and geocell with basal geogrid reinforcements. Similar observations were also reported by Asakereh et al. (2013).

Figure 6B shows the variation of the surface settlement ratio (δ/D) with applied pressure. For the unreinforced case,

TABLE 2 | Test series for different reinforced subgrades.

Test series	Reinforcement details	Depth of reinforcement (*z*/*D*)	Width of reinforcement (*b*/*D*)	No. of tests performed
C0	Unreinforced subgrade	–	–	4
C1	Single geogrid layer reinforced subgrade	0.3	5.8	3
C2	Geocell reinforced subgrade	0.1	4	3
C3	Geocell with a basal geogrid layer reinforced subgrade	0.1	4	2

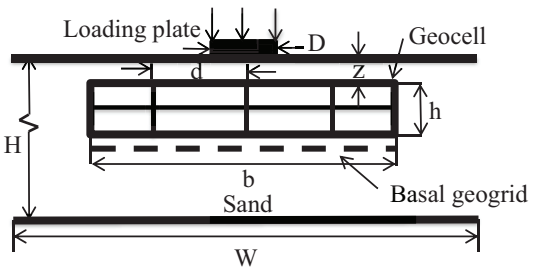

D = diameter of loading plate
b = width of geocell = 3.74 D
d = pocket diameter of geocell = 1.63 D
z = depth of geocell = 0.1 D
h = height of geocell = 0.8 D
H = height of sand bed = 4.2 D
W = width of sand bed = 6.2 D

FIGURE 3 | Detailed sectional view of reinforced test bed.

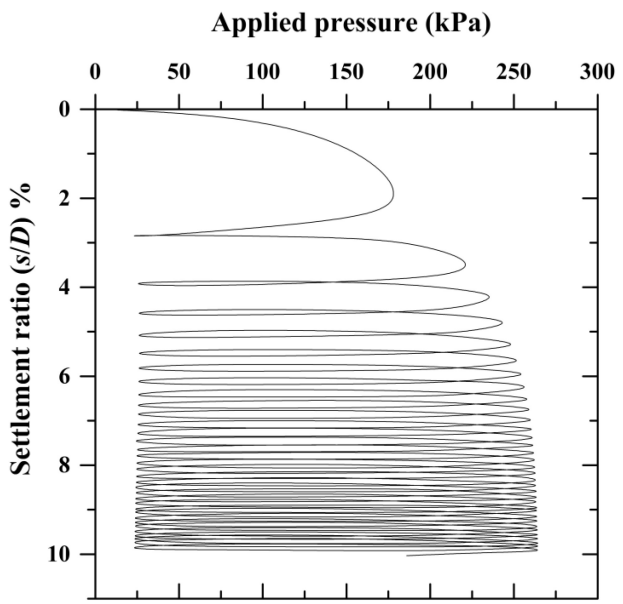

FIGURE 4 | Typical variation of settlement ratio with applied pressure.

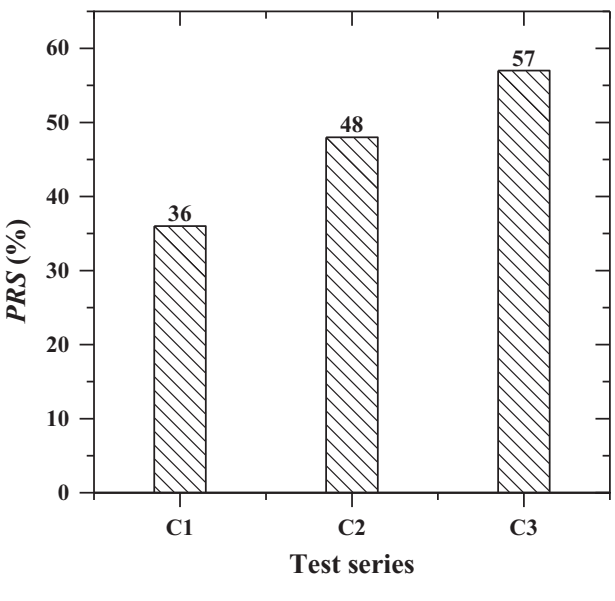

FIGURE 5 | Percentage reduction in settlement for different reinforced subgrades.

heaving was observed at the surface of the subgrade. It could lead to undulations in the road surface, which will cause discomfort to traffic. The reinforced subgrades C1, C2, and C3 showed no heaving in the soil surface. Irrespective of the type of reinforcement provided, the heaving was completely arrested. The reduced surface heaving suggested the uniform distribution of applied pressure over the pavement surface. The soil surface depression reduced by about 65% in case of geocell reinforcement as compared to a single geogrid layer reinforced subgrade. The settlement contours were plotted at different radial distances from the center of the load application. **Figures 7A–D** shows the settlement contours for different cases with the increasing number of loading cycles. In most of the cases, the loading plate was subjected to a differential settlement with the increase in the number of loading cycles. The calculated settlement ratio was less than 5% at a radial distance of 120 mm for all test series irrespective of the type of reinforcement provided.

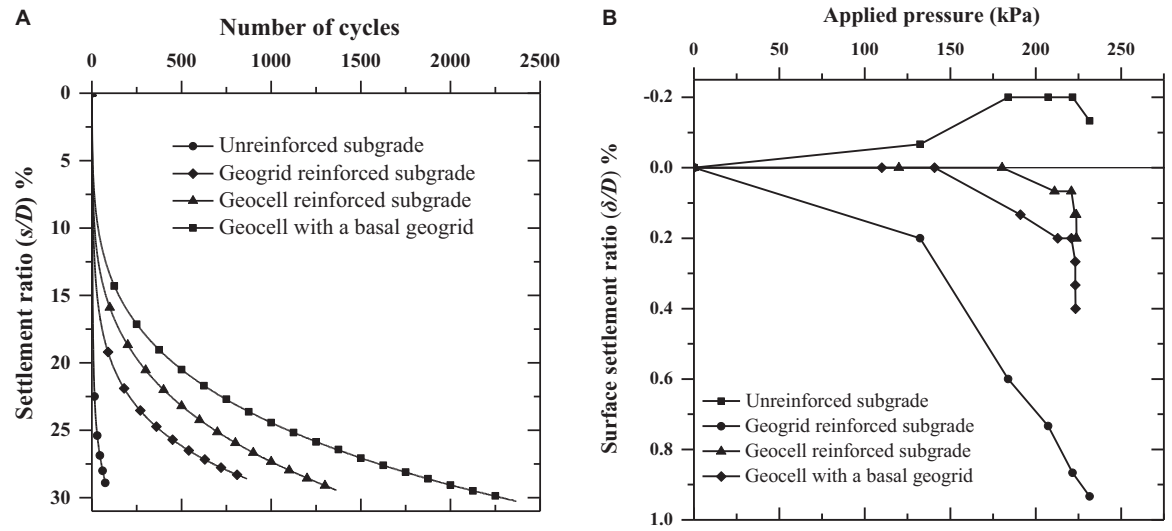

FIGURE 6 | Test results: **(A)** variation of settlement ratio with the number of cycles; **(B)** variation of soil surface settlement with applied pressure.

The subgrade rutting is generally caused due to heavy loads, consolidation or dislocation of soil particles in the subgrade. The rut depth can be measured by calculating the permanent deformation of the pavement section. The cumulative permanent deformation (CPD) was calculated for a specific number of loading cycles. It was measured by adding plastic deformation of the subgrade section cumulatively and expressed as percentage of loading plate diameter. The unreinforced pavement section was found to attain the failure criteria at 75 numbers of loading cycles. Thus the CPD was compared for the first 75 numbers of loading cycles for all reinforced cases. **Figure 8** shows the percentage CPD calculated for planar, and geocell reinforced subgrade sections of equal thickness. Reduction in plastic deformation of about 35% was observed for geocell reinforced pavement section as compared to unreinforced case.

Table 3 shows the values of rut depth reduction (RDR) for various reinforced cases with an increasing number of loading cycles. Saride et al. (2015) defined the term RDR as the ratio of the difference between cumulative permanent deformation of the unreinforced subgrade and reinforced subgrade to that of the unreinforced subgrade for a particular number of loading cycle. The RDR can be calculated as the equation given below.

$$(RDR)_{N=n} = \left(1 - \frac{CPD_r}{CPDu}\right) \times 100 \tag{2}$$

where CPD_r and CPD_u are cumulative permanent deformations for reinforced and unreinforced sand subgrade, respectively. The reduction in percentage RDR was observed with the increase in loading cycles. The maximum RDR was achieved for geocell with a basal geogrid reinforced subgrade.

Pokharel et al. (2018) defined traffic benefit ratio (TBR) as the ratio of the number of cycles necessary to reach a given rut depth. It is useful for quantifying the benefit of extended pavement life or reduced thickness of pavement. TBR was calculated for different reinforced cases as per the equation is given below.

$$TBR_{(S/D=i)} = \left(\frac{N_r}{Nu}\right)_i \tag{3}$$

where N_r and N_u are the number of load cycles corresponding to ith settlement ratio for reinforced and unreinforced cases, respectively. **Figure 9** shows the variation of TBR for different reinforcement combinations. The TBR was found to increase with the increase in the settlement ratio. The densification of the subgrade could be the reason for this behavior. The maximum TBR value of 32 was observed at 12% settlement ratio for the geocell with a basal geogrid reinforced subgrade. Saride et al. (2015) reported a similar TBR variation for the specific height and width of geocell.

Numerical Analysis

The PLAXIS^{2D} was chosen for numerical analysis considering its ability to solve various geotechnical problems. It uses a finite element solution scheme to solve initial and boundary value problems. The axisymmetric model was developed in PLAXIS^{2D} with equal dimensions of model used in laboratory studies. The dynamic analysis was performed for the first 75 cycles to reduce the numerical efforts and time constraints associated with the calculation phase. Further, the unreinforced subgrade failed after 75 loading cycles during experiment. Therefore, the comparison with the reinforced subgrade can be made only up to 75 numbers of loading cycles. In the numerical simulation, the Mohr-Coulomb (drained) model was used to simulate sand fill. The damping characteristics of soil were considered by defining Rayleigh coefficients. The Rayleigh parameters α and β represent the influence of mass and stiffness in the damping of the system, with the values 0.1049 and 0.02383, respectively.

The soil properties were assigned similar to the experimental investigations. The stiffness parameters, like modulus of elasticity

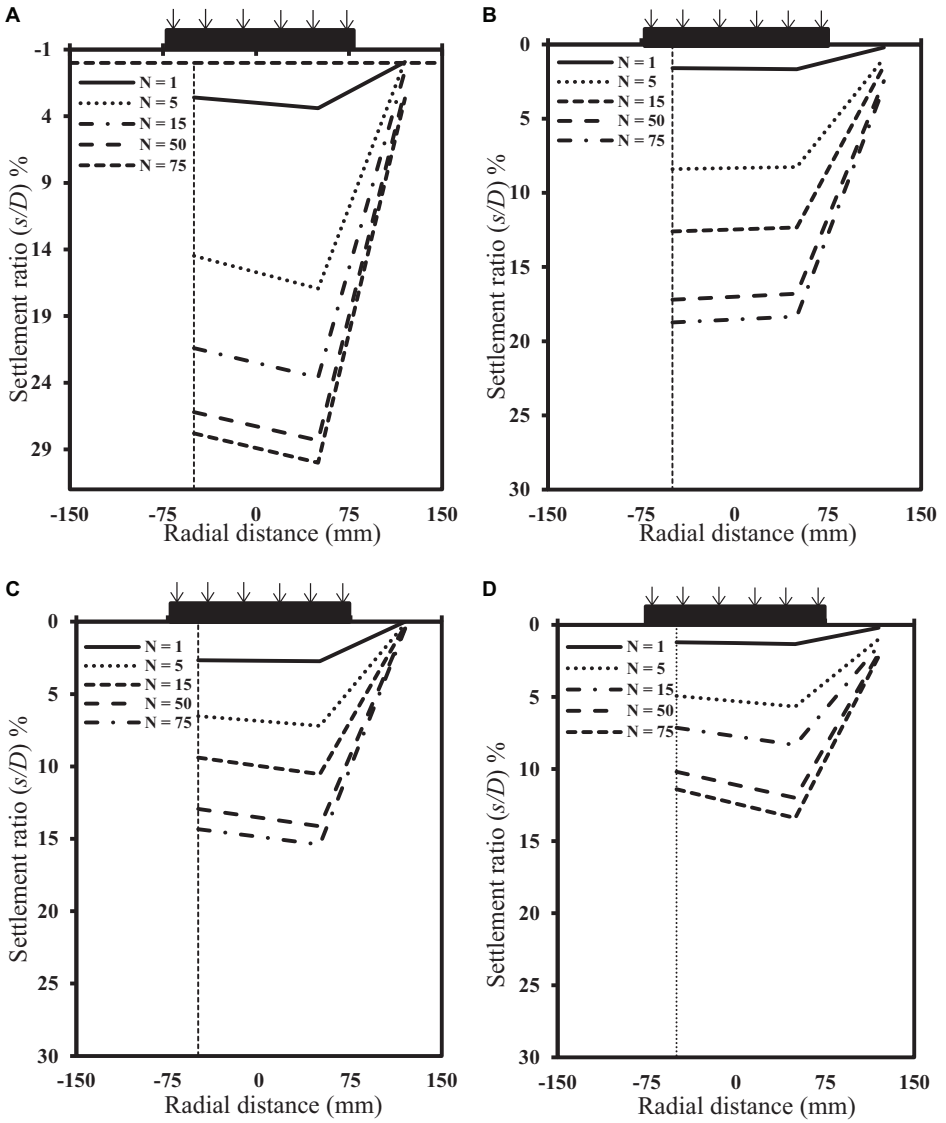

FIGURE 7 | Settlement contours: **(A)** unreinforced subgrade; **(B)** geogrid reinforced subgrade; **(C)** geocell reinforced subgrade; **(D)** geocell with a basal geogrid reinforced subgrade.

(E) and Poisson's ratio (μ), were borrowed from Hegde and Sitharam (2015). The initial void ratio was obtained from the relationship between dry unit weight, specific gravity, and void ratio. The geocell reinforced sand layer was modeled as Geocell-soil composite layer with improved stiffness and strength parameters (Rajagopal et al., 1999; Dash et al., 2003; Venkateswarlu et al., 2018; Ujjawal et al., 2019). The properties of the geocell composite layer were calculated using the equivalent composite approach (ECA), as suggested by Latha et al. (2009). Additional confining stress (σ_h) on the soil due to the provision of geocell was calculated using the equation given by Henkel and Gilbert (1952).

$$\sigma_h = \frac{2M}{d_0} \times \left(\frac{1 - \sqrt{1 - \varepsilon_a}}{1 - \varepsilon_a} \right) \tag{4}$$

The increased apparent cohesion (C_r) is the function of σ_h,

$$c_r = \left(\frac{\sigma_h \times \sqrt{K_p}}{2} \right) \tag{5}$$

The total apparent cohesion of geocell-soil composite mass (C') is given by,

$$c' = c_r + c \tag{6}$$

where σ_h is the horizontal stress increment; M is the secant modulus of geocell material at an axial strain (ε_a) of 2%; d_0 is the equivalent geocell pocket diameter; C_r is the increased apparent cohesion and k_p is the passive earth pressure coefficient. C' is the total apparent cohesion of the geocell composite layer, and C is the cohesion of unreinforced sand. The modulus of elasticity

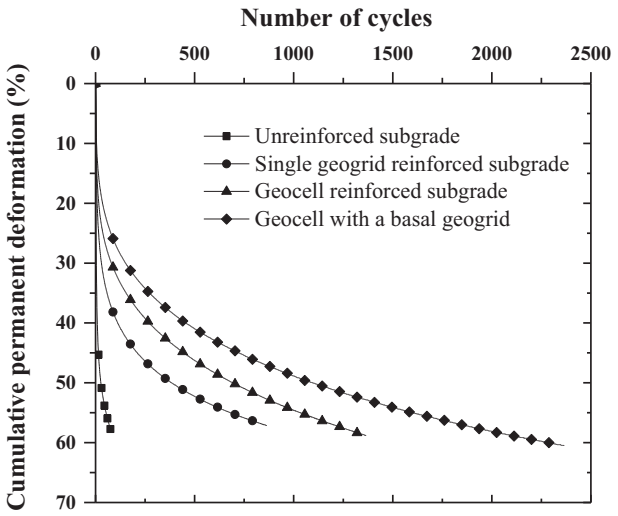

FIGURE 8 | Variation of cumulative permanent deformation with number of cycles.

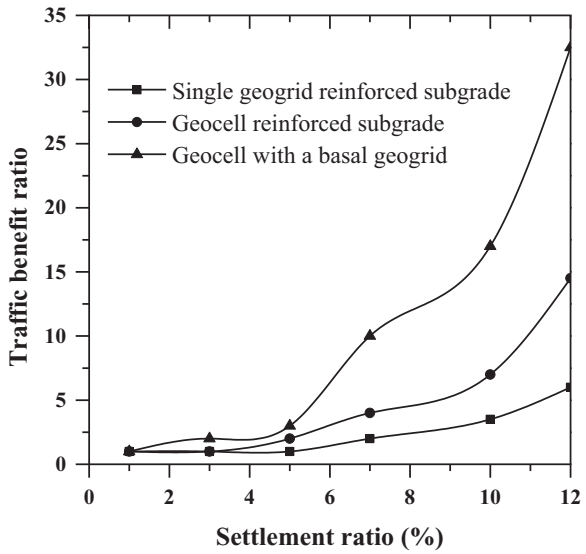

FIGURE 9 | Variation of traffic benefit ratio with settlement ratio.

of the geogrid and geocell was calculated from tensile strength test results. Material properties used in the numerical analysis are listed in **Table 4**.

The dynamic loading was applied as a line load above the loading plate. The isotropic, elastic beam element was used to define the loading plate with a thickness and a specific weight (w) of 25 mm and 4.85 kN/m/m, respectively. The dynamic loading similar to the experiment was applied. The positive and negative interfaces were provided at all contacts between structural elements and the sand. The interface properties were considered same as that of sand. **Figure 10** represents the axisymmetric model for test series "C3." The static and dynamic boundary conditions were provided for the proposed model. The vertical rigid walls of tanks were restricted to move horizontally with fixities in x-direction. The base of the test tank was fully fixed, and the top surface of the pavement boundary was kept free.

The experimental and numerical results for pressure measurements at r/D ratios 0, 0.5, and 1 were compared for the first 75 loading cycles in **Figures 11A,B**. A good agreement was observed with experimental results in the pressure readings for both unreinforced and reinforced cases at all r/D ratios. In unreinforced conditions, the initial reduction in pressure (38 kPa to 35 kPa) was observed below the center of loading plate, which was due to the rearrangement of loosely packed sand particles. Further, the stress distribution in the zone below the loading plate suggested the transfer of stress to deeper depths in case of unreinforced subgrade. However, in presence of reinforcement, the stress contour was confined to shallow depth. The reduction in pressure suggests that the pavement of lesser thickness can be constructed by reinforcing the subgrade with geosynthetics.

TABLE 3 | Rut depth reduction (*RDR*) for different reinforcement cases.

	Test series		
	RDR (%)		
No. of cycles	**C1**	**C2**	**C3**
$N = 5$	46.94	56.28	77.51
$N = 10$	46.50	56.94	77.92
$N = 15$	44.72	55.79	77.11
$N = 30$	40.60	52.95	74.90
$N = 75$	35.91	48.55	71.40

TABLE 4 | Materials properties used in PLAXIS^{2D}.

Materials	**Value**
Sand	
Material model	Mohr-Coulomb (drained)
Dry unit weight, (kN/m^3)	17
Young's modulus, E (MPa)	15
Poisson's ratio, μ	0.3
Shear modulus, G (MPa)	5.77
Cohesion (kPa)	3
Frictional angle, $\phi°$	34
Dilatancy angle, $\psi°$	22
Geogrid	
Material	Isotropic elastic
Axial stiffness EA (kN/m)	122670
Geocell composite layer	
Material model	Mohr-Coulomb (drained)
Dry unit weight (kN/m^3)	17
Young's modulus (MPa)	65
Poisson's ratio, μ	0.3
Cohesion (kPa)	34
Frictional angle, $\phi°$	34
Dilatancy angle, ψ ∘	22

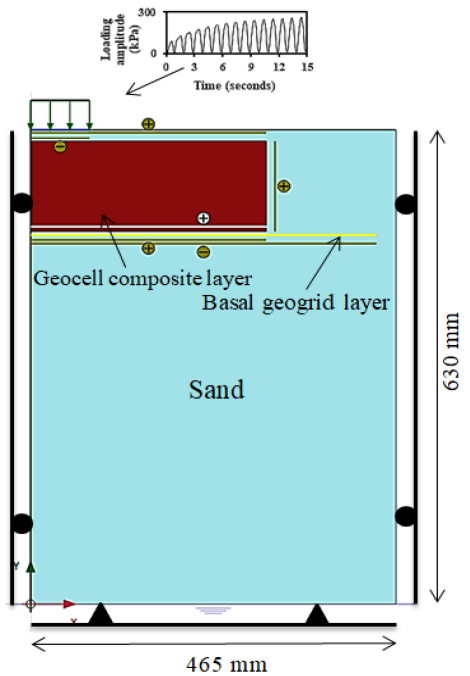

FIGURE 10 | Numerical model of the geocell reinforced subgrade with a basal geogrid layer.

Overall, the provision of reinforcement helps to reduce the material and maintenance associated with pavements.

CONCLUSION

The present study highlighted the efficacy of planar and three-dimensional geosynthetic reinforcement in improving the performance of subgrade under dynamic loads. The following conclusions were drawn from the study:

- Both the planar geogrid as well as 3-dimensional geocell reinforcement yielded a significant improvement compared to the unreinforced subgrade performance. However, 3-dimensional geocell reinforcement proved to be more effective than the planar geogrid layer.
- The subgrade settlement reduced significantly under dynamic load for all reinforced cases. The heaving at the soil surface was completely arrested for all reinforced subgrade conditions. The geocell reinforced pavement showed lesser surface settlements compared to the geogrid reinforced pavement section.
- In comparison to unreinforced condition, the loading cycle count increased by 11, 17, and 30 times for geogrid, geocell and geocell with basal geogrid reinforcement, respectively. The increased number of loading cycles indicates the increase in the service life period of the pavement.
- In the presence of reinforcement, the cumulative permanent deformation, *CPD* of subgrade decreased in a significant way. Subgrade reinforced with geocell and the basal geogrid showed more than 70% reduction in rut depth (*RDR*) compared to the unreinforced case. The improved resistance to the subgrade rutting provides stability to upper pavement layers such as sub-base, base, and top asphalt layer.
- Geocell with basal geogrid reinforcement provides a significant improvement in *TBR* and reduction in rut depth under repeated load. The *TBR* was increased to 32 for geocell with basal geogrid reinforcement as compared to unreinforced subgrade. It indicates that the increase in the working life of pavement.

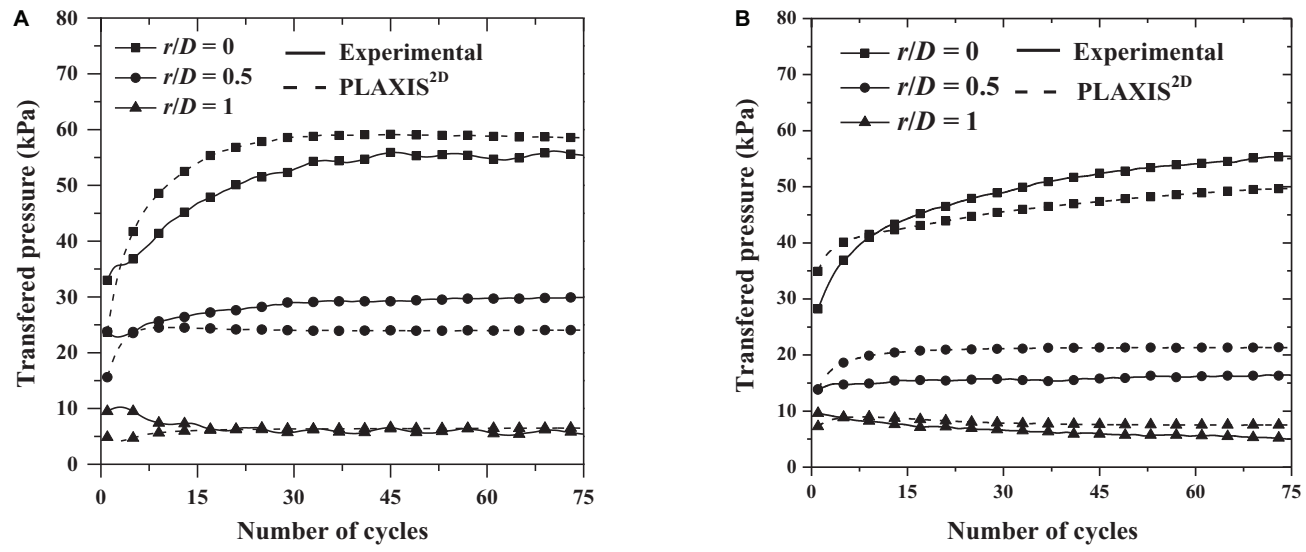

FIGURE 11 | Comparison of experimental and numerical transferred pressures: **(A)** unreinforced subgrade; **(B)** geocell with a basal geogrid reinforced subgrade.

- The numerical analysis showed good agreement with experimental results. The pressure was found to reduce drastically due to the presence of reinforcement.
- The study has certain limitations. The results are prone to scale effects due to the reduced model sizes used in the study. To predict the actual prototype response, either large scale field experiments or centrifuge model studies need to be conducted. The careful consideration of scaling laws as suggested by Butterfield (1999), the results of small-scale model test can be extrapolated to the full-scale cases.

DATA AVAILABILITY STATEMENT

All datasets generated for this study are included in the article/supplementary material.

AUTHOR CONTRIBUTIONS

AH elaborated the manuscript guidelines and corrected the manuscript. PP prepared the manuscript draft.

FUNDING

This work was funded by the Indian Institute of Technology Patna.

ACKNOWLEDGMENTS

The authors would like to express their sincere appreciation to the PRS Geo-Technologies, Israel for providing the geocells for the research work. The PP is thankful to Md. Nurul Hasan, Junior Technical Superintendent, for his help throughout the experimental work.

REFERENCES

Abu-Farsakh, M., Chen, Q., and Sharma, R. (2013). An experimental evaluation of the behavior of footings on geosynthetic-reinforced sand. *Soils Found.* 53, 335–348. doi: 10.1016/j.sandf.2013.01.001

Abu-Farsakh, M., Hanandeh, S., Mohammad, L., and Chen, Q. (2016). Performance of geosynthetic reinforced/stabilized paved roads built over soft soil under cyclic plate loads. *Geotextiles Geomembranes* 44, 845–853. doi: 10.1016/j.geotexmem.2016.06.009

Asakereh, A., Ghazavi, M., and Tafreshi, S. M. (2013). Cyclic response of footing on geogrid-reinforced sand with void. *Soils Found.* 53, 363–374. doi: 10.1016/j.sandf.2013.02.008

ASTM D1195/1195M (2015). *Standard Test Method For Repetitive Static Plate Load Tests of Soils and Flexible Pavement Components, for Use in Evaluation and Design of Airport and Highway Pavements*. West Conshohocken, PA: ASTM International.

ASTM D6637 (2011). *Standard Test Method for Determining the Tensile Properties of Geogrid by the Single or Multi-Rib Tensile Method*. West Conshohocken, PA: ASTM International.

ASTM D6693 (2015). *Standard Test Method for determining tensile properties of nonreinforced polyethylene and nonreinforced flexible polypropylene geomembranes*. West Conshohocken, PA: ASTM International.

Brito, L. A. T., Dawson, A. R., and Kolisoja, P. J. (2009). "Analytical evaluation of unbound granular layers in regard to permanent deformation," in *Proceedings of the 8th International on the Bearing Capacity of Roads, Railways, and Airfields (BCR2A'09)* (Champaign IL: Unversity of Illinois at Urbana Illinois), 187–196. doi: 10.1201/9780203865286.ch21

Butterfield, R. (1999). Dimensional analysis for geotechnical engineers. *Geotechnique* 49, 357–366. doi: 10.1680/geot.1999.49.3.357

Cao, Z., Han, J., Xu, C., Khatri, D. K., Corey, R., and Cai, Y. (2016). Road surface permanent deformations with a shallowly buried steel-reinforced high-density polyethylene pipe under cyclic loading. *Geotextiles Geomembranes* 44, 28–38. doi: 10.1016/j.geotexmem.2015.06.009

Chen, Q., and Abu-Farsakh, M. (2015). Ultimate bearing capacity analysis of strip footings on reinforced soil foundation. *Soils Found.* 55, 74–85. doi: 10.1016/j.sandf.2014.12.006

Dash, S. K., Sireesh, S., and Sitharam, T. G. (2003). Model studies on circular footing supported on geocell reinforced sand underlain by soft clay. *Geotextiles Geomembranes* 21, 197–219. doi: 10.1016/S0266-1144(03)00017-7

El Sawwaf, M., and Nazir, A. K. (2010). Behavior of repeatedly loaded rectangular footings resting on reinforced sand. *Alex. Eng. J.* 49, 349–356. doi: 10.1016/j.aej.2010.07.002

Elleboudy, A. M., Saleh, N. M., and Salama, A. G. (2017). Assessment of geogrids in gravel roads under cyclic loading. *Alex. Eng. J.* 56, 319–326. doi: 10.1016/j.aej.2016.09.023

Elsaied, A. E., Saleh, N. M., and Elmashad, M. E. (2015). Behavior of circular footing resting on laterally confined granular reinforced soil. *HBRC J.* 11, 240–245. doi: 10.1016/j.hbrcj.2014.03.011

Faragher, E., Fleming, P. R., and Rogers, C. D. F. (2000). Analysis of repeated-load field testing of buried plastic pipes. *J. Transp. Eng.* 126, 271–277. doi: 10.1061/(ASCE)0733-947X2000126:3(271)

Gabr, M., and Han, J. (2005). Geosynthetic reinforcement for soft foundations: US perspectives. *Int. Perspect. Soil Reinforc. Appl.* 1–17. doi: 10.1061/40788(167)5

Hegde, A., and Sitharam, T. G. (2013). Experimental and numerical studies on footings supported on geocell reinforced sand and clay beds. *Int J. Geotech. Eng.* 7, 346–354. doi: 10.1179/1938636213Z.00000000043

Hegde, A., and Sitharam, T. G. (2016). Behaviour of geocell reinforced soft clay bed subjected to incremental cyclic loading. *Geomech. Eng.* 10, 405–422. doi: 10.12989/gae.2016.10.4.405

Hegde, A. M., and Sitharam, T. G. (2015). Experimental and numerical studies on protection of buried pipelines and underground utilities using geocells. *Geotextiles Geomembranes* 43, 372–381. doi: 10.1016/j.geotexmem.2015.04.010

Henkel, D. J., and Gilbert, G. D. (1952). The effect measured of the rubber membrane on the triaxial compression strength of clay samples. *Geotechnique* 3, 20–29. doi: 10.1680/geot.1952.3.1.20

Huang, Y. H. (1993). *Pavement Analysis and Design*. Englewood Cliffs, NJ: Prentice Hall cop.

IS 2720-13, (1986). *Methods of Test for Soils- Part XIII: direct Shear Test*. Delhi: Prabhat Offset Press.

IS 2720-14, (1983). *Methods of Test for Soils- Part XIV: Determination of Density Index (Relative Density) of Cohesionless Soils*. Delhi: Prabhat Offset Press.

Khalaj, O., Darabi, N. J., Tafreshi, S. M., and Mašek, B. (2017). "Protection of Buried Pipe under Repeated Loading by Geocell Reinforcement," in *Proceedings of the IOP Conference Series: Earth and Environmental Science*, Vol. 95 (Bristol: IOP Publishing). doi: 10.1088/1755-1315/95/2/022030

Latha, G. M., Dash, S. K., and Rajagopal, K. (2009). Numerical simulation of the behavior of geocell reinforced sand in foundations. *Int. J. Geomech.* 9, 143–152. doi: 10.1061/(ASCE)1532-364120099:4(143)

Leng, J., and Gabr, M. A. (2002). Characteristics of geogrid-reinforced aggregate under cyclic load. *Transp. Res. Rec.* 1786, 29–35. doi: 10.3141/1786-04

Mamatha, K. H., and Dinesh, S. V. (2019). Performance evaluation of geocell-reinforced pavements. *Int. J. Geotech. Eng.* 13, 277–286. doi: 10.1080/19386362.2017.1343988

Pokharel, S. K., Han, J., Leshchinsky, D., and Parsons, R. L. (2018). Experimental evaluation of geocell-reinforced bases under repeated loading. *Int. J. Pavement Res. Technol.* 11, 114–127. doi: 10.1016/j.ijprt.2017.03.007

Rajagopal, K., Krishnaswamy, N. R., and Latha, G. M. (1999). Behaviour of sand confined with single and multiple geocells. *Geotextiles Geomembranes* 17, 171–184. doi: 10.1016/s0266-1144(98)00034-x

Sahu, R., Ayothiraman, R., and Ramana, G. V. (2018). Dynamic Response of Model Footing on Reinforced Sand. *Geotech. Earthquake Eng. Soil Dyn. V* 199–207. doi: 10.1061/9780784481486.021

Saride, S., Rayabharapu, V. K., and Vedpathak, S. (2015). Evaluation of rutting behaviour of geocell reinforced sand subgrades under repeated loading. *Indian Geotech. J.* 45, 378–388. doi: 10.1007/s40098-014-0120-8

Suku, L., Prabhu, S. S., Ramesh, P., and Babu, G. S. (2016). Behavior of geocell-reinforced granular base under repeated loading. *Transp. Geotech.* 9, 17–30. doi: 10.1061/41023(337)52

Tafreshi, S. M., and Dawson, A. R. (2010). Behaviour of footings on reinforced sand subjected to repeated loading–Comparing use of 3D and planar geotextile. *Geotextiles Geomembranes* 28, 434–447. doi: 10.1016/j.geotexmem.2009.12.007

Tafreshi, S. M., and Khalaj, O. (2008). Laboratory tests of small-diameter HDPE pipes buried in reinforced sand under repeated-load. *Geotextiles Geomembranes* 26, 145–163. doi: 10.1016/j.geotexmem.2007.06.002

Tafreshi, S. M., Khalaj, O., Dawson, A. R., and Mašek, B. (2015). Repeated load response of soil reinforced by two layers of geocell. *Procedia Earth Planet. Sci.* 15, 99–104. doi: 10.1016/j.proeps.2015.08.026

Thakur, J. K., Han, J., and Parsons, R. L. (2017). Factors influencing deformations of geocell-reinforced recycled asphalt pavement bases under cyclic loading. *J. Mater. Civil Eng.* 29:04016240. doi: 10.1061/(ASCE)MT.1943-5533.0001760

Ujjawal, K. N., Venkateswarlu, H., and Hegde, A. (2019). Vibration isolation using 3D cellular confinement system: a numerical investigation. *Soil Dyn. Earthquake Eng.* 119, 220–234. doi: 10.1016/j.soildyn.2018.12.021

Venkateswarlu, H., Ujjawal, K. N., and Hegde, A. (2018). Laboratory and numerical investigation of machine foundations reinforced with geogrids and geocells. *Geotextiles Geomembranes* 46, 882–896. doi: 10.1016/j.geotexmem.2018.08.006

Wang, J. Q., Zhang, L. L., Xue, J. F., and Tang, Y. (2018). Load-settlement response of shallow square footings on geogrid-reinforced sand under cyclic loading. *Geotextiles Geomembranes* 46, 586–596. doi: 10.1016/j.geotexmem.2018.04.009

Conflict of Interest: The authors declare that this study received geocell support from PRS Geo-Technologies, Israel. The agency was not involved in the study design, collection, analysis, interpretation of data, the writing of this article or the decision to submit it for publication.

frontiers in Built Environment

ORIGINAL RESEARCH
published: 25 February 2020
doi: 10.3389/fbuil.2020.00020

Application of Geogrids in Stabilizing Rail Track Substructure

Syed Khaja Karimullah Hussaini and Kumari Sweta*

Railway Engineering, Department of Civil and Environmental Engineering, Indian Institute of Technology Patna, Patna, India

Large-scale direct shear tests were conducted to assess the performance of geogrid-reinforced ballast-sub-ballast interface followed by triaxial tests to explore the deformation and degradation response of geogrid-reinforced ballast under cyclic loading. While the direct shear testing was performed at applied normal stresses (σ_n) ranging from 20 to 100 kPa and rate of shearing (S_r) from 2.5 to 10.0 mm/min, the cyclic triaxial tests were performed to capture the role of loading frequency (f) ranging from 10 to 40 Hz. Fresh granite ballast and sub-ballast with mean particle size (D_{50}) of 42 and 3.5 mm, and five geogrids having different aperture shapes and sizes (A) were used in this study. The tests results indicated that the behavior of ballast-sub-ballast interface is highly influenced by σ_n and S_r. The friction (φ) and dilation angles (ψ) of unreinforced and geogrid-reinforced ballast-sub-ballast interface is found to reduce from 67.96 to 47.82° and 14.56 to 3.34° with the increase in σ_n and S_r. Marsal's Breakage (B_g: an index to quantify the breakage of ballast) of unreinforced ballast was found to increase from 2.84 to 6.69% with the increase in σ_n and S_r. However, the inclusion of geogrids significantly enhanced the friction angle (φ), reduced the extent of dilation angle (ψ), and minimized B_g. The interface efficiency factor (α) and B_g were found to be a function of A/D_{50} ratio. Accordingly, a model is developed using multiple linear regression analysis to predict the values of φ, ψ, and B_g in terms of the input parameters σ_n, S_r, and A/D_{50} ratio. The results from triaxial tests indicate the deformation and degradation behavior of ballast under cyclic loading conditions to be influenced by the loading frequency (f). The extent of I_d and S_v of unreinforced ballast increases from 5.48 to 28.32 mm and 20.13 to 45.40 mm with the increase in f. The value of B_g increased from 4.3 to 11.69% when the value of f was increased from 10 to 40 Hz. Similarly, the extent of lateral and vertical deformation of ballast was found to be a function of A/D_{50} ratio.

Keywords: geosynthetics, ballast-sub-ballast interface, direct shear test, cyclic loading, friction angle (φ), settlement (S_v), loading frequency (f), process simulation test (PST) apparatus

OPEN ACCESS

Edited by:
Eduardo Cabrita Fortunato, National Laboratory for Civil Engineering, Portugal

Reviewed by:
Ruilin You, China Academy of Railway Sciences, China
Sujit Kumar Dash, Indian Institute of Technology Kharagpur, India

****Correspondence:***
Syed Khaja Karimullah Hussaini
hussaini@iitp.ac.in

Specialty section:
This article was submitted to Transportation and Transit Systems, a section of the journal Frontiers in Built Environment

Received: *21 August 2019*
Accepted: *11 February 2020*
Published: *25 February 2020*

Citation:
Hussaini SKK and Sweta K (2020) Application of Geogrids in Stabilizing Rail Track Substructure. Front. Built Environ. 6:20. doi: 10.3389/fbuil.2020.00020

INTRODUCTION

Railways are one of the most economical modes of transportation for moving freight as well as passengers from one place to another. With the rapid increase in population and the associated traffic congestion on highways, the demand for high-speed railway lines is on rise. However, the inherent effect of the introduction of high-speed trains is to induce additional cyclic stresses on the substructure of a railway track that comprises mainly of ballast and sub-ballast layers. Ballast distributes the applied train load to the sub-ballast layer at an acceptable level while maintaining the track alignment and allowing the quick drainage of water. On the other hand, the sub-ballast

reduces the extent of stress being transferred to the soil beneath and also acts as a filter medium thereby preventing the upward migration of subgrade soil into the ballast layer. However, due to continuous passage of trains, ballast being unbound in nature undergoes a significant amount of lateral deformation and particle degradation which directly contributes to track settlement. The excessive deformation and degradation of ballast leads to track misalignment that calls for either the imposition of speed restrictions or the conduction of costly track maintenance operations. In this view, the railway organizations around the world have recently started using the geogrids for stabilizing the railway tracks. In practice, the geogrids are generally placed at the bottom of ballast layer (i.e., at ballast-sub-ballast interface) so that the same will not obstruct the track maintenance process. Once in place, geogrids generates non-displacement boundary condition that limits the lateral movement of ballast that subsequently reduces vertical settlement and deformation of ballast.

Realizing the importance of geogrids in rail track application, several researchers have studied the role of geogrids on coarse granular medium under direct shear conditions (Lee and Manjunath, 2000; Liu et al., 2009; Palmeira, 2009; Anubhav and Basudhar, 2010, 2013; Hussaini et al., 2012; Indraratna et al., 2012; Moraci et al., 2014; Sayeed et al., 2014; Biabani and Indraratna, 2015; Liu and Martinez, 2015; Vieira et al., 2015; Choudhary and Krishna, 2016; Liu F.-Y. et al., 2016; Liu S. et al., 2016; Afzali-Nejad et al., 2017; Guler and Khosrowshahi, 2017; Mvelase et al., 2017; Chen et al., 2018; Sweta and Hussaini, 2018, 2019a; Mirzaalimohammadi et al., 2019). Liu et al. (2009) have determined the shear behavior of granular soils stabilized with PET-yarn geogrids. On the other hand, Makkar et al. (2017) have evaluated the behavior of sand when reinforced with geogrid in three dimensional forms. Biabani and Indraratna (2015) have investigated the behavior of sub-ballast when stabilized with geogrids and geomembranes. Indraratna et al. (2012) and Hussaini et al. (2012) have explored the shear behavior of various ballast-geogrid interfaces at constant shearing rate of 2.5 mm/min. Sweta and Hussaini (2018, 2019a) have evaluated the shear behavior of ballast at different applied normal stresses and rates of shearing when stabilized with various geogrids. Similarly, several studies have highlighted the benefits of geogrids in stabilizing ballast under cyclic loading conditions (Bathurst and Raymond, 1987; Matharu, 1994; Brown et al., 2007; Indraratna et al., 2007, 2013, 2015; Mishra et al., 2014; Hussaini et al., 2015a,b, 2016; Biabani et al., 2016; Nimbalkar and Indraratna, 2016). Shin et al. (2002) highlighted the beneficial effect of reinforcement in reducing settlement when a layer of geogrid and geotextiles was placed at the interface of the subgrade and sub-ballast layer. Moreover, Nimbalkar and Indraratna (2016) have evaluated the benefits of inclusion of geosynthetics and rubber shock mats in the critical section of track through a field trial. Indraratna et al. (2015) and Biabani et al. (2016) have investigated the behavior of geocell-reinforced sub-ballast at different frequencies under cyclic loading conditions. Navaratnarajah and Indraratna (2017) have assessed the use of rubber mats in improving the deformation and degradation behavior ballast at different frequencies and axle load. Indraratna et al. (2013) and Hussaini et al. (2015b) are the only studies that have captured the influence of geogrid aperture size (A) in stabilizing the railway ballast under cyclic loading conditions at a constant loading frequency (f) of 20 Hz. In addition, there are several studies that have shown the effect of loading frequency (f) on the behavior of unreinforced ballast under various cyclic loading conditions (Indraratna et al., 2010; Thakur et al., 2013; Sun et al., 2014, 2019). However, the role of geogrids in stabilizing railway ballast at different loading frequencies (f) has not been yet studied. Similarly, there are very limited studies that describe the influence of applied normal stress (σ_n) and rates of shearing (S_r) on various ballast-geogrid-sub-ballast interfaces under direct shear conditions. Moreover, a rail track under operating conditions may be subjected to different shearing rates depending upon the magnitude of cyclic stress and the train speed. In this context, a series of large-scale direct shear tests were carried out to study the influence of σ_n and S_r on ballast-geogrid-sub-ballast interface followed by large-scale cubical triaxial tests to determine the effect of loading frequency (f) on ballast with and without geogrids.

MATERIALS AND TESTING PROCEDURES

Materials

Fresh granite particles and a mixture of sand and crushed granite were used as ballast and sub-ballast, respectively. The particle size distributions (*PSD*) of ballast and sub-ballast used in the present study were as per the standards specified by Indian railways (IRSGE, 2004; RDSOGE, 2007; **Figure 1**). The particle size characteristics of ballast and sub-ballast are presented in **Table 1**. The maximum (D_{max}) and mean diameters (D_{50}) of sub-ballast were 20 and 3.5 mm and that of ballast were 65 and

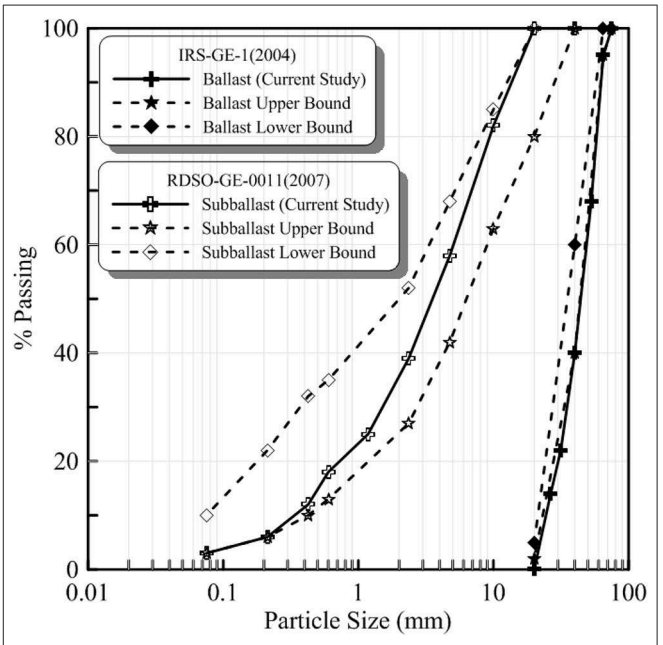

FIGURE 1 | Particle size distributions of ballast and sub-ballast used in this study.

42 mm, respectively. Five types of geogrids were used in the current study to stabilize the rail road ballast. These geogrids have different aperture shapes and sizes. The physical characteristics and technical specifications of geogrids (labeled *G1* to *G5*) used in the present study are described in **Table 2**.

Direct Shear Tests

A series of shear tests were performed using large-scale direct shear apparatus, having plan dimension of 450 × 450 mm and overall depth of 300 mm. The apparatus consists of two square boxes; the lower box is fixed in position while the upper box is allowed to move. The apparatus can allow application of normal stress and can capture the shear stresses up to 300 kN/m^2 and can allow shear displacements up to 100 mm. The dimensions of the apparatus and the capacity of load cells have been suitably selected to explicitly test coarse granular materials like railway ballast at high normal loading and strain rates. **Figure 2A** shows the schematic illustration of large-scale direct shear apparatus.

The specimen preparation involves the mixing of sieved ballast and sub-ballast separately in a required proportion conforming to the PSDs as specified in **Figure 1**. The lower box of shear apparatus was filled with a predetermined quantity of sub-ballast and then compacted in two layers with the help of a vibrating plate to attain a required density (γ_{sb}) of 2,000 kg/m^3 which is the representative of typical field conditions. Then, the ballast is filled in the upper shear box and compacted in two layers with same vibrating plate to attain a field density (γ_b) of 1,470 kg/m^3. In case of reinforced samples, a layer of geogrid is installed at the interface of two shear boxes and fixed with the clamping screws after the compaction of sub-ballast in lower shear box. To reduce the extent of particle breakage during vibration, a 7 mm thick rubber pad was placed beneath the vibrating plate. Tests were conducted at different applied normal stresses (σ_n) ranging from 20 to 100 kPa which is representative of typical track conditions under low confinement and shearing rates (S_r) ranging from 2.5 to 10.0 mm/min. The tests were carried out up to the horizontal displacement of 67.5 mm that represents a horizontal strain of 15%.

TABLE 1 | Grain size characteristics of ballast and sub-ballast.

Material	D_{max} (mm)	D_{10} (mm)	D_{30} (mm)	D_{60} (mm)	D_{50} (mm)	C_u	C_c
Sub-ballast	20	0.35	1.7	5.0	3.5	14.29	1.65
Ballast	65	22	32	48	42	2.18	0.97

Triaxial Tests Using Process Simulation Test (PST) Apparatus

A series of triaxial tests were carried out using large-scale process simulation test (PST) apparatus, consisting of a box of 950 mm length, 650 mm width, and 730 mm overall depth. The plan dimension of 950 mm represents the effective sleeper length that transfers the applied wheel load to the ballast beneath, as defined by Jeffs and Tew (1991) and Atalar et al. (2001). On the other hand, 650 mm represents the center-center spacing between the sleepers in the direction of rail. The mid portion of the two side walls parallel to rails (i.e., along the direction of passage of train) consists of five independent movable plates each measuring 650 mm in width and 75 mm in height. A small gap of 1 mm was provided to allow the free movement of plates in lateral direction. The maximum allowable lateral displacement of each plate is 100 mm that corresponds to a lateral strain (ε_3) of 10.52%. The apparatus used in the current study is similar to that used by Hussaini (2013) and Indraratna et al. (2013) but with five independently movable side walls on both the sides. The apparatus can be used to apply a vertical dynamic load of 200 kN at frequencies of up to 50 Hz. **Figure 2B** illustrates the schematic diagram of process simulation test apparatus.

The specimen preparation involved the placement of sub-ballast (150 mm thick), comprising of crushed granite-sand mixture, in two layers of 75 mm each and their compaction with the help of a vibrating plate to attain a required density (γ_{sb}) of 2,000 kg/m^3. This was overlain by a ballast layer of 380 mm that was placed in three equal layers and compacted to achieve a target field density (γ_b) of 1,520 kg/m^3. It is to be mentioned here that in both the series of tests the ballast particles were painted with bright yellow spray paint in order to clearly distinguish the broken pieces of ballast from underlying sub-ballast. A rail-sleeper assembly (wooden sleeper: 900 × 250 × 150 mm) was then placed over the compacted ballast and the spaces around the sleeper were filled with crib ballast. The rail section used was MR-52 section, as used by the Indian Railways on most of the broad gauge tracks. In case of reinforced samples, a layer of geogrid was placed at the ballast-sub-ballast interface as done in case of direct shear test samples.

TABLE 2 | Physical characteristics and technical characteristics of geogrid used in the current study.

Characteristics	Properties	*G1*	*G2*	*G3*	*G4*	*G5*
Physical	Material	PP	PP	PP	PP	PP
	Aperture shape	Square	Triangular	Rectangular	Triangular	Square
	Aperture size (MD/CMD)	39/39	46/46	34/36	69/69	65/65
	Rib thickness	2.2/2.1	1.2/1.2	2.8/2.8	2.2/2.2	3.6/4.5
Technical	T_{ult}[a] (kN/m)	30	19	40	21	30
	Tensile strength@ 5% strain (kN/m)	21	14	28	15	22

[a] *Ultimate Tensile Strength (manufacturer supplied values).*

MD, machine direction; CMD, cross machine direction; PP, polypropylene.

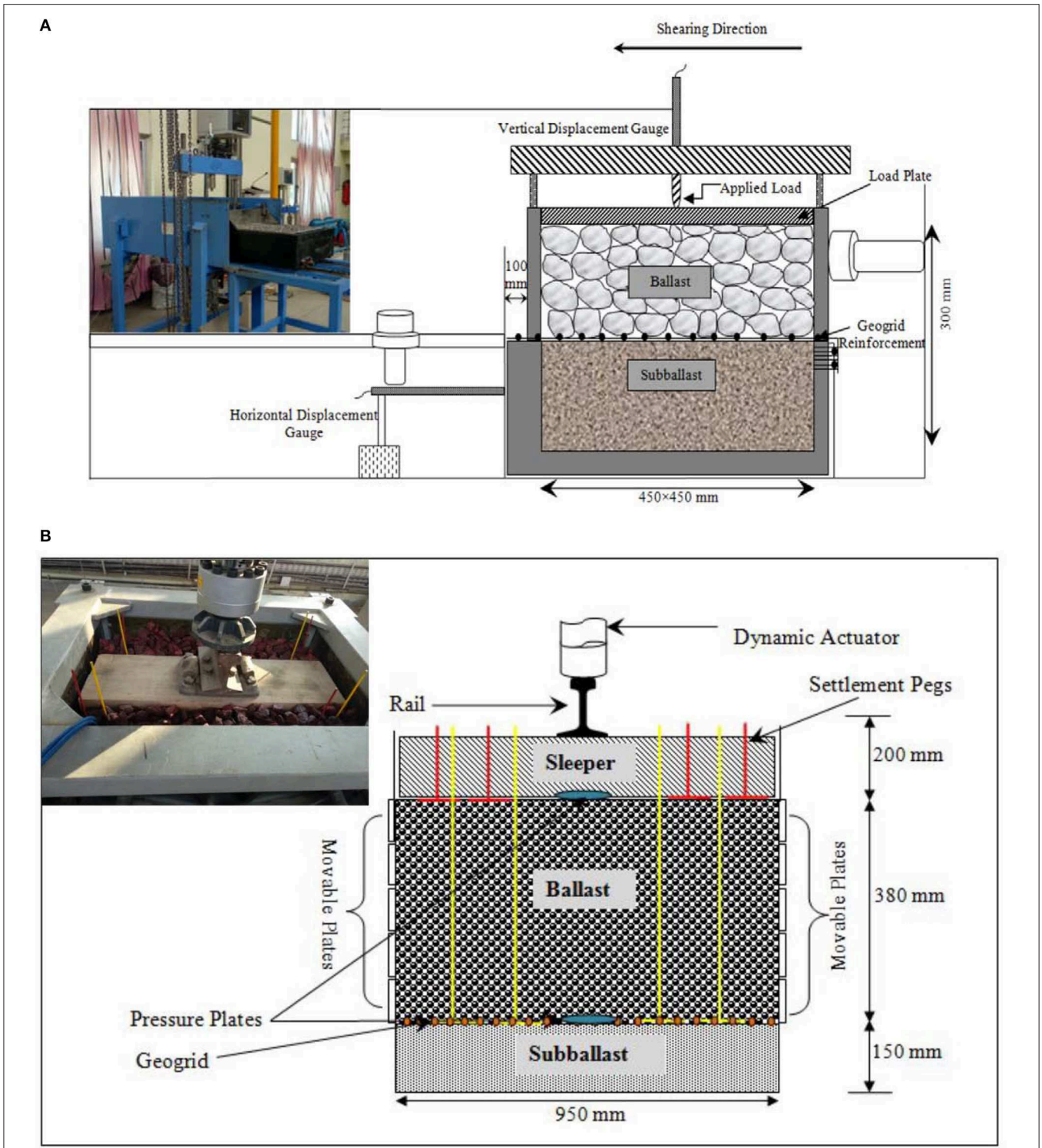

FIGURE 2 | Schematic illustrations of **(A)** direct shear apparatus and **(B)** process simulation test (PST) apparatus.

A cyclic vertical stress of 300 kPa was applied onto the test specimen with the help of vertical dynamic actuator, and a confining pressure of 10 kPa was applied onto the two side walls having five movable plates. It is well-known that the tendency of unbound ballast is to move laterally in outward direction (parallel to sleeper) under track operating conditions. Therefore,

the shorter walls were allowed to move laterally and the other two longitudinal walls were kept fixed to mimic the plane strain conditions ($\varepsilon_2 = 0$) in the direction parallel to rails (i.e., along the direction of passage of train), as was also adapted earlier by Hussaini (2013) and Indraratna et al. (2013). Two earth pressure cells were placed at sleeper-ballast and ballast-sub-ballast interface to measure the vertical stresses during the test. The pressure cells used in the current study had the diameter of 230 mm and the thickness of 12 mm.

Tests were conducted at loading frequencies of 10, 20, 30, and 40 Hz which is representative of higher train speeds (∼73–292 km/h, for an axle spacing of 2.02 m) and up to 250,000 load cycles (N). During the test, the lateral displacement of the movable plates and the vertical settlement of ballast were continuously recorded by the data acquisition system. The extent of vertical settlement was also recorded by placing four settlement plates at sleeper-ballast and ballast-sub-ballast interface. The test was halted at specific number of cycles to record the vertical settlement of ballast and sub-ballast layers. The ballast specimen was retrieved carefully and sieved after each test to evaluate the change in gradation and to quantify the breakage of particles owing to cyclic loading. **Figure 2B** shows the final arrangement of the test specimen ready for testing.

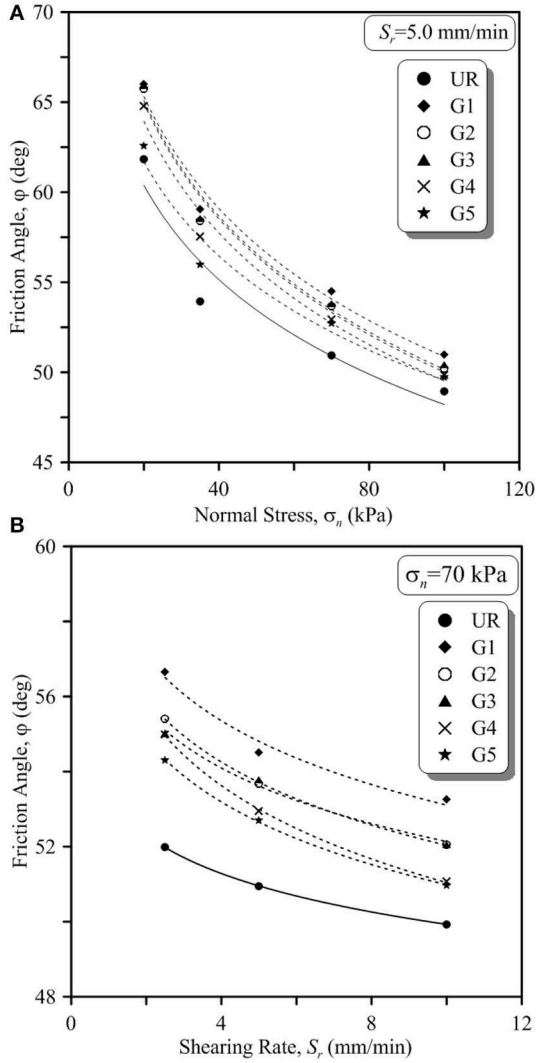

FIGURE 3 | Variation of friction angle of unreinforced and geogrid-reinforced ballast-sub-ballast with **(A)** applied normal stress at $S_r = 5.0$ mm/min and **(B)** shearing rates at $\sigma_n = 70$ kPa.

RESULTS AND DISCUSSION

Friction Angle (φ) of Ballast-Sub-Ballast Interface

Figure 3A shows the variation of friction angle (φ) with applied normal stress (σ_n) for unreinforced ballast-sub-ballast interface and that reinforced with various geogrids at $S_r = 5.0$ mm/min. It is seen that the φ of unreinforced ballast-sub-ballast interface reduces from 61.82 to 48.95° as σ_n increases from 20 to 100 kPa. The decrease in φ with the increase in σ_n is primarily due to the suppression of dilation and also because of the enhanced breakage of particles (as will be described in the latter sections of the paper) at higher normal stresses. Similar to the behavior of unreinforced interface, the apparent friction angle (δ) of ballast-sub-ballast interface when reinforced with geogrids *G1* and *G2* decreases from 66.02 to 50.97° and 65.76 to 50.22°, respectively, as σ_n increases from 20 to 100 kPa. A similar reduction in δ with the increase in σ_n is observed for other rates of shearing (S_r) but is not shown here for the sake of brevity. It is further observed that δ of all reinforced ballast-sub-ballast interfaces is greater than that of unreinforced interfaces (**Figure 3A**). For example, the insertion of geogrids *G4* and *G5* at ballast-sub-ballast interface increases the values of φ from 61.82 to 64.79° and 62.56°, respectively.

Figure 3B depicts the variation of friction angle (φ) with shearing rate (S_r) of unreinforced ballast-sub-ballast interface and that reinforced with various geogrids at $\sigma_n = 70$ kPa. The value of φ of unreinforced ballast-sub-ballast interface decreases from 51.98 to 49.93° as S_r is increased from 2.5 to 10.0 mm/min. The increasing rates of shearing have a similar effect on the friction angle of ballast-geogrid-sub-ballast interfaces. For example, the apparent friction angle (δ) of ballast-sub-ballast reinforced with geogrid *G4* and *G5* reduced from 54.98 to 51.53° and 54.3 to 51° as S_r increased from 2.5 to 10.0 mm/min. The observation with respect to the variation of φ with S_r is in accordance with the studies conducted for ballast (Sweta and Hussaini, 2018) and sub-ballast (Biabani and Indraratna, 2015). In a practical sense, the reduced values of friction angles with the increase in shearing rates indicate the reduction in ballast performance with the increase in train speeds. However, it is seen that the geogrids enhance the friction angle of ballast-sub-ballast interface for all the applied shearing rates (**Figure 3B**), thereby highlighting their effectiveness in enhancing the ballast performance at higher train speeds. For instance, φ of unreinforced ballast-sub-ballast interface increased from 51.98 to 56.66° and 55.41° when stabilized with geogrid *G1* and *G2*, respectively.

Dilation Angle (ψ) of Ballast-Sub-Ballast Interface

The dilation angle (ψ) of ballast-sub-ballast is mainly associated with the rate of dilation and is computed as the ratio of change in vertical displacement (d_v) to the change in horizontal displacement (d_h) (Equation 1; Bolton, 1986; Simoni and Houlsby, 2006) and can be expressed as

$$\psi = \frac{d(d_v)}{d(d_h)} \quad (1)$$

Where ψ is the dilation angle, $d(d_v)$ is the change in vertical displacement, $d(d_h)$ is the change in horizontal displacement.

Figure 4 shows the variation of peak dilation angle (ψ) with peak friction angle (φ) of unreinforced ballast-sub-ballast interface and that stabilized with geogrids for different values of S_r. As expected, dilation angle (ψ) of both unreinforced and reinforced ballast-sub-ballast interface decreases with increasing values of σ_n. For example, the value of ψ in case of unreinforced ballast-sub-ballast interface and that reinforced with *G1* is found to decrease from 14.56 to 8.51° and 11.03 to 4.13° as σ_n increases from 20 to 100 kPa (S_r = 2.5 mm/min). Likewise, for S_r = 5.0 and 10.0 mm/min, the value of ψ decreases from 12.89 to 7.74° & 10.38 to 3.89° and 11.89 to 5.23° & 9.16 to 4.78°, respectively. It is further revealed that dilation angle (ψ) of both unreinforced and reinforced interface decreases with the increase in S_r. The value of ψ of unreinforced ballast-sub-ballast and that reinforced with *G1* decreases from 14.56 to 11.89° and 10.38 to 9.16° as S_r increases from 2.5 to 10.0 mm/min (σ_n = 20 kPa). Likewise, for other normal stresses of 35, 70, and 100 kPa, ψ decreases from 12.78 to 8.95° & 9.24 to 8.00°, 9.73 to 7.42 & 6.78 to 6.34°, and 8.51 to 5.23° & 4.13 to 3.35°, respectively. **Figure 5** also establishes the role of geogrids in diminishing the extent of dilation. For instance, reinforcement of ballast-sub-ballast interface with geogrid *G1* reduces the dilation angle (ψ) from 14.56 to 11.03° (σ_n = 20 kPa; S_r = 2.5 mm/min).

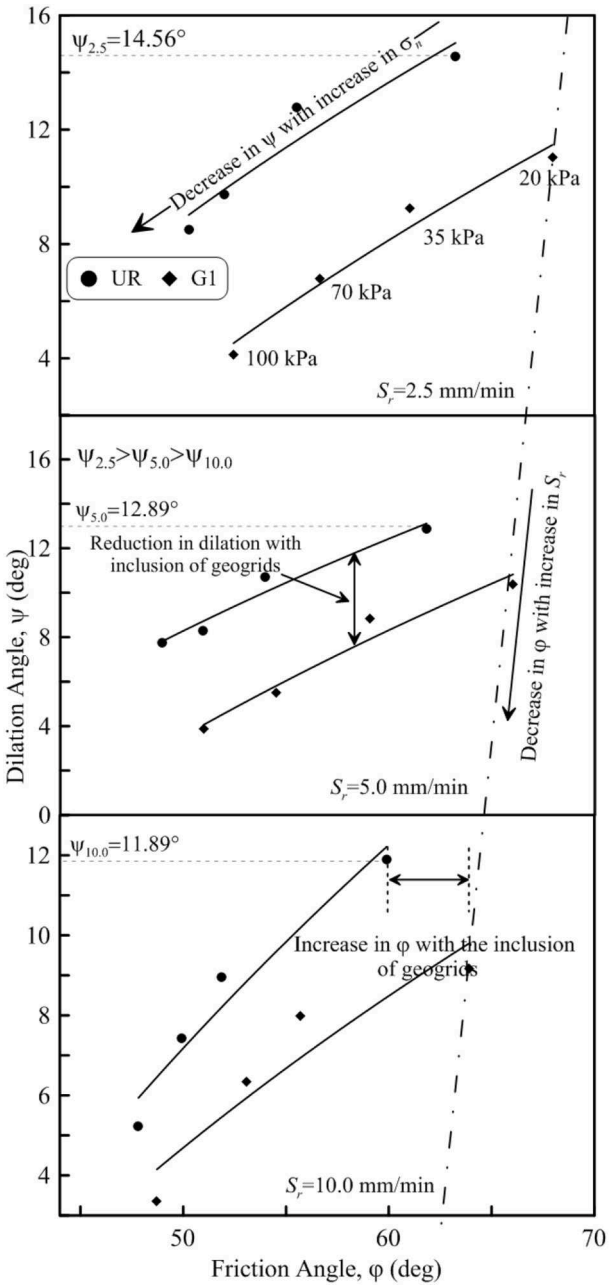

FIGURE 4 | Variation of dilation angle (ψ) with peak friction angle (φ) of unreinforced and geogrid-reinforced ballast-sub-ballast interface.

Breakage of Ballast (B_g) Under Shearing Conditions

The influence of applied normal stress (σ_n) and shearing rate (S_r) on the breakage of ballast for both unreinforced and reinforced ballast-sub-ballast interface is shown in **Figure 5**. It is revealed that B_g increases with the increase in σ_n and S_r. For example, B_g of unreinforced ballast increased from 3.33 to 5.26% as σ_n increased from 20 to 100 kPa. Furthermore, the value of B_g of unreinforced ballast increased from 3.41 to 5.72% as S_r enhanced from 2.5 to 10.0 mm/min (σ_n = 35 kPa; **Figure 5A**). A similar increase in B_g is observed for geogrid-reinforced ballast-sub-ballast interface. For instance, the ballast-sub-ballast interface when reinforced with geogrid *G1* and *G2*, the value of B_g increases from 2.49 to 3.49% and 2.56 to 3.56% as σ_n increases from 20 to 100 kPa. Furthermore, for the applied normal stress of 35 kPa, the value of B_g of ballast-sub-ballast interface reinforced with geogrid *G1* increases from 2.43 to 3.84% as S_r increases from 2.5 to 10.0 mm/min. It is evident from **Figure 5B** that insertion of geogrids at ballast-sub-ballast interface diminishes the extent of B_g in ballast. For example, in case of ballast reinforced with geogrid *G4* and *G5*, the value of B_g reduced from 3.85 to 3.10% and 3.31%, respectively (σ_n = 35 kPa; S_r = 5.0 mm/min).

Regression Models to Determine of Friction (φ), Dilation Angles (ψ), and Breakage (B_g) of Ballast

To emphasize the role of geogrid aperture size (A) in enhancing the shear strength of ballast, the variation of interface efficiency factor (α) and ballast breakage (B_g) with A/D_{50} ratio for different

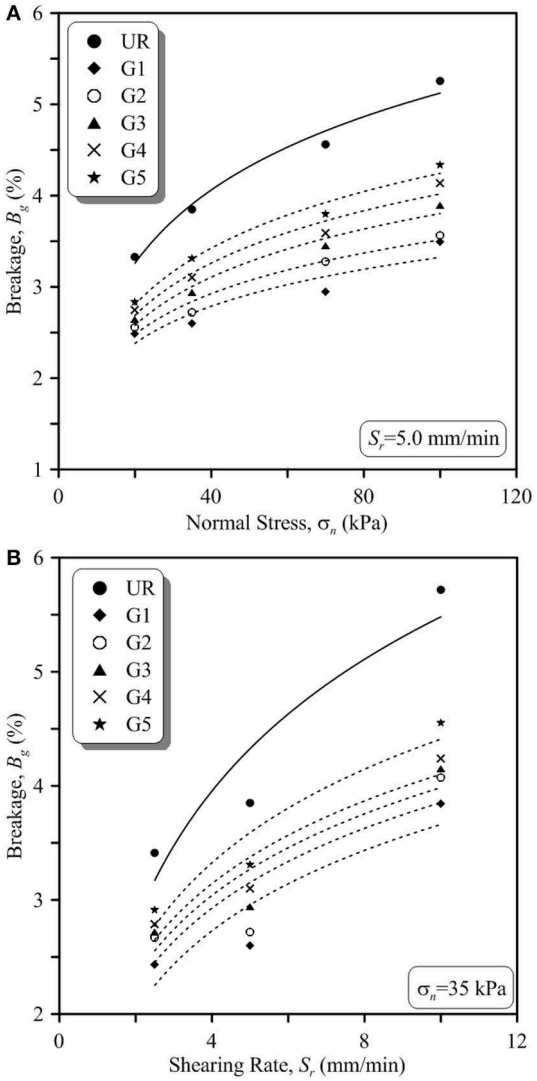

FIGURE 5 | Variation of breakage of unreinforced and geogrid-reinforced ballast with **(A)** applied normal stress at $S_r = 5.0$ mm/min and **(B)** shearing rates at $\sigma_n = 35$ kPa.

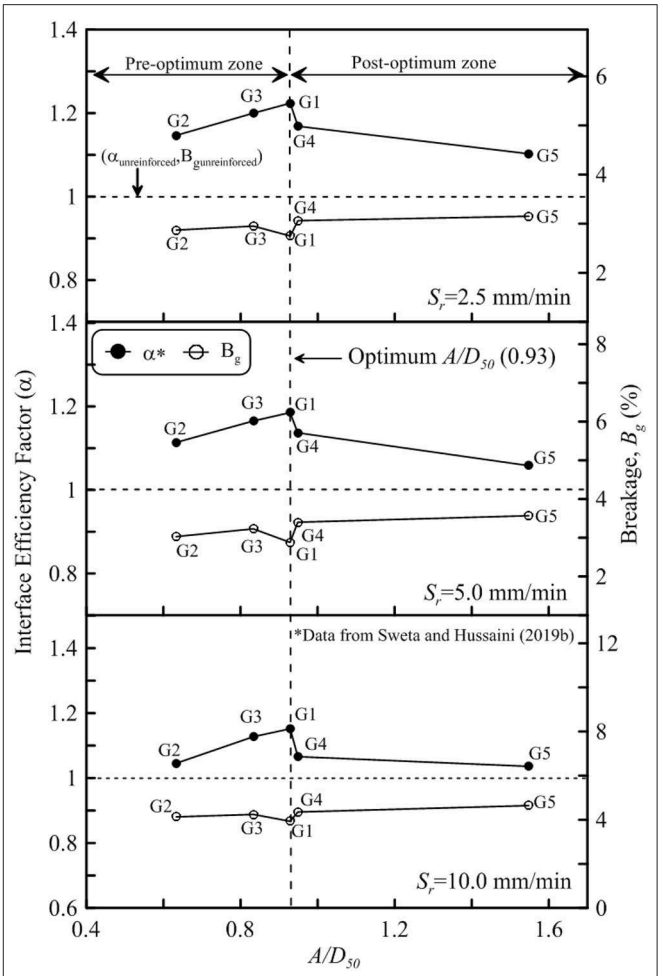

FIGURE 6 | Variation of interface efficiency factor (α) and breakage (B_g) with A/D_{50}.

rates of shearing (S_r) are shown in **Figure 6**. It is revealed from **Figure 6** that as the value of α increases, the extent of B_g decreases. For instance, α attains the maximum value of 1.22 and B_g attains the minimum value of 2.75% at $A/D_{50} = 0.93$ (*G1*) and then α decreases to 1.10 and B_g increases to 3.15% at $A/D_{50} = 1.54$ (*G5*) (S_r: 2.5 mm/min). Similarly, for $S_r = 5.0$ and 10.0 mm/min, geogrid *G1* with an A/D_{50} of 0.93 exhibits the maximum value of α of 1.19 and 1.15 which in turn exhibits the minimum breakage of 2.88 and 3.93%, respectively. This signifies that by suitably selecting the geogrids, the value of α could be enhanced significantly and breakage of ballast particles could be minimized.

It is well-known that the behavior of ballast under track operating conditions is governed by axle load, confining pressure and the train speed. In a real rail track environment, axle load is transferred through the wheels of the trains while the confining pressure is generated due to particle-particle interaction, sleeper resistance, compaction stresses and overburden pressure. Moreover, a track under operating conditions will be often subjected to varying train speeds. Therefore, the field conditions are replicated in the laboratory, by suitably considering the values of applied normal stress and the rate of shearing (Sweta and Hussaini, 2019a). Moreover, the performance of a reinforced railway track depends upon the ratio of aperture size (A) of geogrids and the mean particle sizes, A/D_{50} ratio (Indraratna et al., 2012; Sweta and Hussaini, 2018, 2019a,b). In this context, regression models are developed to determine the values of friction angle (φ), dilation angle (ψ) and breakage of ballast (B_g) in terms of the input parameters σ_n, S_r, and A/D_{50} (Equations 2–7). Based on the variation of α, the A/D_{50} is classified into two zones (i.e., pre-optimum and post-optimum zone) as shown in **Figure 6**. The pre-optimum zone lies in the range of $0.63 \leq A/D_{50} \leq 0.93$ while the post-optimum zone lies in the range of $0.93 \leq A/D_{50} \leq 1.54$. The R^2 values for the models presented here vary from 0.88 to 0.90.

For $0.63 \leq A/D_{50} \leq 0.93$:

$$\varphi = -0.17\sigma_n - 0.55S_r + 4.41A/D_{50} + 66.19 \quad (2)$$

$$\psi = -0.07\sigma_n - 0.19S_r - 0.82A/D_{50} + 13.33 \quad (3)$$

$$B_g = 0.01\sigma_n + 0.17S_r - 0.36A/D_{50} + 1.96 \quad (4)$$

For $0.93 \leq A/D_{50} \leq 1.54$

$$\varphi = -0.15\sigma_n - 0.52S_r - 0.26A/D_{50} + 68.36 \quad (5)$$

$$\psi = 0.06\sigma_n - 0.26S_r + 0.19A/D_{50} + 13.10 \quad (6)$$

$$B_g = 0.01\sigma_n + 0.18S_r + 0.67A/D_{50} + 0.97 \quad (7)$$

Where φ = friction angle, ψ = dilation angle, B_g = breakage, σ_n = applied normal stress, S_r = rate of shearing.

The models presented here will help the rail practitioners to predict the values of φ, ψ, and B_g for ballast under both unreinforced and reinforced conditions once the values of input parameters (σ_n, S_r, and A/D_{50}) are known.

Lateral Displacement (l_d) and Vertical Settlement (S_v) of Ballast During Cyclic Loading

The evolution of lateral displacement (l_d) and vertical settlement (S_v) with number of load cycles (N) in case of unreinforced and geogrid-reinforced ballast at $f = 30$ Hz is shown in **Figure 7**. It is observed that the extent of l_d and S_v increases rapidly during the initial load applications (i.e., for values of N up to 50,000 cycles), and thereafter the displacements remain mostly the same. However, the extent of l_d and S_v of ballast reduces with the inclusion of geogrids. For example, insertion of geogrids *G1* and *G3* reduces the amount of l_d and S_v by 41 & 30% and 33 & 24%, respectively, in comparison to unreinforced ballast. On the other hand, the geogrid *G5* reduces the values of l_d and S_v by 8% only. This is because the aperture sizes of geogrids *G1* and *G3* are nearer to the average particle size of ballast (D_{50}: 42 mm) that ensures effective interlocking of particles thus reducing both l_d and S_v. On the other hand, geogrid *G5* having larger apertures facilitates the free movement of particles within the aperture of the geogrids. The almost constant values of l_d and S_v for $N >$ 50,000 in case of reinforced samples (**Figure 7**) indicate that the effectiveness of ballast-geogrid interlock remains unaffected upon repeated load applications. In a practical sense, this implies that once the required ballast-geogrid interlock is accomplished, the geogrid continues to perform its intended purpose of arresting the lateral displacement and thus reducing the vertical settlement of ballast even at 250,000 load cycles. However, the results indicated that the extent of l_d and S_v increases with the increase in loading frequency but the same are not shown here for the sake of brevity.

Role of Geogrid Aperture Size on the Deformation of Ballast

To highlight the role of geogrid aperture size, the variation of final lateral displacement (l_d) and vertical settlement (S_v) is plotted against A/D_{50}, the ratio of geogrid aperture size to the average particle size of ballast (**Figure 8**). **Figure 8A** shows the variation

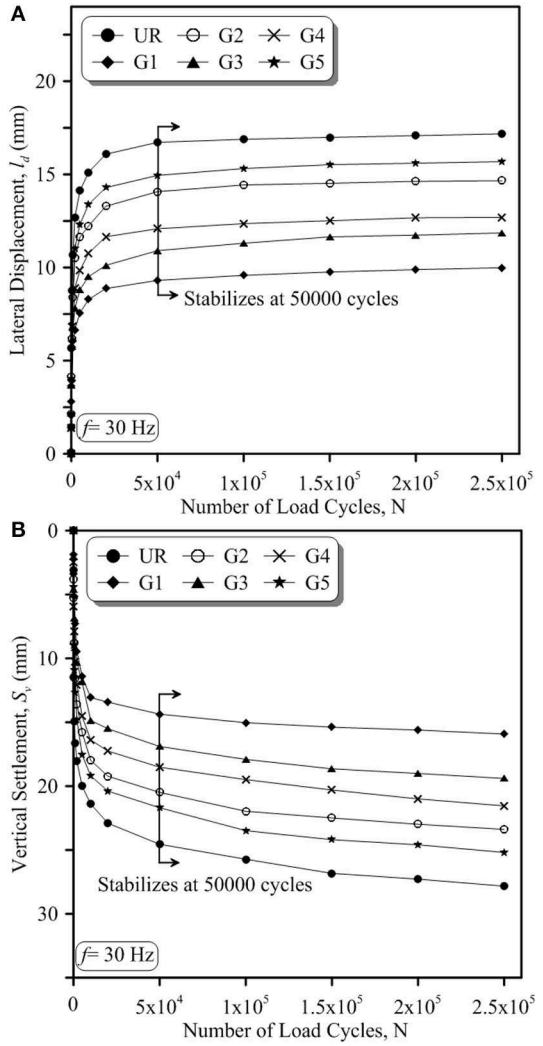

FIGURE 7 | Variation of **(A)** vertical settlement (S_v) and **(B)** lateral displacement (l_d) of unreinforced and geogrid-reinforced ballast with load cycles (N).

of l_d of ballast along the depth of ballast layer as measured at levels of five movable plates with A/D_{50} for $f = 30$ Hz. It is revealed that the placement of geogrids at the ballast-sub-ballast interface has shown negligible effect in arresting the lateral displacements at the level of top three plates. However, inclusion of geogrids shows a remarkable effect in reducing the lateral displacements of the bottom two plates. These observations establish beyond doubt the diminishing role of geogrid in arresting particle movements away from its placement position. The role of A/D_{50} is thus evident in the near vicinity of geogrid placement position (i.e., for the bottom two plates). In case of the bottom most plate, the value of l_d decreases from 14.65 to 9.99 mm as A/D_{50} increases from 0.63 to 0.93 which again increases to 15.68 mm at A/D_{50} of 1.54. An increase in lateral displacement at A/D_{50} of 1.54 subsequent to the minimum lateral displacement at A/D_{50} of 0.93 is mainly due to free movement of the particles within the aperture of geogrids.

Figures 8B,C depicts the variation of lateral displacement (l_d) and vertical settlement (S_v) of ballast with A/D_{50} for various

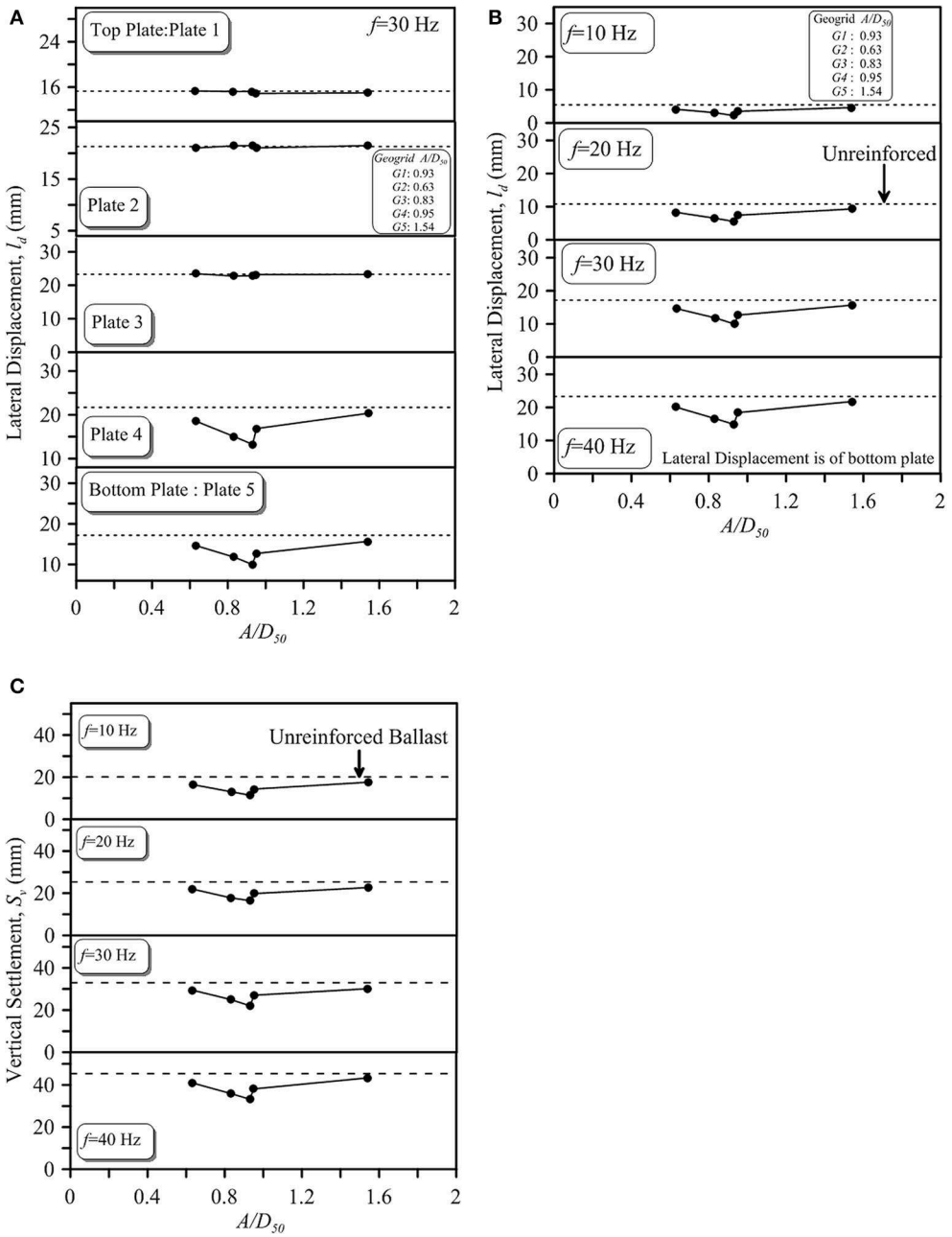

FIGURE 8 | Variation of **(A)** lateral displacement (l_d) of geogrid-reinforced ballast with A/D_{50} at $f = 30$ Hz, **(B)** lateral displacement (l_d) with A/D_{50} at different frequencies, and **(C)** vertical settlement with A/D_{50} at different frequencies.

loading frequencies. It is observed from **Figure 8B** that the value of l_d decreases from 4.14 to 2.25 mm as A/D_{50} increases from 0.63 to 0.93 which then increases to 4.64 mm at A/D_{50} of 1.54 ($f = 10$ Hz). Similarly, the value of S_v decreases from 16.50 to 11.41 mm as A/D_{50} increases from 0.63 to 0.93 and then increases to 17.59 mm at A/D_{50} of 1.54 ($f = 10$ Hz; **Figure 8C**). It is further seen that the variation of l_d and S_v with A/D_{50} remain similar with the increase in loading frequencies albeit with reduced efficiency of geogrids (**Figures 8B,C**). The variation of l_d and S_v with A/D_{50} observed here follows a similar trend as that of variation of interface efficiency factor with A/D_{50} obtained in case of ballast-sub-ballast interface by Sweta and Hussaini (2019b) under direct shear conditions.

Ballast Breakage Under Cyclic Loading Conditions

To highlight the effect of geogrids in reducing the extent of particle breakage, the initial and final *PSDs* of unreinforced ballast and that reinforced with geogrids *G1* and *G5* at $f = 30$ Hz are compared (**Figure 9A**). The final *PSD* of the unreinforced

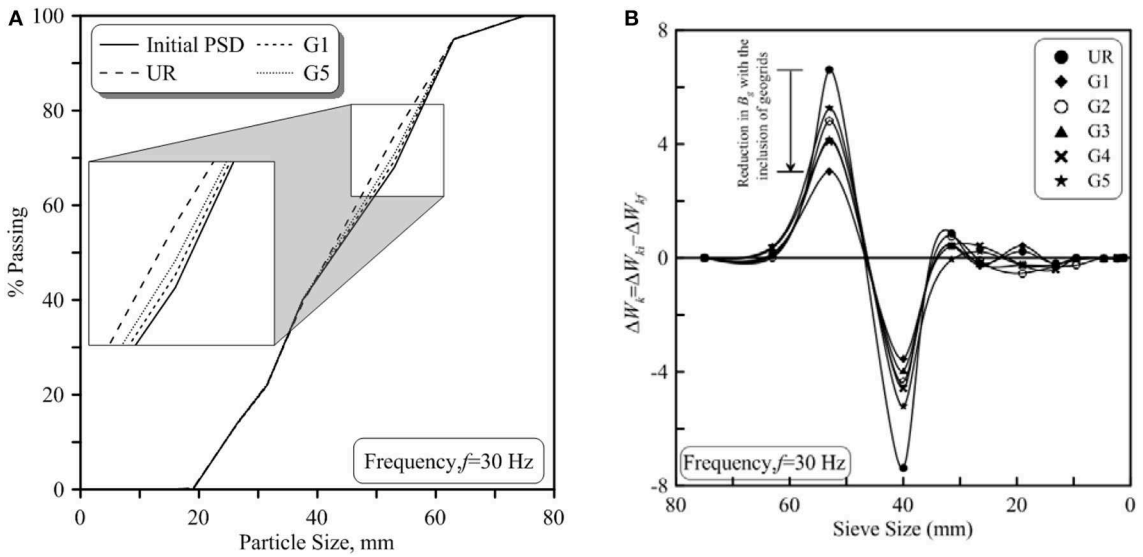

FIGURE 9 | (A) Change in PSD of ballast during cycling loading and **(B)** variation of particle distribution with sieve size for unreinforced and geogrid-reinforced ballast.

ballast lie far away from its initial *PSD* followed by the final *PSD* when reinforced with *G5* and *G1*. Although this highlights the role of geogrids in reducing the overall ballast breakage, but its effect on specific particle sizes is seen clearly from **Figure 9B** that shows the variation of difference in percentage retained before and after the test (ΔW_k) at $f = 30$ Hz. It is evident that bigger particles (>40 mm), due to the presence of natural flaws in them and their tendency to take up higher proportions of applied load, are more susceptible to breakage in comparison to the smaller particles. Further, the effect of various geogrids (*G1* to *G5*) in reducing the extent of breakage in bigger particles is also clearly evident from **Figure 9B**, thus justifying their use for stabilizing the rail tracks.

CONCLUSIONS

The current study investigated the shear behavior of geogrid-reinforced ballast-sub-ballast interface and also the deformation and degradation behavior of geogrid-reinforced ballast under cyclic loading conditions. It was revealed that friction (φ) and dilation angles (ψ) of unreinforced ballast-sub-ballast interface reduces from 63.24 to 47.82° and 14.56 to 5.23° with the increase in σ_n and S_r, respectively. The breakage of ballast (B_g) occurred during shearing was quantified in terms of Marsal's Breakage (B_g). The B_g of unreinforced ballast increases from 2.84 to 6.69% with the increase of σ_n & S_r. The tests results further revealed that inclusion of geogrids enhanced the shear strength of ballast-sub-ballast interface. For example, φ of unreinforced ballast-sub-ballast interface increased from 61.82 to 66.02° and ψ decreased from 12.89 to 10.38° when the ballast-sub-ballast interface was reinforced with geogrid *G1* ($\sigma_n = 20$ kPa; $S_r = 5.0$ mm/min). Moreover, the extent of B_g in case of direct shear test decreases from 3.33 to 2.49 and 2.56% when stabilized with geogrid *G1* and *G2*, respectively ($\sigma_n = 20$ kPa $S_r = 5.0$ mm/min). The interface efficiency factor (α) and B_g were found to be function of A/D_{50} ratio. For the set of geogrids tested in the current study, geogrid *G1* with an optimum A/D_{50} of 0.93 exhibits the maximum value of α and minimum value of B_g. Moreover, regression model is developed using multiple linear regression analysis to predict the values of φ, ψ, and B_g in terms of the input parameters σ_n, S_r, and A/D_{50} ratio.

The results from the cubical triaxial tests revealed that the deformation and degradation behavior of ballast under cyclic loading conditions was highly influenced by the loading frequency (f). It is shown that the extent of lateral displacement (l_d) and vertical settlement (S_v) increases rapidly during the initial number of load cycles and thereafter it remains constant. The extent of l_d and S_v of unreinforced ballast increases from 5.48 to 28.32 mm and 20.13 to 45.40 mm with the increase in f from 10 to 40 Hz. The value of B_g increased from 4.3 to 11.69% when the value of f was increased from 10 to 40 Hz. It is further revealed that the inclusion of geogrids reduced the extent of l_d and S_v of ballast and minimized the extent the particle breakage during cyclic loading. For instance, insertion of geogrid *G1* reduces the extent of l_d and S_v by 42 and 33%, respectively. The current study showed the benefits of geogrids in enhancing the shear strength and also in reducing the deformation and degradation of ballast particles.

DATA AVAILABILITY STATEMENT

All datasets generated for this study are included in the article/supplementary material.

AUTHOR CONTRIBUTIONS

SH and KS have contributed in the preparation of this manuscript.

REFERENCES

Afzali-Nejad, A., Lashkari, A., and Shourijeh, P. T. (2017). Influence of particle shape on the shear strength and dilation of sand-woven geotextile interfaces. *Geotext. Geomembr.* 45, 54–66. doi: 10.1016/j.geotexmem.2016.07.005

Anubhav and Basudhar, P. K. (2010). Modeling of soil-woven geotextile interface behavior from direct shear test results. *Geotext. Geomembr.* 28, 403–408. doi: 10.1016/j.geotexmem.2009.12.005

Anubhav and Basudhar, P. K. (2013). Interface behavior of woven geotextile with rounded and angular particle sand. *J. Mater. Civ. Eng.* 25, 1970–1974. doi: 10.1061/(ASCE)MT.1943-5533.0000774

Atalar, C., Das, B. M., Shin, E. C., and Kim, D. H. (2001). "Settlement of geogrid-reinforced railroad bed due to cyclic load," in *Proceedings of 15th International Conference on Soil Mechanics and Geotechnical Engineering* (Istanbul), 2045–2048.

Bathurst, R. J., and Raymond, G. P. (1987). Geogrid reinforcement of ballasted track. *Transport. Res. Rec.* 1153, 8–14.

Biabani, M. M., and Indraratna, B. (2015). An evaluation of the interface behavior of rail sub-ballast stabilized with geogrids and geomembranes. *Geotext. Geomembr.* 43, 240–249. doi: 10.1016/j.geotexmem.2015.04.002

Biabani, M. M., Indraratna, B., and Ngo, N. T. (2016). Modelling of geocell-reinforced sub-ballast subjected to cyclic loading. *Geotext. Geomembr.* 44, 489–503. doi: 10.1016/j.geotexmem.2016.02.001

Bolton, M. D. (1986). The strength and dilatancy of sands. *Geotechnique* 36, 65–78. doi: 10.1680/geot.1986.36.1.65

Brown, S. F., Kwan, J., and Thom, N. H. (2007). Identifying the key parameters that influence geogrid reinforcement of railway ballast. *Geotext.Geomembr.* 25, 326–335. doi: 10.1016/j.geotexmem.2007.06.003

Chen, X., Jia, Y., and Zhang, J. (2018). Stress-strain response and dilation of geogrid reinforced coarse grained soils in large scale direct shear tests. *Geotech. Test. J.* 41, 1–10. doi: 10.1520/GTJ20160089

Choudhary, A. K., and Krishna, A. M. (2016). Experimental investigation of interface behaviour of different types of granular soil/geosynthetics. *Int. J. Geosynth. Ground Eng.* 2, 1–11. doi: 10.1007/s40891-016-0044-8

Guler, E., and Khosrowshahi, S. K. (2017). Evaluation of geosynthetic reinforcement on railroad subgrade. *Proc. Eng.* 189, 721–728. doi: 10.1016/j.proeng.2017.05.114

Hussaini, S. K. K. (2013). *An experimental study on the deformation Behavior of geosynthetically reinforced ballast* (Ph.D. thesis). Wollongong: University of Wollongong, Australia.

Hussaini, S. K. K., Indraratna, B., and Vinod, J. S. (2012). "Performance of geosynthetically reinforced rail ballast in direct shear conditions," in *11th Australia New Zealand Conference on Geomechanics: Ground Engineering in a Changing World*, eds G.A. Narsilo, A. Arulrajah, and J. Kodikara (Melbourne, VIC: Engineers Australia), 1268–1273.

Hussaini, S. K. K., Indraratna, B., and Vinod, J. S. (2015a). Application of optical fiber bragg grating sensors in monitoring the rail track deformations. *Geotech. Test J.* 38, 387–396. doi: 10.1520/GTJ20140123

Hussaini, S. K. K., Indraratna, B., and Vinod, J. S. (2015b). Performance assessment of geogrid reinforced rail road ballast during cyclic loading. *Transport. Geotech.* 2, 99–107. doi: 10.1016/j.trgeo.2014.11.002

Hussaini, S. K. K., Indraratna, B., and Vinod, J. S. (2016). A laboratory investigation to assess the functioning of railway ballast with and without geogrids. *Transport. Geotech.* 6, 45–54. doi: 10.1016/j.trgeo.2016.02.001

Indraratna, B., Biabani, M. M., and Nimbalkar, S. (2015). Behavior of geocell-reinforced sub-ballast subjected to cyclic loading in plane-strain condition. *J. Geotech. Geoenviron. Eng.* 141:04014081. doi: 10.1061/(ASCE)GT.1943-5606.0001199

Indraratna, B., Hussaini, S. K. K., and Vinod, J. S. (2012). On the shear behavior of ballast-geosynthetic interfaces. *Geotech. Test. J.* 35, 305–312. doi: 10.1520/GTJ103317

Indraratna, B., Hussaini, S. K. K., and Vinod, J. S. (2013). The lateral displacement response of geogrid-reinforced ballast under cyclic loading. *Geotext. Geomembr.* 39, 20–29. doi: 10.1016/j.geotexmem.2013.07.007

Indraratna, B., Shanin, M. A., and Salim, W. (2007). Stabilisation of granular media and formation soil using geosynthetics with special reference to railway engineering. *Proc. Inst. Civ. Eng. Ground Improv.* 11, 27–43. doi: 10.1680/grim.2007.11.1.27

Indraratna, B., Thakur, P. K., and Vinod, J. S. (2010). Experimental and numerical study of railway ballast behavior under cyclic loading. *Int. J. Geomech.* 10, 136–144. doi: 10.1061/(ASCE)GM.1943-5622.0000055

IRSGE (2004). *Specifications for Track Ballast.* Research Design and Standard Organisation (RDSO), Ministry of Railways, India.

Jeffs, T., and Tew, G. P. (1991). *A Review of Track Design Procedures: Sleepers and Ballast*, Vol. 2. Melbourne, VIC: Railways of Australia.

Lee, K. M., and Manjunath, V. R. (2000). Soil-geotextile interface friction by direct shear tests. *Can. Geotech. J.* 37, 238–252. doi: 10.1139/t99-124

Liu, C. N., Ho, Y. H., and Huang, J. W. (2009). Large-scale direct shear tests of soil/PET yarn geogrid interfaces. *Geotext. Geomembr.* 27, 19–30. doi: 10.1016/j.geotexmem.2008.03.002

Liu, F.-Y., Wang, P., Geng, X., Wang, J., and Lin, X. (2016). Cyclic and post-cyclic behavior from sand-geogrid interface large-scale direct shear tests. *Geosynth. Int.* 23, 129–139. doi: 10.1680/jgein.15.00037

Liu, H., and Martinez, J. (2015). Creep behavior of sand-geomembrane interfaces. *Geosynth. Int.* 21, 83–88. doi: 10.1680/gein.13.00036

Liu, S., Huang, H., Qiu, T., and Kwon, J. (2016). Effect of geogrid on railroad ballast particle movement. *Transport. Geotech.* 9, 110–122. doi: 10.1016/j.trgeo.2016.08.003

Makkar, F. M., Chandrakaran, S., and Sankar, S. (2017). Performance of 3-D geogrid reinforced sand under direct shear mode. *Int. J. Geotech. Eng.* 13, 227–235. doi: 10.1080/19386362.2017.1336297

Matharu, M. S. (1994). Geogrid cut ballast settlement rate on soft substructures. *Railway Gazette Int.* 150, 165–166.

Mirzaalimohammadi, A., Ghazavi, M., Roustaei, M., and Lajewardi, S. H. (2019). Pullout response of strengthened geosynthetic interacting with fine sand. *Geotext. Geomembr.* 47, 530–541. doi: 10.1016/j.geotexmem.2019.02.006

Mishra, D., Qian, Y., Kazmee, H., and Tutumluer, E. (2014). Investigation of geogrid-reinforced railroad ballast behavior using large-scale triaxial testing and discrete element modeling. *Transport. Res. Board.* 2462, 98–108. doi: 10.3141/2462-12

Moraci, N., Cardile, G., Gioffrè, D., Mandaglio, M. C., Calvarano, S. M., and Carbone, L. (2014). Soil geosynthetic interaction: design parameters from experimental and theoretical analysis. *Transport. Infrastr. Geotech.* 1, 165–227. doi: 10.1007/s40515-014-0007-2

Mvelase, M. G., Grabe, P. J., and Anochie-Boateng, J. K. (2017). The use of laser technology to investigate the effect of railway ballast roundness on shear strength. *Transport. Geotech.* 11, 97–106. doi: 10.1016/j.trgeo.2017.05.003

Navaratnarajah, S. K., and Indraratna, B. (2017). Use of rubber mats to improve the deformation and degradation behavior of rail ballast under cyclic loading. *J. Geotech. Geoenviron. Eng.* 143:04017015 doi: 10.1061/(ASCE)GT.1943-5606.0001669

Nimbalkar, S., and Indraratna, B. (2016). Improved performance of ballasted rail track using geosynthetics and rubber shock mats. *J. Geootech. Geoenviron. Eng.* 142:04016031. doi: 10.1061/(ASCE)GT.1943-5606.0001491

Palmeira, E. M. (2009). Soil-geosynthetic interaction: modeling and analysis. *Geotext. Geomembr.* 27, 368–390. doi: 10.1016/j.geotexmem.2009.03.003

RDSOGE (2007). *Guidelines for Blanket Layer Provision on Track Formation.* Research Design and Standard Organisation (RDSO), Ministry of Railways, India.

Sayeed, M. M. A., Ramaiah, B. J., and Rawal, A. (2014). Interface shear characteristics of jute/polypropylene hybrid nonwoven geotextiles and sand using large size direct shear test. *Geotext. Geomembr.* 42, 63–68. doi: 10.1016/j.geotexmem.2013.12.001

Shin, E. C., Kim, D. H., and Das, B. M. (2002). Geogrid-reinforced railroad bed settlement due to cyclic load. *Geotech. Geol. Eng.* 20, 261–271. doi: 10.1023/A:1016040414725

Simoni, A., and Houlsby, G. T. (2006). The direct shear strength and dilatancy of sand-gravel mixtures. *Geotech. Geol. Eng.* 24, 523–549. doi: 10.1007/s10706-004-5832-6

Sun, Q., Indraratna, B., and Ngo, N. T. (2019). Effect of increase in load and frequency on the resilience of railway ballast. *Geotechnique* 69, 833–840. doi: 10.1680/jgeot.17.P.302

Sun, Q., Indraratna, B., and Nimbalkar, S. (2014). Effect of cyclic loading frequency on the permanent deformation and degradation

of railway ballast. *Geotechnique* 64, 746–751. doi: 10.1680/geot.14.T.015

Sweta, K., and Hussaini, S. K. K. (2018). Effect of shearing rate on the behavior of geogrid-reinforced railroad ballast under direct shear conditions. *Geotext. Geomembr*. 46, 251–256. doi: 10.1016/j.geotexmem.2017.12.001

Sweta, K., and Hussaini, S. K. K. (2019a). Performance of geogrid-reinforced railroad ballast in direct shear mode. *Proc. Inst. Civ. Eng. Ground Improv*. 172, 244–256 doi: 10.1680/jgrim.18.00107

Sweta, K., and Hussaini, S. K. K. (2019b). Behavior evaluation of geogrid-reinforced ballast-sub-ballast under shear conditions. *Geotext. Geomembr*. 47, 23–31. doi: 10.1016/j.geotexmem.2018.09.002

Thakur, P. K., Vinod, J. S., and Indraratna, B. (2013). Effect of confining pressure and frequency on the deformation of ballast. *Geotechnique* 63, 786–790. doi: 10.1680/geot.12.T.001

Vieira, C. S., Lopes, M. L., and Caldeira, L. M. (2015). Sand-geotextile interface characterization through monotonic and cyclic direct shear tests. *Geosynth. Int*. 20, 26–38. doi: 10.1680/gein.12.00037

Conflict of Interest: The authors declare that the research was conducted in the absence of any commercial or financial relationships that could be construed as a potential conflict of interest.

NOMENCLATURE

A	Aperture Size
B_g	Marsal's Breakage Index
C_c	Coefficient of Curvature
C_u	Coefficient of Uniformity
D_{max}	Maximum particle size
D_{50}	Average particle size
f	Loading frequency
I_d	Lateral displacement
ε_3	Lateral strain
α	Interface efficiency factor
ϕ	Friction angle
δ	Apparent friction angle for ballast geogrid interface
ψ	Dilation angle
γ_b	Density of ballast
γ_{sb}	Density of sub–ballast
σ_n	Applied normal stress
N	Number of load cycles
PSD	Particle size distribution
S_r	Shearing rate
S_v	Vertical settlement
T_{ult}	Ultimate tensile strength
τ_n	Shear stress
W_k	Percentage weight retained

frontiers in Built Environment

ORIGINAL RESEARCH
published: 16 June 2020
doi: 10.3389/fbuil.2020.00071

Design and Sustainability Aspects of Geogrid-Reinforced Flexible Pavements—An Indian Perspective

G. Narendra Goud[1,2], *S. Sasanka Mouli*[3], *Balunaini Umashankar*[1]*, *Saride Sireesh*[1] and *R. Madhav Madhira*[1]

[1] Department of Civil Engineering, IIT Hyderabad, Medak, India, [2] Department of Civil Engineering, MVSREC, Hyderabad, India, [3] Department of Civil Engineering, VNR VJIET, Hyderabad, India

Design of flexible pavements is not straightforward when reinforcement materials such as geogrid, geocell, and other types of geosynthetic materials are used in pavement construction. Presently in India, elasticity theory is used to analyze strains due to wheel load applied on a multi-layered soil system through a pavement analysis program, IITPAVE, to design the unreinforced pavement section as per Indian Roads Congress guidelines (IRC-37, 2018). The improvement in the performance of geogrid-reinforced pavement with respect to unreinforced pavement can be quantified in terms of Layer Coefficient Ratio (LCR) or Traffic Benefit Ratio (TBR). In the present study, both LCR- and TBR-based approaches are proposed to design geogrid-reinforced base courses of pavements with specific goals. These specified goals included designs based on (a) reduction in consumption of aggregates and (b) reduction in the overall cost of construction of pavement reinforced with geogrids. Design charts are provided based on LCR and TBR values corresponding to selected traffic and California Bearing Ratio (CBR) of subgrades. The benefits of reinforcement in the pavement structure are found to be high when used over weak subgrades (CBR<5%). For example, a reduction in thickness of aggregate layer is found to be in the range of 28–45%. Additionally, the sustainability of geogrid-reinforced pavement is quantified by comparing the embodied carbon (EC) generated from construction of geogrid-reinforced and unreinforced pavements. EC of reinforced pavements is found to have reduced by as much as 58–85 tCO_2 e/km in comparison with unreinforced pavement.

Keywords: geogrid-reinforced pavement, pavement design, base reinforcement, layer coefficient ratio (LCR), traffic benefit ratio (TBR), embodied carbon, sustainability

OPEN ACCESS

Edited by:
Castorina Silva Vieira, University of Porto, Portugal

Reviewed by:
Amarnath M. Hegde, Indian Institute of Technology Patna, India
Sujit Kumar Dash, Indian Institute of Technology Kharagpur, India

***Correspondence:**
Balunaini Umashankar
buma@ce.iith.ac.in

Specialty section:
This article was submitted to Transportation and Transit Systems, a section of the journal Frontiers in Built Environment

Received: *29 October 2019*
Accepted: *27 April 2020*
Published: *16 June 2020*

Citation:
Goud GN, Mouli SS, Umashankar B, Sireesh S and Madhira RM (2020) Design and Sustainability Aspects of Geogrid-Reinforced Flexible Pavements—An Indian Perspective. Front. Built Environ. 6:71. doi: 10.3389/fbuil.2020.00071

INTRODUCTION

The design of flexible pavement is complex owing to its non-homogenous nature of multiple pavement layers with different thicknesses and mechanical properties, and the wide range of loading and climatic conditions for which it is designed. There are various pavement design methods such as empirical methods, analytical methods (layered analysis), and performance-based methods (AASHTO, 1993). It is essential to incorporate new materials into the pavement design in order to optimize the material consumption and performance. The new materials such as geosynthetics have been used to reinforce pavement layers to improve their performance in critical site conditions and to sustain heavy loading situations.

Natural and freshly crushed aggregates, which have become a scarce commodity, are required in large quantities every year for construction of new pavements and rehabilitation of existing pavements. Many road project sites have no other option but to procure good-quality aggregates from far away to meet the required quantities for their construction, leading to consequent cost escalations. The reduction in the utilization of non-renewable natural resources such as aggregate is indeed required to preserve the environment. For sustainable development of transportation infrastructure, use of locally available materials in combination with engineered materials such as geosynthetics is considered one of the best solutions to preserve the dwindling natural resources. The use of geogrids offsets and thus partly reduces the aggregate requirement in the pavement layers and impart sustainability in pavement construction by lowering the carbon footprint (Morrison, 2011).

The Indian Road Congress IRC:SP:59 (2019) recently published the guidelines for the design and use of geogrids in flexible pavement applications in India. The availability of suitable design methodologies and guidelines can promote the use of geogrid reinforcement in roadways. This paper critically examines the IRC:SP:59 (2019), and proposes objective based design approaches for geogrid-reinforced pavement along with the design charts based on IRC guidelines. The reduction in thickness of the reinforced-flexible pavement structure can be achieved through two ways: (a) reduction in the thickness of the aggregate layer or (b) reduction in the thickness of bituminous layer. Present study considers the Layer Coefficient Ratios (LCR) and Traffic Benefit Ratios (TBR) that are reported worldwide in literature corresponding to different subgrade conditions. Design charts are then provided based on LCR and TBR values corresponding to selected traffic and subgrade California Bearing Ratio (CBR) values according to the two objectives specified above. Additionally, the sustainability of the proposed solution is quantified in terms of embodied carbon (EC) values of materials utilized. Thus, an attempt is made to compute EC values for the unreinforced and geogrid-reinforced pavements with similar service life.

BACKGROUND

Many researchers have studied the benefits of incorporating geogrids in the flexible pavements through large-scale model experiments (Perkins et al., 2004; Chen et al., 2009; Qian et al., 2013; Abu-Farsakh et al., 2014), full-scale accelerated pavement testing (Webster, 1993; Collin et al., 1996; Perkins and Cortez, 2005; Al-Qadi et al., 2012; Jersey et al., 2012), and numerical simulations (Bhandari, 2011; Pandey et al., 2012). However, the implementation of flexible pavement reinforcement technique is handicapped by non-availability of a detailed design to incorporate these materials in pavement layers.

Popular design methods available for reinforced pavements include (1) Giroud and Han's (2004a,b) method for unpaved roads and (2) AASHTO R50 (2009) method for geosynthetic reinforced paved roads. As paved roads have become the need of society, the discussion in this paper is restricted to only design of reinforced paved roads. AASHTO R50 (2009) provides the guidance to design geosynthetic-reinforced aggregate base course in flexible pavement structures and outlines the overall design considerations. Design steps provided in this document were initially reported by Berg et al. (2000a). The pavement design parameters typically used to quantify the benefit of geogrid reinforcement include layer coefficient ratio (LCR) and traffic benefit ratio (TBR), and are generally derived from experiments. LCR of the reinforced section may be defined as a back-calculated modifier applied to the layer coefficient of the base layer. Zhao and Foxworthy (1999) observed high layer coefficient ratios (LCR) for subgrades of low CBR (equal to 1%). Perkins (2001) found that the improvement increases with increase in geosynthetic stiffness, while it decreases with increase in the subgrade stiffness and bituminous layer thickness. TBR is defined as the ratio between the number of load cycles on a reinforced section to reach a defined failure state and the number of load cycles on an unreinforced section with the same geometry and material constituents to reach the same defined failure state. This ratio ranges from 1.2 to 50 depending on type of geogrid used, depth of geogrid placement, thickness of base provided, and strength of soil subgrade (Berg et al., 2000b).

Flexible Pavement Design Based on IRC-37 (2018)

The important components of the Mechanistic-Empirical Pavement Design method include (a) a mechanistic model to calculate the critical responses of the system and (b) empirical performance or damage models that relate the critical responses to the accumulated damage and distress levels. Two critical responses of pavement used to assess the performance are (a) horizontal tensile strain at the bottom of the bituminous layer (fatigue strains) and (b) vertical strain at the top of the subgrade (rutting strains). The cracking and rutting models in IRC: 37 are based on the findings of the research schemes of the Ministry of Road Transport & Highways (MoRTH), Government of India, under which pavement performance data were collected from all over India to evolve the fatigue and rutting criteria for pavement design using a semi-analytical approach. IITPAVE software program, developed for layered system analysis, may be adopted and different combinations of traffic and pavement layer compositions are considered to meet the performance criteria. The designer inputs the number of layers, the thicknesses of individual layers, wheel load, contact pressure, and the layer elastic properties in the program, and the outputs from the program are in terms of radial strains and compressive strains at required locations. Traffic is expressed as 80 kN standard axles. The adequacy of design is checked by comparing the computed strains from the program with the allowable strains as predicted by the fatigue and rutting models. A satisfactory pavement design can be achieved through iterative process by varying layer thicknesses or by changing the pavement layer materials. Das (2007) emphasizes the need of developing performance based/ related pavement design for various unconventional material seeking potential application in pavement construction.

In the following sections, existing unreinforced flexible pavement design procedure was extended to account for the design of geogrid-reinforced pavement design methods based on LCR and TBR values according to two objectives in hand: (a) reduction in thickness of aggregate layer (resulting in material reduction), or (b) reduction in the thickness of bituminous layer (resulting in overall cost reduction).

GEOGRID-REINFORCED PAVEMENT DESIGNS

The design of reinforced flexible pavement is similar to that of design of unreinforced pavement. However, the improved elastic modulus of the reinforced pavement layer is modified according to the LCR of the reinforced pavement layer (using IRC:SP:59, 2019). The detailed design procedures that consider geogrid benefit in terms of either LCR or TBR are provided. The LCR-based design approach (IRC:SP:59, 2019) employs IITPave software (mechanistic-empirical approach) to check the strains at critical points and revise layer thicknesses accordingly (IRC:SP:59, 2019). Studies are available in the literature on the reduction of base layer thickness with the inclusion of geogrid reinforcement in a pavement. Webster (1993) reported the results of full-scale traffic testing on geogrid reinforced flexible pavement and proposed the equivalent reinforced base layer thickness corresponding to unreinforced base layer thickness. Perkins (1999) reported results from large-scale pavement testing under cyclic loads. It has been observed that the structural contribution of a geosynthetic reinforcement in a pavement is very similar to that of a pavement section with additional base layer thickness. In the light of available performance data of the geogrid-reinforced flexible pavements, the reduction in thickness of base layer is targeted. When a reinforcement layer is introduced into a pavement layer, the overall stiffness of that particular layer increases. In LCR method, the increase in the elastic modulus of the reinforced layer is quantified by increasing the value of layer coefficient of the particular layer. However, in the case of TBR method, the increase in the serviceability of the pavement due to reinforcement is quantified using the Traffic Benefit Ratio. Then the layer thicknesses are reduced accordingly to arrive at the design life period. However, both LCR values and TBR values depends on the various factors such as stiffness of geogrid, subgrade stiffness and thickness of pavement above geogrid.

LCR-Based Design

The following steps may be adopted to design geogrid- reinforced pavement using appropriate values of design traffic, subgrade CBR, and LCR values. Steps 1 through 7 correspond to the design of unreinforced flexible pavement as per IRC-37 (2018), while Steps 8 through 11 are additional steps to be followed for the design of reinforced flexible pavement as per IRC:SP:59 (2019).

Step 1. Determine the design traffic requirements on the pavement in terms of cumulative number of million standard axles (MSA)

Step 2. Determine 90th percentile California Bearing Ratio (CBR) of the subgrade

Step 3. The resilient modulus of subgrade can be calculated from Equation (1)

$$M_R = 10 * CBR \text{ for CBR up to } 5$$
$$M_R = 17.6 * CBR^{0.64} \text{ for CBR} > 5 \quad (1)$$

where M_R is the resilient modulus of subgrade soil in MPa and CBR is the California Bearing Ratio of subgrade layer in %

Step 4. Resilient modulus of subbase and base layers can be found using Equations (2) and (3). Thickness of the layers is assumed initially.

$$M_{R\_gsb} = 0.2 * h^{0.45} * M_{R\_sg} \quad (2)$$

where M_{R_gsb} is the resilient modulus of granular subbase layer in MPa, $M_{R_sg}$is the resilient modulus of subgrade in MPa, and h is the thickness of the GSB layer.

$$\text{Similarly, } M_{R\_gb} = 0.2 * h^{0.45} * M_{R\_gsb} \quad (3)$$

where M_{R_gb} is the resilient modulus of granular base layer in MPa, $M_{R_gsb}$is the resilient modulus of granular subbase layer in MPa, and h is the thickness of the GSB layer.

Modulus value of unbound granular materials is stress dependent and since induced stresses decrease with depth, modulus values also decrease with depth. This implies that the modulus of the granular material in each layer is a function of the layer thickness and of the modulus of the under lying layer (Kuo, 1979). It may be noted from Equations (2) and (3) that the resilient modulus of base or subbase layers depend only on the thickness of these layers and resilient modulus of underlying layer but does not depend on the quality of these layers (soft aggregate/crushable aggregate/competent aggregate). This seems counter intuitive and may be an anomaly in the Equations.

Step 5. Determine the wheel load and tire pressures for which the pavement need to be designed [tire pressure usually taken as 560 kPa, which corresponds to equivalent single axle wheel load (ESAL)]

Step 6. Limiting fatigue strains at the bottom of the bitumen layer and limiting rutting strains at the top of the subgrade are calculated using Equations (4) and (5), and Equations (6) and (7) according to the percentage of reliability, respectively:

$$\varepsilon_t = \left[2.21 * 10^{-4} \times \left[1/N_f\right] \times \left[1/M_R\right]^{0.854}\right]^{\frac{1}{3.89}} \quad \text{(80\%reliability)} \quad (4)$$

$$\varepsilon_t = \left[0.711 * 10^{-4} \times \left[1/N_f\right] \times \left[1/M_R\right]^{0.854}\right]^{\frac{1}{3.89}} \quad \text{(90\%reliability)} \quad (5)$$

where ε_t is the maximum tensile strain at the bottom of the bituminous layer, N_f is the fatigue life in number of

standard axles, and M_R is the resilient modulus of the bituminous layer in MPa

$$\varepsilon_v = \left[4.1656 * 10^{-8} \times [1/N]\right]^{\frac{1}{4.5337}} \text{ (80\% reliability)} \quad (6)$$

$$\varepsilon_v = \left[1.41 * 10^{-8} \times [1/N]\right]^{\frac{1}{4.5337}} \text{ (90\% reliability)} \quad (7)$$

where ε_v is the vertical strain in the subgrade and N is the number of cumulative standard axles

Step 7. Using IITPave software, the tensile strains at the bottom of the bitumen layer and compressive strains at the top of the subgrade in the assumed pavement section are calculated for the unreinforced pavement section by trial and error. The design of unreinforced flexible pavement is accomplished by ensuring that the fatigue and rutting strains are within the limits as computed in step 6.

Step 8. Determine the Layer Coefficients a_2, a_3 for granular base and subbase material from their elastic (resilient) modulus, E_{BS} and E_{SB}, using Equations (8) and (9) in accordance with AASHTO (1993).

$$a_2 = (0.249\log_{10}E_{BS}) - 0.977 \quad (8)$$

$$a_3 = (0.227\log_{10}E_{SB}) - 0.839 \quad (9)$$

where E_{BS} is the elastic modulus of base layer in psi, and E_{SB} is the elastic modulus of subbase layer in psi

Step 9. Layer coefficients are modified for the reinforced pavement by multiplying with the LCR to the layer in which reinforcement is provided.
Modified Layer coefficient of reinforced pavement layer,

$$a_i' = LCR_i * a_i \quad (10)$$

where a_i is the layer coefficient of i-th layer, and LCR_i is the Layer Coefficient Ratio of i-th layer
LCR values considered in the present designs range from 1.2 to 1.4

Step 10. The improved elastic modulus of reinforced layer is obtained by back calculating it corresponding to the modified layer coefficient using Equations (8) or (9).

Step 11. The improved elastic modulus of reinforced layer is incorporated in IITPave software to obtain the revised thickness of the layers satisfying the conditions of rutting strain at the top of the subgrade and fatigue strain at the bottom of the bitumen layer within the limiting strains

TBR-Based Design

The unreinforced pavement is designed using IRC-37 (2018), guidelines and the corresponding structural number (SN) of the pavement structure is computed according to AASHTO pavement design guidelines (AASHTO, 1993). In order to design the reinforced pavement, Traffic Benefit Ratio (TBR) is used. The effect of geogrid reinforcement is quantified in terms of equivalent structural number by considering traffic to be catered by the pavement and TBR that can be obtained with selected geogrid. The equivalent structural number of the geogrid is then used to reduce the unreinforced pavement layer thicknesses to the extent of reinforcement effect. The step-by-step procedure of design of geogrid-reinforced pavement using TBR approach is as follows:

Step 1. Design the unreinforced pavement by considering subgrade soil CBR and the traffic to be catered as per the guidelines provided by IRC-37 (2018).

Step 2. Compute the total structural number (SN_{UR}) of the unreinforced pavement structure designed in Step 1, taking into account the appropriate layer coefficients and drainage coefficients and thickness of each layer in accordance with AASHTO (1993) using Equation (11).

$$SN_{UR} = a_1 D_1 + a_2 D_2 m_2 + a_3 D_3 m_3 \quad (11)$$

where a_i is the layer coefficient of i-th layer, D_i is the thickness of the i-th layer, and m_i is the drainage coefficient of i-th layer

Step 3. Compute the SN_u required over the subgrade of unreinforced pavement to cater design number of standard axle load passes ($W_{18Unreinforced}$) using the following equation and substituting the appropriate values in Equation (12).

$$\log(W_{18})_{UR} = Z_R S_0 + 9.36 log_{10}(SN_U + 1) - 0.2 + \frac{\log_{10}\left[\frac{\Delta PSI}{4.2-1.5}\right]}{0.4 + \frac{1094}{(SN_U+1)^{5.19}}} + 2.32 log_{10} M_R - 8.02 \quad (12)$$

Step 4. Select an appropriate traffic benefit ratio (TBR) based on full-scale field studies or large-scale laboratory studies which represent similar field conditions and failure criteria. TBR typically ranges from 2 to 6 depending on the stiffness of the geogrid, subgrade CBR, base/subbase thickness, placement depth of geogrid, and bituminous mix layer thickness.

Step 5. Compute the number of standard axle load passes, $W_{18Reinforced}$ that can be allowed on the reinforced pavement structure by multiplying TBR with $W_{18Unreinforced}$.

Step 6. Compute the structural number, SN_r of pavement which can cater computed number of standard axle passes, $W_{18Reinforced}$ with reinforcement using Equation (12).

Step 7. Find the equivalent structural number of the geogrid by subtracting SN_u from SN_r.

Step 8. Reduce the base/ subbase layer thicknesses taking into account the equivalent structural number of the geogrid meeting minimum base/subbase layer thickness criteria and total structural number (SN) of unreinforced pavement.

Table 1 provides the scheme of pavement designs for both LCR- and TBR-based approaches. Two types of subgrades with the CBR

TABLE 1 | Scheme of pavement designs using LCR and TBR approaches.

Subgrade CBR, %	Traffic considered (MSA)	LCR values considered	TBR values considered
3	20	1.2, 1.3, 1.4	2, 3, 4
5			
3	50		
5			
3	100		
5			

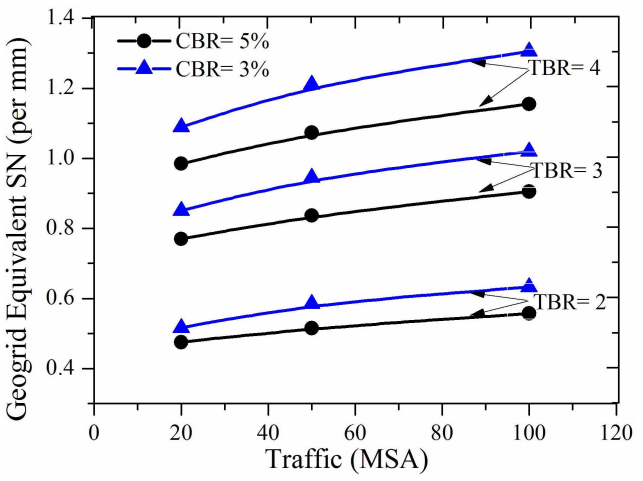

FIGURE 1 | Variation of geogrid equivalent SN of reinforced pavement with various types of subgrades and traffic for TBR equal to 2, 3, and 4.

of 3 and 5% and three types of traffic (20, 30, and 100 MSA) were chosen to observe the changes in pavement structure.

Figure 1 shows the effect of subgrade CBR on equivalent structural number of geogrid-reinforced pavement at different traffic for various TBR values. As the traffic increases, the equivalent structural number also increases. Hence, the benefit from geogrid reinforcement can be high. If the subgrade CBR is increased, the geogrid equivalent structural number decreases indicating the reduced advantage of reinforcement in pavement for stiff subgrades.

OBJECTIVE-BASED GEOGRID-REINFORCED PAVEMENT DESIGN

A client can have two objectives in a project, namely minimizing aggregate consumption in pavement layers (Objective-1) and reduction in construction cost of pavement without compromising the service life (Objective-2). Different design strategies may be adopted according to these two objectives in hand. Accordingly, designs to be adopted for each objective is given below separately.

LCR- and TBR-Based Pavement Designs With Objective-1

In this approach, the reinforced pavement composition is modified by reducing the thickness of aggregate layer (viz., Wet Mix Macadam and Granular Subbase) for a specified bituminous layer thickness. **Figure 2** shows the geogrid-reinforced pavement design charts for a traffic of 100 MSA and subgrade CBRs equal to 3 and 5% at selected LCR values. **Annex A** illustrates the design examples for both LCR and TBR methods for a case of 50 MSA traffic, LCR = 1.4, and TBR = 3 considering Objective-1. Tables B.1.1,B.1.2 (**Annex B.1**) provide the summary of design thicknesses of pavement layers corresponding to a traffic of 50 and 20 MSA at selected subgrade CBR values and LCR values.

Figure 3 shows the geogrid-reinforced pavement design charts for a traffic of 100 MSA and subgrade CBRs equal to 3 and 5% at selected TBR values. Tables C.1.1,C.1.2 (**Annex C**) provide the summary of design thicknesses of pavement layers corresponding to a traffic of 50 and 20 MSA at selected subgrade CBR values and TBR values.

The reduction in thicknesses of granular base and subbase layers in reinforced flexible pavement with respect to that of unreinforced flexible pavement is termed as aggregate layer reduction ratio (ALR). It is expressed in percentage thickness of unreinforced granular base and subbase layers.

$$ALR = \frac{(D_{ur} - D_r)}{D_r} * 100 \tag{13}$$

where D_{ur} = thickness of granular base and subbase layer in unreinforced pavement, and D_r = thickness of granular base and subbase layer in reinforced pavement. **Table 2** presents the aggregate layer reductions for selected subgrade CBR, traffic, LCR, and TBR values.

According to the LCR design approach, the introduction of reinforcement in flexible pavement resulted in the reduction of thickness of granular base and subbase layers of reinforced pavement with respect to unreinforced pavement ranging from 28 to 40% in the case of poor subgrade (CBR = 3%), and up to 45% in the case of relatively stiff subgrades (CBR = 5%). Whereas, per the TBR design approach, the inclusion of geogrid reinforcement resulted in reduction of thickness of base and subbase layers ranging from 12 to 30% in the case of poor subgrade (CBR = 3%) and from 10 to 24% in the case of relatively stiff subgrades (CBR = 5%).

LCR- and TBR-Based Pavement Designs With Objective-2

Among all the pavement layers, bituminous layers are expensive compared to the other layers. Hence, under this objective, the thicknesses of DBM and BC layers are to be reduced in order to economize the reinforced pavement design. **Figure 4** shows the geogrid-reinforced pavement design charts for a traffic of 100 MSA and subgrade CBRs of 3 and 5% at selected LCR values. Tables B.2.1,B.2.2 in **Annex B.2** provide the summary of design thicknesses of pavement layers corresponding to 50 and 20 MSA at selected subgrade CBR values and LCR values.

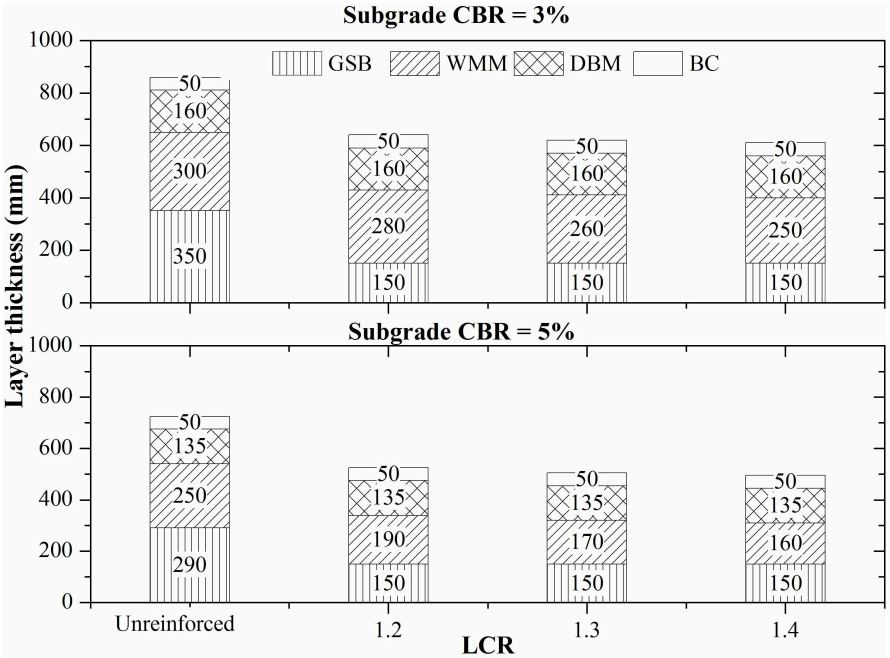

FIGURE 2 | Design charts showing thicknesses of unreinforced and geogrid reinforced flexible pavements using LCR approach based on Objective-1 for the traffic of 100 MSA with subgrade CBRs equal to 3 and 5%.

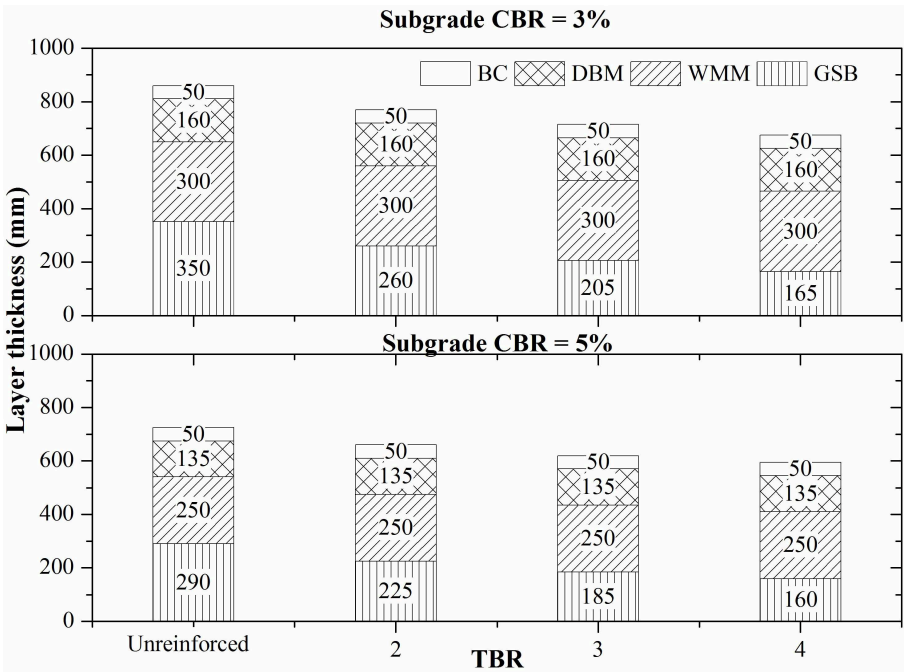

FIGURE 3 | Design charts showing thicknesses of unreinforced and geogrid-reinforced flexible pavements using TBR approach based on Objective-1 for the traffic of 100 MSA with subgrade CBRs equal to 3 and 5%.

Figure 5 shows the geogrid-reinforced pavement design charts for a traffic of 100 MSA and subgrade CBRs of 3 and 5% at selected TBR values. Tables C.2.1,C.2.2 in **Annex C.2** provide the summary of design thicknesses of pavement layers corresponding to a traffic of 50 and 20 MSA at selected subgrade CBR values and TBR values.

The reduction in bituminous layer thickness of reinforced flexible pavement with respect to that of unreinforced flexible pavement with the same design criteria may be defined as bituminous layer reduction ratio (BLR). It is expressed in percentage thickness of unreinforced bituminous layers.

$$BLR = \frac{(B_{ur} - B_r)}{B_r} * 100 \quad (14)$$

where B_{ur} = thickness of bituminous layer in unreinforced pavement, and B_r = thickness of bituminous layer in reinforced pavement.

TABLE 2 | Aggregate layer reduction for selected subgrade CBR, traffic, LCR, and TBR values.

Subgrade CBR, %	Traffic, MSA,	Aggregate layer reduction (ALR), %					
		LCR = 1.2	LCR = 1.3	LCR = 1.4	TBR = 2	TBR = 3	TBR = 4
3	100	33	36	38	16	22	28
	50	28	33	35	14	23	30
	20	34	38	40	12	19	26
5	100	37	40	42	12	19	24
	50	38	41	43	10	17	22
	20	45	45	45	10	16	20

Table 3 presents the bituminous layer reductions for selected subgrade CBR, traffic, LCR, and TBR values.

According to the LCR design approach, the reduction in thickness of bituminous layer ranges from 7 to 31% in case of poor subgrade (CBR = 3%) and from 13 to 48% in case of relatively stiff subgrades (CBR 5%). Whereas, asper the TBR design approach, the reduction in thickness of bituminous layer ranges from 16 to 37% in case of poor subgrade (CBR = 3%) and from 15 to 29% in case of relatively stiff subgrades (CBR = 5%).

SUSTAINABILITY OF GEOGRID-REINFORCED PAVEMENT: COUNTING CARBON

In order to achieve sustainable development goals (SDGs) set by the United Nations program Transforming Our World: The 2030 Agenda for Sustainable Development UN [United Nations] (United Nations General Assembly, 2015), it is essential to analyze the sustainability of alternate options in terms of design methods, construction techniques, and materials used to build the infrastructure. Carbon footprint is a measure of total greenhouse gases (GHG) emissions caused directly and indirectly by a person, organization, event or product. It is measured in ton of carbon dioxide equivalent (tCO_2 e). The carbon footprint covers emissions over the whole life of a product, service, or solution (i.e., including the construction solution). Comparison of calculated carbon footprints for alternative solutions can be

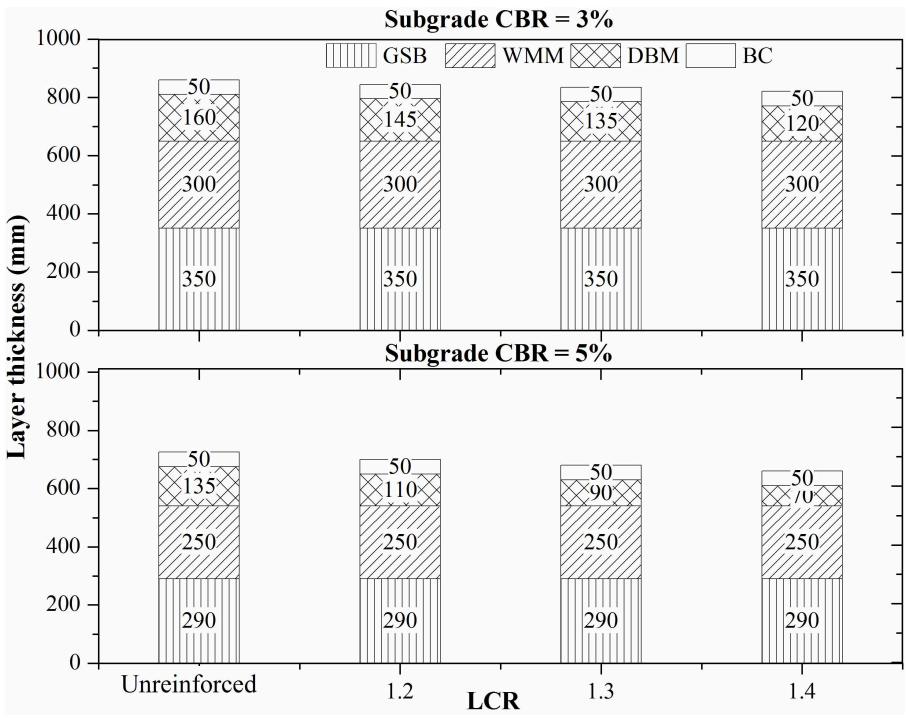

FIGURE 4 | Design charts showing thicknesses of unreinforced and geogrid reinforced flexible pavements using LCR approach based on Objective-2 for the traffic of 100 MSA with subgrade CBRs equal to 3 and 5%.

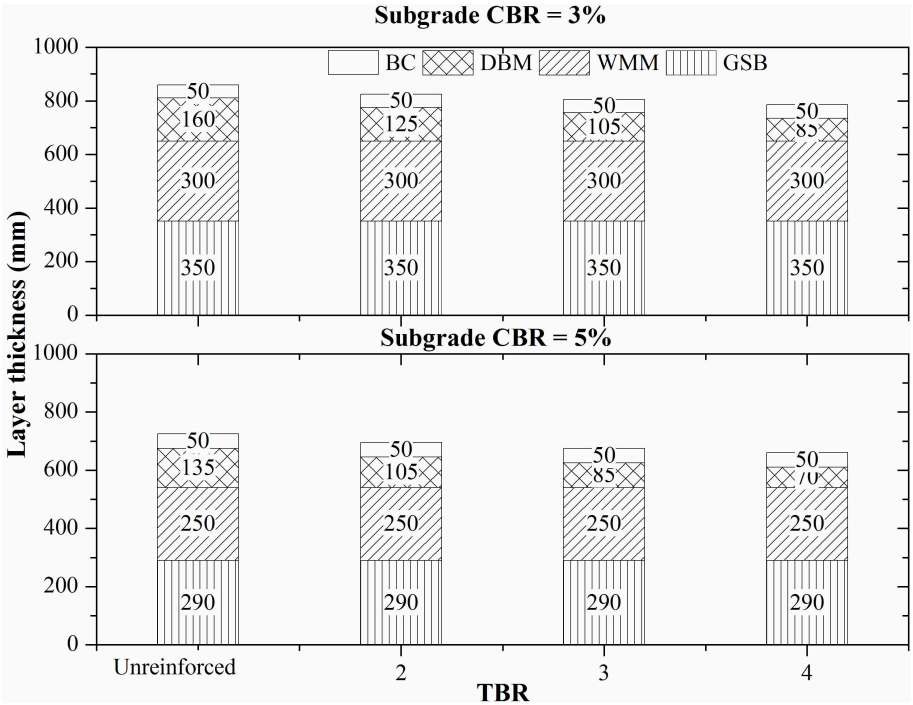

FIGURE 5 | Design charts showing thicknesses of unreinforced and geogrid-reinforced flexible pavements using TBR approach based on Objective-2 for the traffic of 100 MSA with subgrade CBRs equal to 3 and 5%.

TABLE 3 | Bituminous layer reduction for selected subgrade CBR, traffic, LCR, and TBR values.

Subgrade CBR, %	Traffic, MSA,	Bituminous layer reduction (BLR), %					
		LCR = 1.2	LCR = 1.3	LCR = 1.4	TBR = 2	TBR = 3	TBR = 4
3	100	7	11	19	16	26	35
	50	7	10	15	15	28	36
	20	15	25	31	18	28	37
5	100	13	24	35	16	27	35
	50	19	35	48	19	29	38
	20	42	42	42	17	28	35

TABLE 4 | Unit EC values for selected materials from the literature.

Materials	Unit EC values for cradle to the gate (tCO_2 e/t)	References
Bituminous concrete	0.0385 (5.5% Bitumen)	Gupta et al., 2017
Crushed aggregate	0.0176	Gupta et al., 2017
Geogrid	2.97	Raja, 2015

used to select the most "sustainable" option (Dixon et al., 2016). Embodied carbon (EC) is an indicator of cumulative carbon emissions used in the solution adopted. EC of a material can be defined as the amount of CO_2 emissions released in the extraction, manufacture, and transport of the material. It is calculated in ton of CO_2 per mass of construction material produced (e.g., tCO_2/t) (Huang et al., 2016).

Owing to use of geogrids in pavements, a reduction in aggregate utilization directly results in reduction in material handling and emission of green-house gases (GHG) leading to decrease in carbon footprint. However, there will be an increase in carbon footprint due to the introduction of geogrid. If the net carbon footprint is reduced, the proposed pavement design solution with geogrid reinforcement and reduced thickness of pavement layers makes it a sustainable pavement for the same service life as that of conventional pavement.

The carbon emission quantification may be done within the limits of four stages of material processing and utilization: material manufacture, transportation, construction, and disposal (Huang et al., 2016). In the present case, EC values from cradle to gate were considered, which takes into account the extraction and manufacture of pavement construction material. Transportation of material to construction site is site specific and hence it was not accounted for in the present study. **Table 4** presents unit EC values reported in literature for extraction and manufacturing stages of selected pavement material.

Unreinforced pavement section with subgrade CBR equal to 3, 5, and 10%, and catering to a traffic of 20, 50, and 100 MSA, and reinforced sections with LCR of 1.2, 1.3, and 1.4 were considered to compare EC values of the pavement materials. In the case of geogrid-reinforced pavements, only aggregate layer reduction was considered. Based on laboratory

TABLE 5 | Pavement layer thickness and width details for unreinforced and geogrid-reinforced pavements with granular layer reduction in reinforced cases.

Type of pavement	Pavement layer thickness* and width in mm				
	BC	DBM	WMM	GSB	Geogrid
Unreinforced pavement	40, 7,500	150, 7,580	250, 7,880	350, 8,380	NA
Geogrid reinforced pavement with LCR = 1.2	40, 7,500	150, 7,580	250, 7,880	180, 8,380	2, 8,380
Geogrid reinforced pavement with LCR = 1.3	40, 7,500	150, 7,580	250, 7,880	150, 8,380	2, 8,380
Geogrid reinforced pavement with LCR = 1.4	40, 7,500	150, 7,580	235, 7,880	150, 8,350	2, 8,350

**Layer thicknesses are used from table B.1.1 for 50 MSA traffic and subgrade CBR of 3%.*

TABLE 6 | EC values for unreinforced and reinforced pavements with granular layer reduction in reinforced cases.

Materials	Bituminous	Crushed aggregate	Geogrid (extruded)	Total tCO_2 e/km
Unit EC, tCO_2 e/t	0.0385	0.0176	2.97	
Unreinforced pavement				
Material quantity[a], ton/km	3520.7	11345.5	–	
EC[b], tCO_2 e	135.5	199.7	–	335.2
Geogrid-reinforced pavement with LCR = 1.2				
Material quantity, ton/km	3520.6	8049.0	3.4	
EC, tCO_2 e	135.5	141.7	10	287.2
Geogrid-reinforced pavement with LCR = 1.3				
Material quantity, ton/km	3520.6	7467.3	3.4	
EC, tCO_2 e	135.5	131.4	10.0	276.9
Geogrid-reinforced pavement with LCR = 1.4				
Material quantity, ton/km	3520.6	7183.4	3.3	
EC, tCO_2 e	135.5	126.4	9.9	271.2

[a]*Material quantity, ton/km = layer thickness*layer width*1,000*material unit weight.*
[b]*EC, tCO_2 e = Unit EC* Material quantity.*

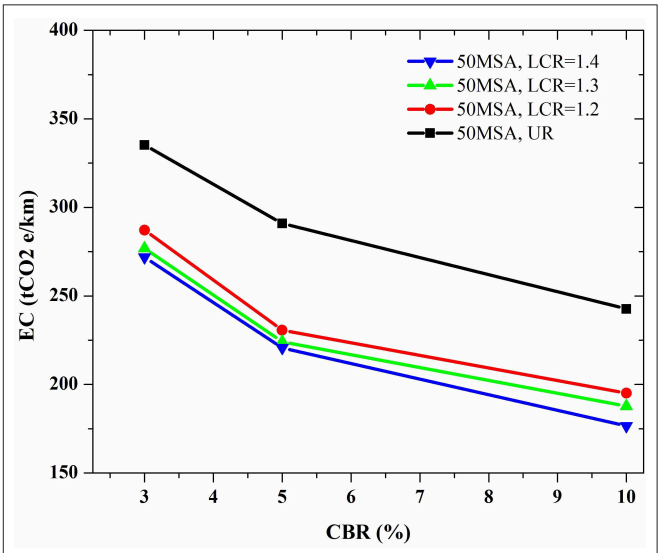

FIGURE 6 | Variation of EC values with subgrade CBR for unreinforced and geogrid reinforced pavement structures that cater to a traffic of 50 MSA.

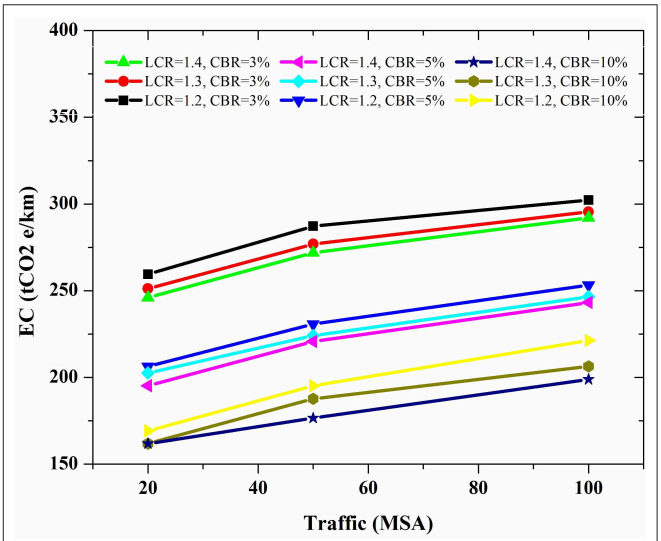

FIGURE 7 | Variation of EC values with traffic for different subgrades and LCR values of geogrid reinforced pavements.

testing, the densities of bituminous mix and aggregate mix were found to be equal to 2.450 and 2.314 ton/m^3, and geogrid mass as 0.0004 ton/m^2. The calculation was carried out for a two-lane road of surface width equal to 7.5 m considering 1 km stretch. As followed in the construction of pavement layers, the width of lower pavement layers was increased by two times the thickness of top layer to accommodate the construction of top layer. **Annex D** provides the detailed procedure of computation of EC values for unreinforced and geogrid-reinforced flexible pavement. **Tables 5**, **6** present the pavement crust details and EC values for unreinforced and geogrid-reinforced pavements with only granular layer thickness reduction, respectively.

Figure 6 shows the variation of EC values with subgrade CBR for unreinforced and geogrid-reinforced pavement structures corresponding to a traffic of 50 MSA and for selected LCR range. It was observed that the EC value reduces with increase in subgrade CBR. The pavement with softer subgrade (3% CBR) requires more pavement material, hence higher EC value were observed compared to the pavement with stiffer subgrade (CBR = 10%). The geogrid-reinforced pavement yielded lower EC values than unreinforced pavement for various LCR values and subgrade CBR values. **Figure 7** presents the variation of EC values with traffic for different subgrades and LCR values of geogrid-reinforced pavements. It indicates that EC values decrease with increase in traffic levels. In addition, for a given traffic level and subgrade, the EC value increases with a decrease in LCR value. **Figure 8** shows the variation of reduction in EC

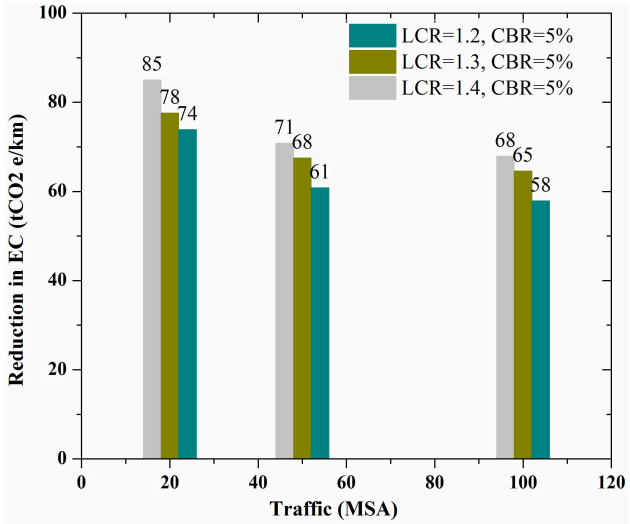

FIGURE 8 | Variation of reduction in EC with traffic for a subgrade CBR of 5%.

with traffic for a subgrade CBR of 5%. The reduction in EC of geogrid-reinforced pavement ranges from 58 to 85 tCO_2 e/km for the traffic range of 20–100 MSA and LCR of 1.2–1.4. It is observed that reduction in EC is more (74–85 tCO_2 e/mm) for the traffic of 20 MSA compared to the traffic of 100 MSA (58–68 tCO_2 e/Km).

Additionally, the construction cost of reinforced pavements can be reduced due to the reduced material handling, processing, and consumption in comparison with unreinforced pavements. Hence, a solution that considers reinforcement of flexible pavement with geogrid can be a sustainable option.

CONCLUSIONS AND COMMENTS

In this study, LCR- and TBR-based approaches are adopted to design geogrid-reinforced flexible pavements. The design of pavement structure is carried out according to two objectives in mind: (a) minimizing the use of aggregates (in base and subbase layers) and (b) minimizing the overall cost of construction of the pavement.

Depending on the objective in hand, owing to the introduction of geogrid-reinforcement in flexible pavement, the thickness of *granular base and subbase layers* of reinforced pavement can be reduced by at least 10% to as high as 45% for subgrades with CBR <5%. Similarly, it is possible to reduce the thickness of the *bituminous layer* of geogrid-reinforced pavement by at least 7% to as high as 48% with respect to unreinforced pavement when the subgrade CBR is <5%. Designs have been carried out for subgrades with different CBR values (3 and 5%) and traffic (20, 50, and 100 MSA). Additionally, the sustainability of geogrid-reinforced pavements is quantified. The EC values are found to have reduced in the range of 58–85 tCO_2 e/Km for geogrid-reinforced cases compared to an unreinforced pavement.

The paper thus highlights several well-known advantages of using geosynthetics in pavements, such as (i) saving in money and material, (ii) increased life of pavement with consequent reduction in annual maintenance costs, and (iii) lesser construction time, along with hidden benefits such as less carbon footprint, improved riding quality, and less vehicle maintenance.

DATA AVAILABILITY STATEMENT

All datasets generated for this study are included in the article/**Supplementary Material**.

AUTHOR CONTRIBUTIONS

BU, SS, and RM conceived the presented idea of geogrid reinforced pavement design method for Indian conditions and sustainability aspects of geogrid reinforced pavements and verified the methods. GG and SM developed the method and performed the computations based on suggestions from BU, SS, and RM. In brief, all authors have discussed the findings and contributed to the final manuscript.

FUNDING

This work was conducted as part of sponsored research by National Highways Authority of India (NHAI). Grant Number: NHAI/TIC/R&D/108/2016.

SUPPLEMENTARY MATERIAL

The Supplementary Material for this article can be found online at: https://www.frontiersin.org/articles/10.3389/fbuil.2020.00071/full#supplementary-material

REFERENCES

AASHTO (1993). *Guide for Design of Pavement Structures*. Washington, DC: AASHTO.

AASHTO R50 (2009). *Standard Practice for Geosynthetic Reinforcement of the Aggregate Base Course of Flexible Pavement Structures*. Washington, DC: American Association of Highway and Transportation Officials.

Abu-Farsakh, M. Y., Akond, I., and Chen, Q. (2014). "Evaluation of performance of geosynthetic-reinforced unpaved roads using plate load tests," in *93rd TRB Annual Meeting* (Washington, DC: Transportation Research Board), 901–912.

Al-Qadi, I. L., Dessouky, S. H., Kwon, J., and Tutumluer, E. (2012). Geogrid-reinforced low-volume flexible pavements : pavement response and geogrid optimal location. *ASCE J. Transp. Eng.* 138, 1083–1090. doi: 10.1061/(ASCE)TE.1943-5436.0000409

Berg, R. R., Christopher, B. R., and Perkins, S. W. (2000a). *Geosynthetic Reinforcement of the Aggregate Base/Subbase Courses of Pavement Structures*. Roseville, CA.

Berg, R. R., Christopher, B. R., and Perkins, S. W. (2000b). *Geosynthetic Reinforcement of the Aggregate Base Course of Flexible Pavement Structures*. GMA White Paper II (Roseville, MN: Geosynthetic Materials Association), 130.

Bhandari, A. (2011). *Micromechanical Analysis of Geosynthetic-Soil Interaction under Cyclic Loading*. Lawrence, KS: University of Kansas School of Engineering.

Chen, Q., Abu-Farsakh, M. Y., and Tao, M. (2009). Laboratory evaluation of geogrid base reinforcement and corresponding instrumentation program. *Geotech. Test. J.* 32, 516–525. doi: 10.1520/GTJ102277

Collin, J. G., Kinney, T. C., and Fu, X. (1996). Full scale highway load test of flexible pavement systems with geogrid reinforced base courses. *Geosynth. Int*. 3, 537–549. doi: 10.1680/gein.3.0074

Das, A. (2007). "Principles of Bituminous Pavement Design and the Recent Trends," in *Short Term Course on Pavement Engineering with Geosynthetics : Looking Ahead*. Kanpur: IIT Delhi.

Dixon, N., Raja, J., Fowmes, G., and Frost, M. (2016). "Sustainability aspects of using geotextiles," in *Geotextiles: From Design to Applications* (Loughborough: Woodhead Publishing Elsevier), 577–596.

Giroud, J. P., and Han, J. (2004a). Design method for geogrid-reinforced unpaved roads. I. development of design method. *J. Geotechnical Geoenviron. Eng*. 130, 775–786. doi: 10.1061/(ASCE)1090-0241(2004)130:8(775)

Giroud, J. P., and Han, J. (2004b). Design method for geogrid-reinforced unpaved Roads. II. calibration and applications. *J. Geotechnical Geoenviron. Eng*. 130, 787–797. doi: 10.1061/(ASCE)1090-0241(2004)130:8(787)

Gupta, G., Sood, H., and Gupta, P. K. (2017). "Life-cycle cost analysis of brick kiln dust stabilized perpetual pavements for lowering greenhouse gas emissions in India," in *Urbanization Challenges in Emerging Economies* (New Delhi: ASCE), 377–390.

Huang, Y., Ning, Y., Zhang, T., and Wu, J. (2016). Measuring carbon emissions of pavement construction in China. *Sustainability* 8:723. doi: 10.3390/su8080723

IRC:SP:59 (2019). *Guidelines for Use of Geosynthetics in Road Pavements and Associated Works*. 1st Rev. New Delhi: Indian Roads Congress.

IRC-37 (2018). *Guidelines for the Design of Flexible Pavements*. New Delhi: Indian Roads Congress-New Delhi.

Jersey, S. R., Tingle, J. S., Norwood, G. J., Kwon, J., and Wayne, M. H. (2012). *Full-Scale Evaluation of Geogrid Reinforced Thin Flexible Pavements*. Pittsburgh, PA: Transportation Research Record.

Kuo, S. S. (1979). *Development of Base Layer Thickness Equivalency*. Research Project 68 E-42 Research Report No. R-1119. Michigan Department of Transportation, Lansing, MI.

Morrison, B. (2011). "Geosynthetics as a component of sustainability in pavement structure design for arterial roadways," in *2011 Conference and Exhibition of the Transportation Association of Canada* (Edmonton, AB: Alberts), 13. Available online at: http://conf.tac-atc.ca/english/annualconference/tac2011/docs/sm2/morrison.pdf

Pandey, S., Rao, K. R., and Tiwari, D. (2012). "Effect of geogrid reinforcement on critical responses of bituminous pavements," in *ARRB Conference, 25th*. (Perth, WA), 1–17. Available online at: http://trid.trb.org/view.aspx?id=1224083 (accessed January 25, 2014).

Perkins, S. W. (1999). Mechanical response of geosynthetic-reinforced flexible pavements. *Geosynth. Int*. 6, 347–382. doi: 10.1680/gein.6.0157

Perkins, S. W. (2001). *Numerical Modeling of Geosynthetic Reinforced Flexible Pavements*. Bozeman, MT: Montana State University.

Perkins, S. W., Christopher, B. R., Eli, C. L., Eiksund, G. R., Hoff, I., Schwartz, C. W., et al. (2004). *Development of Design Methods for Geosynthetic Reinforced Flexible Pavements*. Available online at: http://www.westerntransportationinstitute.org/documents/reports/426202_Final_Report.pdf (accessed January 25, 2014).

Perkins, S. W., and Cortez, E. R. (2005). Evaluation of base-reinforced pavements using a heavy vehicle simulator. *Geosynth. Int*. 12, 86–98. doi: 10.1680/gein.2005.12.2.86

Qian, Y., Han, J., Pokharel, S. K., and Parsons, R. L. (2013). Performance of triangular aperture geogrid-reinforced base courses over weak subgrade under cyclic loading. *J. Mater. Civil Eng.* 25, 1013–1021. doi: 10.1061/(ASCE)MT.1943-5533.0000577

Raja, J. M. (2015). *Reducing the Environmental Impact of Construction Through Use of* Geosynthetics. Loughborough: Loughborough University.

United Nations General Assembly (2015). *Transforming Our World: The 2030 Agenda for Sustainable Development*. A/RES/70/1, 16301 (New York, NY: United Nations General Assembly), 13–14.

Webster, S. L. (1993). *Geogrid Reinforced Base Courses for Flexible Pavements for Light Aircraft : Test Section Construction, Behavior Under Traffic, Laboratory Tests and Design Criteria*. Vicksburg, MI: Federal Aviation Administration.

Zhao, A., and Foxworthy, P. T. (1999). *Geogrid Reinforcement of Flexible Pavements: A Practical Perspective*. Avaiable online at: http://trid.trb.org/view.aspx?id=503862

Conflict of Interest: The authors declare that the research was conducted in the absence of any commercial or financial relationships that could be construed as a potential conflict of interest.

NOTATIONS

M_R is the resilient modulus
CBR is the California Bearing Ratio of subgrade layer in %
LCR is the Layer Coefficient Ratio
TBR is the Traffic Benefit Ratio
M_{R_gsb} is the resilient modulus of granular subbase layer
M_{R_sg} is the resilient modulus of subgrade
M_{R_gb} is the resilient modulus of granular base layer
N_f is the fatigue life in number of standard axles
ε_t is the maximum tensile strain at the bottom of the bituminous layer
N is the number of cumulative standard axles
ε_v is the vertical strain in the subgrade
E_{BS} is the elastic modulus of base layer
E_{SB} is the elastic modulus of subbase layer
a_i is the layer coefficient of i-th layer
LCR_i is the Layer Coefficient Ratio of i-th layer
a_i' is the modified layer coefficient of i-th layer
SN_{UR} is the structural number of the unreinforced pavement
D_i is the thickness of the i-th layer
m_2 is the drainage coefficient of base layer
m_3 is the drainage coefficient of subbase layer
SN_u is the structural number required
W_{18Ur} is the number of standard axle load passes allowable on unreinforced pavement
Z_R is the Standard normal deviate
S_0 is the overall standard deviation for flexible pavement
PSI is the change in present serviceability index
$W_{18Reinforced}$ is the number of standard axle load passes allowable on reinforced pavement
SN_r is the structural number of the reinforced pavement
D_{ur} is the thickness of granular base and subbase layer in unreinforced pavement
D_r is the thickness of granular base and subbase layer in reinforced pavement
B_{ur} is the thickness of bituminous layer in unreinforced pavement
B_r is the thickness of bituminous layer in reinforced pavement

frontiers in Built Environment

ORIGINAL RESEARCH
published: 16 July 2020
doi: 10.3389/fbuil.2020.00116

Interaction Between a Lateritic Soil and a Non-woven Geotextile in Different Moisture Conditions

Gabriel Steluti Marques†† and Jefferson Lins da Silva†*

Laboratory of Geosynthetics, Department of Geotechnical Engineering, São Carlos School of Engineering, University of São Paulo, São Carlos, Brazil

This work evaluates the increase in stiffness provided by the variation of moisture content (matrix suction) and the grain size structure at the interface between a cohesive tropical soil (lateritic clay) and a non-woven geotextile. For this purpose, monotonic pullout tests with soil suction monitoring were performed on small-sized equipment under three scenarios ("O" Optimum, "D" Dry and "DP" Dry Post-Compaction) and two vertical pressures (14 and 28 kPa). The Dry Post-Compaction tests were conducted with the same matrix suction of the Dry tests. The monotonic pullout tests evaluated the soil-geosynthetic interaction under constant displacement to calculate the apparent confined stiffness of the geosynthetic (Jc). The Wide Width Tensile tests were conducted to assess the unconfined stiffness of the non-woven geotextile (Jn). The Dry scenario, compacted with higher compaction energy than the others and, consequently, altering its grain size structure, presented the best performance. This indicates that other parameters besides the suction may be influencing the interaction between the soil and the non-woven geotextile. Even under small vertical pressures, the apparent confined stiffness improves considerably compared to the unconfined stiffness. This indicates that the use of the unconfined stiffness obtained by index tests may be a conservative measure in paving projects.

Keywords: geotextile, lateritic soil, unsaturated soils, confined stiffness, soil-geosynthetic interaction

OPEN ACCESS

Edited by:
Sujit Kumar Dash,
Indian Institute of Technology Kharagpur, India

Reviewed by:
Anindya Pain,
Central Building Research Institute (CSIR), India
Ali Behnood,
Purdue University, United States

***Correspondence:**
Gabriel Steluti Marques
gabrielstmarques@gmail.com

ORCID:
Gabriel Steluti Marques
orcid.org/0000-0002-6713-2425
Jefferson Lins da Silva
orcid.org/0000-0002-2226-4950

Specialty section:
This article was submitted to Transportation and Transit Systems, a section of the journal Frontiers in Built Environment

Received: *19 August 2019*
Accepted: *25 June 2020*
Published: *16 July 2020*

Citation:
Marques GS and Lins da Silva J (2020) Interaction Between a Lateritic Soil and a Non-woven Geotextile in Different Moisture Conditions. Front. Built Environ. 6:116. doi: 10.3389/fbuil.2020.00116

INTRODUCTION

In recent years, the search for alternative materials in infrastructure works has been increasing rapidly once the exploration of natural deposits and the extraction of relevant materials are onerous services, especially in places where this material is scarce resulting in high transport distances (Vilar and Bueno, 2008).

In tropical countries, there are abundant natural materials known as lateritic soils, normally classified as inappropriate material for pavement purposes by many soil classification systems based on the grain size distribution and soil consistency (Villibor et al., 2009). However, the tropical climate intensifies the process of leaching and chemical weathering of the soil, which accumulates in a considerable amount of iron and aluminum oxides providing high load-bearing capacity and low expansibility (Nogami and Villibor, 1981).

Another alternative material available to control the pathological manifestation, which increases the service life of the pavement and reduces the thickness of the base layer, is the geosynthetic. The non-woven geotextile was one of the first geosynthetics used in paving as reinforcement. However,

with the emergence of geogrids, the non-woven geotextiles have been mostly used as a drainage material. This can be explained by its high deformation and, consequently, low stiffness modulus in unconfined tests. However, the non-woven fabric exhibits a high increase in stiffness in confined situations and can become an economic alternative as a reinforcement.

In order to ensure a good performance of the reinforced structure, efficient interaction between the geosynthetic and the base material is necessary, increasing the lateral confinement and the stiffness of the system. Thus, the stiffness modulus of the system under low deformation often becomes a more representative parameter of the soil-geosynthetic interaction than the maximum pullout resistance (Chang et al., 1998).

This work evaluates the increase in stiffness provided by the variation of moisture content (matrix suction) and the grain size structure at the interface between a cohesive tropical soil (lateritic clay) and a non-woven geotextile. For this purpose, monotonic pullout tests with soil suction monitoring were performed on small-sized equipment under three scenarios ("O" Optimum, "D" Dry, and "DP" Dry Post-Compaction) and two vertical pressures (14 and 28 kPa). The Dry Post-Compaction tests were conducted with the same matrix suction of the Dry tests. The monotonic pullout tests evaluated the soil-geosynthetic interaction under constant displacement to calculate the apparent confined stiffness of the geosynthetic (Jc). The Wide Width Tensile tests were conducted to assess the unconfined stiffness of the non-woven geotextile (Jn). Although there is no general rule in the literature that specifies how best to obtain the complex confined stiffness parameter of a geosynthetics, this paper aims to contribute to making the choice of the most suitable scenario for the studied soil and to compare the confined and unconfined stiffness of the non-woven geotextile.

MATERIALS AND METHODS

Soil and Geotextile Properties

In order to use a soil with tropical characteristics, a clayey tropical soil was chosen, classified as a silt of high plasticity (MH), according to the Unified Soil Classification System (USCS). This material was collected near the city of São Carlos, São Paulo, Brazil.

The predominantly clayey soil has approximately 70% fines, with D_{50} = 0.007 mm and D_{Maz} = 0.6 mm. The soil has a California Bearing Ratio (CBR) of 22% and expansion of 0.02%.

The use of local fine soils in their natural or even stabilized condition requires a more detailed study of their geotechnical properties. For this reason, in order to know the applicability of this soil in pavement structures, we used the MCT (Miniature, Compacted, Tropical) methodology, which addresses a different methodology for tropical soils, proposed by Nogami and Villibor (1981). Based on these results, the soil was classified as a Clayey Lateritic (LG'), which can be used in the base of low-cost pavements.

The non-woven geotextile is needled with continuous filaments and composed by polyester (PET). The results of the Wide-width tensile test showed a maximum tensile strength of 33.48 kN/m (catalog strength of 30 kN/m) and average deformation at rupture of 61.20%. The average stiffness modulus for a deformation of 2 and 5% was 104.40 and 77.50 kN/m, respectively.

Scenario Definition

Table 1 summarizes the initial and final molding conditions during the preparation of the test box prior to testing. All scenarios were tested with a compaction degree (GC) of 98%. The Optimum Scenario "O" has an estimated test suction of 15 kPa, while the Dry Scenario "D" and the Dry Post-compaction Scenario "DP" presented suctions of 75 kPa.

Figure 1 illustrates the representation and trajectories of the three molding condition points in the soil compaction curve. It is noted that the "O" and "DP" scenarios are compacted at the same point, but only the "O" condition remains at this point for the pull-out tests, whereas the "DP" scenario would lose moisture (DP trajectory) until it reaches the same moisture content of the "D" scenario. The dry "D" scenario was tested at the same point as "DP," with similar suctions at the time of testing. However, in order to achieve a test condition at the same compaction degree as the "DP" condition, the test had to be subjected to higher compaction energy (Trajectory D), which provided a more flocculated soil structure.

Pullout Apparatus

The pullout tests were performed for different suctions, which required more precise control of soil moisture content and the use of a constant soil drying temperature. For this reason, we opted to use a small box.

Although ASTM D 6706-01 (2013) specifies dimensions larger than those in the small box, Kakuda (2005) demonstrated a good performance of this box to use cohesive soils in monotonic pullout tests. After that, research was carried out using this equipment, emphasizing Ferreira (2007), who compared the confined stiffness between different geogrids and Pereira (2010) that evaluated the pullout resistance of a geogrid under different moisture conditions.

The small-sized equipment consists of a rigid steel box with inner dimensions of 24.5 cm long, 30 cm wide and 14.5 cm high (**Figure 2**). The upper surface has a reaction cap coupled to a pressure-controlled air bag for the application of the overload. In the rear region, there is a support for the fitting of four tell-tales, which are connected to the geosynthetic by inextensible wires.

There are two holes on the side of the box with a diameter of 7 mm in which it was possible to insert a tensiometer to check the interstitial water pressures developed in the cohesive soil during the pullout test. The tensiometer was installed just 1.0 cm below the soil-reinforcement interface.

The displacements of the non-woven geotextile were measured in four different points nominated D1, D2, D3, and D4. The Geotextile was confined 210 mm long and 260 mm transverse inside the box (**Figure 2**). All points were spaced 45 mm longitudinally from each other and only the D2 and D3 (central) sensors were used in the present analysis in order to minimize the effects of the edges in the apparent confined stiffness calculations.

TABLE 1 | Initial and final molding conditions.

Scenario	W Compacted (%)	W tested (%)	Degree of Compaction DC (%)	ρ dmax (g/cm^3)	Estimated Suction (kPa)
O	22.75	22.75	98	1.593	15
D	18.75	18.75	98	1.593	75
DP	22.75	18.75	98	1.593	75

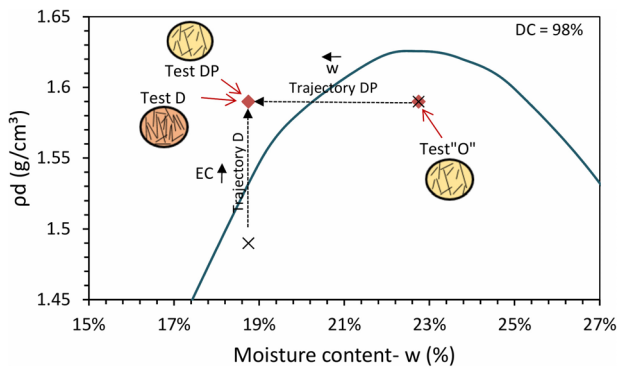

FIGURE 1 | Illustration of the trajectories and study points of the "O", "D," and "DP" scenarios in the compaction curve.

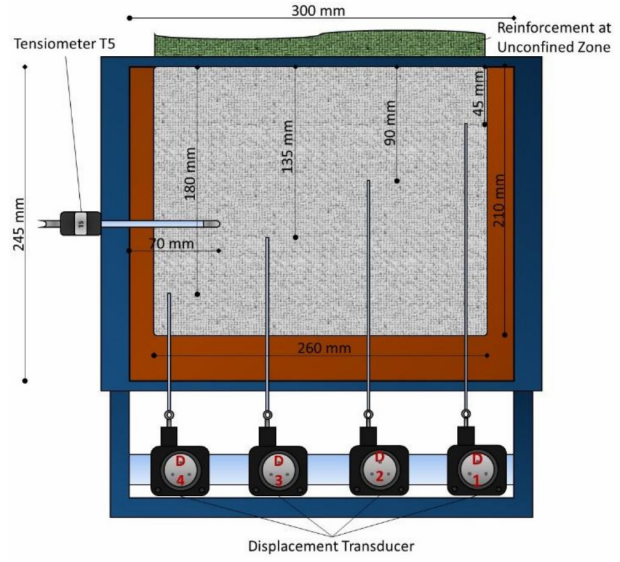

FIGURE 2 | Small box and measuring points of non-woven geotextile displacement.

In order to inhibit the yielding effect of the non-woven geotextile, provided by the high deformation of the geotextile in the unconfined region between the box and the traction grab, a reinforcement for the geosynthetic was performed along this range. For this, on the surface of the non-woven geotextile up to 20 mm inside the box, epoxy glue was used, superimposed by a plastic blanket on the upper and lower surfaces of the geosynthetic. **Figure 3** illustrates the exhumation of pilot tests performed with and without reinforcement in the unconfined region of the non-woven geotextile. The importance of the reinforcement in the unconfined region can be observed since the reduction of the confined area by the yielding effect was completely minimized.

Test Procedure

The monotonic pullout test was performed according to the procedures described in ASTM D 6706-01 (2013). The applied loads were 14 and 28 kPa having as a limiting factor the maximum resistance of the non-woven geotextile in the wide-width tensile test. Larger confining stresses would result in ruptures of the geotextile in the unconfined region before the pullout occurs. These overloads are in the order of values usually found in the literature (Ferreira et al., 2008) which represent the tensions acting on the layers of the base and sub-base of pavements.

The tests started only after stabilizing the tensiometer readings with an average time of 5 min. The pullout speed adopted was 1.0 mm/min.

For the tests in the "DP" scenario, the box, where all the soil was compacted, was placed inside the oven at a constant temperature of 30°C, so as to simulate drying at room temperature and temperatures commonly found in the interior of the floor structure. The moisture loss was controlled through the initial mass of the box in relation to the final weight at the time of weighing.

After the soil had reached the desired moisture content, the box was packed with film paper and inserted into two tightly closed plastic bags in order to prevent the exchange of moisture with the medium, so that the suction was homogenously balanced throughout the volume of soil.

In order to simulate the drying effect of the soil in a constant ambient temperature, after the compaction of the soil, the box of the tests in the "DP" scenario was placed inside the oven at a constant temperature of 30°C. The loss of moisture was controlled through the difference between the initial and final mass of the box. The drying process was finished after the sample reached a moisture content of 18.75%. Then the box was packed with film paper and inserted into two tightly closed plastic bags in order to prevent the exchange of moisture with the environment and to balance the suction of the soil through the box.

Calculating the Confined Stiffness

In order to use the geosynthetics as a reinforcement for pavements, the initial stiffness of the system from a pullout stress becomes more representative than the maximum pullout resistance. The reinforced pavement design methods, such as French Geotextile Committee (1981), Giroud and Han (2004) and the Swiss Society of Geotextiles Professionals (1985), for

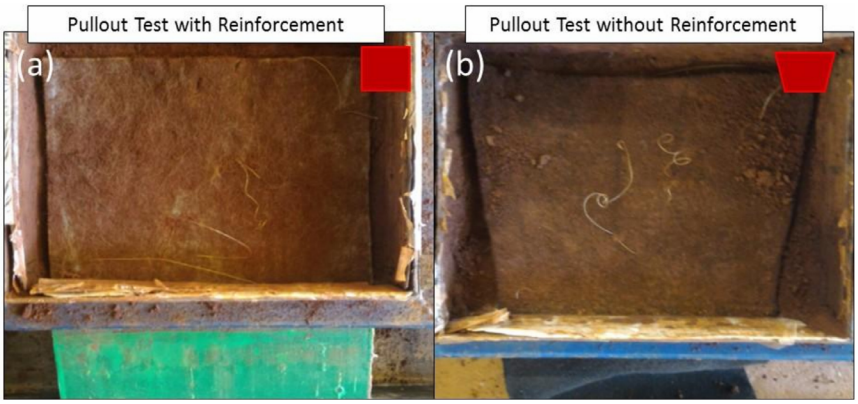

FIGURE 3 | Exhumation of non-woven geotextile after Pullout Test: **(a)** with reinforcement **(b)** without reinforcement.

example, use the tensile strength and the unconfined stiffness (Jn) of the geosynthetic as a design parameter.

As the reinforcement used in the work is in a confined system, the mechanical behavior of the geosynthetic inserted in the pavement structure differs from that observed in tensile strength tests. Thus, it is assumed that the geogrid deformations in a field situation are smaller than those obtained in unconfined tensile tests.

During the pullout test, readings of the tensile load and displacements along the geosynthetic were made by the load cell and the four tell-tales, respectively. The apparent confined deformation was obtained by the displacement difference between the sensors called D2 and D3 (**Figure 2**), whose initial relative distance is 4.5 cm.

Although the pullout test is not the most suitable test for this calculation, the criterion for obtaining the confined stiffness modulus (Jc) was defined as the ratio between the pullout force and the deformation of the geosynthetic between two sensors, as an approach for a quantitative analysis (Equation 1).

$$Jc = \frac{\text{Pullout Force } (\frac{\text{kN}}{\text{m}})}{\textit{Deformation between D3 and D2 (\%)}}$$

Ferreira et al. (2008) used the same method and the same pullout apparatus to obtain the confined stiffness of geogrids and woven geotextiles. Moraci and Recalcati (2006) and Cardile et al. (2016) used a similar approach, where the slope of the curves of displacement *vs.* position along the specimen represented the local strain.

Geosynthetics are extensible reinforcements whose deformation in the confined region usually is larger in the frontal zone and smaller at the bottom of the box. However, for short inclusions, due to the extensibility effect, the distribution of the displacement, and therefore, of the shear stress was almost uniform along the length of the reinforcement (Cardile et al., 2016). The purpose of the pullout test is not to take the geotextile to rupture. The test would not simulate the confinement throughout the geotextile for large displacements, since the pressure bag would act in a limited area of the sample. With the pullout test, we intend to study only the load-elongation behavior of the confined geotextile at low deformations, as in geotextile-reinforced pavements, deformation greater than 2% was not observed (Lanz, 1992; Martins, 2000; Mendes, 2006).

Fannin and Raju (1993) used strain gages to check the longitudinal deformation along the geosynthetic. Authors such as Palmeira (2009), Ferreira and Zornberg (2015), Bathurst and Ezzein (2017), and Zornberg et al. (2017) also presented different proposals and more complex approximations for the calculation of the confined stiffness of the geosynthetics using pullout tests. These approximations appear to be significantly better for the calculation of confined deformation of the geotextile than the calculation of the deformations directly by the displacement between two consecutive points.

RESULTS AND DISCUSSION

Figure 4 illustrates the behavior of the unconfined stiffness modulus curves and deformation of the non-woven geotextile. Unconfined stiffness was obtained by the ratio of tensile force and deformation between two points known in the wide-width tensile test (ABNT NBR ISO 10319, 2013). The curves did not present considerable variability between the specimens.

Figure 5 shows the pullout test curves with the non-woven geotextile in the Optimum Scenario (O) with an overload of 14 kPa, as well as its suction measured by the tensiometer. It can be observed that the closer to the frontal region of the box, the greater the displacements of the transducers. As expected, all the tests presented the same behavior pattern as the sensors. The suction showed a slight variation after reaching the maximum pullout strength.

Figure 6 shows the curves obtained by the average displacements of the tell-tales in the pullout tests, as well as their suctions.

Figure 7 shows the comparison between J_N (unconfined stiffness modulus) and J_C (confined stiffness modulus) of the non-woven geotextile used under different scenarios. In these charts, the Jn curve was that of the specimen that provided the intermediate values among the four specimens tested at the

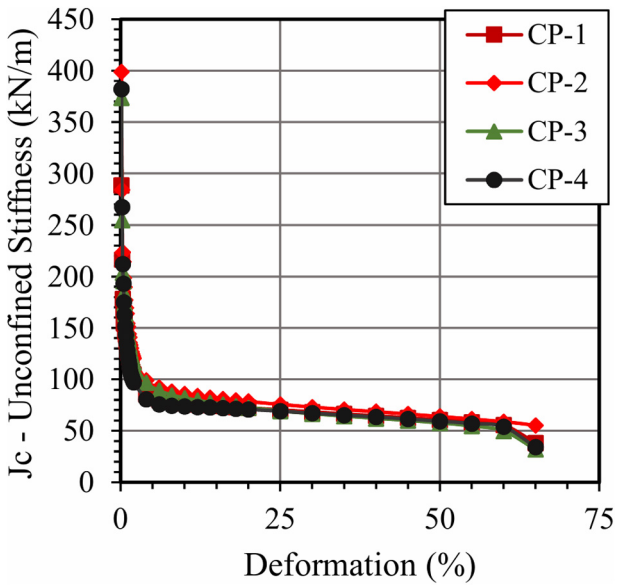

FIGURE 4 | Unconfined stiffness modulus curves of the wide-width tensile test.

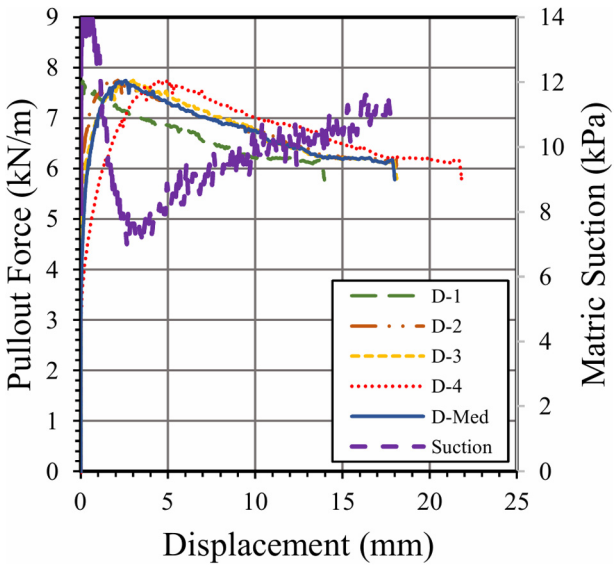

FIGURE 5 | Pull-out curves for different points along the geosynthetic and suction measured by the tensiometer (Condition O-14).

wide-width tensile test. The results presented stiffness curves with the same order of magnitude as the curves obtained by Ferreira et al. (2008) tested in the same small scale apparatus, but with granular soil in the upper layers. The curves obtained by Cardile et al. (2016), even using large boxes and an extruded geogrid with nominal tensile strength of 60 kN/m and vertical pressure of 50 kPa, also presented the same order of magnitude of the stiffness.

According to **Figure 7**, the tests in the "D" Scenario presented the greatest increase of stiffness caused by the overload, which agrees with the results obtained in marginal soils by Esmaili et al. (2014) and Portelinha et al. (2018), where the tests directly compacted at a moisture content lower than the optimum moisture content presented better performances than the tests in the Optimum Scenario. The confined stiffness was not evaluated in these works. Esmaili et al. (2014) suggested a possible influence of the soil structure in soils initially placed and compacted at the dry moisture content (D Scenario).

The "DP" and "O" scenarios presented a similar stiffness curve behavior for the two overloads. However, the "DP" Scenario has a higher matrix suction than "O" by the drying process and greater confined stiffness curves were expected, similar to the "S" Scenario presented (tested with the same suction). This may

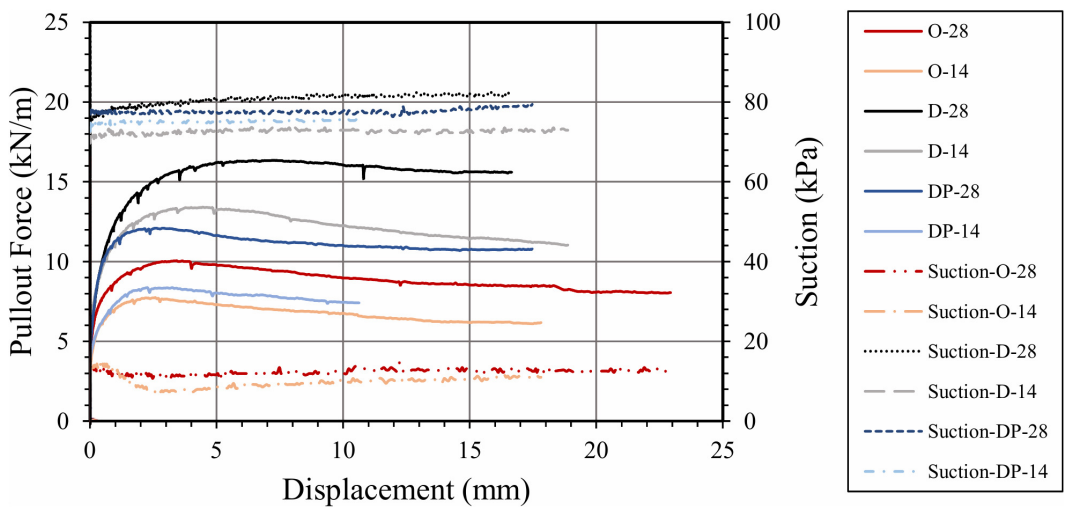

FIGURE 6 | Average displacement pull-out curves and their suction.

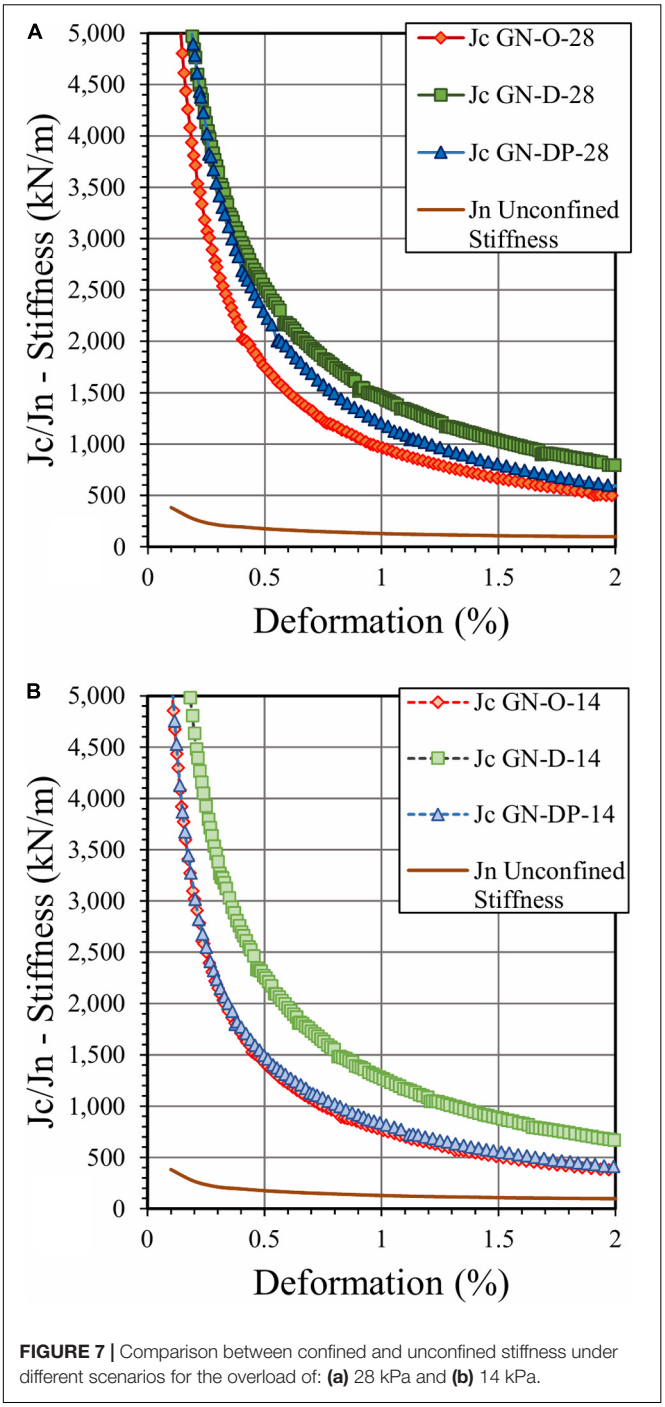

FIGURE 7 | Comparison between confined and unconfined stiffness under different scenarios for the overload of: **(a)** 28 kPa and **(b)** 14 kPa.

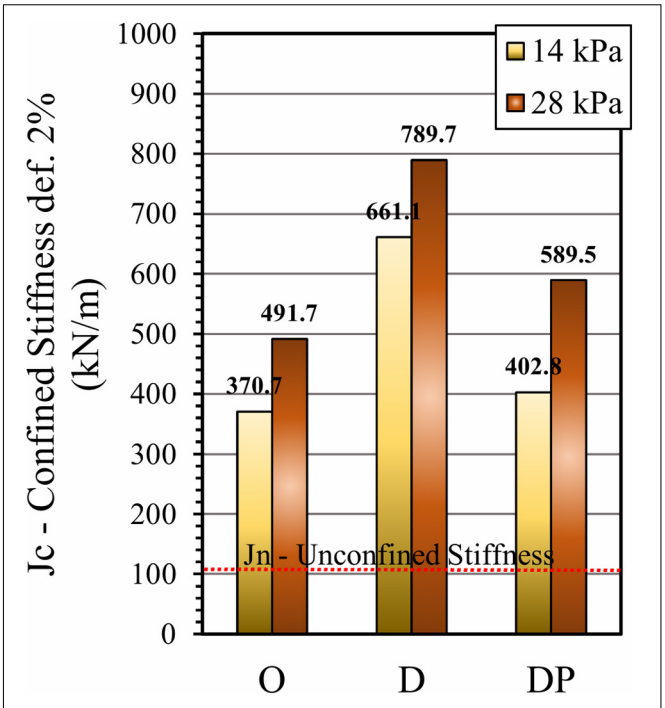

FIGURE 8 | Secant stiffness modulus obtained for a deformation of 2%.

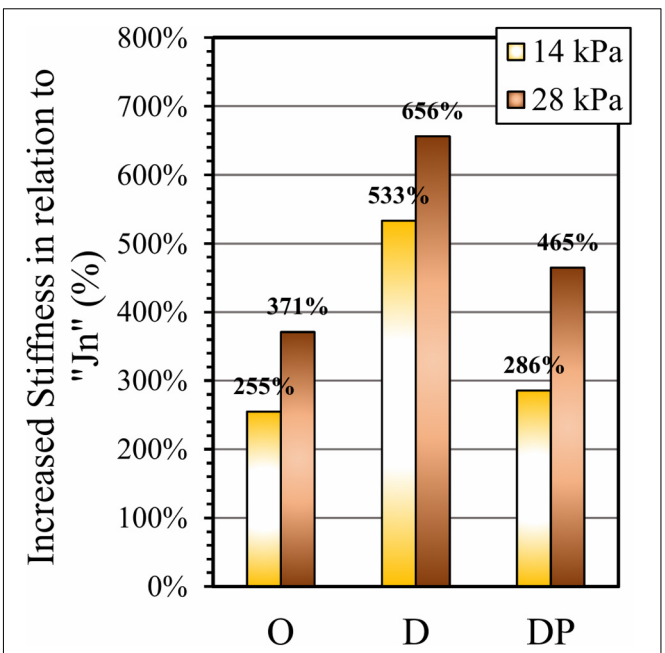

FIGURE 9 | Increase of stiffness to a deformation of 2% in relation to unconfined stiffness.

indicate the existence of other parameters involved in non-woven soil-geotextile interaction, such as soil structure or compaction energy, which may influence interface resistance even more than soil matrix suction itself, as suggested but not verified by Esmaili et al. (2014). The quantification of these parameters requires a parametric statistical analysis of the pullout tests, which does not contemplate the main objectives of this work.

Jotisankasa and Rurgchaisri (2018) investigated a geocomposite with marginal soils in controlled suction direct shear tests. In the sample preparation, the soil was compacted at the optimum moisture content with a subsequent drying process (DP scenario). The results showed a small increase in strength with suction (less than <15%) for MH and CH soils, which agrees with the results reported in the DP scenario of

the present research for pullout tests. The D scenario was not investigated by Jotisankasa and Rurgchaisri (2018).

Based on the secant stiffness modulus for a 2% deformation, usually required for engineering designs, **Figure 8** illustrates that all scenarios (O, D, and DP) presented a stiffness modulus above the unconfined stiffness, whose representation is given by the dashed horizontal line (104.4 kN/m). The increase in the overload provided an increase in the confined stiffness in all scenarios. The penetration of cohesive soil particles into the non-woven geotextile pores and the matrix suction at the interface of the geotextile, considered a draining material, are factors that may also have contributed to the increase in the confined stiffness of the geosynthetic. In the optimum scenario, Cardile et al. (2016) presented a magnitude of confined stiffness in the order of 800 kN/m for a 2% deformation, which was the same as unconfined stiffness.

Figure 9 illustrates the increase of secant stiffness in a 2% deformation in relation to the unconfined stiffness values "Jn." The "D" scenario in an overload of 28 kPa presented a stiffness increase of 656%. Even under low overloads, the lowest increase of stiffness presented was 255%, which attests the best performance of non-woven geotextile under confined conditions.

CONCLUSION

This work evaluated the confined stiffness of a non-woven geotextile, under different molding conditions, using monotonic pullout tests. After comparing these results with the unconfined stiffness, the following conclusions are reached:

The "D" Scenario had a stiffness on average 50% higher than the "DP" Scenario, both tested with the same suction of 75 kPa. It indicates that other parameters may be influencing the interaction between the soil and the geosynthetic, such as soil structure or changes in lateritic soil properties caused by the increase of compaction energy. A small increase of strength in DP Scenarios was also reported by Jotisankasa and Rurgchaisri (2018) in direct shear tests.

Although non-woven geotextiles are considered low stiffness materials and are often excluded as an option of reinforcement, these are presented as a favorable material when confined. In addition, in drier scenarios, typical in lateritic pavements, the geotextile also has an increase of stiffness. However, a larger number of tests, as well as additional analyses in real case studies, are needed to validate this statement in the field. In any case, the use of unconfined stiffness of non-woven geotextiles in projects can be considered a conservative attitude.

DATA AVAILABILITY STATEMENT

The datasets generated for this study are available on request to the corresponding author.

AUTHOR CONTRIBUTIONS

All authors listed have made a substantial, direct and intellectual contribution to the work, and approved it for publication.

FUNDING

The authors are grateful for the financial support received from the CAPES.

REFERENCES

ABNT NBR ISO 10319 (2013). *Geossintéticos - Ensaio de Tração Faixa Larga*. Rio de Janeiro: ABNT.

ASTM D 6706-01 (2013). *Standard Test Method for Measuring Geosynthetic Pullout Resistance in Soil*. West Conshohocken, PA: ASTM International.

Bathurst, R. J., and Ezzein, F. M. (2017). Insights into geogrid–soil interaction using a transparent granular soil. *Géotech. Lett.* 7, 179–183. doi: 10.1680/jgele.16.00191

Cardile, G., Moraci, N., and Calvarano, L. S. (2016). Geogrid pullout behavior according to the experimental evaluation of the active length. *Geosynth. Int.* 23, 194–205. doi: 10.1680/jgein.15.00042

Chang, D. T., Wang, W. J., and Wang, Y. H. (1998). "Laboratory study of the dynamic test system on geogrid reinforced subgrade soil," in *Proceedings of the International Conference on Geosynthetics*, Atlanta, 967–970.

Esmaili, D., Hatami, K., and Miller, G. A. (2014). Influence of matric suction on geotextile reinforcement-marginal soil interface strength. *Geotext. Geomembr.* 42, 139–153. doi: 10.1016/j.geotexmem.2014.01.005

Fannin, R. J., and Raju, D. M. (1993). On the pullout resistance of geosynthetics. *Can. Geotech. J.* 30, 408–417.

Ferreira, J. A. Z. (2007). *Estudo de Reforço de Pavimentos Com Ensaios de Arrancamento em Equipamento de Pequenas Dimensões*. dissertation/master's thesis, University of São Paulo, São Carlos.

Ferreira, J. A. Z., Bueno, B. S., and Zornberg, J. G. (2008). "Pavement reinforcement study using small dimension pullout equipment," in *Proceedings of the First Pan American Geosynthetics Conference & Exhibition*, Cancun, 963–972.

Ferreira, J. A. Z., and Zornberg, J. G. (2015). A transparent pullout testing device for 3D evaluation of soil–geogrid interaction. *Geotech. Test. J.* 38, 686–707.

French Geotextile Committee (1981). *Recommendations Pour l'emploi Des Geotextiles Dans Les Voles de Circulation Provisoures, Les Voies a Faible Traffic et les Couches de Forme*. Boulogne: Committee François des Geotextiles.

Giroud, J. P., and Han, J. (2004). Design method for geogrid-reinforced unpaved roads. I. Development of design method. *J. Geotech. Geoenviron. Eng.* 130, 775–786. doi: 10.1061/(asce)1090-0241(2004)130:8(775)

Jotisankasa, A., and Rurgchaisri, N. (2018). Shear strength of interfaces between unsaturated soils and composite geotextile with polyester yarn reinforcement. *Geotext. Geomembr.* 46, 338–353. doi: 10.1016/j.geotexmem.2017.12.003

Kakuda, F. M. (2005). *Estudo de Ensaios de Arrancamento de Geogrelha Com Utilização de Um Equipamento Reduzido*. dissertation/master's thesis, University of São Paulo, São Carlos.

Lanz, D. (1992). *Estudo de Deformabilidade e Tensões em Estruturas de Arrimo em Solo Reforçado com Geotêxteis*. dissertation/master's thesis, University of Brasilia, Brasília.

Martins, C. C. (2000). *Análise e Reavaliação de Estruturas em Solos Reforçados com Geotêxteis*. dissertation/master's thesis, Federal University of Ouro Preto, Ouro Preto.

Mendes, M. J. A. (2006). *Comportamento Carga-Alongamento de Geotêxteis Não Tecidos Submetidos à Tração Confinada*. dissertation/master's thesis, University of Brasilia, Brasília.

Moraci, N., and Recalcati, P. (2006). Factors affecting the pullout behavior of extruded geogrids embedded in a compacted granular soil. *Geotext. Geomembr.* 24, 220–242. doi: 10.1016/j.geotexmem.2006.03.001

Nogami, J. S., and Villibor, D. F. (1981). "Uma nova classificação de solos para finalidades rodoviárias," in *Proceedings of the Simpósio Brasileiro de Solos Tropicais em Engenharia*, Rio de Janeiro, 30–41.

Palmeira, E. M. (2009). Soil–geosynthetic interaction: modelling and analysis. *Geotextext. Geomembr.* 27, 368–390. doi: 10.1016/j.geotexmem.2009.03.003

Portelinha, F. H. M., Pereira, V. R. G., and Correia, N. S. (2018). Small-scale pullout test of a geogrid-reinforced unsaturated soil with suction monitoring. *Geotech. Test. J.* 41, 787–804. doi: 10.1520/GTJ20150182

Swiss Society of Geotextiles Professionals (1985). *Le Manuel des Geotextiles. Association Suisse des Professionels des Geotextiles*. Dübendorf: EMPA.

Vilar, O. M., and Bueno, B. S. (2008). "Some topics regarding the influence of non-saturation on the behavior of reinforced soil structures built with tropical soils," in *Proceedings of the First Pan American Geosynthetics Conference & Exhibition*, Cancun, 272–280.

Villibor, D. F., Nogami, J. S., Cincerre, J. R., Serra, P. R. M., and Neto, A. Z. (2009). *Pavimentos de Baixo Custo para Vias Urbanas*, 2ª Edn. São Paulo: Arte & Ciência.

Zornberg, J. G., Roodi, G. H., and Gupta, R. (2017). Stiffness of soil–geosynthetic composite under small displacements: I. Model development. *J. Geotech. Geoenviron. Eng.* 143:135153460. doi: 10.1061/GT.1943-5606.0001768

Conflict of Interest: The authors declare that the research was conducted in the absence of any commercial or financial relationships that could be construed as a potential conflict of interest.

frontiers in Built Environment

ORIGINAL RESEARCH
published: 08 March 2021
doi: 10.3389/fbuil.2021.628016

Probabilistic Bearing Capacity of a Pavement Resting on Fibre Reinforced Embankment Considering Soil Spatial Variability

*Kouseya Choudhuri and Debarghya Chakraborty**

Department of Civil Engineering, Indian Institute of Technology, Kharagpur, India

This paper intends to examine the influence of spatial variability of soil properties on the probabilistic bearing capacity of a pavement located on the crest of a fibre reinforced embankment. An anisotropic random field, in combination with the finite difference method, is used to carry out the probabilistic analyses. The cohesion and internal friction angle of the soil are assumed to be lognormally distributed. The Monte Carlo simulations are carried out to obtain the mean and coefficient of variation of the pavement bearing capacity. The mean bearing capacity of the pavement is found to decrease with the increase in horizontal scale of fluctuation for a constant vertical scale of fluctuation; whereas, the coefficient of variation of the bearing capacity increases with the increase in horizontal scale of fluctuation. However, both the mean and coefficient of variation of bearing capacity of the pavement are observed to be increasing with the increase in vertical scale of fluctuation for a constant horizontal scale of fluctuation. Apart from the different scales of fluctuation, the effects of out of the plane length of the embankment and randomness in soil properties on the probabilistic bearing capacity are also investigated in the present study.

Keywords: fibre-reinforced embankment, probabilistic analysis, spatial variability, finite difference method, Monte Carlo simulations, out of the plane length of the embankment

OPEN ACCESS

Edited by:
Castorina Silva Vieira,
University of Porto, Portugal

Reviewed by:
Sanjay Shrawan Nimbalkar,
University of Technology Sydney, Australia
Deepthi Dilip,
Birla Institute of Technology and Science, United Arab Emirates

****Correspondence:***
Debarghya Chakraborty
debarghya@civil.iitkgp.ac.in

Specialty section:
This article was submitted to Transportation and Transit Systems, a section of the journal Frontiers in Built Environment

Received: *10 November 2020*
Accepted: *15 January 2021*
Published: *08 March 2021*

Citation:
Choudhuri K and Chakraborty D (2021) Probabilistic Bearing Capacity of a Pavement Resting on Fibre Reinforced Embankment Considering Soil Spatial Variability. Front. Built Environ. 7:628016. doi: 10.3389/fbuil.2021.628016

INTRODUCTION

Soil reinforced with fibres in optimum quantity is proven to be one of the most efficient and economical means of ground improvement technique over the past few decades. Fibre reinforcement not only improves the unconfined compressive strength and shear strength properties of the soil (Cai et al., 2006; Consoli et al., 2010), it also increases the tensile strength (Tang et al., 2016; Cristelo et al., 2017). Both the natural and synthetic fibres are used as reinforcement to enhance the mechanical properties of the soil. Because of cost-effectiveness, easy availability, and eco-friendly nature, the use of natural fibres (such as jute, sisal, coir, etc.) has gained popularity over the period. Several studies are there on the soil reinforced with natural fibre (Prabakar and Sridhar, 2002; Ghosh et al., 2005; Babu and Vasudevan, 2008; Chaple and Dhatrak, 2013; Singh and Bagra, 2013). The major drawback of using natural fibre is its biodegradation caused by microorganisms in soil which may reduce the long term applicability of the reinforcement (Tang et al., 2016). Thus it gives rise to the use of synthetic fibres as soil reinforcement. Many researchers have studied the effectiveness of using synthetic fibre-reinforced soil (Michalwoski and Cermak, 2002; Kumar et al., 2007; Tang et al., 2007; Consoli et al., 2010; Chen et al., 2015; Correia et al., 2015; Ates, 2016; Bouaricha et al., 2017; Cristelo

et al., 2017; Sharma and Kumar, 2017). The reinforcing effects of fibres on the behavior of soils have been investigated numerically by several authors (Babu et al., 2007; Toh et al., 2017; Arora and Kumar, 2019; Sharma and Kumar, 2019; Wang et al., 2019).

All of the studies, as mentioned above, are deterministic in which the soil is assumed to be a single homogeneous layer or a stratified medium with uniform soil properties. It is well known that soil is very much heterogeneous and random because of its different geological formation processes and mineralogical constituents. Thus considering soil as a homogeneous medium may lead to the unreliable design of civil engineering structures. Many researchers conducted the probabilistic studies assessing the randomness in the soil as well as spatial variability (Fenton and Griffiths, 2001; Griffiths et al., 2002; Fenton and Griffiths, 2005; Luo et al., 2011; Cassidy et al., 2012; Li et al., 2014; Jha, 2016; Zaskórski et al., 2017). There is a huge possibility that the mixing of fibres with soil may not be uniform, which may lead to the randomness in fibre reinforced soil. Very few probabilistic and reliability based studies are available on fibre reinforced soil (Ranjan et al., 1996; Moghal et al., 2016; Diab et al., 2017; Moghal et al., 2017; Syed and GuhaRay, 2020). Johari and Kalantari (2016) carried out a probabilistic analysis of slope stability of embankment reinforced with discrete polypropylene fibre. But spatial variability of soil properties was not considered in their study. However, it is essential to consider the spatial variability as over a certain length of soil domain the strength properties may change. In past, many literature (Griffiths and Fenton, 2004; Suchomel and Masin, 2009; Kasama and Whittle, 2015) considered the soil spatial variability in slope stability problems. Recently, Luo and Bathurst (2018); Halder and Chakraborty (2019) have carried out the probabilistic analyses on geogrid reinforced embankment considering soil spatial variability to investigate the load-settlement behavior.

The main objective of this paper is to investigate the effect of soil spatial variability on the performance of a pavement located on the top of the fibre-reinforced embankment. Different horizontal and vertical scales of fluctuation are chosen to study the influence of soil spatial variability. It is to be noted that all the probabilistic studies stated above were based on plane strain condition. To the best of authors' knowledge, there is no probabilistic study available on the fibre-reinforced embankment considering spatially variable soil parameters. Note that, for spatially variable soil it is essential to consider the length of the model in out of plane direction as it significantly affects the mean and coefficient of variation of load-carrying capacity of the geotechnical structures (Kawa and Pula, 2019). Hence, the influence of different out of the plane lengths of the embankment on the bearing capacity of the pavement is also explored based on both deterministic and probabilistic studies. Here only the embankment soil is assumed to be fibre-reinforced. In contrast to that, the foundation soil is kept as unreinforced. The randomness and spatial variability of the soil properties are considered for both embankment and foundation soil, and their effects are included by associating the finite difference mesh and random field. Three-dimensional finite-difference software ($FLAC^{3D}$) is used to carry out the numerical analyses. The probabilistic results are obtained using the Monte Carlo simulation technique. Finally, failure probabilities of the bearing capacity of the pavement are computed for different horizontal and vertical scales of fluctuation.

PROBLEM DEFINITION

Figure 1 depicts the embankment slope geometry considered in the present numerical analyses. The embankment having a height of 5 m and an inclination of 1.5 H:1 V is filled with fibre-reinforced soil consisting of improved cohesion (c) and angle of internal friction (ϕ); whereas, the foundation soil is assumed to be unreinforced with lower shear strength properties. A pavement of width 3.5 m (B = 3.5 m) is located at the crest of the embankment. The present work means to estimate the probabilistic bearing capacity of the pavement for a certain settlement value, which can be expressed as mean (μ_q) and coefficient of variation (COV_q) of bearing capacity of the pavement.

NUMERICAL MODELING

Three-dimensional explicit finite difference software, $FLAC^{3D}$ is engaged to generate the three-dimensional modeling of the embankment and to accomplish the numerical analyses. The domain size of the problem, in both horizontal and vertical direction, is chosen in such a way that there should not be any boundary effect. The displacement along the bottom boundary edge is fixed in both horizontal and vertical directions; whereas, the side boundaries are horizontally restricted in order to allow the vertical displacement only. Eight noded brick shaped elements are used for discretization of the problem domain. A comparatively finer mesh is generated to model the embankment soil; while, coarser mesh is chosen in order to model the foundation soil. The Mohr-Coulomb yield criterion is incorporated to simulate the behavior of embankment and foundation soil. However, it should be mentioned that embankment soil and foundation soil may differ in terms of type, composition and strength requirements. Hence, the use of only Mohr-Coulomb yield criterion for both type of soil may not represent the real scenario. It can be considered as one of the limitations of this study. The soil parameters of fibre-reinforced embankment soil and unreinforced foundation soil considered in the numerical analyses are taken as provided by Sharma and Kumar (2019) and given in **Table 1**.

After modeling the embankment slope geometry and allocating the soil properties node wise, the loading is simulated on the nodes representing pavement width (and along with the out of the plane length of the pavement) by implementing a very small amount of downward velocity in vertical direction. An optimized velocity of magnitude 5×10^{-6} m/step is taken after few trials, as it is found to be less time-consuming as well as does not affect the pavement bearing pressure settlement response (Halder and Chakraborty, 2020). The numerical model is then run for numerous steps until the plastic steady state is achieved.

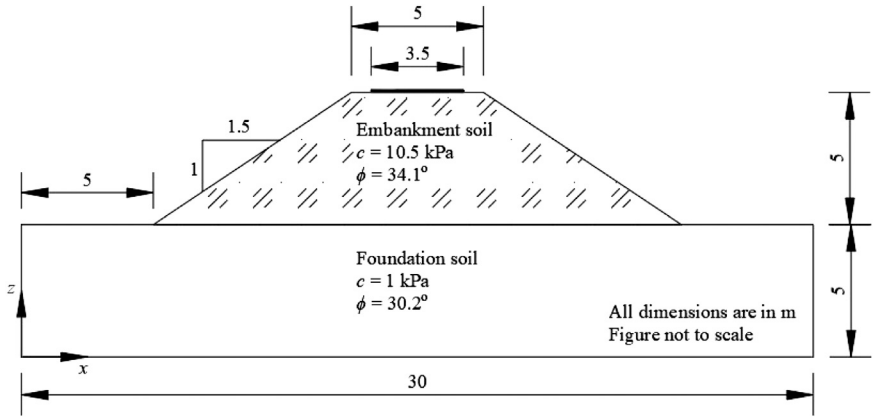

FIGURE 1 | Schematic diagram of the fiber reinforced embankment.

TABLE 1 | Parameters used for embankment and foundation soil.

Parameters	Fibre-reinforced embankment soil	Unreinforced foundation soil
% of fibre	1.25	0
Elastic modulus, E (kPa)	9,000	6,800
Poisson's ratio, μ	0.3	0.3
Dry unit weight, γ_d (kN/m^3)	15.1	15.1
Cohesion, c (kPa)	10.5	1.0
The angle of internal friction, ϕ (°)	34.1	30.2

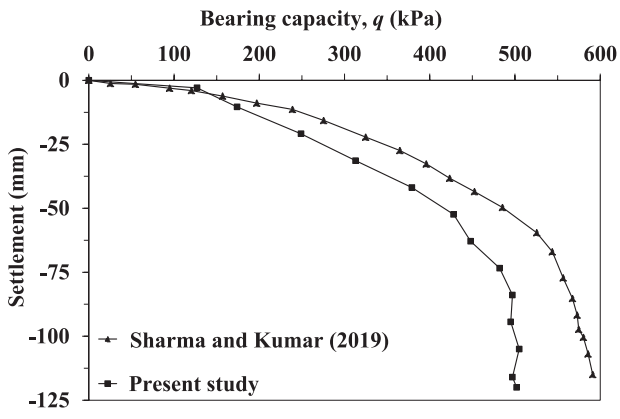

FIGURE 2 | Comparison between present study and Sharma and Kumar (2019).

VALIDATION OF THE PRESENT STUDY

Before carrying out the numerical analyses, the finite difference model is validated with the available study. Since there is no probabilistic study available on fibre-rerinforced embankment considering soil spatial variability, the present result is verified with the deterministic results of Sharma and Kumar (2019). They carried out a deterministic three-dimensional numerical study on bearing capacity of ring and circular foundation resting on two-layered sand using finite element method in which top layer sand is reinforced with fibre, and the underlying layer of sand is kept as unreinforced. In the present work, only the circular footing and the two-layered soil system are modeled with identical geometry and soil properties. The bearing capacity and footing settlement curve is obtained and compared with that of Sharma and Kumar (2019). **Figure 2** illustrates that the present bearing pressure-settlement response is comparatively lower than that obtained in literature which may be due to the difference in mesh generation and applied numerical scheme. The obtained result from present study is observed to be in the conservative side.

DETERMINISTIC ANALYSIS

Before implementing the probabilistic analyses, deterministic analyses are carried out on the numerical model where both the foundation and embankment soil properties are considered to be uniform or homogeneous. At first, the whole system is modeled using unreinforced soil properties for different out of the plane lengths (L_{op}). Then only the embankment soil is modeled considering reinforced soil properties. Both the unreinforced and reinforced bearing capacity-settlement response curves obtained for different L_{op} are illustrated in **Figure 3**. It is quite obvious that the embankment soil reinforced with fibre is having a higher bearing capacity than

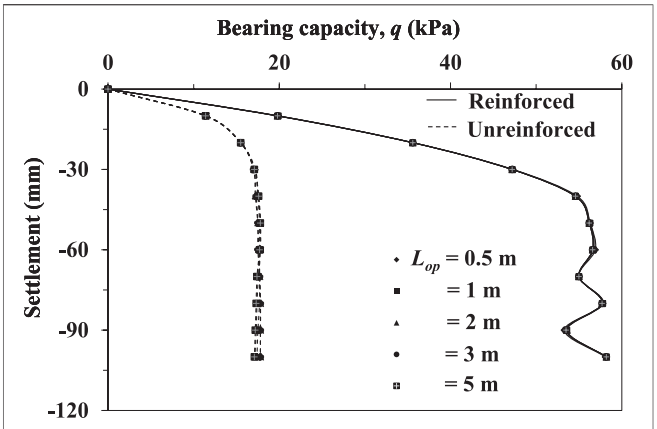

FIGURE 3 | Bearing capacity-settlement response curve for unreinforced and reinforced embankment with different L_{op} without considering spatial variability.

the unreinforced soil. As an example, the bearing capacity of the pavement for L_{op} = 3 m is increased from 17.5 kPa to 56.6 kPa corresponding to 60 mm of settlement value when the unreinforced embankment is replaced with fibre reinforcement. The bearing capacity of the pavement for unreinforced embankment tends to increase from 17.7 kPa for L_{op} = 0.5 m to 17.8 kPa for L_{op} = 1 m, then it decreases to 17.5 kPa for L_{op} = 3 m and further increase to 17.7 kPa for L_{op} = 5 m corresponding to the same settlement value as stated earlier. In case of reinforced embankment, it decreases from 56.9 kPa for L_{op} = 0.5 m to 56.6 kPa for L_{op} = 2 m. Beyond L_{op} = 2 m, it remains almost unaltered. Although the differences in bearing capacity for different L_{op} are very negligible, it signifies the importance of carrying out the probabilistic analysis to investigate the influence of different L_{op} on the probabilistic bearing capacity of the pavement.

PROBABILISTIC ANALYSIS

Random Field Generation

The variations of the properties of the in–situ soil can be represented by the mean value, coefficient of variation and scales of fluctuation (SOFs) (Haldar and Babu, 2008). Most of the studies (Griffiths et al., 2002; Haldar and Babu, 2008; Ahmed and Soubra, 2014) have considered the cohesion (c) as lognormally distributed random field represented by mean (μ_c) and standard deviation (σ_c). The lognormal distribution is chosen to avoid the generation of negative values of soil parameters. Due to the fundamental nature of the parameter tanϕ in the equation of Mohr-Coulomb yield criterion, it is modeled as a lognormally distributed random field rather than ϕ itself. A lognormal distribution of tanϕ ensures that the friction angle is bounded by $0 < \phi < 90^{\circ}$ (Griffiths et al., 2011).

A lognormally distributed random field can be expressed as:

$$c\left(\tilde{X}_i\right) = \exp\left\{\mu_{\ln c}\left(\tilde{X}\right) + \sigma_{\ln c}\left(\tilde{X}\right) \cdot G_c\left(\tilde{X}\right)\right\} \quad (1)$$

$$\phi\left(\tilde{X}_i\right) = \tan^{-1}\left[\exp\left\{\mu_{\ln \tan\phi}\left(\tilde{X}\right) + \sigma_{\ln \tan\phi}\left(\tilde{X}\right) \cdot G_\phi\left(\tilde{X}\right)\right\}\right] \quad (2)$$

where $\tilde{X} = \tilde{X}(\tilde{x}, \tilde{y}, \tilde{z})$ is the spatial position at which c and ϕ are desired. $G(\tilde{X})$ is a normally distributed random field with zero mean and unit variance. The values of $\mu_{\ln c}, \mu_{\ln \tan\phi}$ and $\sigma_{\ln c}, \sigma_{\ln \tan\phi}$ are determined using Lognormal distribution transformation given by

$$\sigma^2_{\ln c} = \ln\left(1 + \frac{\sigma_c^2}{\mu_c^2}\right) = \ln\left(1 + COV_c^2\right) \quad (3)$$

$$\sigma^2_{\ln \tan\phi} = \ln\left(1 + \frac{\sigma^2_{\tan\phi}}{\mu^2_{\tan\phi}}\right) = \ln\left(1 + COV^2_{\tan\phi}\right) \quad (4)$$

$$\mu_{\ln c} = \ln \mu_c - \frac{1}{2}\sigma^2_{\ln c} \quad (5)$$

$$\mu_{\ln \tan\phi} = \ln \mu_{\tan\phi} - \frac{1}{2}\sigma^2_{\ln \tan\phi} \quad (6)$$

where $\mu_{\tan\phi}$ and $\sigma_{\tan\phi}$ are the mean and standard deviation of tanϕ, which is lognormally distributed.

The correlation function $[\rho(\tau)]$ which is also known as Markov correlation function, can be expressed as

$$\rho\left(\tau_x, \tau_y, \tau_z\right) = \exp\left(\frac{-2|\tau_x|}{\delta_x} + \frac{-2|\tau_y|}{\delta_y} + \frac{-2|\tau_z|}{\delta_z}\right) \quad (7)$$

where $\tau_x = |\tilde{x}_2 - \tilde{x}_1|$, $\tau_y = |\tilde{y}_2 - \tilde{y}_1|$ and $\tau_z = |\tilde{z}_2 - \tilde{z}_1|$ are the absolute distance between two points. Parameters δ_x, δ_y and δ_z are the SOFs in x, y and z directions, respectively. The correlation matrix is decomposed into the product of a lower triangular matrix (L_t) and its transpose by Cholesky decomposition,

$$\rho\left(\tau_x, \tau_y, \tau_z\right) = L_t L_t^T \quad (8)$$

Using the lower triangular matrix, the random field can be generated which is shown by

$$G = \sum_{j=1}^{i} L_{t_{ij}} Z_j, \quad i = 1, 2, \ldots, n \quad (9)$$

where Z_j is the sequence of independent standard normal random variables.

In the present study, both the c and tanϕ for embankment soil are considered as random variables. Since the foundation soil is having very low value of cohesion (c = 1 kPa), it is considered as constant; whereas, only tanϕ is chosen as the random variable. The mean values of c and tanϕ used in the probabilistic analysis are taken as the constant property values for deterministic analysis. Typical values of coefficient of variation (COV) for tanϕ and c and the horizontal SOF ($\delta_x/B = \delta_y/B$) as well as the vertical SOF (δ_z/B) are selected from Phoon and Kulhawy (1999). The probabilistic parameters considered in the present study are listed in **Table 2**. It should be mentioned here that there is no cross-correlation considered between tanϕ and c.

The nodal coordinates of the finite difference mesh are taken from FLAC^{3D} and imported to MATLAB. In MATLAB, the Markov correlation function given in **Eq. 7** is used to generate the random field. The randomly distributed c and ϕ values generated in MATLAB are again taken back to FLAC^{3D} and are allocated node wise (Halder and Chakraborty, 2018; Halder and Chakraborty, 2020). In this way, the random fields are generated in FLAC^{3D}.

TABLE 2 | Probabilistic parameters considered in the present study.

Parameters	Fibre-reinforced embankment soil	Unreinforced foundation soil
Mean cohesion, μ_c (kPa)	10.5	—
Mean of the tangent of the angle of internal friction, $\mu_{\tan\phi}$	tan (34.1°)	tan (30.2°)
Coefficient of variation of cohesion, COV_c (%)	25	—
Coefficient of variation of the tangent of the angle of internal friction, $COV_{\tan\phi}$ (%)	10, 20	10, 20
Horizontal scale of fluctuation ($\delta_x/B = \delta_y/B$)	0.5, 1, 1.5, 2, 4, 10	0.5, 1, 1.5, 2, 4, 10
Vertical scale of fluctuation (δ_z/B)	0.25, 0.5, 0.75, 1, 2, 8	0.25, 0.5, 0.75, 1, 2, 8

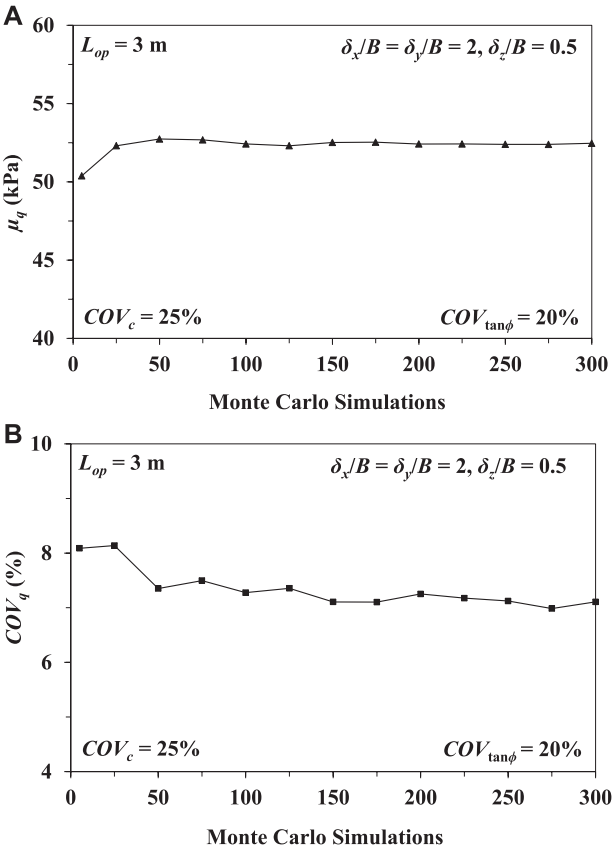

FIGURE 4 | Variation of **(A)** mean bearing capacity of the pavement with respect to number of Monte Carlo simulations; **(B)** coefficient of variation of bearing capacity of the pavement with respect to number of Monte Carlo simulations.

Monte Carlo Simulations

For each set of statistical parameters, such as COV_c, $COV_{\tan\phi}$ and δ_i (where $i = x, y$ and z), the Monte Carlo simulations are carried out in probabilistic analyses to evaluate the mean and COV of the bearing capacity (μ_q and COV_q) of the pavement. It should be mentioned here that the number of realizations of the Monte Carlo simulations should be such that the stable solution of μ_q and COV_q are achieved. The fluctuations between two consecutive realizations of μ_q and COV_q should fall within a tolerable range, which is between 5% and 10% (Haldar and Babu, 2008). Each realization, while having the identical underlying statistical values, may have a quite different spatial pattern of the soil strength parameters under the pavement and hence different magnitude of bearing capacity is obtained after each realization. In the present study, FISH codes are written in FLAC^{3D} to carry out the Monte Carlo simulations. It has been observed that 300 simulations are required to achieve a stable estimate of mean and coefficient of variation of bearing capacity. As a representative case, the variations of μ_q and COV_q (corresponding to 60 mm settlement) as a function of the Monte Carlo simulations for fiber-reinforced embankment with L_{op} = 3 m, are shown in **Figures 4A,B**.

Results Obtained in the Probabilistic Analyses

Effects of the spatial variablity, randomness in the soil properties and different out of the plane lengths of the embankment on the mean and COV of bearing capacity of the pavement are discussed in the following sub-sections. All the probabilistic analyses carried out here are only for fibre-reinforced embankment. As the variation of soil properties of natural deposit in the horizontal direction is generally quite less compared to that of the vertical direction due to the process of deposition, an anisotropic random field is generated for the present study where the vertical SOFs are chosen to be less than the horizontal one. The horizontal and vertical SOFs are varied as per **Table 2**. However, during the parametric study, there may be some situations where isotropic random fields are generated and vertical SOF is greater than horizontal SOF.

Effect of the out of the Plane Length of the Embankment (L_{op}) on Probabilistic Bearing Capacity

The effect of different L_{op} on μ_q and COV_q is investigated by considering $\delta_x/B = \delta_y/B$ = 2 and δ_z/B = 0.5 for both embankment and foundation soil, and COV_c = 25% for embankment soil only. The effects of two different coefficients of variation of soil friction angle ($COV_{\tan\phi}$) for both embankment and foundation soil are also studied in this section. **Figures 5A,B** illustrate the behavior of μ_q and COV_q for different L_{op} and $COV_{\tan\phi}$. As per **Figure 5A** the magnitude of μ_q for a particular value of $COV_{\tan\phi}$, at first tends to decrease with an increase in L_{op} from 0.5 to 1 m, then it increases and after L_{op} = 3 m the change in μ_q is found to be insignificant. As an example, μ_q decreases from 52.36 kPa for L_{op} = 0.5 m to 51.95 kPa for L_{op} = 1 m and then increases to 52.41 kPa for L_{op} = 3 m for a constant value of $COV_{\tan\phi}$ = 20%. The increase in μ_q beyond L_{op} = 3 m is quite less. The effect of $COV_{\tan\phi}$ on μ_q is quite prominent. It is evident that with an increase in $COV_{\tan\phi}$, there is an increase in variability in the angle of internal friction, which in

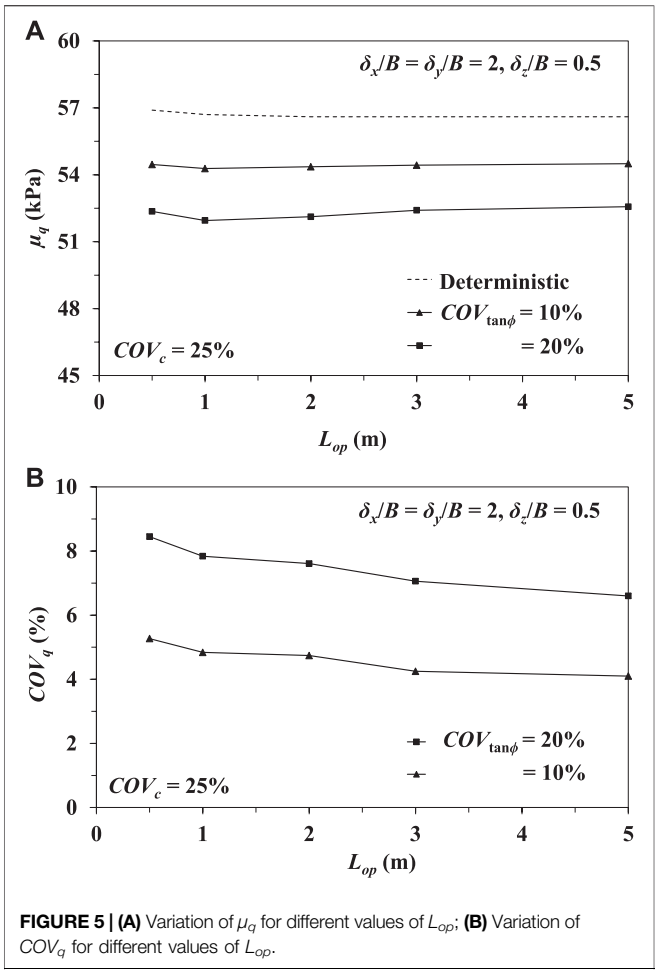

FIGURE 5 | (A) Variation of μ_q for different values of L_{op}; **(B)** Variation of COV_q for different values of L_{op}.

turn reduces the value of μ_q. For a particular value of L_{op} = 3 m, μ_q decreases from 54.43 to 52.41 kPa with an increase in $COV_{\tan\phi}$ from 10 to 20%. However, in all the cases, the magnitudes of μ_q are less than the deterministic bearing capacity values.

The effect of L_{op} on COV_q is depicted in **Figure 5B**. In contrast to μ_q, COV_q is decreasing with the increase in L_{op}. As an example, COV_q decreases from 8.45 to 6.6% as L_{op} increases from 0.5 to 5 m for a constant value of $COV_{\tan\phi}$ = 20%. Unlike μ_q, COV_q increases with the increment in the magnitude of $COV_{\tan\phi}$ as the increase in $COV_{\tan\phi}$ causes an increasing randomness of angle of internal friction. For example, the COV_q increases from 4.25 to 7.06% with the increase in $COV_{\tan\phi}$ from 10 to 20% for L_{op} = 3 m.

Random Field Plots Considering Spatial Variability

The random fields are generated by implementing the aforesaid theory using FLAC^{3D} and MATLAB. Since there is no significant difference in μ_q beyond L_{op} = 3 m, all the studies considering spatial variability are done for L_{op} = 3 m only. **Figures 6A–D** represent the random field plots of ϕ for both embankment and foundation soil with different $\delta_x/B = \delta_y/B$, δ_z/B, $COV_{\tan\phi}$ = 20% and out of the plane length (L_{op}) = 3 m for a particular realization. **Figures 6A,B** show that randomness of ϕ decreases in horizontal direction with the increase in $\delta_x/B = \delta_y/B$ value from 0.5 to 4 for the constant value of δ_z/B = 0.5. Similar observation can be made for variation of ϕ in vertical direction from **Figures 6C,D** where δ_z/B is increased from 0.25 to 2 for the constant value of $\delta_x/B = \delta_y/B$ = 2. **Figures 6A,D** both exhibit isotropic spatial variation field where lower values of SOFs represent more erratic field of ϕ and higher values of SOFs represent almost uniform nature of ϕ. **Figures 7A–D** illustrate the same patterns of the random field of c for the embankment soil only with different SOFs, L_{op} = 3 m and COV_c = 25%.

Effect of Horizontal SOFs on the Probabilistic Bearing Capacity

Figures 8A,B demonstrate the variation in μ_q and COV_q corresponding to different values of $\delta_x/B = \delta_y/B$ for the constant values of L_{op} = 3 m, $COV_{\tan\phi}$ = 20%, COV_c = 25%, and δ_z/B = 0.5. The $\delta_x/B = \delta_y/B$, δ_z/B and $COV_{\tan\phi}$ are kept as same for both embankemt and foundation soil; whereas, COV_c = 25% is considered for embankment soil only. The lower value of horizontal SOF indicates that the soil friction angle field is very much erratic in horizontal directions whereas the increased value of horizontal SOF specifies the uniform nature of the soil friction angle in horizontal direction. **Figure 8A** depicts that the μ_q decreases with the increase in $\delta_x/B = \delta_y/B$ values. In contrast to that, the COV_q increases with $\delta_x/B = \delta_y/B$ as illustrated in **Figure 8B**. For an instance, the values of μ_q decreases from 53.78 to 51.91 kPa with the increase in values of $\delta_x/B = \delta_y/B$ from 0.5 to 4, the reduction in μ_q beyond $\delta_x/B = \delta_y/B$ = 4 is quite negligible; whereas, the values of COV_q increases from 3.73 to 10.55% with the increase in values of $\delta_x/B = \delta_y/B$ from 0.5 to 10. However, the rate of increase in COV_q beyond $\delta_x/B = \delta_y/B$ = 4 is comparatively less than that of before $\delta_x/B = \delta_y/B$ = 4.

Effect of Vertical SOFs on the Probabilistic Bearing Capacity

The influences of different vertical SOFs (δ_z/B) on the probabilistic bearing capacity of the pavement are demonstrated in **Figures 9A,B** for the constant values of L_{op} = 3 m, $COV_{\tan\phi}$ = 20%, COV_c = 25%, and $\delta_x/B = \delta_y/B$ = 2. In the present study, the values of δ_z/B are varied from 0.25 to 8. Unlike the horizontal SOF, the μ_q is found to be increasing with the increasing magnitude of δ_z/B. The obtained trend is also true for COV_q. For an example, the value of μ_q increases from 52.03 to 54.57 kPa and COV_q increases from 5.66 to 10.8% as the δ_z/B increases from 0.25 to 8. However, the rate of increase in μ_q and COV_q beyond δ_z/B = 2 is considerably less than that of before δ_z/B = 2.

Effect of Soil Spatial Variability on the Failure of the System

In the present work, the failure of the pavement is presented through the maximum shear stress contour profiles. **Figures 10A–C** demonstrate maximum shear stress contours for the embankment as well as the foundation soil system having either homogenous soil field or spatially distributed soil field with L_{op} = 3 m. The ultimate state loading condition of the pavement is chosen for all the cases. **Figure 10A** shows the maximum shear stress profile for the deterministic analysis

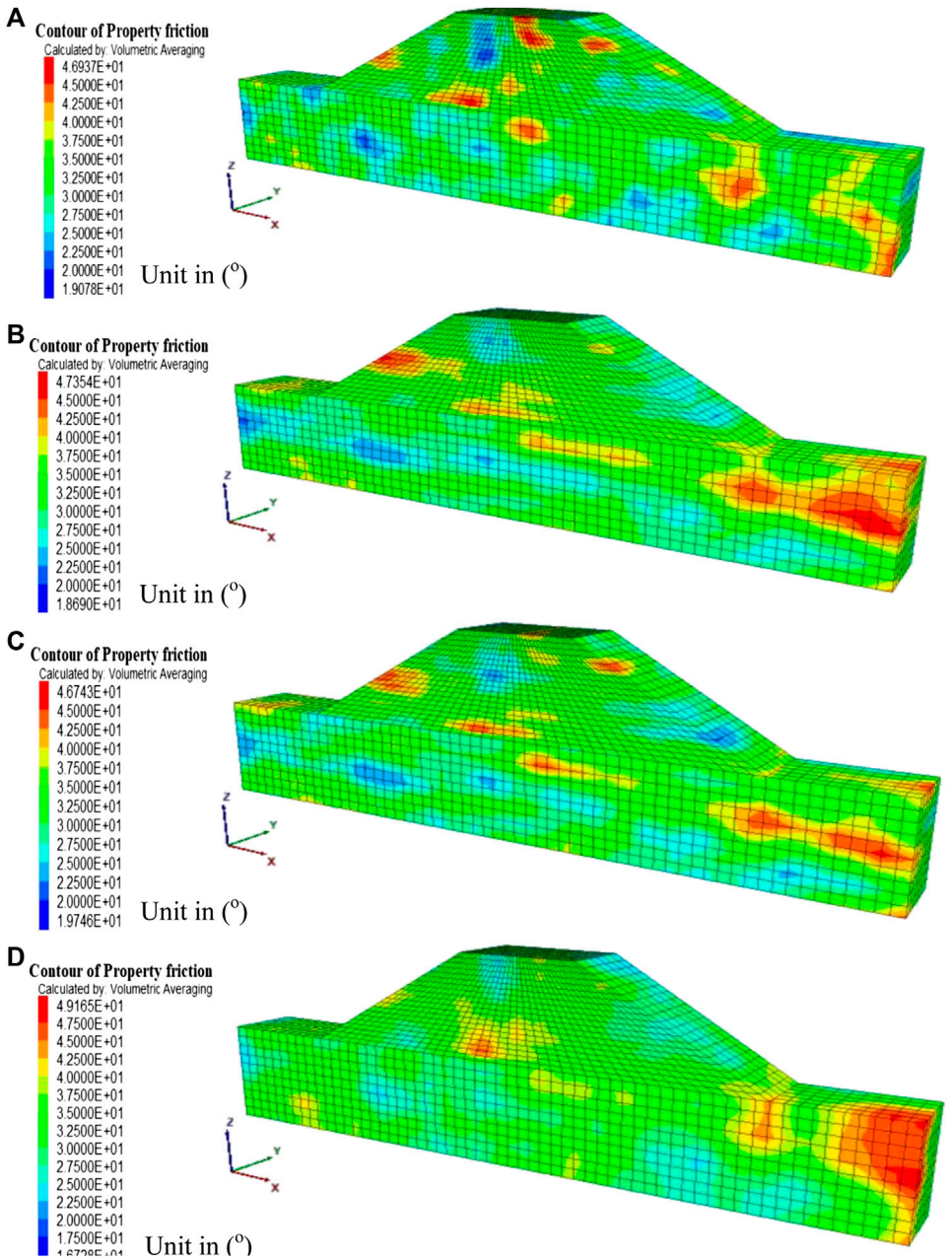

FIGURE 6 | Random distribution of ϕ for both embankment and foundation soil with L_{op} = 3 m, $COV_{\tan\phi}$ = 20% and, **(A)** $\delta_x/B = \delta_y/B = 0.5$, $\delta_z/B = 0.5$; **(B)** $\delta_x/B = \delta_y/B = 4$, $\delta_z/B = 0.5$; **(C)** $\delta_x/B = \delta_y/B = 2$, $\delta_z/B = 0.25$; **(D)** $\delta_x/B = \delta_y/B = 2$, $\delta_z/B = 2$.

where the plastic zones are fully developed under the edges of the pavement and the highest magnitude of the maximum shear stress is found to be 36.22 kPa. The plastic zones are symmetric and extended to the bottom of the embankment soil; whereas, the maximum shear stress contours remain no longer symmetric when the spatial variability of the soil properties is considered. **Figures 10B,C** represent the maximum shear stress profile for the $\delta_x/B = \delta_y/B = 0.5$, $\delta_z/B = 0.5$ and $\delta_x/B = \delta_y/B = 2$, $\delta_z/B = 2$, respectively with the constant values of $COV_c = 25\%$, $COV_{\tan\phi} = 20\%$ and $L_{op} = 3$ m. It is observed that the plastic zones are not fully developed under edges of the pavement for $\delta_x/B = \delta_y/B = 0.5$, $\delta_z/B = 0.5$ which may be due to the presence of higher values of shear strength properties of the soil under the pavement; whereas, they are almost developed in case of $\delta_x/B = \delta_y/B = 2$, $\delta_z/B = 2$. However, in both the cases they are extended to the mid depth of the embankment. The highest values of maximum shear stress reduced from 45.28 kPa for $\delta_x/B = \delta_y/B = 0.5$, $\delta_z/B = 0.5$ to 42.06 kPa for $\delta_x/B = \delta_y/B = 2$, $\delta_z/B = 2$ and both the values are comparatively higher than the deterministic value.

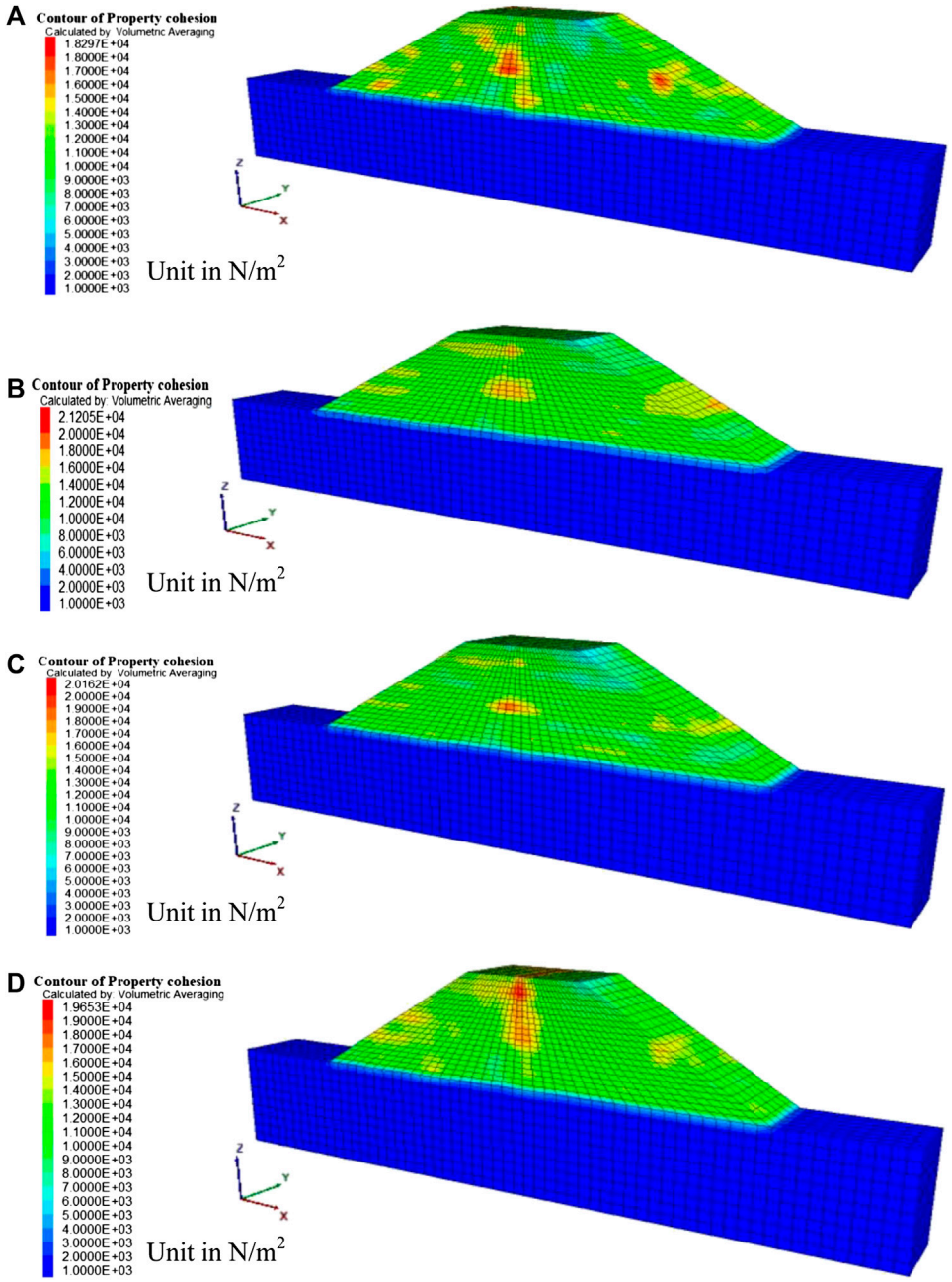

FIGURE 7 | Random distribution of c for embankment soil with L_{op} = 3 m, COV_c = 25% and, **(A)** $\delta_x/B = \delta_y/B = 0.5$, $\delta_z/B = 0.5$; **(B)** $\delta_x/B = \delta_y/B = 4$, $\delta_z/B = 0.5$; **(C)** $\delta_x/B = \delta_y/B = 2$, $\delta_z/B = 0.25$; **(D)** $\delta_x/B = \delta_y/B = 2$, $\delta_z/B = 2$.

Failure Probability of the Pavement

As per the design point of view, the pavement is considered as unserviceable when the applied stress on the pavement (q_{app}) is equal or greater than the allowable bearing capacity (q_{all}) of the pavement. Thus, the limit state of collapse of the pavement can be expressed as $q_{all} \leq q_{app}$. In the present situation, q_{app} is the deterministic bearing capacity and q_{all} is the mean probabilistic bearing capacity. Since the assumed distributions for c and $\tan\phi$ are lognormal, then the q_{all} is most likely to be lognormally distributed. So, the failure probability of the pavement can be expressed by **Eq. 10**.

$$p_f = P\left(q_{all} \leq q_{app}\right) = \Phi\left(\frac{\ln\left(q_{app}/FOS\right) - \mu_{\ln q_{all}}}{\sigma_{\ln q_{all}}}\right) \quad (10)$$

In the above mathematical expression $\Phi(\cdot)$ represents the cumulative normal distribution and FOS denotes the factor of

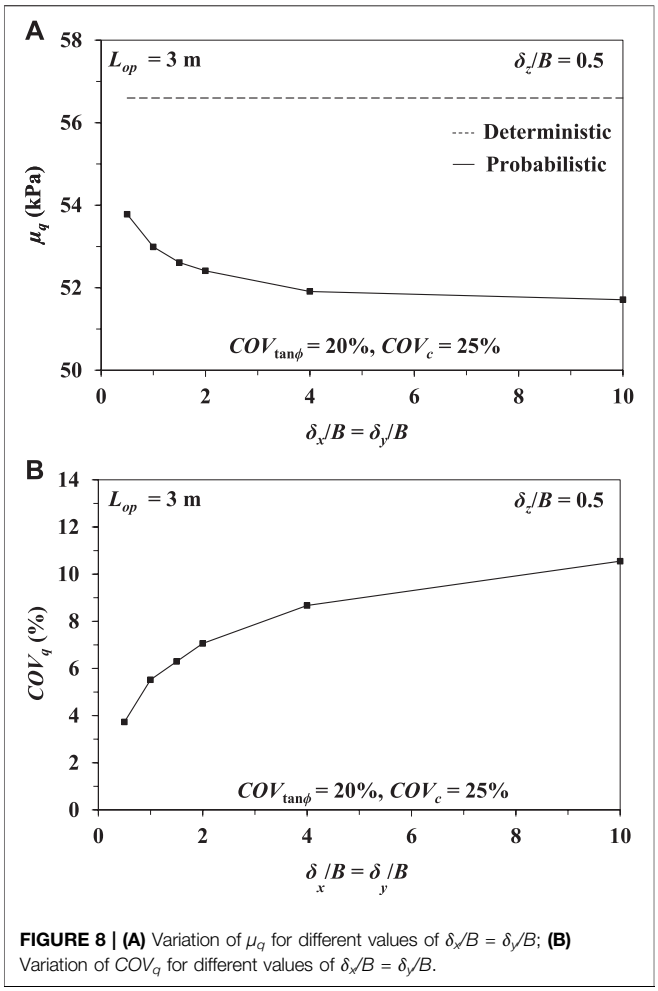

FIGURE 8 | (A) Variation of μ_q for different values of $\delta_x/B = \delta_y/B$; **(B)** Variation of COV_q for different values of $\delta_x/B = \delta_y/B$.

safety considered for the design of the pavement. The assumption of considering allowable bearing capacity as lognormally distributed is further assured by performing Kolmogorov–Smirnov (K–S) "goodness of fit" test which is illustrated in **Figure 11**. The K–S test compares the variation between the actual cumulative frequency and the cumulative distribution function of allowable bearing capacity with assumed theoretical lognormal distribution for L_{op} = 3 m, $COV_{\tan\phi}$ = 20%, COV_c = 25%, $\delta_x/B = \delta_y/B$ = 2.0 and δ_z/B = 0.5. The actual frequency of allowable bearing capacity shows a reasonable resemblance with the lognormal fit.

Figures 12A,B indicate that the failure probability of the system decreases with the increase in *FOS* irrespective of horizontal SOF as well as vertical SOF, which is quite obvious. **Figure 12A** illustrates the variation of failure probability (p_f) for different values of *FOS* and horizontal SOF with the constant values of L_{op} = 3 m, $COV_{\tan\phi}$ = 20%, COV_c = 25%, and δ_z/B = 0.5. For a critical value of *FOS* = 1, the probability of failure reduces with the increase in $\delta_x/B = \delta_y/B$. In contrast, it increases with the increasing values of $\delta_x/B = \delta_y/B$ for higher factor of safety. This can be attributed as while the *FOS* = 1, for small values of $\delta_x/B = \delta_y/B$, the COV_q is comparatively smaller than the larger values of $\delta_x/B = \delta_y/B$. Therefore, the μ_q tends to drop below the limiting value and the failure probability increases. However, with the increase in $\delta_x/B = \delta_y/B$, the failure probability decreases due to the increase in stability for *FOS* = 1. For higher values of *FOS*, the μ_q is found to be pushed above the limiting value which reduces the failure probability for small values of $\delta_x/B = \delta_y/B$. However, the increase in $\delta_x/B = \delta_y/B$ causes increasing instability which in turn increases the failure probability of the system for higher *FOS*.

Similar type of response has been observed in **Figure 12B** which represents the variation of failure probability (p_f) for different values of *FOS* and vertical SOF with the constant values of L_{op} = 3 m, $COV_{\tan\phi}$ = 20%, COV_c = 25%, and $\delta_x/B = \delta_y/B$ = 2. However, in this figure, the failure probability is found to be decreasing with the increasing δ_z/B for *FOS* = 1 and 1.1. For *FOS* greater than 1.1, the failure probability is increasing with the increase in δ_z/B. Beyond a certain scale of fluctuation, the failure probability is observed to be almost insensitive with the scale of fluctuation for both the figures. The similar kind of trend has been observed by Griffiths and Fenton (2004), Chenari and Alaie (2015) and, Halder and Chakraborty (2020).

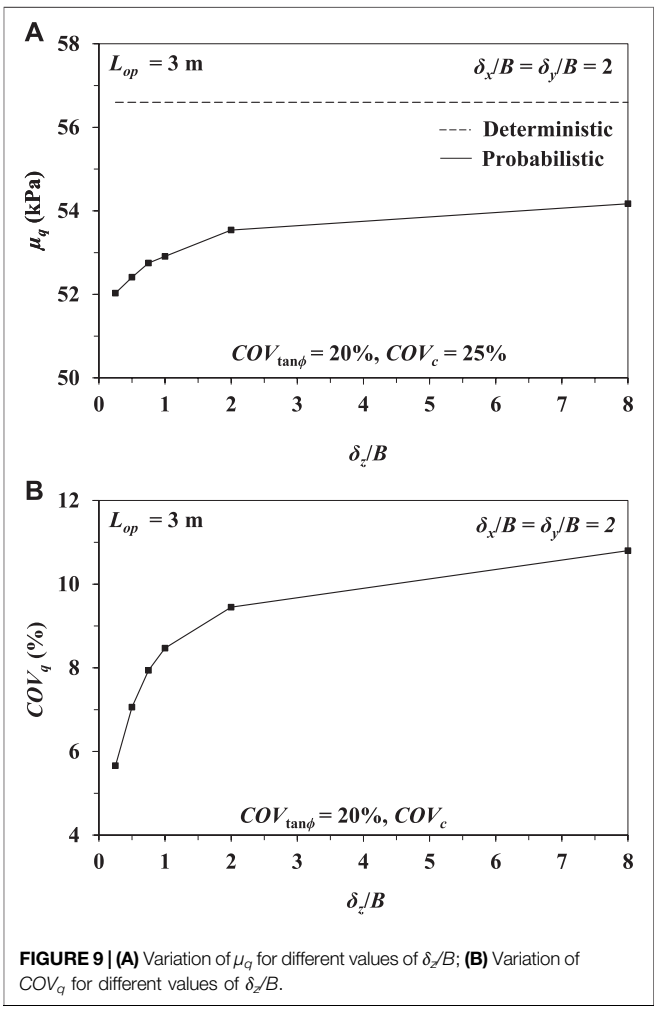

FIGURE 9 | (A) Variation of μ_q for different values of δ_z/B; **(B)** Variation of COV_q for different values of δ_z/B.

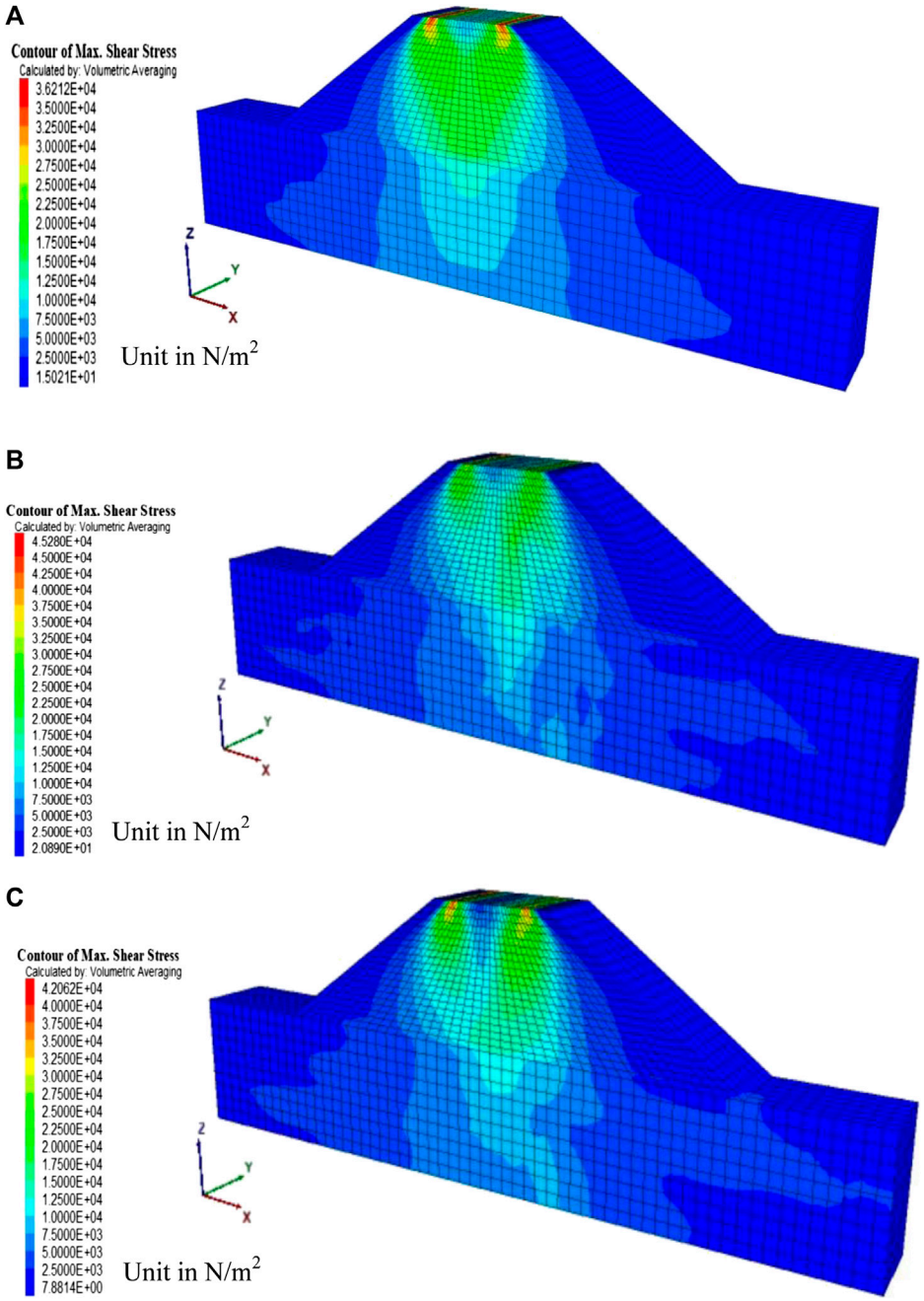

FIGURE 10 | Maximum shear stress distribution for fibre-reinforced embankment with L_{op} = 3 m and, **(A)** Uniform soil properties; **(B)** $\delta_x/B = \delta_y/B = 0.5$, $\delta_z/B = 0.5$, COV_c = 25%, $COV_{\tan\phi}$ = 20%; **(C)** $\delta_x/B = \delta_y/B = 2$, $\delta_z/B = 2$, COV_c = 25%, $COV_{\tan\phi}$ = 20%.

Figures 12A,B also compare the failure probability between the consideration of spatial variability and without consideration of spatial variability for different values of *FOS*. It is evident from the figures that the failure probability without consideration of spatial variability does not depend upon the scale of fluctuation. It is also observed in **Figure 12A** that for *FOS* = 1, the failure probability without considering the spatial variability is lower than that of considering the spatial variability. For *FOS* = 1.1, the probability of failure for smaller values of $\delta_x/B = \delta_y/B$ is found to be lower as compared to that of without consideration of spatial variability; whereas, for higher values of $\delta_x/B = \delta_y/B$, it becomes higher than that of without considering the spatial variability. However, for *FOS* greater than 1.1, the failure probability without considering the spatial variability is found to be quite higher as compared to that of considering the spatial variability. For an instance, p_f drops from 86.99% with the consideration of spatial variability ($\delta_x/B = \delta_y/B = 2$ and $\delta_z/B = 0.5$) to 60.4% without considering the spatial variability for *FOS* = 1. For *FOS* = 1.1, the failure probability for $\delta_x/$

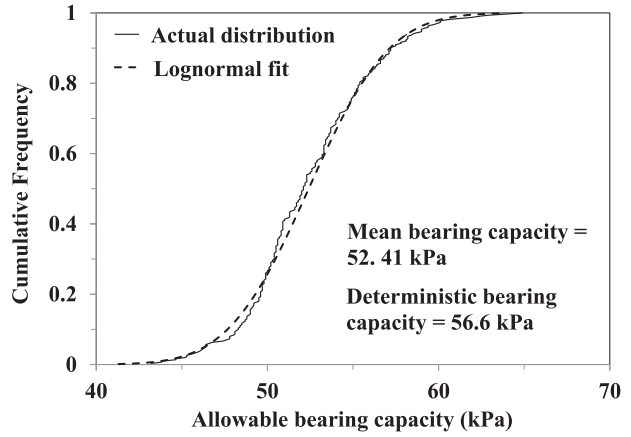

FIGURE 11 | Comparison between actual distribution and the assumed theoretical lognormal distribution of allowable bearing capacity for L_{op} = 3 m, $COV_{\tan\phi}$ = 20%, COV_c = 25%, $\delta_x/B = \delta_y/B$ = 2 and δ_z/B = 0.5.

$B = \delta_y/B$ = 1.5 and δ_z/B = 0.5 becomes 37.4% which is lower as compared to 43.9% (p_f corresponding to without considering the spatial variability); whereas, it increases to 50.2% for $\delta_x/B = \delta_y/B$ = 10 and δ_z/B = 0.5. However, for *FOS* = 1.2, p_f increases from 14.4% with the consideration of spatial variability ($\delta_x/B = \delta_y/B$ = 4 and δ_z/B = 0.5) to 29.7% without undertaking the spatial variability. Similar kind of responses are observed in **Figure 12B**. However, unlike $\delta_x/B = \delta_y/B$, in case of δ_z/B, the probabilities of failure without considering the spatial variability are found to be higher for *FOS* greater than 1, as compared to that of considering the spatial variability. As an example, p_f decreases from 73.8% with the consideration of spatial variability ($\delta_x/B = \delta_y/B$ = 2 and δ_z/B = 2) to 60.4% without considering the spatial variability for *FOS* = 1; whereas, for *FOS* = 1.2, it increases from 10.9% with the consideration of spatial variability ($\delta_x/B = \delta_y/B$ = 2 and δ_z/B = 8) to 29.7% without undertaking the spatial variability.

CONCLUSIONS

The present paper presents the three-dimensional probabilistic bearing capacity–settlement response of the pavement located on the crest of the embankment where the embankment soil is considered to be fibre-reinforced. The deterministic as well as the probabilistic studies are executed. The probabilistic parameters considered for the random field generation are taken from the previous studies. In probabilistic analyses, the effects of soil spatial variability, randomness of soil properties and different out of the plane lengths have been studied. The conclusions drawn from the study are as follows:

1. The mean bearing capacity of the pavement is found to be decreased first with increasing values of the out of the plane length of the embankment (L_{op} = 0.5–1 m), and after that, it starts to increase with the increase in L_{op} (L_{op} = 1–3 m). Beyond L_{op} = 3 m, there is no significant change in it. In contrast to that, the COV_q is observed to be decreasing with the increasing value of L_{op}. It signifies that the consideration of different out of the plane lengths with spatial variability is quite important as it makes the problem more realistic.
2. The mean bearing capacity is found to be reducing with the increment in randomness in the soil friction angle ($COV_{\tan\phi}$); whereas, the COV_q increases with the increase in randomness in the soil friction angle which is quite obvious as it leads to the lower strength paths for failure.
3. The mean and *COV* of bearing capacity of the pavement are turned up to be decreasing and increasing, respectively with the increasing values of horizontal SOF. Unlike the horizontal SOFs, the mean and *COV* of bearing capacity both are found to be increasing with the increasing vertical SOFs.
4. The plastic zones under the pavement edges are found to be fully developed for homogeneous soil; whereas, they are partially developed for spatially variable soil. The highest values of maximum shear stress for spatially varied soil are found to be higher than that of soil with uniform strength

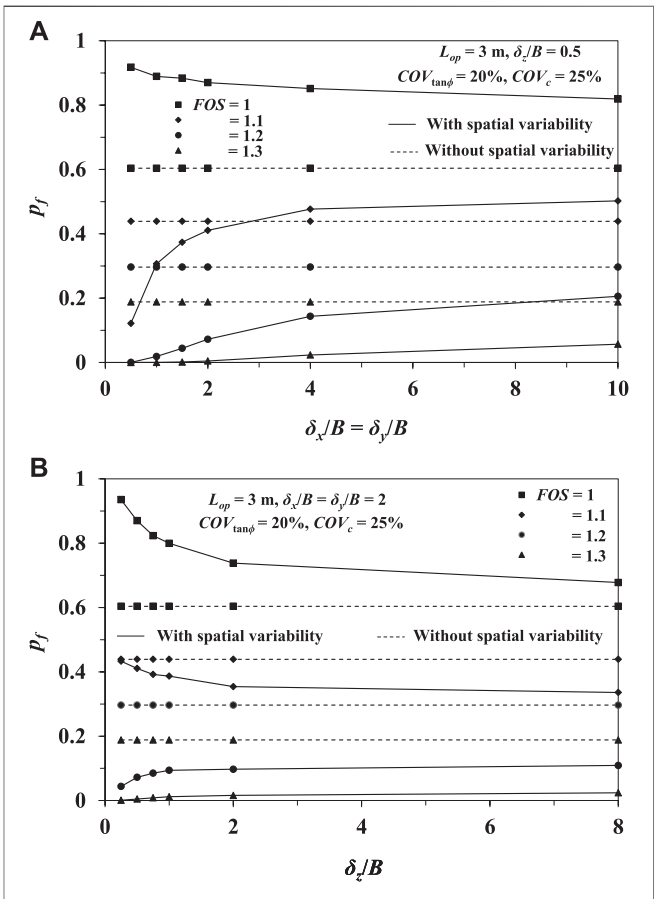

FIGURE 12 | Variation of failure probability for different values of *FOS* with the variation of **(A)** $\delta_x/B = \delta_y/B$; **(B)** δ_z/B.

properties which implicates the importance of using spatial variation of the soil properties.

5. The failure probability of the pavement is found to be decreasing with the increase in scale of fluctuation for lower values of *FOS*; whereas, it is observed to be increasing with the increasing values of scale of fluctuation for higher values of *FOS*.
6. The failure probability of the pavement is observed to be 29.7% for *FOS* = 1.2 when the spatial variation of soil properties is not considered; whereas, it is found to be reduced to 9.73% for *FOS* = 1.2, $\delta_x/B = \delta_y/B = 2$, and $\delta_z/B = 2$. This further signifies the importance of considering spatial variability of the soil shear strength properties.

DATA AVAILABILITY STATEMENT

The raw data supporting the conclusion of this article will be made available by the authors, without undue reservation.

AUTHOR CONTRIBUTIONS

KC generated the MATLAB and FISH codes to carry out the probabilistic study and prepared the initial draft. DC proposed the project, supervised all the works and revised the initial draft to give the final shape of the paper.

REFERENCES

Ahmed, A., and Soubra, A. -H. (2014). Reliability analysis at ultimate and serviceability limit states of obliquely loaded circular foundation. *Geotech. Geol. Eng.* 32, 729–738. doi:10.1007/s10706-014-9750-y

Arora, S., and Kumar, A. (2019). Bearing capacity of circular footing resting on fiber-reinforced pond ash overlying soft clay. *J. Hazard. Toxic Radioact. Waste* 24 (1), 04019037. doi:10.1061/(ASCE)HZ.2153-5515.0000485

Ates, A. (2016). Mechanical properties of sandy soils reinforced with cement and randomly distributed glass fibers (GRC). *Compos. B. Eng.* 96, 295–304. doi:10.1016/j.compositesb.2016.04.049

Babu, G. L. S., Vasudevan, A. K., and Haldar, S. (2007). Numerical simulation of fiber-reinforced sand behaviour. *Geotext. Geomembr.* 26, 181–188. doi:10.1016/j.geotexmem.2007.06.004

Babu, G. L. S., and Vasudevan, A. K. (2008). Strength and stiffness response of coir fiber-reinforced tropical soil. *J. Mater. Civ. Eng.* 20, 571–577. doi:10.1061/(ASCE)0899-1561(2008)20:9(571)

Bouaricha, L., Henni, A. H., and Lancelot, L. (2017). A laboratory investigation on shear strength behaviour of sandy soil: effect of glass fiber and clinker residue content. *Studia Geotech. et Mech.* 39 (4), 3–15. doi:10.1515/sgem-2017-0032

Cai, Y., Shi, B., Ng, C. W. W., and Tang, C. (2006). Effect of polypropylene fiber and lime admixture on engineering properties of clayey soil. *Eng. Geol.* 87, 230–240. doi:10.1016/j.enggeo.2006.07.007

Cassidy, M. J., Uzielli, M., and Tian, Y. (2012). Probabilistic combined loading failure envelopes of a strip footing on spatially variable soil. *Comput. Geotech.* 49, 191–205. doi:10.1061/(ASCE)GT.1943-5606.0001219

Chaple, P. M., and Dhatrak, A. I. (2013). Performance of coir fiber reinforced clayey soil. *Int. J. Eng. Sci.* 2 (4), 54–64.

Chen, M., Shen, S.-L., Arulrajah, A., Wu, H.-N., Hou, D.-W., and Xu, Y.-S. (2015). Laboratory evaluation on the effectiveness of polypropylene fibers on the strength of fiber-reinforced and cement-stabilized Shanghai soft clay. *Geotext. Geomembr.* 43, 515–523. doi:10.1016/j.geotexmem.2015.05.004

Chenari, R. J., and Alaie, R. (2015). Effects of anisotropy in correlation structure on the stability of an undrained clay slope. *Georisk* 9 (2), 109–123. doi:10.1080/17499518.2015.1037844

Consoli, N. C., Bassani, M. A. A., and Festugato, L. (2010). Effect of fiber-reinforcement on the strength of cemented soils. *Geotext. Geomembr.* 28, 344–351. doi:10.1016/j.geotexmem.2010.01.005

Correia, A. A. S., Oliviera, P. J. V., and Custodio, D. G. (2015). Effect of polypropylene fibers on the compressive and tensile strength of a soft clay, artificially stabilised with binders. *Geotext. Geomembr.* 43, 97–106. doi:10.1016/j.geotexmem.2014.11.008

Cristelo, N., Cunha, V. M. C. F., Gomes, A. T., Araujo, N., Miranda, T., and Lopes, M. L. (2017). Influence of fiber reinforcement on the post-cracking behaviour of a cement-stabilised sandy-clay subjected to indirect tensile stress. *Constr. Build. Mater.* 138, 163–173. doi:10.1016/j.conbuildmat.2017.02.010

Diab, A. A., Najjar, S., and Sadek, S. (2017). Reliability-based design of spread footings on fiber-reinforced clay. *Georisk* 12 (2), 135–151. doi:10.1080/17499518.2017.1398332

Fenton, G. A., and Griffiths, D. V. (2005). Three dimensional probabilistic foundation settlement. *J. Geotech. Geoenviron. Eng.* 131 (2), 232–239. doi:10.1061/(ASCE)1090-0241(2005)131:2(232)

Fenton, G. A., and Griffiths, D. V. (2001). "Bearing capacity of spatially random c—ϕ soils," in Proceedings, 10th international conference on computer methods and advances in geomechanics, Tucson, AZ, 7–12 January, 2001, Vol. 1, 1411–1415.

Ghosh, A., Ghosh, A., and Bera, A. K. (2005). Bearing capacity of square footing on pond ash reinforced with jute-textile. *Geotext. Geomembr.* 23, 144–173. doi:10.1016/j.geotexmem.2004.07.002

Griffiths, D. V., and Fenton, G. A. (2004). Probabilistic slope stability analysis by finite elements. *J. Geotech. Geoenviron. Eng.* 130 (5), 507–518. doi:10.1061/(ASCE)1090-0241(2004)130:5(507)

Griffiths, D. V., Fenton, G. A., and Manoharan, N. (2002). Bearing capacity of rough rigid strip footing on cohesive soil: probabilistic study. *J. Geotech. Geoenviron. Eng.* 128 (9), 743–755. doi:10.1061/(ASCE)1090-0241(2002)128:9(743)

Griffiths, D. V., Huang, J., and Fenton, G. A. (2011). Probabilistic infinite slope analysis. *Comput. Geotech.* 38, 577–584. doi:10.1016/j.compgeo.2011.03.006

Haldar, S., and Babu, G. L. S. (2008). Effect of soil spatial variability on the response of laterally loaded pile in undrained clay. *Comput. Geotech.* 35, 537–547. doi:10.1016/j.compgeo.2007.10.004

Halder, K., and Chakraborty, D. (2020). Influence of soil spatial variability on the response of strip footing on geocell—reinforced slope. *Comput. Geotech.* 122, 103533. doi:10.1016/j.compgeo.2020.103533

Halder, K., and Chakraborty, D. (2019). Probabilistic bearing capacity of strip footing on reinforced soil slope. *Comput. Geotech.* 116, 103213. doi:10.1016/j.compgeo.2019.103213

Halder, K., and Chakraborty, D. (2018). Probabilistic stability analyses of reinforced slope subjected to strip loading. *Geotech. Eng. J. SEAGS & AGSSEA* 49 (4), 92–99.

ITASCA (2012). *FLAC 3D Version 5.01 Fast Lagrangian analysis of continua in 3 dimensions*. Minneapolis, MN: ITASCA Consulting Group Inc.

Jha, S. K. (2016). Reliability—based analysis of bearing capacity of strip footings considering anisotropic correlation of spatially varying undrained shear strength. *Int. J. GeoMech.* 16 (5), 06016003. doi:10.1061/(ASCE)GM.1943-5622.0000638

Johari, A., and Kalantari, A. R. (2016). "Probabilistic analysis of slope stability of embankment reinforced with discrete fiber," in 5th international conference on geotechnical engineering and soil mechanics, Tehran, Iran, November 14–16, 2016.

Kasama, K., and Whittle, A. J. (2015). Effect of spatial variability on the slope stability using random field numerical limit analysis. *Georisk* 10 (1), 42–54. doi:10.1080/17499518.2015.1077973

Kawa, M., and Puła, W. (2019). 3D bearing capacity probabilistic analyses of footings on spatially variable c—ϕ soil. *Acta Geotech* 15 (6), 1453–1466. doi:10.1007/s11440-019-00853-3

Kumar, A., Walia, B. S., and Bajaj, A. (2007). Influence of fly ash, lime, and polyester fibers on compaction and strength properties of expansive soil. *J. Mater. Civ. Eng.* 19, 242–248. doi:10.1061/(ASCE)0899-1561(2007)19:3(242)

Li, J., Tian, Y., and Cassidy, M. J. (2014). Failure mechanism and bearing capacity of footings buried at various depths in spatially random soil. *J. Geotech.*

Geoenviron. Eng. 141 (2), 04014099. doi:10.1061/(ASCE)GT.1943-5606.0001219

Luo, N., and Bathurst, R. J. (2018). Deterministic and random FEM analysis of full scale unreinforced and reinforced embankments. *Geosynth. Int.* 25 (2), 164–179. doi:10.1680/jgein.17.00040

Luo, Z., Atamturktur, S., Cai, Y., and Juang, C. H. (2011). Reliability analysis of basal – heave in a braced excavation in a 2D random field. *Comput. Geotech.* 39, 27–37. doi:10.1016/j.compgeo.2011.08.005

MATLAB 8.5 (2015). *[Computer software] natick*. MA: MathWorks.

Michalowski, R. L., and Cermak, J. (2002). Strength anisotropy of fiber-reinforced sand. *Comput. Geotech.* 29, 279–299. doi:10.1016/S0266-352X(01)00032-5

Moghal, A. A. B., Chittoori, B. C. S., Basha, B. M., and Al-Shamrani, M. A. (2017). Target reliability approach to study the effect of fiber reinforcement on UCS behaviour of lime treated semiarid soil. *J. Mater. Civ. Eng.* 1, 04017014. doi:10.1061/(ASCE)MT.1943-5533.0001835

Moghal, A. A. B., Chittoori, B. C. S., and Basha, M. (2016). Effect of fiber reinforcement on CBR behaviour of lime-blended expansive soils: reliability approach. *Road Mater. Pavement Des.* 1, 20. doi:10.1080/14680629.2016.1272479

Phoon, K.-K., and Kulhawy, F. H. (1999). Evaluation of geotechnical property variability. *Can. Geotech. J.* 36, 625–639. doi:10.1139/t99-039

Prabakar, J., and Sridhar, R. S. (2002). Effect of random inclusion of sisal fiber on strength behaviour of soil. *Constr. Build. Mater.* 16, 123–131. doi:10.1016/S0950-0618(02)00008-9

Ranjan, G., Vasan, R. M., and Charan, H. D. (1996). Probabilistic analysis of randomly distributed fiber-reinforced soil. *J. Geotech. Eng.* 122 (6), 419–426. doi:10.1061/(asce)0733-9410(1996)122:6(419)

Sharma, V., and Kumar, A. (2017). Influence of relative density of soil on performance of fiber-reinforced soil foundation. *Geotext. Geomembr.* 45, 499–507. doi:10.1016/j.geotexmem.2017.06.004

Sharma, V., and Kumar, A. (2019). Numerical study of ring and circular foundations resting on fiber-reinforced soil. *Int. J. Geotech. Eng.* 1, 13. doi:10.1080/19386362.2019.1603680

Singh, H. P., and Bagra, M. (2013). Improvement in CBR value of soil reinforced with jute fiber. *Int. J. Innov. Res. Sci. Eng. Technol.* 2 (4), 3448–3452.

Suchomel, R., and Masin, D. (2009). Comparison of different probabilistic method for predicting stability of a slope in spatially variable c—ϕ soil. *Comput. Geotech.* 37, 132–140. doi:10.1016/j.compgeo.2009.08.005

Syed, M., GuhaRay, A., Agarwal, S., and Kar, A. (2020). Stabilization of expansive clays by combined effects of geopolymerization and fiber reinforcement. *J. Inst. Eng. India Ser. A* 101 (1), 163–178. doi:10.1007/s40030-019-00418-3

Syed, M., and GuhaRay, A. (2020). Effect of fiber reinforcement on mechanical behaviour of alkali-activated binder-treated expansive soil: reliability-based approach. *Int. J. GeoMech.* 20 (12), 04020225. doi:10.1061/(ASCE)GM.1943-5622.0001871

Tang, C.-S., Li, J., Wang, D. –Y., and Shi, B. (2016). Investigation on the interfacial mechanical behaviour of wave-shaped fiber reinforced soil by pullout test. *Geotext. Geomembr.* 44 (6), 1–12. doi:10.1016/j.geotexmem.2016.05.001

Tang, C., Shi, B., Gao, W., Chen, F., and Cai, Y. (2007). Strength and mechanical behaviour of short polypropylene fiber reinforced and cement stabilized clayey soil. *Geotext. Geomembr.* 25, 194–202. doi:10.1016/j.geotexmem.2006.11.002

Toh, W., Raju, K., Yeo, C. H., Goh, S. H., and Tan, V. B. C. (2017). "Experimental and numerical analysis of fiber-reinforced composite pipes subjected to underground blasts," in 21st international conference on composite materials, Xi'an, China, August 20–25, 2017.

Wang, Y., Guo, P., Lin, H., Li, X., Zhao, Y., Yuan, B., et al. (2019). Numerical analysis of fiber-reinforced soils based on the equivalent additional stress concept. *Int. J. Geo. Mech.* 19 (11), 04019122. doi:10.1061/(ASCE)GM.1943-5622.0001504

Zaskórski, Ł., Puła, W., and Griffiths, D. V. (2017). Bearing capacity assessment of a shallow foundation on a two-layered soil using the random finite element method. *Georisk*, 468–477. doi:10.1061/9780784480724.042

Conflict of Interest: The authors declare that the research was conducted in the absence of any commercial or financial relationships that could be construed as a potential conflict of interest.

Advantages of publishing in Frontiers

OPEN ACCESS
Articles are free to read for greatest visibility and readership

FAST PUBLICATION
Around 90 days from submission to decision

HIGH QUALITY PEER-REVIEW
Rigorous, collaborative, and constructive peer-review

TRANSPARENT PEER-REVIEW
Editors and reviewers acknowledged by name on published articles

Frontiers
Avenue du Tribunal-Fédéral 34
1005 Lausanne | Switzerland

Visit us: www.frontiersin.org
Contact us: frontiersin.org/about/contact

REPRODUCIBILITY OF RESEARCH
Support open data and methods to enhance research reproducibility

DIGITAL PUBLISHING
Articles designed for optimal readership across devices

FOLLOW US
@frontiersin

IMPACT METRICS
Advanced article metrics track visibility across digital media

EXTENSIVE PROMOTION
Marketing and promotion of impactful research

LOOP RESEARCH NETWORK
Our network increases your article's readership